

**REDOX AND PHOTOACTIVE METAL COMPLEXES WITH  
APPLICATIONS IN CATALYSIS, EMISSIVE MATERIALS, AND SENSING**

by

Gabriel A. Andrade

A dissertation submitted to the Faculty of the University of Delaware in partial fulfillment of the requirements for the degree of Doctor of Philosophy in Chemistry and Biochemistry

Summer 2017

© 2017 Gabriel A. Andrade  
All Rights Reserved

**REDOX AND PHOTOACTIVE METAL COMPLEXES WITH  
APPLICATIONS IN CATALYSIS, EMISSIVE MATERIALS, AND SENSING**

by

Gabriel A. Andrade

Approved: \_\_\_\_\_  
Murray V. Johnston, Ph.D.  
Chair of the Department of Chemistry and Biochemistry

Approved: \_\_\_\_\_  
George H. Watson, Ph.D.  
Dean of the College of Arts and Sciences

Approved: \_\_\_\_\_  
Ann L. Ardis, Ph.D.  
Senior Vice Provost for Graduate and Professional Education

I certify that I have read this dissertation and that in my opinion it meets the academic and professional standard required by the University as a dissertation for the degree of Doctor of Philosophy.

Signed:

---

Joel Rosenthal, Ph.D.  
Professor in charge of dissertation

I certify that I have read this dissertation and that in my opinion it meets the academic and professional standard required by the University as a dissertation for the degree of Doctor of Philosophy.

Signed:

---

Mary P. Watson, Ph.D.  
Member of dissertation committee

I certify that I have read this dissertation and that in my opinion it meets the academic and professional standard required by the University as a dissertation for the degree of Doctor of Philosophy.

Signed:

---

Klaus H. Theopold, PhD.  
Member of dissertation committee

I certify that I have read this dissertation and that in my opinion it meets the academic and professional standard required by the University as a dissertation for the degree of Doctor of Philosophy.

Signed:

---

Raul F. Lobo, Ph.D.  
Member of dissertation committee

## ACKNOWLEDGMENTS

I would like to dedicate this work to my mom, Rose Marie Andrade, she has dedicated her life to her sons and family and without her none of this would be possible. Thank you for always inspiring us to reach the top. I would like to thank my daughter Adelyn Rose, you are my constant motivation to better myself so that you will always have a father to look up to. Your sweetness, love, and silliness are contagious and have given me so many wonderful memories. Last but not least I would like to thank my brothers, Tony, James, and Daniel for all of their support and encouragement over the years with a special thank you to my little brother, Daniel. The kindness you have always shown me means so much and I am ever grateful.

I would like to thank my advisor Joel Rosenthal for the opportunity to work in your lab. Your lab has allowed me to develop greatly as a research chemist. Further I have learned so much from you through coursework and discussions. Also, I would like to thank my committee members, Dr. Mary Watson, Dr. Klaus Theopold, and Dr. Raul Lobo for their time and guidance through serving on my doctoral committee.

Additionally, I would like to thank my coworkers and friends at the University of Delaware for your friendship and help through graduate school. Also, to my longtime friend and undergraduate mentor, Dr. Kris Waynant, who showed me the art of synthesis. Finally, to my girlfriend and colleague, Stephanie Velardo, who has given me so much support in everything I pursue.

## TABLE OF CONTENTS

LIST OF TABLES .....	xiii
LIST OF FIGURES .....	xvii
LIST OF SCHEMES .....	xxiii
ABSTRACT .....	xxiv

### Chapter

1	PALLADIUM NHC COMPLEXES FOR ELECTROCATALYTIC CO <sub>2</sub> REDUCTION .....	1
1.1	Motivation for the Discovery of Transition Metal Complexes for the Electrochemical Transformation of CO <sub>2</sub> to CO. ....	1
1.1.1	Historical and Predicted Global Energy Demand .....	1
1.1.2	Issues Associated with Fossil Fuel Consumption .....	3
1.1.3	Utilization of Solar Energy by Storage in Chemical Bonds .....	5
1.2	Palladium Pincer Complexes for CO <sub>2</sub> Reduction.....	7
1.3	Design of an NHC based Palladium Complex for CO <sub>2</sub> Reduction .....	9
1.3.1	Palladium N-heterocyclic Pincer Complex for CO <sub>2</sub> Reduction ....	9
1.3.2	N-heterocyclic Carbenes vs. Phosphines as Ligands .....	9
1.3.3	Design of [PDC <sup>R</sup> Pd(Y)]X Complex .....	10
1.4	Experimental.....	11
1.4.1	General Materials and Methods.....	11
1.4.2	Compound Characterization .....	11
1.4.3	X-Ray Crystallography.....	12
1.4.4	Electrochemical Measurements.....	14
1.4.5	Synthesis and Characterization.....	15
1.4.5.1	Synthesis of 1-Cyclohexyl-1H-imidazole .....	15
1.4.5.2	Synthesis of 2,6-Bis[3-(ethyl)imidazolium]pyridine dibromide.....	16
1.4.5.3	Synthesis of 2,6-Bis[3-(isopropyl)imidazolium]pyridine dibromide .....	16

1.4.5.4	Synthesis of 2,6-Bis[3-(cyclohexyl)imidazolium]pyridine dibromide.....	17
1.4.5.5	General Procedure (A) for Metalation with Pd(OAc) <sub>2</sub> .	17
1.4.5.6	General Procedure (B) for Metalation/Transmetalation with Ag <sub>2</sub> O and [Pd(Br) <sub>2</sub> (MeCN) <sub>2</sub> ] .....	18
1.4.5.7	Synthesis of [PDC <sup>Et</sup> Pd(Br)]Br.....	18
1.4.5.8	Synthesis of [PDC <sup>Ipr</sup> Pd(Br)]Br .....	19
1.4.5.9	Synthesis of [PDC <sup>Cy</sup> Pd(Br)]Br .....	19
1.4.5.10	Synthesis of [PDC <sup>Mes</sup> Pd(Br)]Br.....	20
1.4.5.11	Synthesis of [PDC <sup>Dipp</sup> Pd(Br)]Br.....	20
1.4.5.12	General Procedure for the Formation of the Acetonitrile Solvato Complex .....	21
1.4.5.13	Synthesis of [PDC <sup>Me</sup> Pd(MeCN)](PF <sub>6</sub> ) <sub>2</sub> .....	21
1.4.5.14	Synthesis of [PDC <sup>Et</sup> Pd(MeCN)](PF <sub>6</sub> ) <sub>2</sub> .....	21
1.4.5.15	Synthesis of [PDC <sup>Ipr</sup> Pd(MeCN)](PF <sub>6</sub> ) <sub>2</sub> .....	22
1.4.5.16	Synthesis of [PDC <sup>Cy</sup> Pd(MeCN)](PF <sub>6</sub> ) <sub>2</sub> .....	22
1.4.5.17	Synthesis of [PDC <sup>Mes</sup> Pd(MeCN)](PF <sub>6</sub> ) <sub>2</sub> .....	22
1.4.5.18	Synthesis of [PDC <sup>Dipp</sup> Pd(MeCN)](PF <sub>6</sub> ) <sub>2</sub> .....	23
1.4.5.19	Synthesis of [PDC <sup>Cy</sup> AgBr] .....	23
1.5	Synthetic Pathway to PDC <sup>R</sup> complexes. ....	24
1.5.1	Synthesis of the Proligands. ....	24
1.5.2	Metalation with Pd(OAc) <sub>2</sub> .....	25
1.5.3	Transmetallation strategy with Ag <sub>2</sub> O .....	26
1.5.4	Synthesis of the Solvato Complex.....	28
1.6	Characterization of the Steric Environment .....	30
1.6.1	%V <sub>Bur</sub> Steric Calculation .....	30
1.6.2	Steric G-value Obtained from Solid Angles.....	32
1.7	Electrochemical Characterization and CO <sub>2</sub> Activation of [PDC <sup>Cy</sup> Pd(MeCN)](PF <sub>6</sub> ) <sub>2</sub> .....	33
1.7.1	Cyclic Voltammetry studies of [PDC <sup>Cy</sup> Pd(MeCN)](PF <sub>6</sub> ) <sub>2</sub> .....	34
1.7.2	Randles–Sevcik Analysis .....	35
1.7.3	Electrochemical Studies Saturated with CO <sub>2</sub> .....	37
1.7.4	Electrochemical Studies with HBF <sub>4</sub> .....	39
1.7.5	Electrochemical Studies with Mg(ClO <sub>4</sub> ) <sub>2</sub> .....	41
1.7.6	Summary of Electrochemical Results with [PDC <sup>Cy</sup> Pd(MeCN)](PF <sub>6</sub> ) <sub>2</sub> .....	44

1.8	Electrochemistry Studies of [PDC <sup>R</sup> Pd(MeCN)](PF <sub>6</sub> ) <sub>2</sub> Complexes.....	44
1.8.1	CV Studies of [PDC <sup>R</sup> Pd(MeCN)](PF <sub>6</sub> ) <sub>2</sub> Complexes.....	44
1.9	Correlation of Steric Environment and Electrochemical Activity .....	46
1.10	Comparison to [PDC <sup>nBu</sup> Pd(Br)](Br) .....	47
1.11	Concluding Remarks .....	48
REFERENCES.....		50
2	A RHENIUM BIPYRIDINE COMPLEX WITH A COVALENTLY TETHERED BODIPY FOR PHOTOCATALYTIC CO <sub>2</sub> CONVERSION.....	52
2.1	Motivation for the Discovery of Rhenium Systems for Photocatalytic CO <sub>2</sub> Conversion.....	52
2.1.1	Photoactive Transition Metal Complexes for Energy Storage ....	52
2.1.2	Photochemical CO <sub>2</sub> Activation.....	53
2.1.3	Rhenium Bipyridine Systems for Photocatalytic CO <sub>2</sub> Activation .....	54
2.1.4	Photocatalytic Cycle of [Re(bpy)(CO) <sub>3</sub> Cl] with CO <sub>2</sub> .....	55
2.1.5	Metrics and Drawbacks of [Re(bpy)(CO) <sub>3</sub> Cl].....	57
2.1.6	Design of Ru System with a Tethered BODIPY Organic Chromophore .....	58
2.2	Experimental.....	59
2.2.1	General Materials and Methods.....	59
2.2.2	Compound Characterization .....	60
2.2.3	Electrochemical Measurements .....	61
2.2.4	UV-Vis Absorption Experiments .....	61
2.2.5	Steady-State Fluorescence Measurements .....	61
2.2.6	Time-Resolved Fluorescence Measurements .....	62
2.2.7	X-Ray Structure Determination.....	63
2.2.8	Photocatalytic CO <sub>2</sub> Reduction and Headspace Analysis.....	63
2.2.9	Synthesis and Characterization.....	64
2.2.9.1	Synthesis of [Re(4-Bromomethyl-4'-methyl-2,2'-bipyridine)(CO) <sub>3</sub> Cl] (2).....	64
2.2.9.2	Synthesis of [Re(4-Azidomethyl-4'-methyl-2,2'-bipyridine)(CO) <sub>3</sub> Cl] (3).....	65
2.2.9.3	Synthesis of N-(benzoyloxy)succinimide.....	66
2.2.9.4	Synthesis of N-propargylbenzamide .....	66
2.2.9.5	Synthesis of [Re(Mebpy)(CO) <sub>3</sub> Cl]-Phenyl.....	67

2.2.9.6	Synthesis of 8-(4-(N-(prop-2-yn-1-yl)benzamide)-2,8-diethyl-1,3,7,9-tetramethyl-BODIPY).....	67
2.2.9.7	Synthesis of [Re(Mebpy)(CO) <sub>3</sub> Cl]-BODIPY .....	68
2.2.9.8	Synthesis of 8-(4-(benzamido)methyl-1-benzyl-1H-1,2,3-triazole)-2,8-diethyl-1,3,7,9-tetramethyl-BODIPY .....	69
2.3	Synthetic Pathway to Re-BODIPY Photocatalyst and Control Compounds.....	70
2.3.1	Synthesis of Rhenium Fragment .....	70
2.3.2	Synthesis of Organic BODIPY Fragment and Coupling.....	71
2.3.3	Synthesis of Control Compounds.....	73
2.4	Electrochemical Studies .....	74
2.5	Photophysical Properties .....	77
2.6	Photocatalytic Studies .....	79
2.7	Concluding Remarks .....	83
	REFERENCES .....	85
3	PALLADIUM CCC PINCER COMPLEXES CONTAINING NHC LIGANDS FOR APPLICATIONS IN EMISSIVE MATERIALS AND SENSING .....	89
3.1	Motivation for the Discovery of Palladium Based Materials for Emissive Materials .....	89
3.1.1	Applications of Photoactive Transition Metal Complexes.....	89
3.1.2	Color of Materials Based on CIE Coordinates .....	90
3.1.3	Successful Metal Based Complexes for OLED Applications and Design Properties.....	91
3.1.4	Group 10 Emissive Metals Systems Supported by NHC Ligands .....	92
3.1.5	Design of a Phenyl Spaced Bis-NHC Palladium Complex .....	94
3.2	Experimental.....	96
3.2.1	General Materials and Methods.....	96
3.2.2	Compound Characterization .....	96
3.2.3	Electrochemical Measurements.....	97
3.2.4	Photophysical Measurements .....	97
3.2.5	X-ray Crystallography .....	98
3.2.6	X-ray Photoelectron Spectroscopy .....	99

3.2.7	Synthesis and Characterization.....	100
3.2.7.1	Synthesis of proligand 1H-Imidazolium, 3,3'-(1,3-phenylene)bis[1-ethyl-, bromide (3).....	100
3.2.7.2	Synthesis of [PhDC <sup>Et</sup> Pd(Br)].....	100
3.2.7.3	Synthesis of [PhDC <sup>Et</sup> Pd(MeCN)]PF <sub>6</sub> .....	101
3.2.7.4	Synthesis of [PhDC <sup>Et</sup> Pd(Py)]PF <sub>6</sub> .....	101
3.2.7.5	Synthesis of [PhDC <sup>Et</sup> Pd( <sup>t</sup> BuNC)]PF <sub>6</sub> .....	102
3.2.7.6	Synthesis of [PhDC <sup>Et</sup> Pd(PPh <sub>3</sub> )]PF <sub>6</sub> .....	103
3.2.7.7	Synthesis of [PhDC <sup>Et</sup> Ni(Br)].....	103
3.2.7.8	Synthesis of [PhDC <sup>Et</sup> Ni(MeCN)]PF <sub>6</sub> .....	104
3.3	Synthetic Pathway to PhDC <sup>Et</sup> Palladium Complexes.....	104
3.3.1	Synthesis of the PhDC <sup>Et</sup> Proligand.....	104
3.3.2	Synthesis of [PhDC <sup>Et</sup> Pd] Complexes .....	105
3.4	Characterization of [PhDC <sup>Et</sup> Pd(Br)] and [PhDC <sup>Et</sup> Pd(MeCN)]PF <sub>6</sub> .....	107
3.4.1	Solid State Characterization and Comparison.....	107
3.4.2	Redox Properties and Comparison .....	109
3.4.3	Solution State Photophysical Properties.....	111
3.4.4	Solid State Photophysical Properties.....	112
3.4.5	CIE Color Coordinates .....	114
3.5	Substitution of the Ancillary Ligand .....	116
3.5.1	Synthetic Pathway to Pyridine, PPh <sub>3</sub> and <sup>t</sup> BuNC Complexes ...	116
3.6	Photophysical Properties of [PhDC <sup>Et</sup> Pd(X)]PF <sub>6</sub> complexes .....	117
3.6.1	Solid State Absorbance of [PhDC <sup>Et</sup> Pd(X)]PF <sub>6</sub> complexes.....	117
3.6.2	Solid State Emission of [PhDC <sup>Et</sup> Pd(X)]PF <sub>6</sub> complexes.....	119
3.7	Solid State Structures and Analysis.....	120
3.8	Vapochromic Behavior of PhDC <sup>Et</sup> Pd Complexes.....	125
3.8.1	Vapochromic Response to Pyridine .....	125
3.8.2	X-ray Photoelectron Spectroscopy Studies .....	128
3.9	Synthesis of PhDC <sup>Et</sup> Ni Complexes .....	132
3.10	Concluding Remarks .....	135
	REFERENCES .....	136

## Appendix

A	CRYSTALLOGRAPHIC DATA FOR PDC COMPLEXES.....	141
A.1	General Numbering Scheme for Solid State Structures of PDC Complexes .....	141
A.2	Crystallographic Experimental Data .....	141
A.2.1	Crystallographic Experimental Data for PDC <sup>Cy</sup> Pd Intermediates .....	141
A.2.2	Crystallographic Experimental Data for [PDC <sup>R</sup> Pd(Br)]Br Complexes .....	142
A.2.3	Crystallographic Experimental Data for [PDC <sup>R</sup> Pd(MeCN)](PF <sub>6</sub> ) <sub>2</sub> Complexes Where R = Me, Et, Ipr ...	143
A.2.4	Crystallographic Experimental Data for [PDC <sup>R</sup> Pd(MeCN)](PF <sub>6</sub> ) <sub>2</sub> Complexes Where R = Cy, Mes, Dipp .....	144
A.3	[PDC <sup>Cy</sup> Pd(Br) <sub>3</sub> ] Crystal Data .....	145
A.3.1	Bond Lengths and Angles for [PDC <sup>Cy</sup> Pd(Br) <sub>3</sub> ] .....	146
A.4	Crystal Data for [PDC <sup>Cy</sup> Ag(Br)] .....	149
A.5	Crystal Data for [PDC <sup>Et</sup> Pd(Br)](Br) .....	155
A.6	Crystal Data for [PDC <sup>Cy</sup> Pd(Br)](Br) .....	157
A.7	Crystal Data for [PDC <sup>Dipp</sup> Pd(Br)](Br) .....	161
A.8	Crystal Data for [PDC <sup>Me</sup> Pd(MeCN)](PF <sub>6</sub> ) <sub>2</sub> .....	166
A.9	Crystal Data for [PDC <sup>Et</sup> Pd(MeCN)](PF <sub>6</sub> ) <sub>2</sub> .....	169
A.10	Crystal Data for [PDC <sup>Ipr</sup> Pd(MeCN)](PF <sub>6</sub> ) <sub>2</sub> .....	172
A.11	Crystal Data for [PDC <sup>Cy</sup> Pd(MeCN)](PF <sub>6</sub> ) <sub>2</sub> .....	174
A.12	Crystal Data for [PDC <sup>Mes</sup> Pd(MeCN)](PF <sub>6</sub> ) <sub>2</sub> .....	177
A.13	Crystal Data for [PDC <sup>Dipp</sup> Pd(MeCN)](PF <sub>6</sub> ) <sub>2</sub> .....	179
B	CRYSTALLOGRAPHIC DATA FOR RE COMPLEXES .....	183
B.1	Crystallographic Experimental Data .....	183
B.1.1	Crystallographic Experimental Data for Compounds (3) and (9) .....	183
B.2	Crystal Data of ReN <sub>3</sub> Intermediate (3) .....	184
B.2.1	Bond Lengths and Angles for Intermediate (3).....	184

B.3	Crystal Data for Transition Metal Control (9).....	187
B.3.1	Bond Lengths and Angles for Complex (9) .....	187
B.4	Permission Letter.....	190
C	CRYSTALLOGRAPHIC DATA FOR PHDC COMPLEXES.....	192
C.1	Crystallographic Experimental Data .....	192
C.1.1	Crystallographic Experimental Data for [PhDC <sup>Et</sup> Pd(Br)] and [PhDC <sup>Et</sup> Pd(MeCN)]PF <sub>6</sub> .....	192
C.1.2	Crystallographic Experimental Data for [PhDC <sup>Et</sup> Pd(Py)]PF <sub>6</sub> , [PhDC <sup>Et</sup> Pd( <sup>t</sup> BuNC)]PF <sub>6</sub> , and [PhDC <sup>Et</sup> Pd(PPh <sub>3</sub> )]PF <sub>6</sub> .....	193
C.1.3	Crystallographic Experimental Data for [PhDC <sup>Et</sup> Ni(Br)] and [PhDC <sup>Et</sup> Ni(MeCN)]PF <sub>6</sub> .....	194
C.2	[PhDC <sup>Et</sup> Pd(Br)] Crystal Data .....	195
C.2.1	Bond Lengths and Angles for [PhDC <sup>Et</sup> Pd(Br)] .....	195
C.3	[PhDC <sup>Et</sup> Pd(MeCN)]PF <sub>6</sub> Crystal Data.....	200
C.3.1	Bond Lengths and Angles for [PhDC <sup>Et</sup> Pd(MeCN)]PF <sub>6</sub> .....	201
C.4	[PhDC <sup>Et</sup> Pd(Py)]PF <sub>6</sub> Crystal Data .....	203
C.4.1	Bond Lengths and Angles for [PhDC <sup>Et</sup> Pd(Py)]PF <sub>6</sub> .....	204
C.5	[PhDC <sup>Et</sup> Pd( <sup>t</sup> BuNC)]PF <sub>6</sub> Crystal Data.....	207
C.5.1	Bond Lengths and Angles for [PhDC <sup>Et</sup> Pd( <sup>t</sup> BuNC)]PF <sub>6</sub> .....	208
C.6	[PhDC <sup>Et</sup> Pd(PPh <sub>3</sub> )]PF <sub>6</sub> Crystal Data.....	211
C.6.1	Bond Lengths and Angles for [PhDC <sup>Et</sup> Pd(PPh <sub>3</sub> )]PF <sub>6</sub> .....	212
C.7	[PhDC <sup>Et</sup> Ni(Br)] Crystal Data.....	216
C.7.1	Bond Lengths and Angles for [PhDC <sup>Et</sup> Ni(Br)] .....	216
C.8	[PhDC <sup>Et</sup> Ni(MeCN)]PF <sub>6</sub> Crystal Data.....	220
C.8.1	Bond Lengths and Angles for [PhDC <sup>Et</sup> Ni(MeCN)]PF <sub>6</sub> .....	221



## LIST OF TABLES

Table 1.1: Selected bond lengths and angles for solid-state structures of the isolated intermediates .....	26
Table 1.2: Selected bond lengths and angles for the series of [PDC <sup>R</sup> Pd(MeCN)](PF <sub>6</sub> ) <sub>2</sub> complexes. The * denotes that due to the mesityl and diisopropylphenyl complexes containing a mirror plane in the solid-state the bond lengths: C1-Pd = C11-Pd, and C2-C3 = C9-C10. ....	30
Table 1.3: Calculated values obtained from crystal data for the steric bulk around the metal center. This data for the G-values were obtained using the online software Solid G, and the %V <sub>Bur</sub> values were obtained using the online software SambVca.....	31
Table 1.4: Parameters and metrics for CPE experiments with [PDC <sup>Cy</sup> Pd(MeCN)](PF <sub>6</sub> ) <sub>2</sub> .....	39
Table 1.5: Observed current enhancement for a series of [PDC <sup>R</sup> Pd(MeCN)](PF <sub>6</sub> ) <sub>2</sub> complexes under CO <sub>2</sub> and N <sub>2</sub> where R = Et, Cy, Mes and Dipp. The values are given for the potential at which the current enhancement is observed.....	46
Table 2.1: Experimental results from photolysis and steady-state and time resolved emission experiments. ....	79
Table 3.1: Selected bond lengths and angles for the PDC <sup>Et</sup> and PhDC <sup>Et</sup> palladium halide and solvato complexes, where the outer sphere counter ions are omitted from the formula and X denotes the ligand at the fourth coordination site which is either Br or MeCN. ....	109
Table 3.2: Top: Selected bond lengths and angles for [PhDC <sup>Et</sup> Pd(X)] complexes, where the outer sphere counter ions (if present) are omitted from the formula and X denotes the ligand at the fourth coordination site which is either bromide (Br), acetonitrile (MeCN), pyridine (Py), tert-butyl isonitrile ( <sup>t</sup> BuNC), or triphenylphosphine (PPh <sub>3</sub> ). Bottom: Closest ligand–ligand and Pd–Pd distances found in the crystal packing. The blue text denotes the complexes which were found to be emissive. ....	122

Table 3.3: Selected bond lengths and angles for the [PDC <sup>Me</sup> Ni(Br)]Br, [PDC <sup>Me</sup> Ni(MeCN)] <sub>2</sub> (OTf), [PhDC <sup>Et</sup> Ni(Br)] and [PhDC <sup>Et</sup> Ni(MeCN)]PF <sub>6</sub> complexes, where X denotes the ligand at the fourth coordination site which is either Br or MeCN and the outer sphere counterions are omitted in the table formula. ....	134
Table A.1: Crystallographic experimental data for PDC <sup>Cy</sup> Pd intermediates .....	142
Table A.2: Crystallographic experimental data for [PDC <sup>R</sup> Pd(Br)]Br complexes .....	143
Table A.3: Crystallographic experimental data for [PDC <sup>R</sup> Pd(MeCN)](PF <sub>6</sub> ) <sub>2</sub> complexes where R = Me, Et, Ipr .....	144
Table A.4 Crystallographic experimental data for [PDC <sup>R</sup> Pd(MeCN)](PF <sub>6</sub> ) <sub>2</sub> complexes where R = Cy, Mes, Dipp .....	145
Table A5: Bond lengths for [PDC <sup>Cy</sup> Pd(Br) <sub>3</sub> ] .....	147
Table A.6: Bond angles for [PDC <sup>Cy</sup> Pd(Br) <sub>3</sub> ] .....	149
Table A.7: Bond lengths for [PDC <sup>Cy</sup> Ag(Br)] .....	152
Table A.8: Bond angles for [PDC <sup>Cy</sup> Ag(Br)] .....	155
Table A.9: Bond lengths for [PDC <sup>Et</sup> Pd(Br)] (Br) .....	156
Table A.10: Bond angles for [PDC <sup>Et</sup> Pd(Br)](Br) .....	157
Table A.11: Bond lengths for [PDC <sup>Cy</sup> Pd(Br)](Br) .....	159
Table A.12: Bond angles for [PDC <sup>Cy</sup> Pd(Br)](Br) .....	161
Table A.13: Bond lengths for [PDC <sup>Dipp</sup> Pd(Br)](Br) .....	163
Table A:14: Bond angles for [PDC <sup>Dipp</sup> Pd(Br)](Br) .....	166
Table A.15: Bond lengths for [PDC <sup>Me</sup> Pd(MeCN)](PF <sub>6</sub> ) <sub>2</sub> .....	168
Table A.16: Bond angles for [PDC <sup>Me</sup> Pd(MeCN)](PF <sub>6</sub> ) <sub>2</sub> .....	169
Table A.17: Bond lengths for [PDC <sup>Et</sup> Pd(MeCN)](PF <sub>6</sub> ) <sub>2</sub> .....	170
Table A.18: Bond angles for [PDC <sup>Et</sup> Pd(MeCN)](PF <sub>6</sub> ) <sub>2</sub> .....	172
Table A.19: Bond lengths for [PDC <sup>Ipr</sup> Pd(MeCN)](PF <sub>6</sub> ) <sub>2</sub> .....	173

Table A.20: Bond angles for [PDC <sup>Ipr</sup> Pd(MeCN)](PF <sub>6</sub> ) <sub>2</sub> .....	174
Table A.21: Bond lengths for [PDC <sup>Cy</sup> Pd(MeCN)](PF <sub>6</sub> ) <sub>2</sub> .....	176
Table A.22: Bond angles for [PDC <sup>Cy</sup> Pd(MeCN)](PF <sub>6</sub> ) <sub>2</sub> .....	177
Table A.23: Bond lengths for [PDC <sup>Mes</sup> Pd(MeCN)](PF <sub>6</sub> ) <sub>2</sub> .....	179
Table A.24: Bond angles for [PDC <sup>Mes</sup> Pd(MeCN)](PF <sub>6</sub> ) <sub>2</sub> .....	179
Table A.25: Bond lengths for [PDC <sup>Dipp</sup> Pd(MeCN)](PF <sub>6</sub> ) <sub>2</sub> .....	181
Table A.26: Bond angles for [PDC <sup>Dipp</sup> Pd(MeCN)](PF <sub>6</sub> ) <sub>2</sub> .....	182
Table B.1: Crystallographic experimental data for complexes (3) and (9) .....	184
Table B.2: Bond Lengths for ReN <sub>3</sub> intermediate (3).....	185
Table B.3 Bond Angles for ReN <sub>3</sub> intermediate (3) .....	187
Table B.4: Bond lengths for complex (9).....	188
Table B.5: Bond angles for complex (9) .....	190
Table C.1: Crystallographic experimental data for [PhDC <sup>Et</sup> Pd(Br)] and [PhDC <sup>Et</sup> Pd(MeCN)]PF <sub>6</sub> .....	193
Table C.2: Crystallographic experimental data for [PhDC <sup>Et</sup> Pd(Py)]PF <sub>6</sub> , [PhDC <sup>Et</sup> Pd( <sup>t</sup> BuNC)]PF <sub>6</sub> , and [PhDC <sup>Et</sup> Pd(PPh <sub>3</sub> )]PF <sub>6</sub> where X is the ancillary ligand. ....	194
Table C.3: Crystallographic experimental data for [PhDC <sup>Et</sup> Ni(Br)] and [PhDC <sup>Et</sup> Ni(MeCN)]PF <sub>6</sub> .....	195
Table C.4: Bond lengths for [PhDC <sup>Et</sup> Pd(Br)].....	197
Table C.5: Bond angles for [PhDC <sup>Et</sup> Pd(Br)] .....	200
Table C.6: Bond lengths for [PhDC <sup>Et</sup> Pd(MeCN)]PF <sub>6</sub> .....	202
Table C.7: Bond angles for [PhDC <sup>Et</sup> Pd(MeCN)]PF <sub>6</sub> .....	203
Table C.8: Bond lengths for [PhDC <sup>Et</sup> Pd(Py)]PF <sub>6</sub> .....	206
Table C.9: Bond angles for [PhDC <sup>Et</sup> Pd(Py)]PF <sub>6</sub> .....	207

Table C.10: Bond lengths for $[\text{PhDC}^{\text{Et}}\text{Pd}(\text{tBuNC})]\text{PF}_6$ .....	209
Table C.11: Bond angles for $[\text{PhDC}^{\text{Et}}\text{Pd}(\text{tBuNC})]\text{PF}_6$ .....	211
Table C.12: Bond lengths for $[\text{PhDC}^{\text{Et}}\text{Pd}(\text{PPh}_3)]\text{PF}_6$ .....	214
Table C.13: Bond angles for $[\text{PhDC}^{\text{Et}}\text{Pd}(\text{PPh}_3)]\text{PF}_6$ .....	216
Table C.14: Bond lengths for $[\text{PhDC}^{\text{Et}}\text{Ni}(\text{Br})]$ .....	218
Table C.15: Bond angles for $[\text{PhDC}^{\text{Et}}\text{Ni}(\text{Br})]$ .....	220
Table C.16: Bond lengths for $[\text{PhDC}^{\text{Et}}\text{Ni}(\text{MeCN})]\text{PF}_6$ .....	222
Table C.17: Bond angles for $[\text{PhDC}^{\text{Et}}\text{Ni}(\text{MeCN})]\text{PF}_6$ .....	223

## LIST OF FIGURES

Figure 1.1: Global Energy Consumption with historical data in blue and predicted data in red. <sup>1</sup> .....	1
Figure 1.2: Global energy consumption by type for historical data (2015 and previous) and predicted data (2020 to 2040). <sup>1</sup> .....	3
Figure 1.3: Seasonally corrected atmospheric CO <sub>2</sub> concentration taken at the Mauna Loa observatory from 1980 to 2015 (black trace), as well as the global temperature anomaly over the same period (red trace). .....	4
Figure 1.4: The process of how CO <sub>2</sub> can be converted to synthetic fuels through the water gas shift followed by the Fischer-Tropsch process. ....	6
Figure 1.5: CO <sub>2</sub> electrochemical activation mechanism by palladium triphos systems. ....	7
Figure 1.6: (a) and (b) show triphos and PDC palladium complexes with an acetonitrile ancillary ligand. ....	10
Figure 1.7: Solid-state structures of the intermediates isolated during the metalation and transmetalation reactions. [PDC <sup>Cy</sup> Pd(Br) <sub>3</sub> ] is displayed at the 50 % thermal ellipsoid probability while [PDC <sup>Cy</sup> Ag(Br)] is shown at the 30 % probability level to better display the structure, a Br <sup>-</sup> counterion was also omitted for clarity on the Ag structure. ....	25
Figure 1.8: Solid state structures of all derivatives of the [PDC <sup>R</sup> Pd(MeCN)] complexes from left to right R=: methyl, ethyl, isopropyl, cyclohexyl, mesityl, and diisopropylphenyl at 50 % probability. Hydrogen atoms and PF <sub>6</sub> <sup>-</sup> counterions have been omitted for clarity. ....	29
Figure 1.9: Images obtained from the Solid G software for the methyl and diisopropylphenyl derivatives. The blue and yellow colors show the percentage of the sphere shielded by the PDC and MeCN ligands respectively.....	33

Figure 1.10: Voltammogram of 2,6-Bis[3-(cyclohexyl)imidazolium]pyridine dibromide (green trace) and [PDC <sup>cy</sup> Pd(MeCN)](PF <sub>6</sub> ) <sub>2</sub> (blue trace).....	34
Figure 1.11: Scan rate study and Randles–Sevcik plot of [PDC <sup>cy</sup> Pd(MeCN)](PF <sub>6</sub> ) <sub>2</sub> ..	36
Figure 1.12: Voltammogram of [PDC <sup>cy</sup> Pd(MeCN)](PF <sub>6</sub> ) <sub>2</sub> under N <sub>2</sub> (blue trace) and CO <sub>2</sub> (red trace) at 0.25 V/s. ....	37
Figure 1.13: Current density vs. time plot for the CPE experiment of [PDC <sup>cy</sup> Pd(MeCN)](PF <sub>6</sub> ) <sub>2</sub> (a), and CVs before and after the CPE experiment (b). ....	38
Figure 1.14: CV and CPE results for the addition of HBF <sub>4</sub> to [PDC <sup>cy</sup> Pd(MeCN)](PF <sub>6</sub> ) <sub>2</sub> .....	40
Figure 1.15: Voltammogram of [PDC <sup>cy</sup> Pd(MeCN)](PF <sub>6</sub> ) <sub>2</sub> under N <sub>2</sub> (blue trace), CO <sub>2</sub> (red trace), and CO <sub>2</sub> with added Mg(ClO <sub>4</sub> ) <sub>2</sub> (purple trace). ....	42
Figure 1.16: CPE results for the addition of Mg(ClO <sub>4</sub> ) <sub>2</sub> to [PDC <sup>cy</sup> Pd(MeCN)](PF <sub>6</sub> ) <sub>2</sub> . ....	43
Figure 1.17: Voltammograms for [PDC <sup>R</sup> Pd(MeCN)](PF <sub>6</sub> ) <sub>2</sub> complexes under N <sub>2</sub> (black trace) and CO <sub>2</sub> (red trace) where R = Et (a), Cy (b), Mes (c), and Dipp (d).....	45
Figure 2.1: Energy storage and fuels production through photocatalytic CO <sub>2</sub> reduction. ....	53
Figure 2.1: Photocatalytic activation of CO <sub>2</sub> by [Re(bpy)(CO) <sub>3</sub> Cl].....	56
Figure 2.3: Solar power spectrum from 280 to 900 nm. ....	57
Figure 2.4: Voltammogram of photocatalyst (7) (blue trace), transition metal control (9) (red trace) and photo control (10) (orange trace) .....	75
Figure 2.5: Voltammograms of photocatalyst (7) (blue data, left box) and transition metal control (9) (red data, right box) under a N <sub>2</sub> environment (solid traces) and under CO <sub>2</sub> (dashed traces) .....	76
Figure 2.6: Absorbance profile of photocatalyst (7) (blue trace), transition metal control (9) (red trace), and photo control (10) (orange trace) .....	78
Figure 2.7: Solid state structure of the bromide homologue of the transition metal control compound (9). Thermal ellipsoids are shown at the 50% probability level and hydrogen atoms have been removed for clarity ....	82

Figure 3.1: 1931 CIE diagram .....	90
Figure 3.2: RGB emissive transition metal complexes .....	91
Figure 3.3: Platinum and palladium phenyl spaced bis-NHC pincer complexes .....	93
Figure 3.4: Palladium metalation of pincer systems .....	95
Figure 3.5: Thermal ellipsoids of PDC and PhDC palladium halide and solvato structures shown at the 50% probability level with hydrogens and counterions omitted for clarity. ....	108
Figure 3.6: Cyclic voltammograms of the PDC <sup>Et</sup> and PhDC <sup>Et</sup> palladium solvato complexes .....	110
Figure 3.7: Absorbance profile of [PhDC <sup>Et</sup> Pd(Br)] (black trace) and [PhDC <sup>Et</sup> Pd(MeCN)]PF <sub>6</sub> (blue trace) in DMF.....	111
Figure 3.8: Solid state absorbance profile of [PhDC <sup>Et</sup> Pd(Br)] (black trace) and [PhDC <sup>Et</sup> Pd(MeCN)]PF <sub>6</sub> (blue trace). ....	112
Figure 3.9: Solid state absorbance (black trace) and emission (blue trace) of [PhDC <sup>Et</sup> Pd(MeCN)]PF <sub>6</sub> .....	113
Figure 3.10: CIE coordinates of [PhDC <sup>Et</sup> Pt(MeCN)]PF <sub>6</sub> (white dot) and fac-Ir(pmp) <sub>3</sub> (black dot).....	115
Figure 3.11: Solid state absorbance profiles of [PhDC <sup>Et</sup> Pd(X)]PF <sub>6</sub> and [PhDC <sup>Et</sup> Pd(Br)] (green trace) complexes where X = MeCN (blue trace), pyridine (red trace), PPh <sub>3</sub> (purple trace), and <sup>t</sup> BuNC (yellow trace). ....	118
Figure 3.12: Solid state emission of [PhDC <sup>Et</sup> Pd(MeCN)]PF <sub>6</sub> (blue trace) and [PhDC <sup>Et</sup> Pd(Py)]PF <sub>6</sub> (red trace).....	119
Figure 3.13: Solid state thermal ellipsoid plots for the [PhDC <sup>Et</sup> Pd(X)]PF <sub>6</sub> derivatives, from left to right, Py, <sup>t</sup> BuNC, and PPh <sub>3</sub> . All structures are shown at the 50% probability level with hydrogens and a PF <sub>6</sub> counterion omitted for clarity.....	120
Figure 3.14: Thermal ellipsoid plots of the crystal packing of [PhDC <sup>Et</sup> Pd(MeCN)]PF <sub>6</sub> (left) and [PhDC <sup>Et</sup> Pd(PPh <sub>3</sub> )]PF <sub>6</sub> (right) complexes shown at the 30% probability level and hydrogens and PF <sub>6</sub> counterions omitted for clarity. ....	123

Figure 3.15: Emission studies of $[\text{PhDC}^{\text{Et}}\text{Pd}(\text{PPh}_3)]\text{PF}_6$ exposed to pyridine vapors with excitation at 310 nm. ....	127
Figure 3.16: High resolution XPS spectra of the phosphorus region for the material obtained after the solid-state exchange reaction (green trace), synthesized $[\text{PhDC}^{\text{Et}}\text{Pd}(\text{Py})]\text{PF}_6$ (blue trace), synthesized $[\text{PhDC}^{\text{Et}}\text{Pd}(\text{PPh}_3)]\text{PF}_6$ (maroon trace), and $\text{PPh}_3$ (pink trace) .....	129
Figure 3.17: High resolution XPS spectra of the palladium region for the material obtained after the solid-state exchange reaction (green trace), synthesized $[\text{PhDC}^{\text{Et}}\text{Pd}(\text{Py})]\text{PF}_6$ (blue trace), synthesized $[\text{PhDC}^{\text{Et}}\text{Pd}(\text{PPh}_3)]\text{PF}_6$ (maroon trace). ....	130
Figure 3.18: High resolution XPS spectra of the nitrogen region for the material obtained after the solid-state exchange reaction (green trace), synthesized $[\text{PhDC}^{\text{Et}}\text{Pd}(\text{Py})]\text{PF}_6$ (blue trace), synthesized $[\text{PhDC}^{\text{Et}}\text{Pd}(\text{PPh}_3)]\text{PF}_6$ (maroon trace). ....	131
Figure 3.19: Thermal ellipsoid plots of the solid-state structure of $[\text{PhDC}^{\text{Et}}\text{Ni}(\text{Br})]$ (left) and $[\text{PhDC}^{\text{Et}}\text{Ni}(\text{MeCN})]\text{PF}_6$ (right) displayed at the 50% probability level with hydrogens and outer sphere counterions omitted (if present) for clarity. ....	133
Figure A.1: General numbering scheme used to label the solid-state structures, except for the Mes and Dipp derivative, which contained mirror planes down the center of the complexes in which case C1=C11, N1=N5, C2=C10, C3=C9, N2=N4, etc. ....	141
Figure A2: Fully labeled thermal ellipsoid plot of $[\text{PDC}^{\text{Cy}}\text{Pd}(\text{Br})_3]$ with hydrogens omitted at the 50% probability level .....	146
Figure A.3: Labeled thermal ellipsoid plot of $[\text{PDC}^{\text{Cy}}\text{Ag}(\text{Br})]$ with hydrogens and an outer sphere $\text{Br}^-$ omitted and shown at the 30% probability level. Numbering follows the general numbering scheme in the appendix. ....	149
Figure A.4: Fully labeled thermal ellipsoid plot of $[\text{PDC}^{\text{Et}}\text{Pd}(\text{Br})](\text{Br})$ with hydrogens and an outer sphere $\text{Br}^-$ omitted and shown at the 50% probability level.....	155
Figure A.5: Fully labeled thermal ellipsoid plot of $[\text{PDC}^{\text{Cy}}\text{Pd}(\text{Br})](\text{Br})$ with hydrogens and an outer sphere $\text{Br}^-$ omitted and shown at the 50% probability level.....	158

Figure A.6: Labeled thermal ellipsoid plot of [PDC <sup>Dipp</sup> Pd(Br)](Br) with hydrogens and an outer sphere Br <sup>-</sup> omitted and shown at the 50% probability level .....	162
Figure A.7: Fully labeled thermal ellipsoid plot of [PDC <sup>Me</sup> Pd(MeCN)](PF <sub>6</sub> ) <sub>2</sub> with hydrogens and two outer sphere PF <sub>6</sub> <sup>-</sup> ions omitted and shown at the 50% probability level .....	167
Figure A.8: Fully labeled thermal ellipsoid plot of [PDC <sup>Et</sup> Pd(MeCN)](PF <sub>6</sub> ) <sub>2</sub> with hydrogens and two outer sphere PF <sub>6</sub> <sup>-</sup> ions omitted and shown at the 50% probability level .....	170
Figure A.9: Fully labeled thermal ellipsoid plot of [PDC <sup>IPr</sup> Pd(MeCN)](PF <sub>6</sub> ) <sub>2</sub> with hydrogens and two outer sphere PF <sub>6</sub> <sup>-</sup> ions omitted and shown at the 50% probability level .....	172
Figure A.10: Fully labeled thermal ellipsoid plot of [PDC <sup>Cy</sup> Pd(MeCN)](PF <sub>6</sub> ) <sub>2</sub> with hydrogens and two outer sphere PF <sub>6</sub> <sup>-</sup> ions omitted and shown at the 50% probability level .....	175
Figure A.11: Fully labeled thermal ellipsoid plot of [PDC <sup>Mes</sup> Pd(MeCN)](PF <sub>6</sub> ) <sub>2</sub> with hydrogens and two outer sphere PF <sub>6</sub> <sup>-</sup> ions omitted and shown at the 50% probability level .....	178
Figure A.12: Fully labeled thermal ellipsoid plot of [PDC <sup>Dipp</sup> Pd(MeCN)](PF <sub>6</sub> ) <sub>2</sub> with hydrogens and two outer sphere PF <sub>6</sub> <sup>-</sup> ions omitted and shown at the 50% probability level .....	180
Figure B.1: Fully labeled thermal ellipsoid plot of ReN <sub>3</sub> Intermediate (3) with hydrogens omitted at the 50% probability level.....	184
Figure B.2: Fully labeled thermal ellipsoid plot of the transition metal control complex (9) with hydrogens omitted at the 50% probability level .....	187
Figure C.1: Fully labeled thermal ellipsoid plot of [PhDC <sup>Et</sup> Pd(Br)] with hydrogens omitted at the 50% probability level .....	195
Figure C.2: Fully labeled thermal ellipsoid plot of [PhDC <sup>Et</sup> Pd(MeCN)]PF <sub>6</sub> with hydrogens and a PF <sub>6</sub> counterion omitted, displayed at the 50% probability level.....	201
Figure C.3: Fully labeled thermal ellipsoid plot of [PhDC <sup>Et</sup> Pd(Py)]PF <sub>6</sub> with hydrogens and a PF <sub>6</sub> counterion omitted, displayed at the 50% probability level.....	204

Figure C.4: Fully labeled thermal ellipsoid plot of $[\text{PhDC}^{\text{Et}}\text{Pd}(\text{tBuNC})]\text{PF}_6$ with hydrogens and a $\text{PF}_6$ counterion omitted, displayed at the 50% probability level.....	208
Figure C.5: Labeled thermal ellipsoid plot of $[\text{PhDC}^{\text{Et}}\text{Pd}(\text{PPh}_3)]\text{PF}_6$ with hydrogens and a $\text{PF}_6$ counterion omitted, displayed at the 50% probability level..	212
Figure C.6: Fully labeled thermal ellipsoid plot of $[\text{PhDC}^{\text{Et}}\text{Ni}(\text{Br})]$ with hydrogens omitted, displayed at the 50% probability level. ....	216
Figure C.7: Fully labeled thermal ellipsoid plot of $[\text{PhDC}^{\text{Et}}\text{Ni}(\text{MeCN})]\text{PF}_6$ with hydrogens and an outer sphere $\text{PF}_6$ counterion omitted, displayed at the 50% probability level. ....	221

## LIST OF SCHEMES

Scheme 1.1: Formation of Pd(I)–Pd(I) dimer upon electrochemical reduction. ....	9
Scheme 1.2: Synthetic Pathway to [PDC <sup>R</sup> Pd(Y)]X complexes. ....	24
Scheme 2.1: Synthetic strategy to BODIPY–Re photocatalyst.....	59
Scheme 2.2: Synthetic pathway to inorganic rhenium fragment (3). ....	70
Scheme 2.3: Synthesis of the BODIPY fragment (6) and photocatalyst (7) .....	72
Scheme 2.4: Synthesis of control compounds (9) and (10).....	73
Scheme 3.1: Synthetic pathway to PhDC <sup>Et</sup> proligand .....	104
Scheme 3.2: Synthetic pathway to PhDC <sup>Et</sup> palladium complexes .....	105
Scheme 3.3: Synthesis of [PhDC <sup>Et</sup> Pd(X)]PF <sub>6</sub> derivatives, where X = pyridine (Py), tert-Butyl isonitrile ( <sup>t</sup> BuNC), and triphenylphosphine (PPh <sub>3</sub> ).....	116
Scheme 3.4: Solid-state ligand exchange of non-emissive complexes to the emissive (Py) bound complex. ....	126
Scheme 3.5: Synthesis of [PhDC <sup>Et</sup> Ni(Br)] and [PhDC <sup>Et</sup> Ni(MeCN)]PF <sub>6</sub> .....	132

## ABSTRACT

In Chapter 1 a series of imidazolium based, pyridyl spaced dicarbene complexes were synthesized with varying N-substituents, or ligand wingtips, with increasing steric value (methyl, ethyl, isopropyl, cyclohexyl, mesityl, and diisopropylphenyl). The synthesis of this library of complexes revealed that metalation conditions with Pd(OAc)<sub>2</sub> at elevated temperatures resulted in formation of impurities, which made the purification difficult and resulted in decreased yields. Altering the metalation procedure to formation of the silver carbene followed by transmetallation to palladium resulted in a much cleaner reaction, with increased yield and simple chromatography. Conversion to the acetonitrile bound solvato complex was easily accomplished in high yields and targeted due to a previous study which indicated a labile ancillary ligand enhanced electrocatalytic conversion of CO<sub>2</sub>. The entire solvato bound library, including many intermediates, were characterized through X-ray crystallography. Further, the solid-state structures of the solvato complexes were used to calculate the percent buried volume (%V<sub>Bur</sub>) and ligand solid angles, which characterized the steric environment around the metal center. It was determined that despite an increase in molecular size, all alkyl groups showed a similar steric environment around the metal. The mesityl and diisopropylphenyl derivatives showed significant steric encumbrance when compared to the alkyl systems. Voltammetry studies were performed and indicated a current enhancement under CO<sub>2</sub>, albeit the observed current enhancement was slight. Current enhancement values followed the

same trend observed as the steric environment calculations where  $\text{Dipp} > \text{Mes} > \text{alkyl}$  (alkyl systems gave similar values). Controlled potential electrolysis studies showed that applied potentials past the  $\text{Pd}^{\text{I}}/\text{Pd}^0$  couple resulted in passivation of the electrode. Applied potentials at or below the  $\text{Pd}^{\text{I}}/\text{Pd}^0$  couple resulted in stable currents and no passivation was observed, however, the complexes only produced trace amounts of CO. While the synthesized complexes were inadequate for the electrochemical conversion of  $\text{CO}_2$ , the correlation between steric environment and current enhancement could be useful in future design of molecular systems for the electrochemical reduction of  $\text{CO}_2$ .

In Chapter 2, a rhenium-based molecular photocatalyst supported by a BODIPY appended bipyridine ligand was synthesized and studied for the photocatalytic conversion of  $\text{CO}_2$  to CO. The synthesis of the target complex was completed in two parts, an inorganic fragment, and the organic chromophore. The two fragments were then coupled using a Huisgen reaction to form the target photocatalyst. Similar synthetic strategies were used to generate a series of control compounds, a rhenium complex without the appended chromophore, and a chromophore without the appended inorganic fragment. The photophysical properties of all complexes were studied and revealed that the BODIPY bound rhenium complex was able to absorb visible light out to 600 nm with a molar absorptivity of  $60,000 \text{ M}^{-1}\cdot\text{cm}^{-1}$ . Voltammetry studies showed that the designed photocatalyst maintained the activity of previously studied rhenium bipyridine complexes for the electrochemical conversion of  $\text{CO}_2$ . Through a collaboration, we were able to characterize the photocatalytic properties and found that our designed photocatalyst was able to photochemically convert  $\text{CO}_2$  to CO with metrics of:  $\text{TOF} = 4 \text{ hr}^{-1}$ , and  $\text{TON} = 20$ . Unfortunately, our

control complex displayed similar metrics. After obtaining the solid-state structure and through further probing of the photophysical properties, we found that the inactivity may be due to weak or absent electronic communication as evident through the luminescence quantum yield and lifetime of the photocatalyst and control compound. Further, the long distance (about 15.7 Å) between the chromophore and the metal center may also hinder electronic communication in the designed complex.

In Chapter 3, while complexes containing imidazolium based, phenyl spaced dicarbene CCC pincer ligands, are prevalent in the literature for many transition metals, there is an absence in the primary literature for palladium systems incorporating these ligands. This may be due to the three C–H activations that need to take place for metalation. While the two imidazolium protons are easily deprotonated, the aryl C–H is not easily activated. Based on strategies used for analogous platinum compounds, we found success in using a transmetallation procedure in which zirconium is used to generate an intermediate followed by transmetallation to palladium. We have successfully synthesized a library of phenyl spaced dicarbene palladium complexes with varying ancillary ligands (Br, acetonitrile, pyridine, tertbutyl isonitrile, and triphenylphosphine), all complexes contain ethyl substituents on the ligand wingtips. Through analysis of the solid-state structures we have found that, when compared to the pyridyl spaced systems, we see a lengthening of the bond length of the ancillary ligand, due to the strong electron donation of the trans C<sub>Phenyl</sub> when compared to N<sub>Pyridyl</sub>. Electrochemical analysis via cyclic voltammetry showed about a 1 V difference in Pd<sup>II</sup>/Pd<sup>I</sup> couples where the phenyl spaced system is at a more negative potential due to a more electron dense metal from the stronger donating ligand. Photophysical properties in the solid-state showed that the N-bound ancillary

ligands (MeCN and pyridine) were luminescent materials with a deep blue color and International Commission on Illumination (CIE) coordinates of (0.16, 0.12) and (0.16, 0.13) respectively. We further discovered that the triphenylphosphine complex could act as a sensor through solid-state exchange of the ancillary ligand, yielding a luminescent material in a matter of minutes. This material was characterized through XPS and supported the solid-state exchange of the ancillary ligands. The synthetic strategy was extended to nickel analogs, another absent complex in the literature supported by this ligand system. While we were successful in synthesizing the nickel complexes, they were found to be non-luminescent, likely due to available non-radiative pathways.

## Chapter 1

### PALLADIUM NHC COMPLEXES FOR ELECTROCATALYTIC CO<sub>2</sub> REDUCTION

#### 1.1 Motivation for the Discovery of Transition Metal Complexes for the Electrochemical Transformation of CO<sub>2</sub> to CO.

##### 1.1.1 Historical and Predicted Global Energy Demand

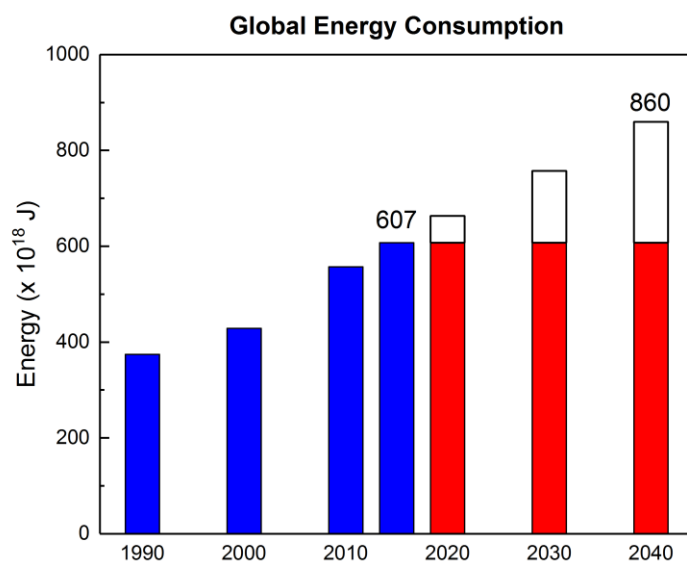


Figure 1.1: Global Energy Consumption with historical data in blue and predicted data in red.<sup>1</sup>

To understand the importance of CO<sub>2</sub> conversion, global energy demand must be first discussed. Data gathered from the International Energy Outlook shows that the global energy demand has been increasing steadily over the past few decades (blue data, Figure 1.1)<sup>1</sup>. The global energy consumed in 2015 was  $607 \times 10^{18}$  J. This increasing trend is expected to continue, and conservative estimates predict that in 2040 the global energy consumption will increase to  $860 \times 10^{18}$  J (red data, Figure 1.1).

The global energy consumption data can also be viewed by type (Figure 1.2). From historical data (2015 and previous), the global energy consumed is primarily from nonrenewable sources, specifically oil, coal, and natural gas. Other sources such as nuclear and renewables only represent a small contribution to the total energy consumption (Figure 1.2). Due to the projected increase in global energy consumption, the question arises, will the trend of being heavily dependent on nonrenewable sources continue? It is predicted that while the contribution of nuclear and renewables will slightly increase, nonrenewable sources will still dominate the energy portfolio (Figure 1.2).<sup>1</sup>

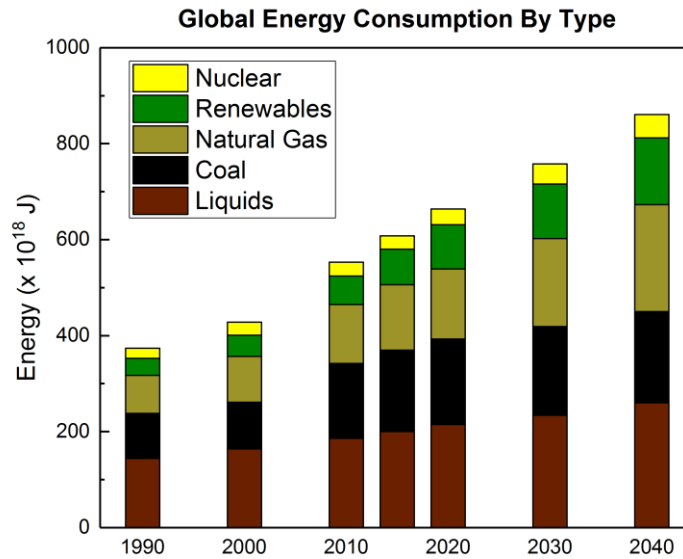


Figure 1.2: Global energy consumption by type for historical data (2015 and previous) and predicted data (2020 to 2040).<sup>1</sup>

### 1.1.2 Issues Associated with Fossil Fuel Consumption

Fossil fuel sources are incredibly inexpensive when compared to renewable energy sources, however there is a major drawback to their consumption. A byproduct of fossil fuel consumption is CO<sub>2</sub>, a known greenhouse gas. As the increasing global energy demand is met with nonrenewable sources, it can be expected that atmospheric CO<sub>2</sub> concentrations will similarly increase.<sup>2</sup> This is indeed observed and can be seen in Figure 1.3, which shows the atmospheric CO<sub>2</sub> concentration from 1980 to 2015 in parts per million (ppm) (black trace).<sup>3</sup>

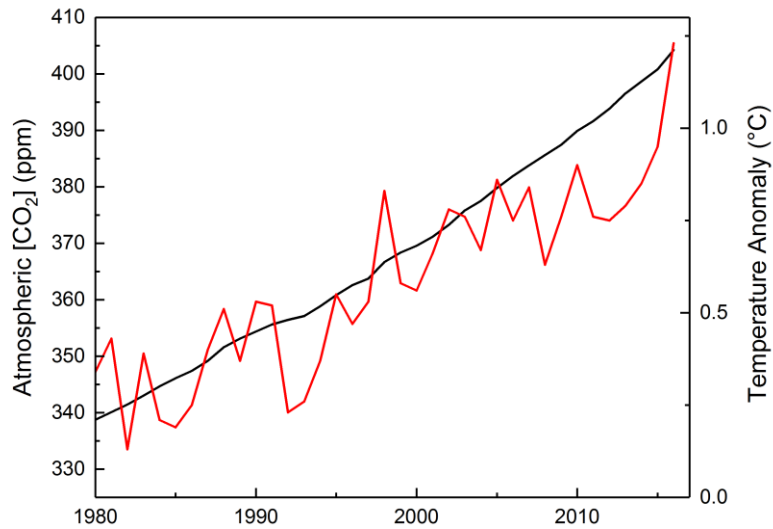
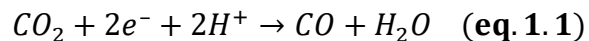


Figure 1.3: Seasonally corrected atmospheric CO<sub>2</sub> concentration taken at the Mauna Loa observatory from 1980 to 2015 (black trace), as well as the global temperature anomaly over the same period (red trace).

There are many global issues associated with increased concentrations of atmospheric CO<sub>2</sub>. One such issue is global climate change. Data obtained and shown in Figure 1.3 (red trace) show a warming trend in the temperature anomaly over the same period.<sup>4</sup> As is evident from the two plots, we can see a correlation between atmospheric CO<sub>2</sub> concentration and increasing global temperature. Global warming has been associated with many environmental and political issues.<sup>5-8</sup> One way to mitigate the increasing consumption of fossil fuels is development of renewable and carbon neutral energy sources.<sup>9</sup>

### 1.1.3 Utilization of Solar Energy by Storage in Chemical Bonds

Of the many possible sources of renewable energy, solar energy is the only source that scales to meet global energy demand. This is highlighted by the fact that more energy from the sun strikes the surface of the earth than what is consumed in an entire year.<sup>9</sup> However, there are some drawbacks to solar energy. Solar energy is not easily stored or transported. One method to overcome these drawbacks is to store solar energy in the form of chemical bonds through thermodynamically uphill chemical reactions. One such reaction is the electrochemical conversion of CO<sub>2</sub> to CO.<sup>9</sup> As can be seen from Equation 1.1 this two-proton, two-electron electrochemical transformation has a negative standard reduction potential, meaning that the product of the reaction (CO) is higher in energy than the starting material (CO<sub>2</sub>). The energy from this transformation is stored in the chemical bonds of CO and can be used later in many processes (vide infra). This can be defined as solar energy storage when the electrons supplied for this transformation are provided from a photovoltaic device.



$$E^\circ = -0.53V \text{ vs. NHE at } pH = 7$$

As can be seen in Figure 1.4 the energy stored in CO can subsequently be used to generate fuels through two processes, the water gas shift and the Fischer-Tropsch process.

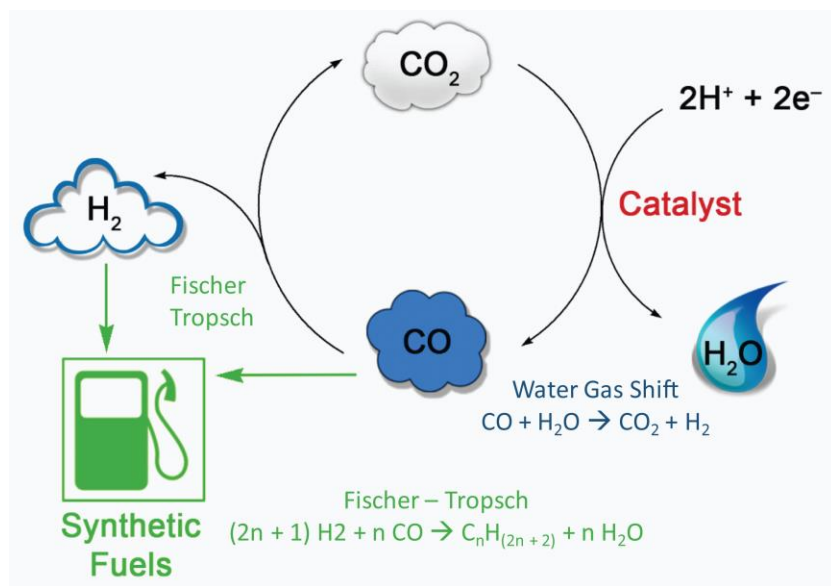


Figure 1.4: The process of how CO<sub>2</sub> can be converted to synthetic fuels through the water gas shift followed by the Fischer-Tropsch process.

As described above, the electrochemical transformation of CO<sub>2</sub> produces CO and H<sub>2</sub>O. These chemicals can then be used in the water gas shift reaction to produce H<sub>2</sub> and CO<sub>2</sub>. The generated CO<sub>2</sub> can then go through the transformation once more to generate syngas, a mixture of H<sub>2</sub> and CO, which are the reagents needed for the Fischer-Tropsch process to generate synthetic carbon-based fuels. To make this a carbon-neutral process, the CO<sub>2</sub> produced from the combustion of the synthetic fuels would then be used again in this transformation.

Due to the uphill nature of CO<sub>2</sub> conversion (Equation 1.1), a catalyst is needed to facilitate the transformation. Many redox-active, transition metal-based complexes have been designed to catalyze this process, including nickel complexes supported by tetra-aza macrocycles,<sup>10</sup> rhenium complexes with derivatized 2,2'-bipyridyl (bipy) ligands,<sup>11</sup> and palladium complexes supported by pincer phosphine ligands.<sup>12,13</sup> The

latter of the examples was reported to be highly efficient and selective towards CO<sub>2</sub> conversion to CO.

## 1.2 Palladium Pincer Complexes for CO<sub>2</sub> Reduction

Metal complexes supported by phosphine ligands for CO<sub>2</sub> activation were initially studied for rhodium systems<sup>14</sup> and multi-metallic nickel systems.<sup>15</sup> Palladium complexes supported by tridentate phosphine (triphos) pincer ligands (Figure 1.5), studied by DuBois and coworkers, have also shown success for this electrocatalytic transformation.<sup>13</sup> These complexes have been suggested to operate through the mechanism shown in Figure 1.5.

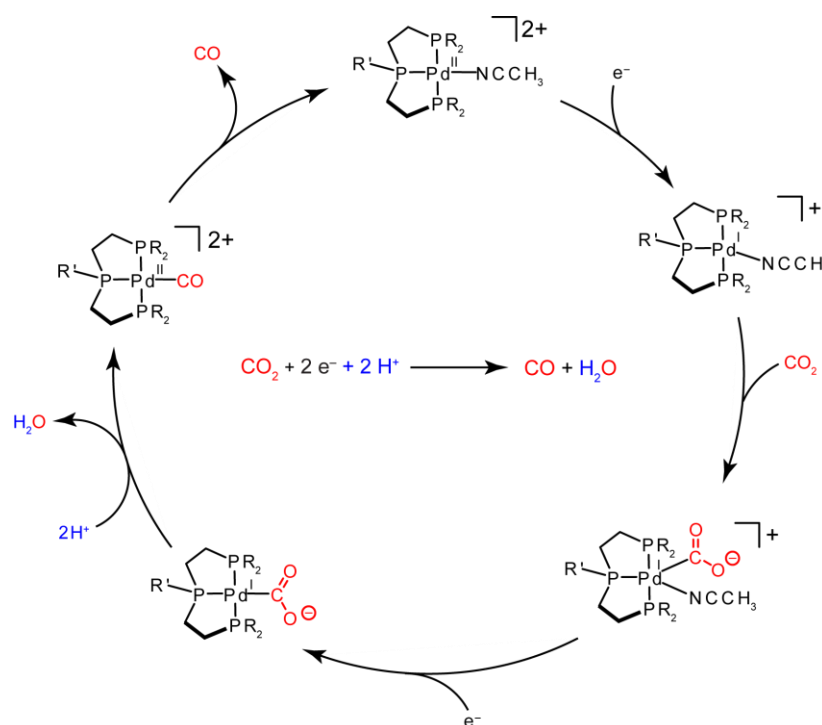
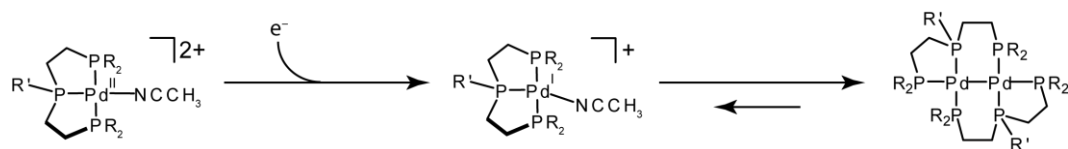


Figure 1.5: CO<sub>2</sub> electrochemical activation mechanism by palladium triphos systems.

The mechanism in Figure 1.5 begins with a Pd(II) complex (top center), which is reduced by one electron at an electrode surface to form a distorted four coordinate Pd(I) complex. This complex then reacts with CO<sub>2</sub> to form a five-coordinate complex. Loss of the acetonitrile and a second electrochemical reduction result in the formation of a palladium metallocarboxylate. This intermediate then reacts with protons to release water and form a palladium carbonyl. Dissociation of the carbonyl produces CO, and association of the solvato ligand completes the catalytic cycle.

This system was studied with several R and R' substituents, and it was found that the steric bulk at these positions influenced catalysis. The most active complex contained substituents of R' = phenyl and R = cyclohexyl.<sup>13</sup> This complex was found to have a faradaic efficiency for CO production of 85%, where faradaic efficiency relates the electrons consumed to the products formed. Thus, 85% of the electrons consumed during electrolysis went toward the production of CO, with the remaining 15% was attributed to H<sup>+</sup> reduction to form H<sub>2</sub>.

While the palladium triphos complex was demonstrated to be highly active toward CO<sub>2</sub> activation, the major drawback to this system is that upon electrochemical reduction of the Pd(II) complex, an off catalytic cycle reaction occurs (Scheme 1.1). Once reduced, the triphos ligand becomes labile and reacts with another Pd(I) species to form bridged dimers (Scheme 1.1). These dimers are thermodynamically favored and are inactive toward CO<sub>2</sub>.<sup>13</sup> While this system was highly efficient, due to this drawback, the active complex was siphoned from the catalytic cycle yielding relatively low turnover numbers.



Scheme 1.1: Formation of Pd(I)–Pd(I) dimer upon electrochemical reduction.

### 1.3 Design of an NHC based Palladium Complex for CO<sub>2</sub> Reduction

#### 1.3.1 Palladium N-heterocyclic Pincer Complex for CO<sub>2</sub> Reduction

Palladium complexes supported by N-heterocyclic carbene (NHC) ligands have been successful in many catalytic applications including Mizoroki-Heck,<sup>16,17</sup> Suzuki,<sup>18</sup> and Sonogashira<sup>18</sup> coupling, and palladium complexes supported by NHC pincer ligands have been reviewed for their broad use in catalytic applications.<sup>19</sup> At the beginning of this project, NHC-based pincer palladium complexes had yet to be investigated for their applications in homogeneous electrocatalytic CO<sub>2</sub> conversion.

#### 1.3.2 N-heterocyclic Carbenes vs. Phosphines as Ligands

N-heterocyclic carbenes were initially discovered by Wanzlick and Öfele in the 1960s<sup>20-22</sup> and the first stable NHC was later reported by Arduengo.<sup>23,24</sup> NHCs are known to act as phosphine mimics for transition metal complexes, and their broad application in catalysis for many transition metals has been reported.<sup>25</sup> NHCs are attractive ligands when compared to phosphines due to many features, such as stronger electron donation, and greater complex stability arising from the strong bonds formed with the metal center.<sup>26</sup> As such, we became interested in designing a palladium complex supported by NHC ligands that would address the drawbacks of the DuBois pincer triphos complex.<sup>13</sup>

### 1.3.3 Design of $[\text{PDC}^{\text{R}}\text{Pd}(\text{Y})]\text{X}$ Complex

As mentioned above we were interested in designing a palladium complex that was similar to the  $\text{CO}_2$  active triphos complex,<sup>13</sup> but incorporated NHC ligands. We found the 2,6-bis[3-(R)imidazolium]pyridine to be a good ligand candidate, as this ligand would allow for the same square planar coordination geometry as the triphos system, and contains two imidazole based NHCs (Figure 1.6 a and b). As such we named the complex  $[\text{PDC}^{\text{R}}\text{Pd}(\text{Y})]\text{X}$  where PDC stands for pyridyl spaced dicarbene, R denotes the substitution on the wingtip, Y denotes the ancillary ligand, and X denotes the outer sphere counterion.

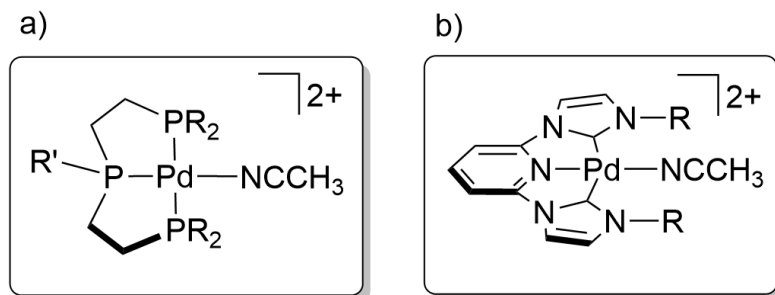


Figure 1.6: (a) and (b) show triphos and PDC palladium complexes with an acetonitrile ancillary ligand.

Incorporating the less labile and more strongly donating NHCs should prevent the unwanted dimer formation, as well as provide a more electron-rich metal to aid in the nucleophilic attack on  $\text{CO}_2$  during the catalytic cycle. Furthermore, we would be able to control the steric environment around the metal center with substitution of the R substituent. Thus, we were also interested in the effect of steric bulk on the catalytic performance with this ligand system. To study this, we synthesized a library of

complexes with varying substituents at the R position. The synthesis is described below.

## 1.4 Experimental

### 1.4.1 General Materials and Methods

Reactions were performed in oven-dried round-bottomed flasks unless otherwise noted. Reagents and solvents were purchased from Sigma Aldrich, Acros, Fisher, Strem, Pressure Chemical or Cambridge Isotopes Laboratories.  $[\text{Pd}(\text{Br})_2(\text{MeCN})_2]$  was synthesized from a literature procedure.<sup>27</sup> Solvents for synthesis were of reagent grade or better and were dried by passage through activated alumina and then stored over 4 Å molecular sieves prior to use.<sup>28</sup> Column chromatography was performed with 40-63 µm silica gel with the eluent reported in parentheses. Analytical thin-layer chromatography (TLC) was performed on precoated glass plates and visualized by UV light. The following compounds were previously reported and were prepared according to the literature procedure: 1-(2,4,6-trimethylphenyl)-1H-imidazole<sup>29</sup>, 1-(2,6-Diisopropylphenyl)-1H-imidazole<sup>29</sup>, 1-(isopropyl)-1H-imidazole<sup>30</sup>, 2,6-di(1H-imidazol-1-yl)pyridine<sup>31</sup>, 2,6-Bis[3-(mesityl)imidazolium]pyridine dibromide<sup>32</sup>, 2,6-Bis[3-(2,6-diisopropylphenyl)imidazolium]pyridine dibromide<sup>32</sup>,  $[\text{PDC}^{\text{me}}\text{Pd}(\text{Br})]\text{Br}$ <sup>17</sup>.

### 1.4.2 Compound Characterization

<sup>1</sup>H NMR and <sup>13</sup>C NMR spectra were recorded at 25 °C on a Bruker 400 MHz spectrometer. Proton spectra are referenced to the residual proton resonance of the deuterated solvent ( $\text{CDCl}_3 = \delta$  7.26;  $\text{CD}_3\text{CN} = \delta$  1.94;  $(\text{CD}_3)_2\text{SO} = \delta$  2.50) and carbon spectra are referenced to the carbon resonances of the solvent ( $\text{CDCl}_3 = \delta$  77.16;

CD<sub>3</sub>CN =  $\delta$  1.32, 118.26; (CD<sub>3</sub>)<sub>2</sub>SO =  $\delta$  39.52). All chemical shifts are reported using the standard  $\delta$  notation in parts-per-million. LR-GCMS data were obtained using an Agilent gas chromatograph consisting of a 6850 Series GC System equipped with a 5973 Network Mass Selective Detector. Low resolution MS data was obtained using either a LCQ Advantage from Thermofinnigan or a Shimadzu LC/MS-2020 single quadrupole MS coupled with an HPLC system, with dual ESI/APCI source. High-resolution mass spectrometry analyses were either performed by the Mass Spectrometry Laboratory in the Department of Chemistry and Biochemistry at the University of Delaware or at the University of Illinois at Urbana-Champaign.

### 1.4.3 X-Ray Crystallography

Crystals were mounted using viscous oil onto a plastic mesh and cooled to the data collection temperature. Data were collected on a Bruker-AXS APEX II DUO CCD diffractometer with Cu-K $\alpha$  radiation ( $\lambda = 1.54178 \text{ \AA}$ ) and was focused by Goebbel mirrors for [(PDC<sup>Cy</sup>)Pd(Br)]Br. All other data were collected with Mo-K $\alpha$  radiation ( $\lambda = 0.71073 \text{ \AA}$ ) monochromated with graphite. Unit cell parameters were obtained from 36 data frames, 0.5°  $\omega$ , from three different sections of the Ewald sphere. The unit-cell parameters and systematic absences were uniquely consistent to the reported space groups for [(PDC<sup>Dipp</sup>)Pd(MeCN)](PF<sub>6</sub>)<sub>2</sub>, [(PDC<sup>Cy</sup>)Pd(Br)]<sub>3</sub>, [(PDC<sup>Cy</sup>)Pd(MeCN)](PF<sub>6</sub>)<sub>2</sub>, and proligand **4**; and for *Pna*2<sub>1</sub> and *Pnam* [*Pnma*] for [(PDC<sup>Mes</sup>)Pd(MeCN)](PF<sub>6</sub>)<sub>2</sub>. No symmetry higher than triclinic was observed in [(PDC<sup>Et</sup>)Pd(Br)]Br, [(PDC<sup>Cy</sup>)AgBr]<sub>2</sub>Ag]Br, [(PDC<sup>Cy</sup>)Pd(Br)]Br, [(PDC<sup>Dipp</sup>)Pd(Br)]Br, [(PDC<sup>iPr</sup>)Pd(MeCN)](PF<sub>6</sub>)<sub>2</sub>, [(PDC<sup>Dipp</sup>)Pd(MeCN)](PF<sub>6</sub>)<sub>2</sub>, and [(PDC<sup>Me</sup>)Pd(MeCN)](PF<sub>6</sub>)<sub>2</sub>. In all cases wherein pairs of space groups are possible, excepting [(PDC<sup>Mes</sup>)Pd(MeCN)](PF<sub>6</sub>)<sub>2</sub>, the centrosymmetric space group

option yielded chemically reasonable and computationally stable results of refinement. In the case of  $[(\text{PDC}^{\text{Mes}})\text{Pd}(\text{MeCN})](\text{PF}_6)_2$ , only the noncentrosymmetric space group yielded chemically reasonable and computationally stable results of refinement. The data were treated with multi-scan absorption corrections. The structures were solved using direct methods or intrinsic phasing and refined with full-matrix, least-squares procedures on  $F^2$ . The compound molecule resides on a mirror plane in  $[(\text{PDC}^{\text{Dipp}})\text{Pd}(\text{MeCN})](\text{PF}_6)_2$ . Two compound molecules ( $Z' = 2$ ) were located in the asymmetric units of  $[(\text{PDC}^{\text{Et}})\text{Pd}(\text{Br})]\text{Br}$  and  $[(\text{PDC}^{\text{Cy}})\text{AgBr}]_2\text{AgBr}$ .

In the case of  $[(\text{PDC}^{\text{Dipp}})\text{Pd}(\text{MeCN})](\text{PF}_6)_2$ , the slight but significant disorder in the  $\text{PF}_6^-$  leads to a level B alert in the checkCIF report with a second alert caused by an AFIX 33 methyl H-atoms that require a large DAMP value because of their proximity to a mirror plane. The co-crystallized chloroform solvent molecule in  $[(\text{PDC}^{\text{Cy}})\text{Pd}(\text{Br})]\text{Br}$  was modeled isotropically with refined site occupancy of 54/46. An ethyl group was found disordered in  $[(\text{PDC}^{\text{Et}})\text{Pd}(\text{MeCN})](\text{PF}_6)_2$  and was modeled with rigid-bond restraints with refined site occupancy of 56/44. An acetonitrile molecule of solvation was located in the asymmetric unit of  $[(\text{PDC}^{\text{Mes}})\text{Pd}(\text{MeCN})](\text{PF}_6)_2$ , and one of two counterions was found disordered in two positions with a refined site occupancy of 70/30. The disorder in the counterions in proligand **4**, and, the solvent molecules in  $[(\text{PDC}^{\text{Cy}})\text{AgBr}]_2\text{AgBr}$ , precluded satisfactory modeling and were treated as diffused contributions.<sup>33</sup>

All non-hydrogen atoms, excluding the disordered solvent in  $[(\text{PDC}^{\text{Dipp}})\text{Pd}(\text{Br})]\text{Br}$ , were refined with anisotropic displacement parameters. All hydrogen atoms were treated as idealized contributions with geometrically calculated positions and with  $U_{iso}$  equal to 1.2, or 1.5 for methyl,  $U_{eq}$  of the attached atom.

Atomic scattering factors are contained in various versions of the SHELXTL program library. The CIFs have been deposited at the Cambridge Crystallographic Data Centre: CCDC 1539130, [(PDC<sup>Cy</sup>)Pd(Br)]Br; CCDC 1539131, [(PDC<sup>Cy</sup>)Pd(MeCN)](PF<sub>6</sub>)<sub>2</sub>; CCDC 1539132, [(PDC<sup>Dipp</sup>)Pd(Br)]Br; CCDC 1539133, [(PDC<sup>Dipp</sup>)Pd(MeCN)](PF<sub>6</sub>)<sub>2</sub>; CCDC 1539134, [(PDC<sup>Et</sup>)Pd(MeCN)](PF<sub>6</sub>)<sub>2</sub>; CCDC 1539135, [(PDC<sup>iPr</sup>)Pd(MeCN)](PF<sub>6</sub>)<sub>2</sub>; CCDC 1539136, [(PDC<sup>Cy</sup>)Pd(Br)]<sub>3</sub>; CCDC 1539137, [(PDC<sup>Mes</sup>)Pd(MeCN)](PF<sub>6</sub>)<sub>2</sub>; CCDC 1539138, [(PDC<sup>Me</sup>)Pd(MeCN)](PF<sub>6</sub>)<sub>2</sub>; CCDC 1539139, proligand **4**; CCDC 1539140, [(PDC<sup>Et</sup>)Pd(Br)]Br; CCDC 1539141, [(PDC<sup>Cy</sup>)AgBr]<sub>2</sub>AgBr.

#### 1.4.4 Electrochemical Measurements

All electrochemistry was performed using either a CHI-620D potentiostat/galvanostat or a CHI-760D bipotentiostat. Cyclic voltammetry was performed using a standard three-electrode configuration. CV scans were recorded for quiescent solutions using a glassy carbon working disk electrode (3.0 mm diameter CH Instruments) and a platinum wire auxiliary electrode. All potentials were measured against a Ag/AgCl reference electrode. CV experiments were performed in DMF using 0.1 M tetrabutylammonium hexafluorophosphate (TBAPF<sub>6</sub>) as the supporting electrolyte. Concentrations of analytes were 1 mM. Controlled Potential Electrolysis (CPE) experiments were carried out using a platinum mesh counter electrode and the same working and reference electrodes as above. CPE experiments were performed at 1 atm in an air tight single compartment cell which was saturated with CO<sub>2</sub>. Faradaic efficiencies for CO production were determined using a single-compartment electrolysis cell. The electrolysis cell was sparged with DMF saturated

CO<sub>2</sub> for approximately 30 minutes, following which time the system was sealed and electrolysis initiated. The headspace of the electrolysis cell was sampled periodically by manually removing 1.0 mL aliquots using a gas-tight syringe. These aliquots were analyzed by manual injection into a gas-sampling loop of a Shimadzu GC-2014 gas chromatograph (GC). This GC was equipped with two 10 port injection valves in line with 2m HaySepT 80/100 columns. Quantification of CO was accomplished using a flame ionization detector (FID) with methanizer after passage through a 3m HaySepD 80/100 column using helium (99.999%) as the carrier gas. Quantification of H<sub>2</sub> was accomplished using a thermal conductivity detector (TCD) after passage through a packed MolSieve 5A 60/80 column, using argon as the carrier gas (99.999%).

#### **1.4.5 Synthesis and Characterization**

##### **1.4.5.1 Synthesis of 1-Cyclohexyl-1H-imidazole**

This compound was prepared by amending a previously described method.<sup>34</sup> Ammonium chloride (10.7 g, 0.2 mol), glyoxal (40 %, 15.3 mL, 0.134 mol), formaldehyde (30 %, 16 mL, 0.134 mol), and DI water (250 mL) were combined in a 1 L round bottom flask. In a separate flask, a solution of cyclohexylamine (11.5 mL, 0.1 mol) in DI water (100 mL) was acidified with phosphoric acid (85 %, 15 mL). The acidified amine was added to the ammonium chloride solution, resulting in a clear colorless solution. After 12 hours of reflux, the clear orange solution was cooled to room temperature and subsequently poured into a 1 L beaker half-full with ice. The resulting mixture was made basic with sodium hydroxide (40 %). The product was then extracted into ethyl acetate and the organic layer was washed with water and dried over sodium sulfate. Following removal of the solvent under reduced pressure,

the desired product was purified via vacuum distillation (105 °C) to give 7.5 g of the title compound as a colorless oil. 50 % yield. <sup>1</sup>H NMR (400 MHz, CDCl<sub>3</sub>, 25 °C) δ/ppm: 7.53 (s, 1H), 7.04 (s, 1H), 6.95 (s, 1H), 3.90 (tt, *J* = 11.8, 3.8 Hz, 1H), 2.12-2.09 (m, 2H), 1.92-1.87 (m, 2H), 1.79-1.70 (m, 1H), 1.67-1.57 (m, 2H), 1.45-1.35 (m, 2H), 1.29-1.18 (m, 1H). <sup>13</sup>C NMR (101 MHz, CDCl<sub>3</sub>, 25 °C) δ/ppm: 135.43, 129.03, 117.10, 56.90, 34.54, 25.54, 25.34. HR-EI-MS [M]<sup>+</sup> *m/z*: calculated for C<sub>9</sub>H<sub>14</sub>N<sub>2</sub> 150.1157; found, 150.1162.

#### 1.4.5.2 Synthesis of 2,6-Bis[3-(ethyl)imidazolium]pyridine dibromide

The preparation of this compound was based on literature preps.<sup>32,35</sup> 2,6-Bis(1-imidazolyl)pyridine (.201g, 0.095 mmol), bromoethane (0.70 ml, 0.944 mmol), and a small amount of xylenes (3 ml) were added to a pressure tube. The tube was sealed with a screw top cap equipped with a rubber o-ring and the vessel was heated to 150 °C for 4 days. The material was triturated several times with ether and the solid was collected yielding an off white solid (0.386 g, 94% yield) <sup>1</sup>H NMR (400 MHz, DMSO-d<sub>6</sub>) δ 10.74 (s, 2H), 8.88 (s, 2H), 8.61 (t, *J* = 8.1 Hz, 1H), 8.29 (d, *J* = 8.1 Hz, 2H), 8.21 (s, 2H), 4.40 (q, *J* = 7.3 Hz, 4H), 1.55 (t, *J* = 7.3 Hz, 6H). <sup>13</sup>C NMR (101 MHz, DMSO) δ 145.31, 144.84, 135.66, 123.52, 119.39, 114.12, 45.15, 15.03. HR-LIFDI-MS [M-Br]<sup>+</sup> *m/z*: calculated for C<sub>15</sub>H<sub>19</sub>N<sub>5</sub>Br 348.0824; found, 348.0830.

#### 1.4.5.3 Synthesis of 2,6-Bis[3-(isopropyl)imidazolium]pyridine dibromide

The preparation of this compound was based on a literature prep.<sup>36</sup> Isopropyl imidazole (1.40 g, 12.7 mmol) was added to 2,6-dibromopyridine (1.50 g, 6.33 mmol) in a high-pressure tube. The two compounds were stirred and heated at 150 °C for 4 days. The brown solid was dissolved in dichloromethane and the white solid was

filtered off. Yield: 2.24 g 77% yield. All analytical data matched what was previously reported.<sup>36</sup> <sup>1</sup>H NMR (400 MHz, *d*<sub>6</sub>-DMSO) δ 10.60 (s, 2H, 2-imidazolium H), 8.90 and 8.31 (2 × t, *J* = 1.94 Hz, 2H, 4/5-imidazolium H), 8.62 (t, *J* = 8.16 Hz, 1H, 4-pyridyl H), 8.32 (d, *J* = 8.16 Hz, 2H, 3,5-pyridyl H), 4.87 (septet, *J* = 6.66 Hz, 2H, CH(CH<sub>3</sub>)<sub>2</sub>), 1.63 (d, *J* = 6.66 Hz, 12H, CH(CH<sub>3</sub>)<sub>2</sub>).

#### 1.4.5.4 Synthesis of 2,6-Bis[3-(cyclohexyl)imidazolium]pyridine dibromide

Preparation of the compound was completed using a modified literature method.<sup>36</sup> 2,6-Dibromopyridine (8.365 g, 0.035 mol) and 1-Cyclohexyl-1H-imidazole (10.593 g, 0.706 mol) were mixed in a 50 mL pressure tube. The tube was sealed and heated to 150 °C for 4 days. The ligand was recrystallized from the resulting black solid by dissolving the solid in room temperature DCM then cooling the solution in the freezer to give 9.6 g of the title compound as a white solid 51 % yield. <sup>1</sup>H NMR (400 MHz, (CD<sub>3</sub>)<sub>2</sub>SO, 25 °C) δ/ppm: 10.60 (s, 2H), 8.91 (s, 2H), 8.62 (t, *J* = 8.1, 1H), 8.13-8.31 (m, 4H), 4.54-4.43 (m, 2H), 2.17 (d, *J* = 9.0, 4H), 1.95-1.89 (m, 8H), 1.70 (d, *J* = 12.5, 2H), 1.48-1.38 (m, 4H), 1.32-1.22 (m, 2H). <sup>13</sup>C NMR (101 MHz, DMSO) δ 145.35, 144.71, 134.65, 122.16, 119.52, 114.33, 59.80, 32.28, 24.56, 24.37.

#### 1.4.5.5 General Procedure (A) for Metalation with Pd(OAc)<sub>2</sub>

Adapted from a literature procedure.<sup>17</sup> Pd(OAc)<sub>2</sub> (1 equiv) and the proligand (1 equiv) were added to a round bottom flask and placed under vacuum. DMSO (10 ml), which had been saturated with with N<sub>2</sub> for 30 minutes, was added to the reaction flask via syringe and the headspace was evacuated. The septum was then sealed with copper wire and the solution was heated to 150 °C for 3 hours. Once the solution had returned to room temperature it was filtered through celite and the solvent was removed under

reduced pressure. The crude material was then purified through column chromatography on silica with the eluent mixture noted for each compound.

#### 1.4.5.6 General Procedure (B) for Metalation/Transmetalation with Ag<sub>2</sub>O and [Pd(Br)<sub>2</sub>(MeCN)<sub>2</sub>]

The following procedure was based on literature work<sup>32:37</sup>. The proligand (1 equiv) and Ag<sub>2</sub>O (1 equiv) were added to a round bottom flask and DMSO was added. The solution was protected from light with aluminum foil and magnetically stirred for 12 hours at room temperature. [Pd(Br)<sub>2</sub>(MeCN)<sub>2</sub>] (1.05 equiv) was then added and magnetically stirred for an additional 3 hours. The solution was then filtered and the solvent was removed under reduced pressure yielding a crude solid. The crude material was then purified via column chromatography on silica.

#### 1.4.5.7 Synthesis of [PDC<sup>Et</sup>Pd(Br)]Br

Via Procedure A: Ligand (0.259 g, 0.060 mmol) and Pd(OAc)<sub>2</sub> (0.135 g, 0.060 mmol). Purified on silica using 20 % MeOH in DCM as the eluent to yield an off white solid (0.180 g, 56 % yield). X-ray quality crystals were grown via vapor diffusion of ether into a concentrated DCM:MeOH solution. <sup>1</sup>H NMR (400 MHz, DMSO-*d*<sub>6</sub>) δ 8.58 (t, *J* = 8.2 Hz, 1H), 8.47 (d, *J* = 2.2 Hz, 2H), 8.02 (d, *J* = 8.2 Hz, 2H), 7.80 (d, *J* = 2.2 Hz, 2H), 4.56 (q, *J* = 7.2 Hz, 4H), 1.38 (t, *J* = 7.1 Hz, 6H). <sup>13</sup>C NMR (101 MHz, DMSO) δ 165.48, 150.26, 146.54, 123.91, 118.43, 108.83, 45.34, 16.49. HR-LIFDI-MS [M–Br]<sup>+</sup> *m/z*: calculated for C<sub>15</sub>H<sub>17</sub>N<sub>5</sub>PdBr 453.9697; found, 453.9684.

#### 1.4.5.8 Synthesis of [PDC<sup>Pr</sup>Pd(Br)]Br

Via Procedure A: Proligand (0.400 g, 0.875 mmol) and Pd(OAc)<sub>2</sub> (0.196 g, 0.875 mmol). Yield: 0.32 g 65% yield. <sup>1</sup>H NMR (400 MHz, *d*<sub>6</sub>-DMSO) δ 8.58 (t, *J* = 8.23 Hz, 1H), 8.55 and 7.98 (2 × d, *J* = 1.95 Hz, 2H), 8.04 (d, *J* = 8.23 Hz, 2H), 5.78 (septet, *J* = 6.83 Hz, 2H), 1.47 (d, *J* = 6.83 Hz, 12H). <sup>13</sup>C NMR (101 MHz, CDCl<sub>3</sub>) δ 164.76, 150.29, 146.52, 120.39, 118.88, 108.75, 52.05, 39.52, 22.38. HR-ESI-MS [M–Br]<sup>+</sup> *m/z*: calculated for C<sub>17</sub>H<sub>21</sub>N<sub>5</sub>BrPd 480.0015; found, 480.0016.

#### 1.4.5.9 Synthesis of [PDC<sup>Cy</sup>Pd(Br)]Br

Via Procedure A: Pd(OAc)<sub>2</sub> (0.335 g, 1.5 mmol) and proligand (0.802 g, 1.5 mmol). The crude material was purified through column chromatography using a 1:5 methanol/DCM mixture as the eluent which gave the complex as a yellow solid. 0.408 g, 43 % yield. <sup>1</sup>H NMR (400 MHz, DMSO-*d*<sub>6</sub>) δ 8.58 (t, *J* = 8.2 Hz, 1H), 8.51 (d, *J* = 2.2 Hz, 2H), 8.01 (d, *J* = 8.2 Hz, 2H), 7.95 (d, *J* = 2.2 Hz, 2H), 5.44 (t, *J* = 12.1 Hz, 2H), 2.12 – 1.61 (m, 14H), 1.53 – 1.11 (m, 7H). <sup>13</sup>C NMR (101 MHz, DMSO) δ 165.20, 150.32, 146.51, 120.73, 118.66, 108.83, 58.64, 32.65, 25.01, 24.51. HR-ESI-MS [M–Br]<sup>+</sup> *m/z*: calculated for C<sub>23</sub>H<sub>29</sub>N<sub>5</sub>PdBr 562.0638; found, 562.0651

Via Procedure B: The proligand (0.336 g, 0.63 mmol) and Ag<sub>2</sub>O (0.145 g, 0.63 mmol) were added to a round bottom flask and DMSO (15 ml) was added and stirred as stated above. [Pd(Br)<sub>2</sub>(MeCN)<sub>2</sub>] (0.229 g, 0.66 mmol) was then added and stirred. The crude material was then purified with column chromatography using a 1:10 MeOH:DCM solution as the eluent. All analytical data was the same as reported above using Pd(OAc)<sub>2</sub>. (0.193 g, 55 % yield)

#### 1.4.5.10 Synthesis of [PDC<sup>Mes</sup>Pd(Br)]Br

Via Procedure A: Proligand (1.01 g, 1.66 mmol) and Pd(OAc)<sub>2</sub> (0.372 g, 1.66 mmol). Purified by column chromatography on silica with a gradient from 0% MeOH/DCM to 20% MeOH/DCM giving an off white solid. 0.39 g 40% yield. <sup>1</sup>H NMR (400 MHz, *d*<sub>6</sub>-DMSO) δ 8.73 and 7.70 (2 × d, *J* = 2.22 Hz, 2H), 8.68 (t, *J* = 8.17 Hz, 1H), 8.20 (d, *J* = 8.17 Hz, 2H), 6.94 (s, 4H), 2.25 (s, 6H), 1.96 (s, 12H). <sup>13</sup>C NMR (101 MHz, CD<sub>3</sub>CN) δ 171.16, 151.90, 147.01, 140.47, 135.38, 135.27, 129.51, 125.76, 119.55, 118.26, 110.21, 21.00, 17.91. HR-ESI-MS [M–Br]<sup>+</sup> *m/z*: Calculated for C<sub>29</sub>H<sub>29</sub>N<sub>5</sub>BrPd 632.0641, found, 632.0640.

Via Procedure B: Proligand (0.505 g, 0.829 mmol), Ag<sub>2</sub>O (0.192 g, 0.829 mmol) and [Pd(Br)<sub>2</sub>(MeCN)<sub>2</sub>] (0.303 g, 0.870 mmol). Purified by column chromatography on silica using a 20 % MeOH in DCM giving an off white solid. 0.396 g 67% yield. All analytical data agreed with above.

#### 1.4.5.11 Synthesis of [PDC<sup>Dipp</sup>Pd(Br)]Br

Via Procedure B: Proligand (0.129 g, 0.186 mmol), Ag<sub>2</sub>O (0.043 g, 0.186 mmol) and [Pd(Br)<sub>2</sub>(MeCN)<sub>2</sub>] (0.068 g, 0.195 mmol). Purified by column chromatography on silica using a 15 % MeOH in DCM giving an off white solid. 0.093 g, 63% yield. <sup>1</sup>H NMR (400 MHz, DMSO-*d*<sub>6</sub>) δ 8.73 (d, *J* = 2.2 Hz, 2H), 8.68 (t, *J* = 8.2 Hz, 1H), 8.18 (d, *J* = 8.3 Hz, 2H), 7.88 (d, *J* = 2.1 Hz, 2H), 7.38 (t, *J* = 7.8 Hz, 2H), 7.20 (d, *J* = 7.8 Hz, 4H), 2.39 (p, *J* = 6.8 Hz, 4H), 1.10 (d, *J* = 6.8 Hz, 12H), 1.05 (d, *J* = 6.8 Hz, 12H). <sup>13</sup>C NMR (101 MHz, DMSO) δ 169.38, 150.45, 146.30, 144.23, 133.78, 130.05, 126.49, 123.54, 118.77, 109.76, 28.03, 24.36, 22.93. HR-ESI-MS [M–2Br]<sup>2+</sup> *m/z*: calculated for C<sub>37</sub>H<sub>44</sub>N<sub>6</sub>Pd 339.1326; found, 339.1330.

#### 1.4.5.12 General Procedure for the Formation of the Acetonitrile Solvato Complex

1 equivalent of the halide complex and 2 equivalents  $\text{AgPF}_6$  were added to a round bottom flask in a  $\text{N}_2$  glovebox. Dry Acetonitrile was added and the reaction vessel was sealed with a rubber septum supported by copper wire and shielded from light with aluminum foil. The reaction vessel was then taken out of the glovebox and heated in an oil bath to  $70\text{ }^\circ\text{C}$  for 3 hours. The solution was then filtered to remove the  $\text{AgBr}$  side product and the solvent was evaporated. The material was then recrystallized using acetonitrile and ether yielding a white solid which was collected via vacuum filtration. X-ray quality crystals of the complexes were grown by vapor diffusion of ether into a concentrated acetonitrile solution.

#### 1.4.5.13 Synthesis of $[\text{PDC}^{\text{Me}}\text{Pd}(\text{MeCN})](\text{PF}_6)_2$

$[\text{PDC}^{\text{Me}}\text{PdBr}]\text{Br}$  (0.125 g, 0.024 mmol) and  $\text{AgPF}_6$  (0.125 g, 0.049 mmol) yielding a white solid (0.139 g, 83 % yield)  $^1\text{H}$  NMR (400 MHz,  $\text{DMSO-d}_6$ )  $\delta$  8.62 (t,  $J = 8.2$  Hz, 1H), 8.47 (d,  $J = 2.2$  Hz, 2H), 8.03 (d,  $J = 8.3$  Hz, 2H), 7.74 (d,  $J = 2.1$  Hz, 2H), 3.93 (s, 6H).  $^{13}\text{C}$  NMR (101 MHz,  $\text{DMSO}$ )  $\delta$  165.68, 150.99, 147.52, 125.39, 118.45, 109.18, 99.56, 36.92, 1.25. HR-ESI-MS  $[\text{M}-\text{MeCN}-2\text{PF}_6]^{2+}$   $m/z$ : calculated for  $\text{C}_{13}\text{H}_{11}\text{N}_5\text{Pd}$  172.5105; found, 172.5093

#### 1.4.5.14 Synthesis of $[\text{PDC}^{\text{Et}}\text{Pd}(\text{MeCN})](\text{PF}_6)_2$

$[\text{PDC}^{\text{Et}}\text{PdBr}]\text{Br}$  (0.235 g, 0.044 mmol) and  $\text{AgPF}_6$  (0.223 g, 0.088 mmol) yielding a white solid (0.269 g, 87% yield)  $^1\text{H}$  NMR (400 MHz, Acetonitrile- $\text{d}_3$ )  $\delta$  8.44 (t,  $J = 8.3$  Hz, 1H), 7.90 (d,  $J = 2.2$  Hz, 2H), 7.67 (d,  $J = 8.3$  Hz, 2H), 7.42 (d,  $J = 2.3$  Hz, 2H), 4.24 (q,  $J = 7.3$  Hz, 4H), 1.52 (t,  $J = 7.3$  Hz, 6H).  $^{13}\text{C}$  NMR (101 MHz,  $\text{CD}_3\text{CN}$ )  $\delta$  166.54, 152.45, 149.23, 124.54, 119.45, 110.44, 47.14, 16.64, 1.32.

Elemental Analysis ( $C_{17}H_{20}N_6PdP_2F_{12} + CH_3OH$ : C 29.34; H, 3.28; N, 11.41, Found C, 29.48; H, 2.86, N, 11.67) HR-ESI-MS  $[M-2PF_6]^{2+}$   $m/z$ : calculated for  $C_{17}H_{20}N_6Pd$  207.0388; found, 207.0387

#### 1.4.5.15 Synthesis of $[PDC^{IPr}Pd(MeCN)](PF_6)_2$

$AgPF_6$  (0.72 g, 2.86 mmol) and  $[PDC^{IPr}PdBr]Br$  (0.80 g, 1.43 mmol). Yield: 0.66 g (63%).  $^1H$  NMR (400 MHz,  $CD_3CN$ )  $\delta$  8.45 (t,  $J = 8.28$  Hz, 1H), 7.94 and 7.51 ( $2 \times d$ ,  $J = 2.16$  Hz, 2H), 7.69 (d,  $J = 8.28$  Hz, 2H), 4.71 (septet,  $J = 6.73$  Hz, 2H), 1.59 (d,  $J = 6.73$  Hz, 12H).  $^{13}C$  NMR (101 MHz, DMSO)  $\delta$  163.91, 150.95, 147.56, 120.45, 119.37, 109.13, 51.86, 39.52, 22.57, 1.24. ESI-MS  $[M-2PF_6]^{2+}$   $m/z$ : calculated for  $C_{19}H_{24}N_6Pd$  221.0549; found, 221.0552.

#### 1.4.5.16 Synthesis of $[PDC^{Cy}Pd(MeCN)](PF_6)_2$

$[PDC^{Cy}PdBr]Br$  (0.333 g, 0.5 mmol) and  $AgPF_6$  (0.262 g, 1.0 mmol). Yield 0.422 g (92%) as an off white solid.  $^1H$  NMR (400 MHz,  $CD_3CN$ )  $\delta$  8.45 (t,  $J = 8.2$  Hz, 1H), 7.93 (d,  $J = 1.9$  Hz, 2H), 7.66 (d,  $J = 8.3$  Hz, 2H), 7.50 (d,  $J = 2.0$  Hz, 2H), 4.30 (tt,  $J = 12.2, 3.8$  Hz, 2H), 2.14 – 1.96 (m, 12H), 1.81 (ddd,  $J = 24.5, 12.1, 2.9$  Hz, 7H), 1.51 – 1.25 (m, 7H).  $^{13}C$  NMR (101 MHz,  $CD_3CN$ )  $\delta$  165.61, 152.33, 149.20, 121.34, 119.63, 110.34, 61.42, 33.92, 26.15, 25.30. HR-ESI-MS  $[M-2PF_6]^{2+}$   $m/z$ : calculated for  $C_{25}H_{32}N_6Pd$  261.0856; found, 261.0857.

#### 1.4.5.17 Synthesis of $[PDC^{Mes}Pd(MeCN)](PF_6)_2$

$AgPF_6$  (0.24 g, 0.96 mmol) and  $[PDC^{Mes}PdBr]Br$  (0.34 g, 0.48 mmol). Yield: 0.30 g (70%) as an off white solid.  $^1H$  NMR (400 MHz,  $CD_3CN$ )  $\delta$  8.55 (t,  $J = 8.24$  Hz, 1H), 8.13 and 7.39 ( $2 \times d$ ,  $J = 2.10$  Hz, 2H), 7.83 (d,  $J = 8.24$  Hz, 2H), 7.07 (s, 4H), 2.29 (s, 6H), 2.07 (s, 12H).  $^{13}C$  NMR (101 MHz,  $CD_3CN$ )  $\delta$  169.02, 152.74,

149.41, 141.54, 135.86, 133.84, 130.09, 125.68, 120.29, 111.08, 20.90, 17.64. HR-ESI-MS  $[M-PF_6]^+$   $m/z$ : calculated for  $C_{31}H_{32}N_6PF_6Pd$  739.1371; found, 739.1377.

#### 1.4.5.18 Synthesis of $[PDC^{Dipp}Pd(MeCN)](PF_6)_2$

$AgPF_6$  (0.222 g, 0.877 mmol) and  $[PDC^{Dipp}PdBr]Br$  (0.350 g, 0.439 mmol). Quantitative yield as an off white solid.  $^1H$  NMR (400 MHz, Acetonitrile- $d_3$ )  $\delta$  8.61 (t,  $J = 8.3$  Hz, 1H), 8.18 (d,  $J = 2.2$  Hz, 2H), 7.88 (d,  $J = 8.4$  Hz, 2H), 7.57 – 7.50 (m, 4H), 7.39 (d,  $J = 7.8$  Hz, 4H), 2.52 (hept,  $J = 6.8$  Hz, 4H), 1.99 (s, 3H), 1.18 (d,  $J = 6.9$  Hz, 12H), 1.15 (d,  $J = 6.8$  Hz, 12H).  $^{13}C$  NMR (101 MHz,  $CD_3CN$ )  $\delta$  168.81, 152.79, 149.61, 146.43, 133.23, 132.69, 126.60, 125.35, 120.24, 111.24, 29.18, 24.17, 23.94. HR-ESI-MS  $[M-PF_6]^+$   $m/z$ : calculated for  $C_{37}H_{44}N_6PF_6Pd$  823.2299, found 823.2303.

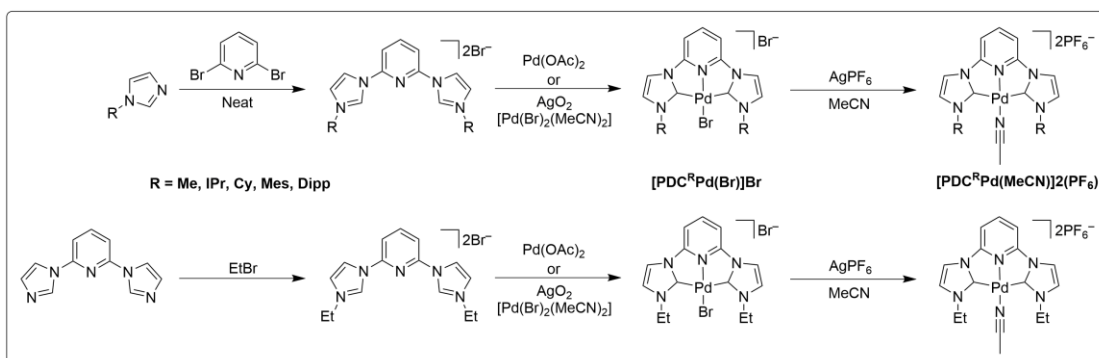
#### 1.4.5.19 Synthesis of $[PDC^{Cy}AgBr]$

The silver intermediate was synthesized using a modified literature procedure as follows<sup>37</sup>.  $Ag_2O$  (0.046 g, 0.2 mmol) and the proligand (0.107 g, 0.2 mmol) were added to a round bottom flask and 25 ml of DCM was added. The reaction flask was shielded from light with aluminum foil and magnetically stirred for 12 hours. The mixture was then filtered through celite and the solvent was removed under reduced pressure to yield the intermediate without further purification. (0.067 g, 60 % yield). Single crystals were grown by solvent diffusion of pentane into a saturated DCM solution in an aluminum foil covered vial.  $^1H$  NMR (400 MHz,  $DMSO-d_6$ )  $\delta$  8.50 (t,  $J = 8.0$  Hz, 1H), 8.42 (s, 2H), 8.06 (d,  $J = 8.1$  Hz, 2H), 7.79 (s, 2H), 3.88 (s, 2H), 1.69 – 1.28 (m, 13H), 1.05 (dd,  $J = 23.5, 16.4$  Hz, 5H), 0.94 – 0.54 (m, 4H). HR-LIFDI-MS  $[M+H]^+$   $m/z$ : calculated for  $C_{23}H_{30}N_5AgBr$  564.0724; found, 564.0734.

## 1.5 Synthetic Pathway to PDC<sup>R</sup> complexes.

### 1.5.1 Synthesis of the Proligands.

The synthetic pathway to the palladium complexes is shown in Scheme 1.2 and detailed in the experimental section. The process began with synthesis of the substituted imidazoles via condensation reactions with the R-substituted amine, glyoxal, and ammonium chloride under acidic conditions. The alkyl imidazoles were then purified via distillation while the aryl derivatives were purified through sublimation. The imidazoles were then reacted neat in a pressure tube at elevated temperatures over the course of 4 days to accomplish the S<sub>N</sub>Ar reaction and form the proligands. The imidazoles were then reacted neat in a pressure tube at elevated temperatures over the course of 4 days to accomplish the S<sub>N</sub>Ar reaction and form the proligands.



Scheme 1.2: Synthetic Pathway to [PDC<sup>R</sup>Pd(Y)]X complexes.

In the case of the ethyl derivative, we first synthesized 2,6-di(1H-imidazol-1-yl)pyridine and subsequently used ethylbromide in a substitution reaction to attach the ethyl wingtips.

### 1.5.2 Metalation with Pd(OAc)<sub>2</sub>

We initially followed a metalation procedure described in the literature using Pd(OAc)<sub>2</sub> at various temperatures over time.<sup>17</sup> However, we found that the reaction could occur over the course of 3 hours at 150 °C. We also discovered that these complexes were stable to silica chromatography and could be purified using mixtures of methanol and DCM as the eluent. While this method was successful, the purification was, at times, problematic. Specifically, in the case of [PDC<sup>Cy</sup>Pd(Br)] we found that our metalation yield was low and a dark-colored material was also collected during the purification process. After isolation, we were able to crystallize this material and found that under these metalation conditions we were also forming a palladium complex which was only bound to one NHC and had three bromides bound in the remaining coordination sites (Figure 1.7a).

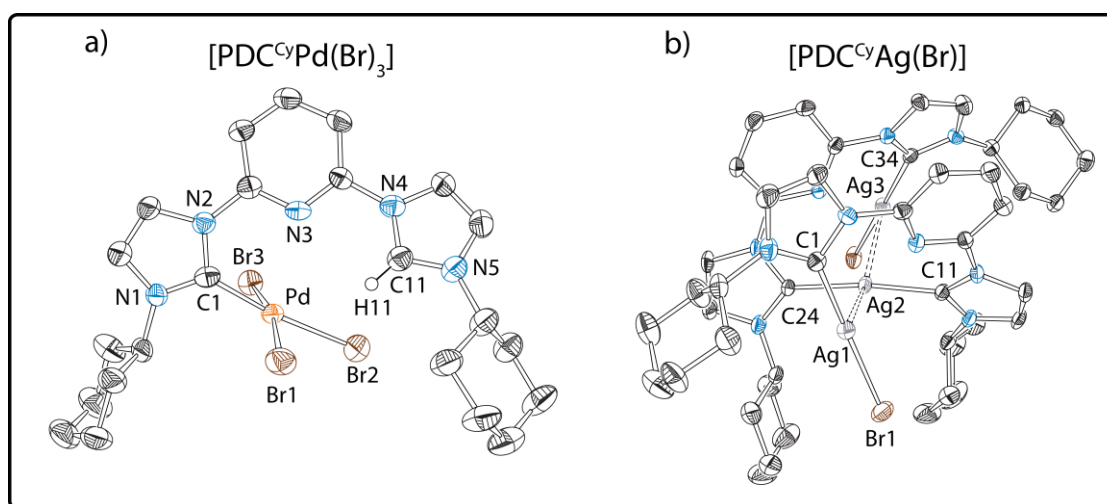


Figure 1.7: Solid-state structures of the intermediates isolated during the metalation and transmetalation reactions. [PDC<sup>Cy</sup>Pd(Br)<sub>3</sub>] is displayed at the 50 % thermal ellipsoid probability while [PDC<sup>Cy</sup>Ag(Br)] is shown at the 30 % probability level to better display the structure, a Br<sup>-</sup> counterion was also omitted for clarity on the Ag structure.

The other side of the PDC ligand remained as the cationic H-bound imidazole to counter the charge. Further reaction time under these conditions did not alter the yield, or the production of side products. We investigated the solid-state structure to determine if H-bonding from one of the bromide ligands was aiding in stabilization of this side product. However we found the closest interaction between Br1 and H11 to be 2.864 Å, with a Pd–Br1–H11 angle of 71.35° (Table 1.1) indicating a weak interaction, if any.<sup>38,39</sup>

	<b>[PDC<sup>Cy</sup>Pd(Br)<sub>3</sub>]</b>		<b>[PDC<sup>Cy</sup>PdAgBr]</b>
<b>C1–Pd (Å)</b>	1.957	<b>C1–Ag1 (Å)</b>	2.106
<b>Pd–Br1 (Å)</b>	2.458	<b>Ag1–Br1 (Å)</b>	2.447
<b>Pd–Br2 (Å)</b>	2.483	<b>Ag1–Ag2 (Å)</b>	2.998
<b>Pd–Br3 (Å)</b>	2.429	<b>C11–Ag2 (Å)</b>	2.092
<b>H11–Br1 (Å)</b>	2.864	<b>C24–Ag2 (Å)</b>	2.087
<b>C2–C3 (Å)</b>	1.338	<b>Ag2–Ag3 (Å)</b>	3.068
<b>C9C–C10 (Å)</b>	1.348	<b>C34–Ag3 (Å)</b>	2.091
<b>Pd–Br1–H11 (°)</b>	71.35	<b>Ag3–Br2 (Å)</b>	2.443

Table 1.1: Selected bond lengths and angles for solid-state structures of the isolated intermediates

### 1.5.3 Transmetalation strategy with Ag<sub>2</sub>O

Due to the complications in purification, we looked to another common method for metalation of NHC palladium complexes, which is accomplished through a

silver intermediate followed by transmetallation.<sup>37</sup> This route could proceed either via a two-step process where the silver intermediate is formed and isolated, followed by the transmetallation reaction; or by a one-pot, two-step process. While the one-pot process is preferred, we decided to also isolate and fully characterize the PDC<sup>Cy</sup>Ag intermediate. The intermediate was synthesized by combining the proligand and Ag<sub>2</sub>O in DCM in a reaction vessel that was shielded from light for 12 hours. After filtration, [PDC<sup>Cy</sup>AgBr] was isolated without purification, and single crystals were obtained. The solid-state structure of the complex is shown in Figure 1.7b, with selected bond lengths given in Table 1.1. The solid-state structure shows two PDC ligands coordinating three silver atoms, where Ag1 is bound to a Br<sup>-</sup> ion and C1 in a trans fashion with a bond angle of 171.05°. Ag2 is then coordinated to two different PDC ligands through C11 and C24 and displays an Ag-Ag interaction between Ag1 and Ag2 (~3 Å, Table 1.) slightly over twice the Ag radius of 2.889 Å. As shown in Figure 1.6b this pattern is repeated once more to bridge the second PDC ligand and Br2. Similar bond distances and angles are reported for a similar pyridine spaced dicarbene Ag complex<sup>40</sup> and similar geometries and bonding modes have been reported in many reviews of Ag NHC complexes.<sup>41-43</sup> This intermediate was then carried on to the palladium complex using [Pd(Br)<sub>2</sub>(MeCN)<sub>2</sub>] in DMSO at room temperature. As stated above this was also accomplished in a one pot synthesis. After removal of the solvent the palladium complex was purified on silica with a mixture of methanol in DCM. Not only was this reaction carried out under milder conditions than the Pd(OAc)<sub>2</sub> route, but we found the chromatography to be much simpler and higher yielding. We were successful at synthesizing all derivatives using the routes described above and obtained solid-state structures for the ethyl, cyclohexyl, and

diisopropylphenyl halide complexes. The figures and experimental data can be found in Appendix A. The  $[\text{PDC}^{\text{Me}}\text{Pd}(\text{Br})]$  solid state structure had been reported previously and our bond lengths and angles compare well with the reported values.<sup>17</sup>

#### **1.5.4 Synthesis of the Solvato Complex**

The synthesis of the PDC complexes was completed via formation of the solvato complex using two equivalents of  $\text{AgPF}_6$  in acetonitrile. This complex was targeted as a labile solvato ancillary ligand was found to be beneficial in the DuBois system.<sup>12</sup> Purification was easily accomplished through filtration followed by precipitation of the complex using acetonitrile and ether. Single crystals were obtained for all complexes through solvent diffusion of ether into a solution of the complex in acetonitrile. The solid-state structures are shown in Figure 1.8 and selected bond lengths are reported in Table 1.2.

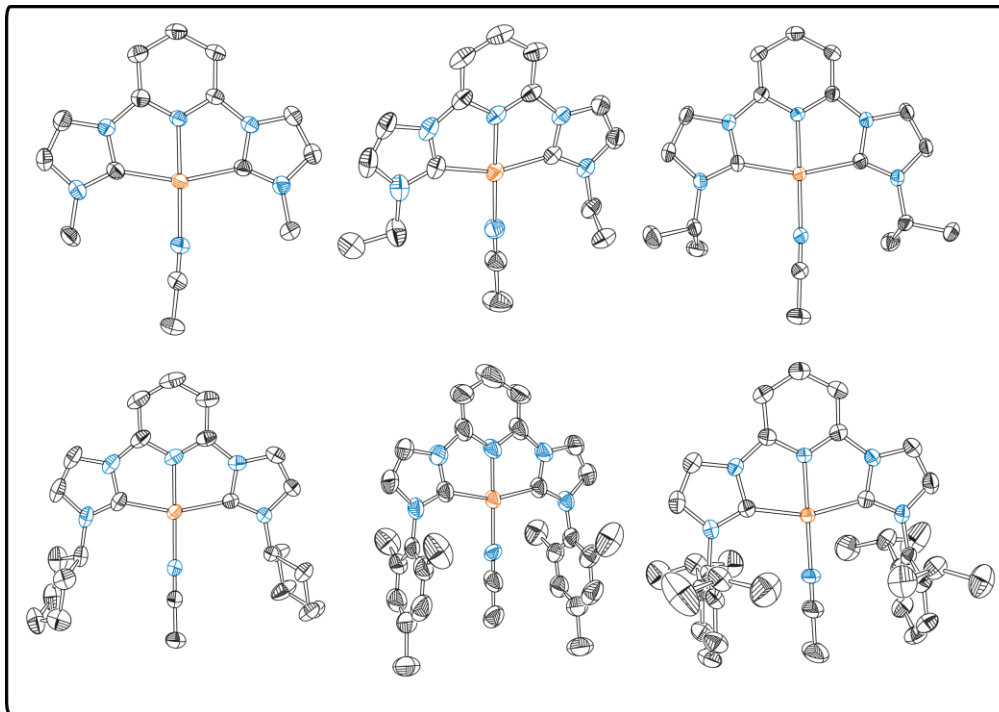


Figure 1.8: Solid state structures of all derivatives of the  $[\text{PDC}^{\text{R}}\text{Pd}(\text{MeCN})]$  complexes from left to right  $\text{R} =$ : methyl, ethyl, isopropyl, cyclohexyl, mesityl, and diisopropylphenyl at 50 % probability. Hydrogen atoms and  $\text{PF}_6^-$  counterions have been omitted for clarity.

All structures display a pseudo square planar geometry with a C1-Pd-C11 bond angle around  $158^\circ$ . As can be seen in Table 1.2 the bond lengths around the palladium center and the imidazole ring are similar throughout the entire series, suggesting that there is no significant electronic difference from the substitutions on the wingtips. Full bond lengths and angles with crystallographic experimental tables can be found in the appendix.

<b>R</b>	<b>Me</b>	<b>Et</b>	<b>lpr</b>	<b>Cy</b>	<b>Mes*</b>	<b>Dipp*</b>
<b>C1–Pd (Å)</b>	2.030	2.029	2.039	2.038	2.016	2.019
<b>N3–Pd (Å)</b>	1.961	1.966	1.961	1.963	1.957	1.959
<b>C11–Pd (Å)</b>	2.031	2.034	2.040	2.040	2.035	2.019
<b>N6–Pd (Å)</b>	2.003	2.004	2.002	2.003	1.999	2.008
<b>C2–C3 (Å)</b>	1.338	1.325	1.339	1.329	1.338	1.347
<b>C9–C10 (Å)</b>	1.347	1.335	1.336	1.334	1.337	1.347
<b>C1–Pd–C11 (°)</b>	158.85	158.31	158.45	158.46	157.94	158.52

Table 1.2: Selected bond lengths and angles for the series of [PDC<sup>R</sup>Pd(MeCN)](PF<sub>6</sub>)<sub>2</sub> complexes. The \* denotes that due to the mesityl and diisopropylphenyl complexes containing a mirror plane in the solid-state the bond lengths: C1–Pd = C11–Pd, and C2–C3 = C9–C10.

## 1.6 Characterization of the Steric Environment

While electronically the complexes are all similar, as evident through solid state X-ray analysis, we were interested in investigating the steric environment around the metal center by our library of PDC ligands. Two methods that have been used in the literature to describe the steric effects of the ligand are the %V<sub>Bur</sub><sup>44</sup> and the use of solid angles.<sup>45</sup> Both methods use xyz coordinate files which we obtained from our crystal data.

### 1.6.1 %V<sub>Bur</sub> Steric Calculation

The percent buried volume (%V<sub>Bur</sub>) can be described as the percentage of space occupied by a ligand within a sphere, of radius of 3.5 Å, centered at the metal. Software designed to calculate the %V<sub>Bur</sub> is free of charge and can be found online.<sup>46</sup> Two calculations were performed on each complex, one without the acetonitrile ligand

(%  $V_{\text{BurPDC}}$ ), and one with the acetonitrile (%  $V_{\text{BurComplex}}$ ), the difference was then taken to obtain the %  $V_{\text{Bur}}$  contribution from the coordinated acetonitrile (%  $V_{\text{BurMeCN}}$ ) and the results are shown in the bottom portion of Table 1.3.

	<b>Me</b>	<b>Et</b>	<b>lpr</b>	<b>Cy</b>	<b>Mes</b>	<b>Dipp</b>
<b>G(L)PDC (%)</b>	51.45	53.21	54.63	54.51	62.60	69.43
<b>G(L)MeCN (%)</b>	17.46	17.47	17.49	17.47	17.13	17.35
<b>Sum G(L) (%)</b>	68.91	70.68	72.12	71.98	79.73	86.78
<b>G(L)Complex (%)</b>	67.42	68.29	69.05	68.77	73.89	80.53
<b><math>V_{\text{BurPDC}}</math> (%)</b>	51.5	52.8	53.8	51.9	57.1	63.4
<b><math>V_{\text{BurComplex}}</math> (%)</b>	64.2	65.3	66.1	64.8	69.4	75.7
<b><math>V_{\text{BurMeCN}}</math> (%)</b>	12.7	12.5	12.3	12.9	12.3	12.3

Table 1.3: Calculated values obtained from crystal data for the steric bulk around the metal center. This data for the G-values were obtained using the online software Solid G, and the %  $V_{\text{Bur}}$  values were obtained using the online software SambVca.

As can be seen in Table 1.3. the %  $V_{\text{BurPDC}}$  for the alkyl groups is surprisingly similar, around 52%, suggesting that the N-alkyl substituents do not contribute significantly to the steric bulk around the metal center. When calculations were performed with the bound acetonitrile, the %  $V_{\text{Bur}}$  for the alkyl series increased to around 65%. As mentioned above the difference was obtained for the two calculations and showed the %  $V_{\text{Bur}}$  contribution of MeCN to be consistently near 12.5%. As the wingtips are substituted with the sterically demanding mesityl and diisopropylphenyl groups we see an increase in the %  $V_{\text{Bur}}$  values. The mesityl group adds near an additional 5% to the steric value when compared to the alkyl series while

diisopropylphenyl adds around 11%. As expected the acetonitrile contributes similarly for the aryl series. As mentioned above the %  $V_{\text{Bur}}$  calculation considers a sphere of 3.5 Å, it has been reported that substituents farther away are sometimes not accounted for using this method.<sup>47</sup>

### 1.6.2 Steric G-value Obtained from Solid Angles

As the distance from the metal to the bottom (para) aryl carbon and the closest isopropyl group carbon on the diisopropylphenyl derivative are 5.623 Å and 4.359 Å respectively, we sought to use a second method to investigate the steric properties. Solid angles have been used to describe the steric properties of ligands and software has been created to obtain numerical values, called G-values<sup>45</sup>. The solid angle has been described visually, as replacing the metal atom with a light source and a sphere outside of the complex, ligands then block light from reaching the sphere, casting a shadow. Numerically it is sum of the shadowed areas over the volume of a full sphere, multiplied by 100 for percent. The values obtained are given in Table 1.3 where G(L)PDC and G(L)MeCN are the G values obtained for the PDC and MeCN ligands respectively. Sum G(L) is the sum of the two values and G(L)Complex is the G-value obtained when the PDC and MeCN ligands are treated as one ligand i.e. overlap of the shadows are not considered. As shown in Table 1.3 we see a similar trend in the alkyl substituted series for the G(L)PDC values that we saw with the %  $V_{\text{Bur}}$  calculations; where although there is a small increase across the series, it is very slight. The G(L)PDC for the mesityl and diisopropylphenyl groups show a large increase in G-value when compared to the cyclohexyl derivative by 8% and almost 15% respectively. The G(L)MeCN is similar across the entire series with a value of around 17%. A graphical representation is shown in Figure 1.9 for the smallest and largest

ligands (methyl and diisopropylphenyl) and displays the solid angles of the PDC ligand in blue and the coordinated MeCN in yellow. The results from both calculations suggest that the steric difference is very small when comparing alkyl wingtips, however, we observe a significant difference for the two larger aryl groups when compared to the alkyl groups and each other.

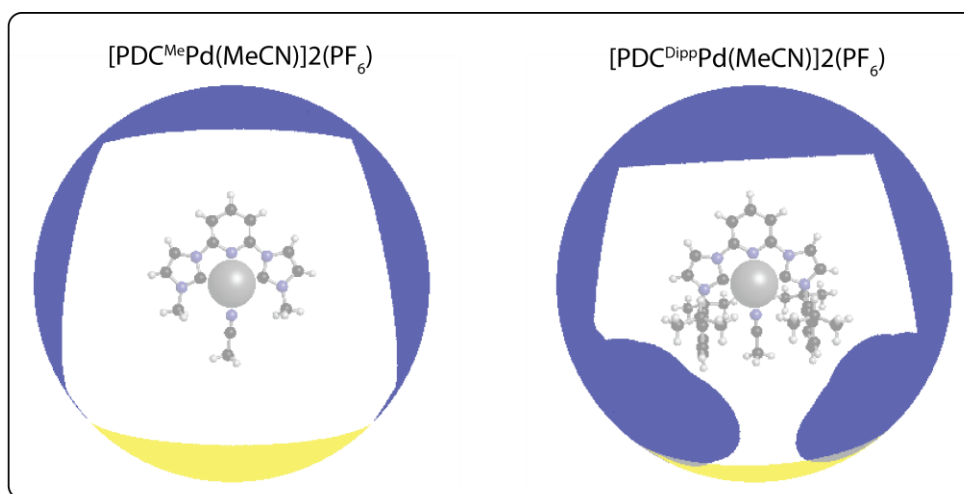


Figure 1.9: Images obtained from the Solid G software for the methyl and diisopropylphenyl derivatives. The blue and yellow colors show the percentage of the sphere shielded by the PDC and MeCN ligands respectively.

### 1.7 Electrochemical Characterization and CO<sub>2</sub> Activation of $[PDC^{cy}Pd(MeCN)](PF_6)_2$

As the palladium triphos system with cyclohexyl substituents was reported to be the most active for CO<sub>2</sub> reduction<sup>12</sup>, we decided to initially target our PDC<sup>cy</sup> complex.

### 1.7.1 Cyclic Voltammetry studies of $[\text{PDC}^{\text{cy}}\text{Pd}(\text{MeCN})](\text{PF}_6)_2$

Cyclic voltammetry (CV) experiments were performed in dimethylformamide (DMF) with 0.1 M tetrabutylammonium hexafluorophosphate ( $\text{TBAPF}_6$ ) as the supporting electrolyte, and an analyte concentration of 1 mM. A three-electrode configuration was used where the working electrode was a glassy carbon disk, the counter electrode was a platinum wire, and a  $\text{Ag}/\text{AgCl}$  electrode was used as the reference. Figure 1.10 (blue trace) shows the voltammogram obtained for the  $[\text{PDC}^{\text{cy}}\text{Pd}(\text{MeCN})](\text{PF}_6)_2$  complex under a  $\text{N}_2$  environment at a scan rate of 0.25 V/s. The voltammogram shows four reductions at  $-0.91$ ,  $-1.16$ ,  $-1.53$ , and  $-1.76$  V vs.  $\text{Ag}/\text{AgCl}$ . As our complex is a  $\text{Pd}(\text{II})$  species we would only expect to see two reductions corresponding to  $\text{Pd}^{\text{II/I}}$  and  $\text{Pd}^{\text{I/0}}$  couples, however, it has been reported that this class of ligand is redox active<sup>48</sup> and thus we attributed the two additional redox events to ligand based reductions.

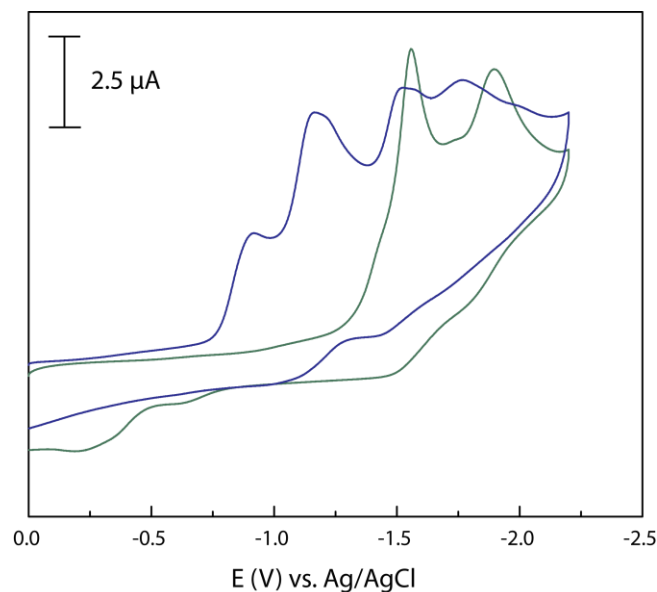


Figure 1.10: Voltammogram of 2,6-Bis[3-(cyclohexyl)imidazolium]pyridine dibromide (green trace) and  $[\text{PDC}^{\text{cy}}\text{Pd}(\text{MeCN})](\text{PF}_6)_2$  (blue trace).

Indeed, when we obtain the voltammogram for the proligand (2,6-Bis[3-(cyclohexyl)imidazolium]pyridine dibromide) we see two reductions that overlay well with the final two reductions seen for the palladium complex (Figure 1.10 green trace), suggesting that the final two reductions are ligand based. Due to this finding we focused our electrochemical studies on the initial two reductions which we attributed to a palladium (II/I) couple, followed by a palladium (I/0) couple.

### 1.7.2 Randles–Sevcik Analysis

As the major drawback to the palladium triphos complex was formation of the Pd(I)–Pd(I) dimer, prior to the catalytic studies we wanted to determine if our system also succumbed to dimerization upon electrochemical reduction. While there is no literature evidence for bridged dimers with this ligand scaffold, unbridged Pd(I)–Pd(I) dimers have been reported for palladium PNP pincer complexes.<sup>49</sup> Dimer formation can be studied through voltammograms obtained at various scan rates and Randles–Sevcik analysis (Equation 1.2) which determines if the electrochemical process is diffusion controlled.<sup>50</sup> The Randles–Sevcik equation relates the peak current ( $I_p$ ) and scan rate ( $\nu$ ) to a linear relationship where  $\alpha$  is the transfer coefficient (assumed to be 0.5),  $A$  is area of the electrode surface, and  $D$  is the diffusion constant. For an electrochemical process that is simply diffusion controlled a linear plot of peak current vs. square root of scan rate should be obtained. If there is a chemical step involved during the redox process (not a diffusion controlled process), i.e. an electrochemical reduction followed by formation of a dimer species, a nonlinear plot would be obtained.

$$\frac{I_p}{\nu^{1/2}} = (2.99 \times 10^5) \alpha^{1/2} A C D^{1/2} \quad (\text{eq. 1.2})$$

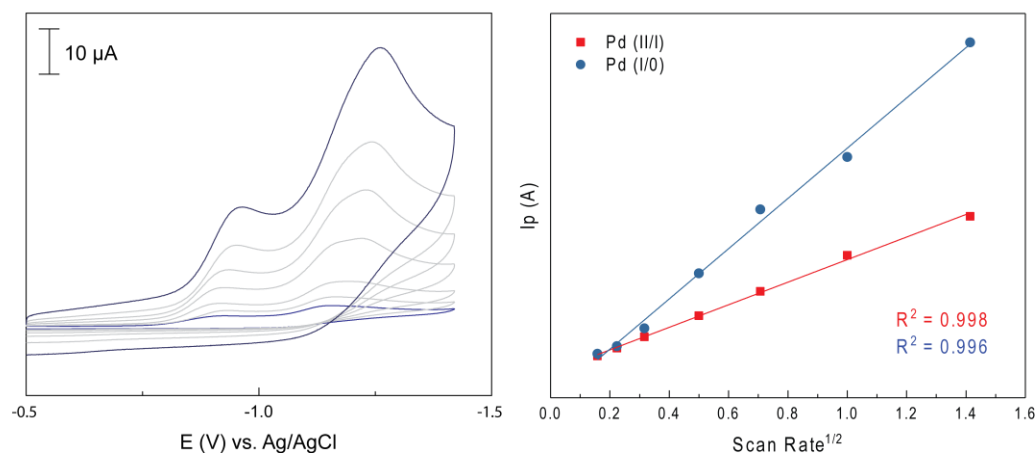


Figure 1.11: Scan rate study and Randles–Sevcik plot of  $[\text{PDC}^{\text{Cy}}\text{Pd}(\text{MeCN})](\text{PF}_6)_2$

A scan rate study was obtained using identical experimental conditions as the CV analysis described above. Voltammograms were obtained at scan rates of 0.025, 0.050, 0.1, 0.25, 0.5, 1, and 2 V/s and are shown in Figure 1.11 (left plot). A plot of peak current vs. square root of the scan rate was then obtained for both the observed palladium reductions and is shown in Figure 1.11 (right plot). As we can see both reductions give a linear relationship for peak current vs square root of the scan rate with  $R^2$  values of 0.998 for the Pd (II/I) couple (red data) and 0.996 for the Pd(I/0) couple (blue data). This suggests that upon electrochemical reduction to the Pd (I) species, our  $\text{PDC}^{\text{Cy}}$  system does not undergo a sequential chemical step to form bridged or unbridged dimers.

### 1.7.3 Electrochemical Studies Saturated with CO<sub>2</sub>

CV studies were performed for the PDC<sup>cy</sup> complex by saturating the solution with CO<sub>2</sub>. This was done by bubbling CO<sub>2</sub> in the analyte solution for thirty minutes prior to obtaining the voltammogram. The experimental conditions were the same as previously described and obtained at a scan rate of 0.25 V/s.

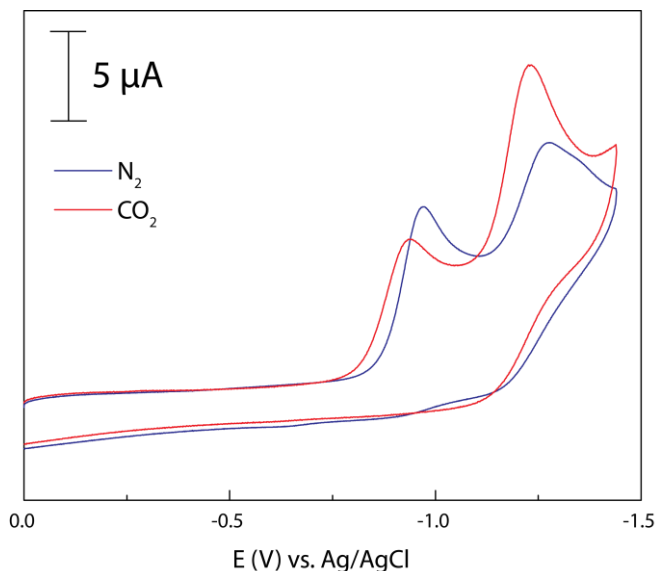


Figure 1.12: Voltammogram of [PDC<sup>cy</sup>Pd(MeCN)](PF<sub>6</sub>)<sub>2</sub> under N<sub>2</sub> (blue trace) and CO<sub>2</sub> (red trace) at 0.25 V/s.

Figure 1.12 shows the voltammogram for [PDC<sup>cy</sup>Pd(MeCN)](PF<sub>6</sub>)<sub>2</sub> under N<sub>2</sub> (blue trace) and the reductions were previously assigned (*vide supra*). When the solution is saturated with CO<sub>2</sub> a current enhancement is observed over the Pd (I/0) couple (-1.28 V vs. Ag/AgCl), indicating electrochemical activity toward CO<sub>2</sub>. To determine the reduction products formed for the activation of CO<sub>2</sub> by our complex, controlled potential electrolysis experiments (CPE) were performed.

CPE experiments were performed in a gas tight electrolysis cell with a three-electrode configuration consisting of a glassy carbon working electrode, a platinum mesh counter electrode, and a Ag/AgCl reference electrode. Concentrations and the supporting electrolyte were identical to the CV experiments described above. Electrolysis was performed for 100 minutes in CO<sub>2</sub> saturated DMF at the peak potential for the Pd (I/0) couple. Gaseous products were monitored throughout the experiment by gas chromatography analysis of the headspace.

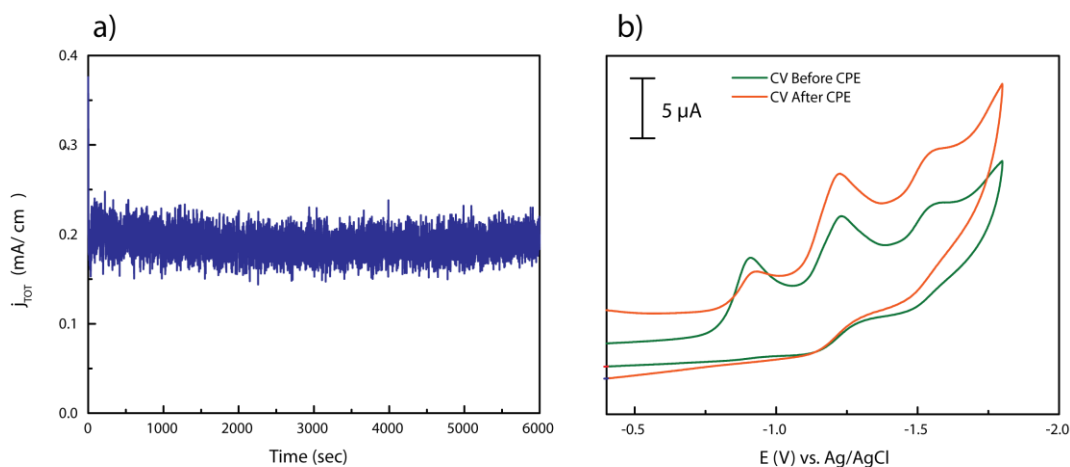


Figure 1.13: Current density vs. time plot for the CPE experiment of  $[\text{PDC}^{\text{cy}}\text{Pd}(\text{MeCN})](\text{PF}_6)_2$  (a), and CVs before and after the CPE experiment (b).

Figure 1.13a shows the current density vs. time plot for the CPE of  $[\text{PDC}^{\text{cy}}\text{Pd}(\text{MeCN})](\text{PF}_6)_2$  at  $-1.28$  V vs Ag/AgCl. As we can see the complex shows a stable current density of  $0.2 \text{ mA/cm}^2$  for the duration of the experiment. Furthermore, CVs obtained prior to, and after the CPE experiment show retention of redox features (Figure 1.13b). Taken together, these results suggest that the  $[\text{PDC}^{\text{cy}}\text{Pd}(\text{MeCN})](\text{PF}_6)_2$

complex is stable to prolonged electrolysis. Also, as we do not observe a loss of current throughout the CPE experiment, this further supports that this system does not succumb to dimers produced through electrochemical reduction of the complex. When looking at the metrics for catalysis, we see that this system is selective for CO<sub>2</sub> reduction, as no H<sub>2</sub> was detected by GC. However, this complex showed a low faradaic efficiency of 15% and only 12 ppm of CO was produced (Table 1.4 first entry).

Additive	Potential (V)	CO (FE/ppm)	H <sub>2</sub> (FE/ppm)
None	-1.28	15 ± 2/ 12 ± 3	None
HBF <sub>4</sub> (3 mM)	-1.11	9 ± 12/ 31 ± 41	252 ± 9/ 54 ± 10
Mg(ClO <sub>4</sub> ) <sub>2</sub>	-1.28	41 ± 8/ 17 ± 6	None

Table 1.4: Parameters and metrics for CPE experiments with [PDC<sup>cy</sup>Pd(MeCN)](PF<sub>6</sub>)<sub>2</sub>

#### 1.7.4 Electrochemical Studies with HBF<sub>4</sub>

It has been reported that the addition of acids aids in the catalysis of CO<sub>2</sub> reduction by homogeneous transition metal systems.<sup>13,51,52</sup> As such, we were interested in determining if the addition of HBF<sub>4</sub> could enhance our catalytic results, as it did for the pallidum triphos system<sup>13</sup>. CV analysis was used to observe current enhancement and the results are shown in Figure 1.14. The concentrations of analyte and electrolyte were as previously described. One equivalent aliquots (1 mM) of HBF<sub>4</sub> were titrated into the analyte solution and the current response was recorded.

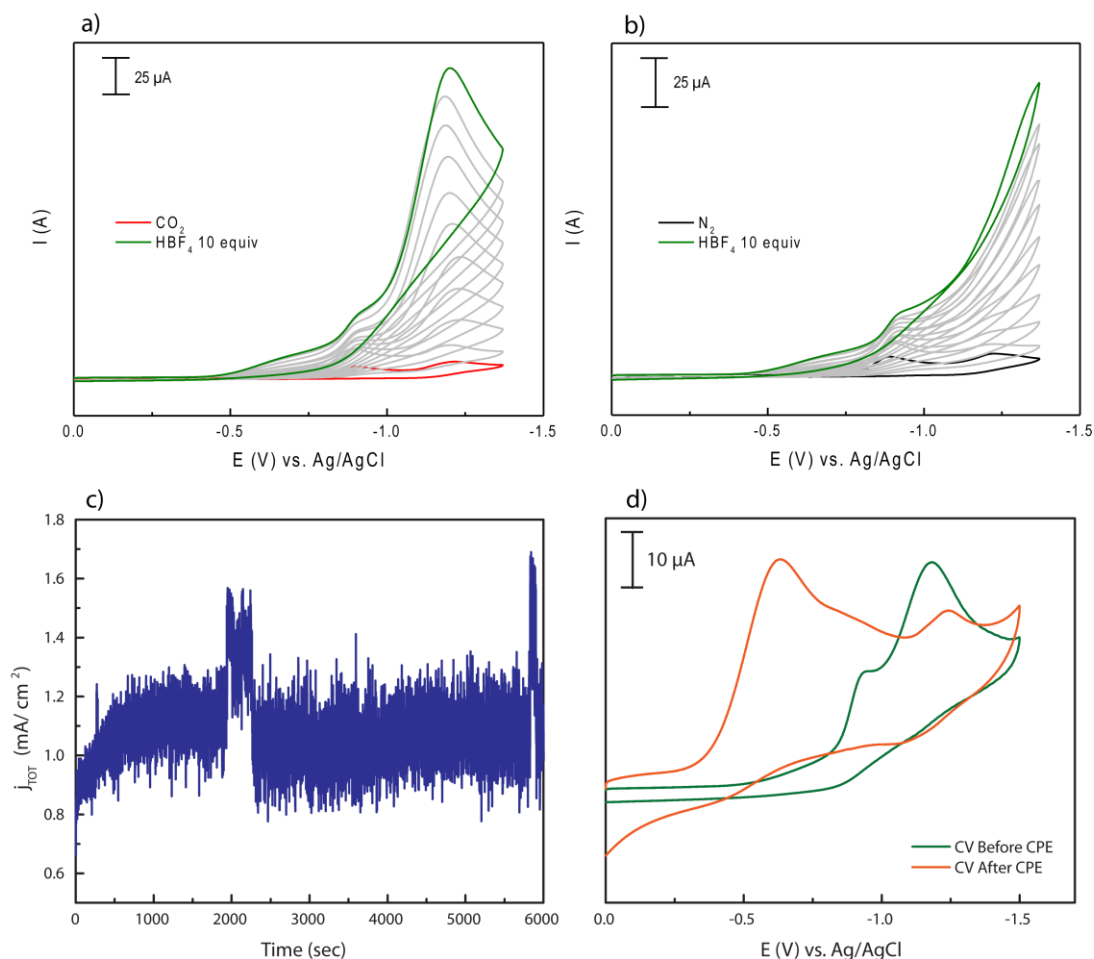


Figure 1.14: CV and CPE results for the addition of HBF<sub>4</sub> to [PDC<sup>cy</sup>Pd(MeCN)](PF<sub>6</sub>)<sub>2</sub>

The titration of HBF<sub>4</sub> into a CO<sub>2</sub> saturated solution results in a large current enhancement (Figure 1.14a) as well as a shift in onset potential towards more positive values, typical of proton coupled electron transfers. As we perform a control experiment under N<sub>2</sub>, we also see a large current enhancement (Figure 1.14b) suggesting proton reduction is likely happening. We found that when the addition of HBF<sub>4</sub> exceeds 3 equivalents, we begin to lose the redox feature of the Pd (I/0) couple, suggesting that the H<sup>+</sup> reduction at the glassy carbon electrode is becoming the

dominant pathway. Due to these results, the CPE experiments were performed with the addition of 3 equivalents of  $\text{HBF}_4$  and at a potential of  $-1.1$  V vs Ag/AgCl as electrolysis at the onset potential should help to prevent  $\text{H}^+$  reduction at the electrode surface. The current density vs. time plot is shown in Figure 1.14c and displays a stable current for the duration of the CPE experiment. Further, we see a larger current density when comparing the data from CPE experiment with no additive,  $1 \text{ mA/cm}^2$  vs.  $0.2 \text{ mA/cm}^2$  (Figure 1.14c and Figure 1.13a) suggesting that this system is more active. However, when looking at the metrics for catalysis we see that the addition of  $\text{HBF}_4$  resulted in a lower faradaic efficiency for CO production (9%) with the majority of current going towards  $\text{H}^+$  reduction to form  $\text{H}_2$  (54%) (Table 1.4 second entry). Lastly when looking at the voltammograms before and after the CPE experiment we see a new peak at  $-0.7$  V, suggesting that a new species was formed during electrolysis (Figure 1.14d). Unfortunately, we were unable to identify this species and did not pursue further studies due to the low production of CO.

### 1.7.5 Electrochemical Studies with $\text{Mg}(\text{ClO}_4)_2$

Savéant reported that the addition of Lewis acids, such as  $\text{Mg}^{2+}$ , can also enhance  $\text{CO}_2$  reduction catalysis through formation of a stabilized metalcarboxylate.<sup>53</sup> As before, we initially studied the effect of added  $\text{Mg}(\text{ClO}_4)_2$  through CV analysis and the results are shown in Figure 1.15.

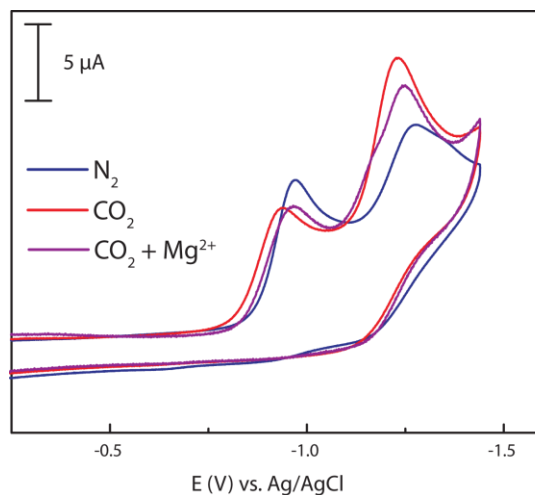


Figure 1.15: Voltammogram of  $[\text{PDC}^{\text{cy}}\text{Pd}(\text{MeCN})](\text{PF}_6)_2$  under  $\text{N}_2$  (blue trace),  $\text{CO}_2$  (red trace), and  $\text{CO}_2$  with added  $\text{Mg}(\text{ClO}_4)_2$  (purple trace).

Voltammetry experiments were performed as previously described and with a 215 mM addition of  $\text{Mg}(\text{ClO}_4)_2$  (Figure 1.15 purple trace). As we can see from the voltammograms in Figure 1.15, the addition of  $\text{Mg}^{2+}$  cations have little effect on the observed current. We still see a small enhancement of current (purple trace vs blue trace), although it is slightly less that what is observed with no additive (red trace). As the peak potential under  $\text{CO}_2$  with added  $\text{Mg}(\text{ClO}_4)_2$  did not shift, CPE experiments were performed at  $-1.28$  V vs. Ag/AgCl and the results are shown in Figure 1.16 below.

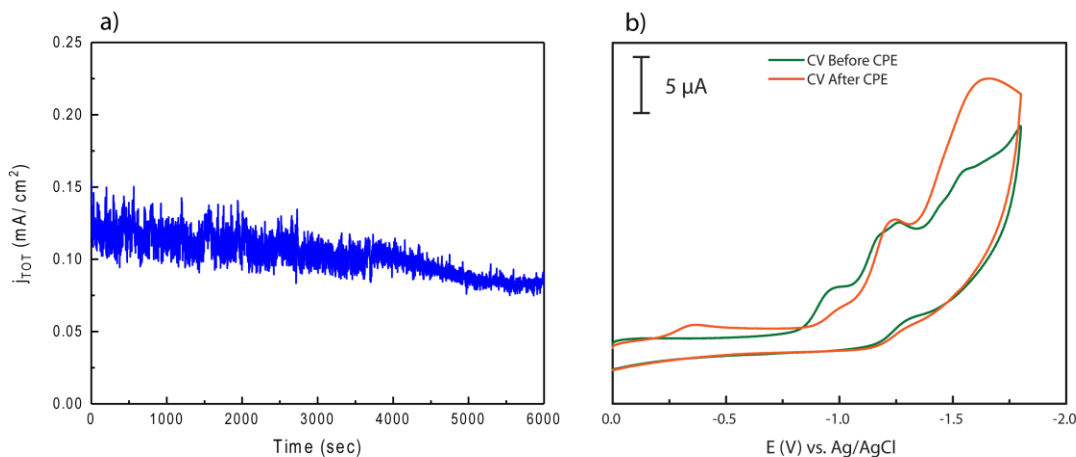


Figure 1.16: CPE results for the addition of  $\text{Mg}(\text{ClO}_4)_2$  to  $[\text{PDC}^{\text{cy}}\text{Pd}(\text{MeCN})](\text{PF}_6)_2$

The current density vs. time plot shows a slight decay in current through the duration of the electrolysis, starting near  $0.125 \text{ mA/cm}^2$  and decaying to  $0.1 \text{ mA/cm}^2$  (Figure 1.16a). The current density is about half of what is observed when compared to the CPE experiments done with no additive ( $0.2$  vs  $0.1 \text{ mA/cm}^2$ ). This is not surprising as the voltammetry experiments showed a slight decrease in current with added  $\text{Mg}^{2+}$  cations, described above. The voltammograms obtained before and after the CPE experiments show retention of redox features (Figure 1.16b). While a slight loss of current is observed during the electrolysis, the complex appears to be stable, as evident through CVs prior to and after electrolysis. The catalytic metrics are given in Table 1.4 (last entry) and show that with added  $\text{Mg}^{2+}$  cations we observe an increase in faradaic efficiency to 41% and further, this system is selective for  $\text{CO}_2$  reduction as no  $\text{H}_2$  was observed. However, when we look at the amount of  $\text{CO}$  produced, we see that we are, within error, producing the same amount as with no additive.

### 1.7.6 Summary of Electrochemical Results with $[\text{PDC}^{\text{cy}}\text{Pd}(\text{MeCN})](\text{PF}_6)_2$

The designed  $[\text{PDC}^{\text{cy}}\text{Pd}(\text{MeCN})](\text{PF}_6)_2$  complex shows selectivity for  $\text{CO}_2$  without additives and with the addition of  $\text{Mg}(\text{ClO}_4)_2$  with faradaic efficiencies of 15% and 41% respectively. The addition of  $\text{HBF}_4$  decreases the faradaic efficiency for CO production to 9% with most of the current going toward  $\text{H}_2$  production. While this system is not as efficient as the analogous palladium triphos catalyst (85% faradaic efficiency)<sup>13</sup>, we have demonstrated that the  $\text{PDC}^{\text{cy}}$  complex does not form unwanted dimers during electrolysis.

## 1.8 Electrochemistry Studies of $[\text{PDC}^{\text{R}}\text{Pd}(\text{MeCN})](\text{PF}_6)_2$ Complexes

Steric shielding of the metal has been reported to play a role in NHC palladium cross coupling catalysis<sup>47</sup>, in zinc complexes for  $\text{CO}_2$  activation<sup>54</sup> as well as in the DuBois system for electrochemical  $\text{CO}_2$  activation<sup>13</sup>. As described above, this ligand system easily allows for substitution at the wingtips of the ligand. We were successful in synthesizing a library of complexes with varying steric bulk on the wingtips, with substituents of methyl, ethyl, isopropyl, cyclohexyl (described above), mesityl, and diisopropylphenyl. As the steric bulk of the R position increases along the series, we were interested in investigating if this influenced catalysis. A subset of these complexes were chosen (Et, Mes, Dipp) to study through cyclic voltammetry and compare their results to our previously studied cyclohexyl complex.

### 1.8.1 CV Studies of $[\text{PDC}^{\text{R}}\text{Pd}(\text{MeCN})](\text{PF}_6)_2$ Complexes

As before voltammograms were obtained with a glassy carbon working electrode, a platinum wire counter electrode and a Ag/AgCl reference electrode under an inert  $\text{N}_2$  environment and in  $\text{CO}_2$  saturated DMF. Concentrations were as

previously described. Figure 1.17 shows the voltammograms obtained for the subset of complexes at a scan rate of 0.1 V/s.

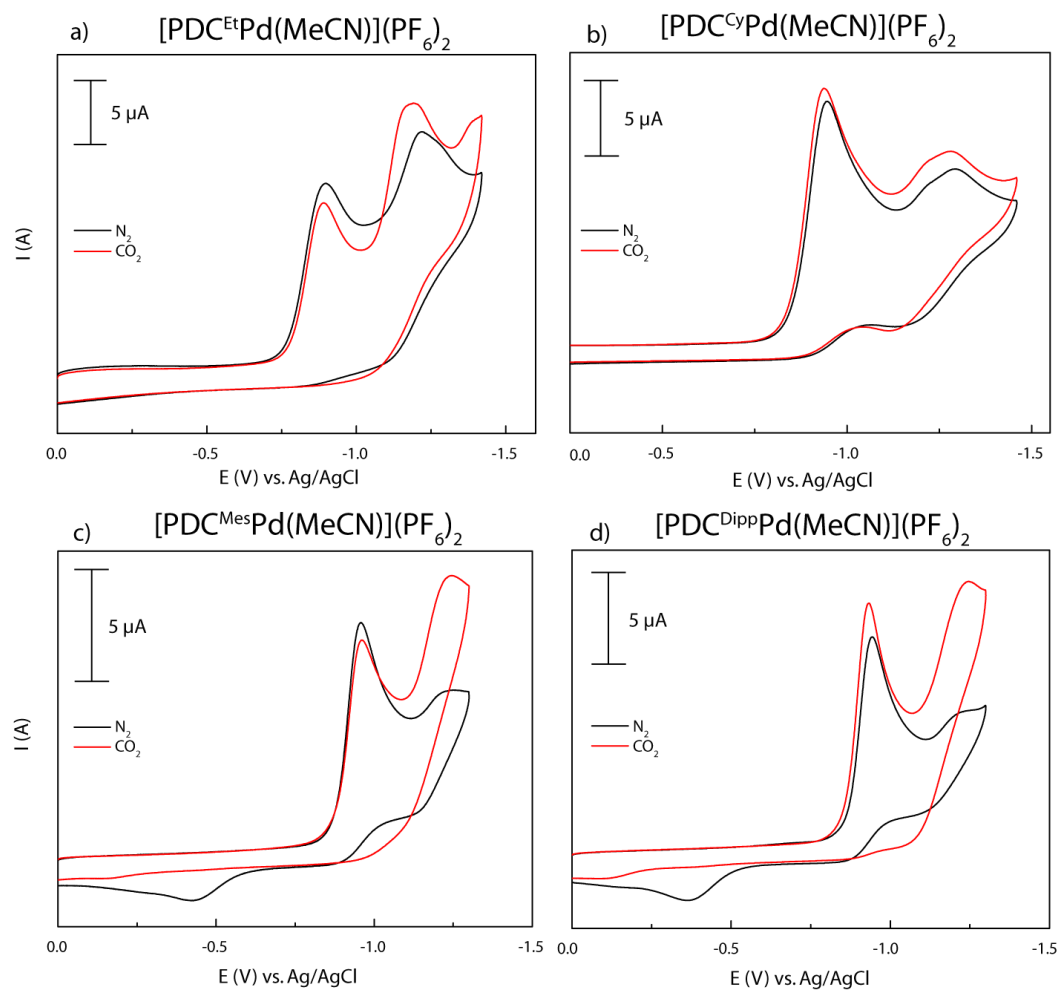


Figure 1.17: Voltammograms for  $[\text{PDC}^{\text{R}}\text{Pd}(\text{MeCN})](\text{PF}_6)_2$  complexes under  $\text{N}_2$  (black trace) and  $\text{CO}_2$  (red trace) where  $\text{R} = \text{Et}$  (a),  $\text{Cy}$  (b),  $\text{Mes}$  (c), and  $\text{Dipp}$  (d).

As is shown in Figure 1.17 a-d, all PDC complexes show activity towards the electrochemical reduction of CO<sub>2</sub>, as there is a current enhancement over the Pd (I/O) couple when the solution is saturated with CO<sub>2</sub> (black trace vs. red). Table 1.5 summarizes the observed current enhancement as the difference of peak current (I<sub>p</sub>) under CO<sub>2</sub> and N<sub>2</sub> at the given potentials.

R	Et	Cy	Mes	Diip
<b>Peak Potential (V)</b>	<b>- 1.21</b>	<b>- 1.28</b>	<b>- 1.25</b>	<b>- 1.25</b>
<b>I<sub>p</sub> CO<sub>2</sub> (μA)</b>	11.10	13.53	12.85	15.24
<b>I<sub>p</sub> N<sub>2</sub> (μA)</b>	9.97	12.31	7.68	8.14
<b>I<sub>p</sub> Difference (μA)</b>	1.13	1.22	5.17	7.10

Table 1.5: Observed current enhancement for a series of [PDC<sup>R</sup>Pd(MeCN)](PF<sub>6</sub>)<sub>2</sub> complexes under CO<sub>2</sub> and N<sub>2</sub> where R = Et, Cy, Mes and Diip. The values are given for the potential at which the current enhancement is observed.

As displayed in Table 1.5, all [PDC<sup>R</sup>Pd(MeCN)](PF<sub>6</sub>)<sub>2</sub> complexes show current enhancement near -1.25 V vs Ag/AgCl. When comparing the observed current enhancement, we see that the ethyl and cyclohexyl complexes display similar values, a little over 1 μA. However, when compared to the alkyl substituents, the mesityl and diisopropylphenyl substituted complexes show significant enhancement near 5 and 7 μA respectively.

### 1.9 Correlation of Steric Environment and Electrochemical Activity

Interestingly, when comparing the values of electrochemical activity (Table 1.5) and steric environment (Table 1.3) we observe a similar trend. As described above, both the %V<sub>Bur</sub> and solid angle calculations gave similar results for steric

environment when R = alkyl substituents. Similarly, we observe similar current enhancement for the Et and Cy complexes. When R is Mes or Dipp, we observe a greater steric shielding of the metal center, which increases as the substituent size increases. Likewise, we see the same trend in electrochemical activity by CV where the Dipp complex is more active than the Mes complex. Thus, the trend for electrochemical activity  $\text{Et} \approx \text{Cy} < \text{Mes} < \text{Dipp}$ , correlates well with the calculated steric environment suggesting that steric environment around the metal center is important in catalyst design.

### 1.10 Comparison to $[\text{PDC}^{\text{nBu}}\text{Pd}(\text{Br})](\text{Br})$

During our study, similar work was reported on palladium complexes with PDC and LDC (Lutidine spaced dicarbene) ligands with n-butyl (<sup>n</sup>Bu) wingtips for the electrochemical reduction of CO<sub>2</sub> to CO<sup>55</sup>. This group went on to investigate the substitution on the back bone of the imidazole, studying benzimidazole as well as larger aromatic rings<sup>56</sup>, and more recently the para substitution on the pyridine ring<sup>57</sup>. However, the N substitution on the imidazole, or the wingtips of the ligand, was limited to only the alkyl substituent <sup>n</sup>Bu in all studies. When comparing the reported data to ours, we see that the  $[\text{PDC}^{\text{nBu}}\text{Pd}(\text{MeCN})](\text{BF}_4)_2$  complex shows a similar shaped voltammogram with a Pd(II/I) couple at  $-0.93 \text{ V vs. SCE}$ <sup>55</sup>. When we convert our Pd (II/I) potential ( $-0.91 \text{ V vs Ag/AgCl}$ ) to SCE, we obtain a potential of  $-0.95 \text{ V}$  which agrees well with the <sup>n</sup>Bu complex. This group reported CPE experiments with the halide complex,  $[\text{PDC}^{\text{nBu}}\text{Pd}(\text{Br})](\text{Br})$ , and found that applied potentials beyond the Pd(II/I) couple resulted in formation of an insulating material on the electrode surface, which resulted in low activity and efficiencies. Similarly, applied potentials more negative of the Pd(II/I) couple for  $[\text{PDC}^{\text{nBu}}\text{Pd}(\text{MeCN})](\text{BF}_4)$  complex gave

comparable results. Lastly, they reported that all current was accounted for during their CPE experiments (100% faradaic efficiency) for the production of H<sub>2</sub>. Contrary to their findings, our CPE experiments carried out for the Cy derivative did not produce H<sub>2</sub> (unless HBF<sub>4</sub> was added) and was stable to electrolysis up to the Pd(I/O) couple (described above). We also discovered that applied potentials, for CPE experiments, at or beyond where we observe ligand reductions (potentials > 1.4 V vs. Ag/AgCl) results in passivation of the electrode through formation of a black solid on the electrode surface, similar to what was reported. While our results and the literature results are slightly different, they are similar in that we both found the PDC<sup>R</sup>Pd complexes to be weakly active toward the electrochemical reduction of CO<sub>2</sub>. Due to these findings and the lack of electrochemical activity of the reported <sup>n</sup>Bu and our Cy complex, we decided to not pursue further CPE experiments.

### 1.11 Concluding Remarks

A library of [PDC<sup>R</sup>Pd(MeCN)](PF<sub>6</sub>)<sub>2</sub> complexes were synthesized where R, or the wingtip of the ligand, ranged in steric bulk from methyl to diisopropylphenyl. The synthesis of these complexes revealed that when Pd(OAc)<sub>2</sub> in DMSO at elevated temperatures is used for metalation, unwanted side products are formed and were characterized through X-ray crystallography. The use of Ag<sub>2</sub>O to form the Ag carbene followed by transmetallation to pallium resulted in much simpler chromatography and increased yields. Analysis of the solid-state structures of the solvato bound series revealed that the steric environment around the metal center is similar for all alkyl derivatives. The Mes and Dipp wingtips show a much more sterically encumbered environment as evident from the %V<sub>Bur</sub> and solid angle calculations. Voltammograms obtained show agreement with the solid-state analysis in that current enhancement is

similar for alkyl substituents and much greater for the bulky wingtips. Controlled potential electrolysis of the Cy complex revealed that faradaic efficiencies near 40% can be obtained with the addition of  $\text{Mg}(\text{ClO}_4)_2$ , however, only a small amount of CO is produced. Overall the  $\text{PDC}^{\text{R}}$  complexes were found to be only slightly active toward the electrochemical reduction of  $\text{CO}_2$ . While not as active as the Pd triphos system, the PDC palladium complexes have been supported to not undergo dimerization upon electrochemical reduction. Lastly the correlation found between steric shielding of the metal and electrochemical activity may be useful in the design of future homogeneous systems for the reduction of  $\text{CO}_2$ .

## REFERENCES

- (1) EIA, International Energy Outlook 2016, <http://www.eia.gov/forecasts/ieo/> (accessed April 2017)
- (2) Karl, T.; Trenberth, K. *Science* **2003**, *302*, 1719
- (3) Dr. Pieter Tans, NOAA/ESRL ([www.esrl.noaa.gov/gmd/ccgg/trends/](http://www.esrl.noaa.gov/gmd/ccgg/trends/)) and Dr. Ralph Keeling, Scripps Institution of Oceanography ([scrippsco2.ucsd.edu/](http://scrippsco2.ucsd.edu/)).
- (4) NASA GISS ([http://data.giss.nasa.gov/gistemp/graphs\\_v3/](http://data.giss.nasa.gov/gistemp/graphs_v3/))
- (5) Smith, J. B.; Schneider, S. H.; Oppenheimer, M.; Yohe, G. W.; Hare, W.; Mastrandrea, M. D.; Patwardhan, A.; Burton, I.; Corfee-Morlot, J.; Magadza, C. H. D.; Füssel, H.-M.; Pittock, a B.; Rahman, A.; Suarez, A.; van Ypersele, J.-P. *Proc. Natl. Acad. Sci.* **2009**, *106*, 4133.
- (6) Solomon, S.; Plattner, G.; Knutti, R.; Friedlingstein, P. *Proc. Natl. Acad. Sci.* **2009**, *106*, 1704.
- (7) Lenton, T. M.; Held, H.; Kriegler, E.; Hall, J. W.; Lucht, W.; Rahmstorf, S.; Schellnhuber, H. J. *Proc. Natl. Acad. Sci.* **2008**, *105*, 1786.
- (8) Drijfhout, S.; Bathiany, S.; Beaulieu, C.; Brovkin, V.; Claussen, M.; Huntingford, C. *Proc. Natl. Acad. Sci.* **2015**, *112*, 5777.
- (9) Lewis, N. S.; Nocera, D. G. *PNAS.* **2006**, *103*, 15729.
- (10) Fisher, Barbara J.; Eisenberg, R. *J. Am. Chem. Soc.* **1980**, *102*, 7361.
- (11) Hawecker, J.; Lehn, J.; Ziessel, R. *J. Chem. Soc. Chem. Comm.*, **1984**, 328.
- (12) DuBois, D. L. Miedaner, A. *J. Am. Chem. Soc.* **1987**, *109*, 113.
- (13) DuBois, D. L.; Miedaner, A.; Haltiwanger, C. R. *J. Am. Chem. Soc.* **1991**, *113*, 8753.
- (14) Slater, S.; Wagenknecht, J. H. *J. Am. Chem. Soc.* **1984**, *106*, 5367.
- (15) DeLaet, D. L.; Del Rosario, R.; Fanwick, P. E.; Kubiak, C. P. *J. Am. Chem. Soc.* **1987**, *109*, 754.

- 
- (16) Herrmann, W. A.; Elison, M.; Fischer, J.; Köcher, C.; Arthus, G. R. *Angew. Chem. Int. Ed.* **1995**, *34*, 2371.
- (17) Peris, Eduardo; Loch, Jennifer A.; Mata, José; Crabtree, Robert, H. *Chem. Commun.* **2001**, 201.
- (18) Loch, Jennifer A.; Albrecht, Martin; Peris, Eduardo; Mata, José; Faller, Jack W.; Crabtree, Robert, H. *Organometallics* **2002**, *21*, 700.
- (19) Selander, Nicklas; Szabó, Kálmán J. *Chem.Rev.* **2011**, *11*, 2048.
- (20) Wanzlick, H-W. *Angew. Chem. Int. Ed.* **1962**, *1*, 75.
- (21) Wanzlick, H-W.; Schönherr, H-J. *Angew. Chem. Int. Ed.* **1968**, *7*, 141.
- (22) Öfele, K. *J. Organomet. Chem.* **1968**, *12*, 42.
- (23) Arduengo III, A. J.; Harlow, R. L.; Kline, M. *J. Am. Chem. Soc.* **1991**, *113*, 361.
- (24) Arduengo III, A. J.; Krafczyk, R. *Chem. Unserer Zeit.* **1998**, *32*, 6.
- (25) Herrmann, W. A. *Angew. Chem. Int. Ed.* **2002**, *41*, 1290.
- (26) Farrell, K.; Albrecht, M. in *The Privileged Pincer-Metal Platform: Coordination Chemistry & Applications*, ed. Van Koten, G.; Gossage, A. R. Springer International Publishing, Cham, **2016**, 45–91.
- (27) Ebner, D. C.; Trend, R. M.; Genet, C.; McGrath, M. J.; O'Brien, P.; Stoltz, B. M. *Angew. Chem. Int. Ed.* **2008**, *47*, 6367.
- (28) Pangborn, A. B.; Giardello, M. A.; Grubbs, R. H.; Rosen, R. K.; Timmers, F. *J. Organometallics* **1996**, *15*, 1518.
- (29) Liu, Jingping; Chen, Jingbo; Zhao, Jingfeng; Zhao, Yuanhong; Li, Liang; Zhang, Hongbin. *Synthesis* **2003**, *17*, 2661.
- (30) Starikova, O. V.; Dolgushin, G. V.; Larina, L. I.; Ushakov, P. E.; Komarova, T. N.; Lopyrev, V. A. *Russian Journal of Organic Chemistry.* **2003**, *39*, 1467.
- (31) Gong, Han-Yuan; Rambo, Brett M.; Karnas, Elizabeth; Lynch, Vincent M.; Sessler, Jonathan L. *Nature Chemistry* **2010**, *2*, 406.

- 
- (32) Danopoulos, Andreas, A.; Tulloch, Arran, A. D.; Winston, Scott.; Eastham, Graham.; Hursthouse, Michael, B. *Dalton Trans.* **2003**, 5, 1009.
- (33) A.L. Spek, *J. Appl. Cryst.*, **2003**, 36, 7.
- (34) Perry, Marc C.; Cui, Xiuhua; Powell, Mark T.; Hou, Duen-Ren; Reibenspies, Joseph H.; Burgess, Kevin. *J. Am. Chem. Soc.* **2003**, 125, 113.
- (35) Clark, Wesley D.; Cho, Joon; Valle, Henry U.; Hollis, T. Keith; Valente, Edward J. *Journal of Organometallic Chemistry.* **2014**, 751, 534.
- (36) McGuinness, David. S.; Gibson, Vernon. C.; Steed, Jonathan. W. *Organometallics* **2004**, 23, 6288.
- (37) Wang, Harrison. M. J.; Lin, Ivan. J. B. *Organometallics* **1998**, 17, 972.
- (38) Jeffery, George. A. *An Introduction to Hydrogen Bonding*, Oxford University Press, Oxford, 1997
- (39) Steiner, Thomas *Angew. Chem. Int. Ed.* **2002**, 41, 48.
- (40) Caballero, Agustín; Díez-Barra, Enrique; Jalón, Félix A.; Merino, Sonia; Rodríguez, Ana M.; Tejeda, Juan. *J. Organomet. Chem.* **2001**, 627, 263.
- (41) Garrison, Jared C.; Youngs, Wiley J. *Chem Rev.* **2005**, 105, 3978.
- (42) Lin, Ivan J. B.; Vasam, Chandra, S. *Coordination Chemistry Reviews* **2007**, 251, 642.
- (43) Pugh, David; Danopoulos, Andreas A. *Coordination Chemistry Reviews* **2007**, 251, 610.
- (44) Poater, Albert; Ragone, Francesco; Giudice, Simona; Costabile, Chiara; Dorta, Reto; Nolan, Steven P.; Cavallo, Luigi *Organometallics* **2008**, 27, 2679.
- (45) Guzei, Ilia, A; Wendt, Mark *Dalton Trans.* **2006**, 3991.
- (46) Poater, Albert; Cosenza, Biagio; Correa, Andrea; Giudice, Simona; Ragone, Francesco; Scarano, Vittorio; Cavallo, Luigi *Eur. J. Inorg. Chem.* **2009**, 1759.

- 
- (47) Dible, Benjamin R.; Cowley, Ryan E.; Holland, Patrick L. *Organometallics* **2011**, *30*, 5123.
- (48) Yu, R. Y.; Darmon, J. M.; Milsman, C.; Margulieux, G. W.; Stieber, S. C. E.; DeBeer, S. Chirik, P. J. *J. Am. Chem. Soc.* **2013**, *135*, 13168.
- (49) Fafard, C. M.; Adhikari, D.; Foxman, B. M.; Mindiola, D. J.; Ozerov, O.V. *J. Am. Chem. Soc.* **2007**, *129*, 10318.
- (50) Bard, A. *Electrochemical Methods: Fundamentals and Applications*, Wiley, New York, **2001**
- (51) Smieja, J. M.; Sampson, M. D.; Grice, K. A.; Benson, E. E.; Froehlich, J. D.; Kubiak, C. P. *Inorg. Chem.* **2013**, *52*, 2484.
- (52) Rosenthal, J. *Prog. Inorg. Chem.* **2014**, *59*, 299.
- (53) Bhugun, I.; Lexa, D.; Savéant, J. M. *J. Phys. Chem.* **1996**, *100*, 19981.
- (54) Siek, Sopheavy; Dixon, Natalie A.; Kumar, Mukesh; Kraus, Jodi S.; Wells, Kirsten R.; Rowe, Brittany W.; Kelley, Steven P.; Zeller, Matthias; Yap, Glenn P. A.; Papish, Elizabeth T. *Eur. J. Inorg. Chem.* **2016**, 2495.
- (55) Therrien, Jeffery A.; Wolf, Michael O.; Patrick, Brian O. *Inorg. Chem.* **2014**, *53*, 12962.
- (56) Therrien, Jeffery A.; Wolf, Michael O.; Patrick, Brian O. *Inorg. Chem.* **2015**, *54*, 11721.
- (57) Therrien, Jeffery A.; Wolf, Michael O. *Inorg. Chem.* **2017**, *56*, 1161.

## Chapter 2

### A RHENIUM BIPYRIDINE COMPLEX WITH A COVALENTLY TETHERED BODIPY FOR PHOTOCATALYTIC CO<sub>2</sub> CONVERSION

#### 2.1 Motivation for the Discovery of Rhenium Systems for Photocatalytic CO<sub>2</sub> Conversion

##### 2.1.1 Photoactive Transition Metal Complexes for Energy Storage

As highlighted in Chapter 1, the conversion of CO<sub>2</sub> to CO is a promising method for energy storage.<sup>1-3</sup> Many transition metal complexes have been designed for the homogeneous electrocatalytic reduction of CO<sub>2</sub> to CO.<sup>4-8</sup> This method requires the electron equivalents for the redox processes to be provided via electrodes in solution. Another approach to homogeneous CO<sub>2</sub> reduction is through photoactivation, where the electron equivalents are provided through molecular photosensitizers. (Figure 2.1)

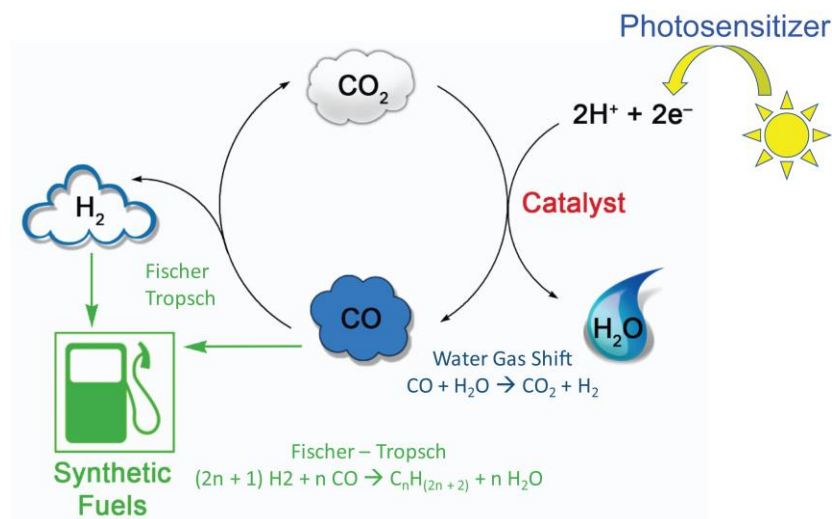
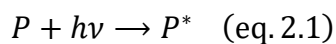


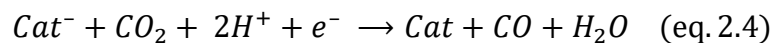
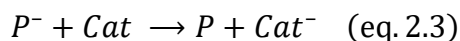
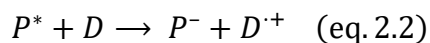
Figure 2.1: Energy storage and fuels production through photocatalytic  $\text{CO}_2$  reduction.

The same scheme of energy storage and fuels production, that was explained in Chapter 1, can again be utilized. However, for photochemical  $\text{CO}_2$  reduction the electrons are provided through direct absorption of solar energy by molecular photosensitizers, and subsequently energy transfer to a transition metal complex to form the catalytically active species (Figure 2.1). This reduced species can then facilitate the transformation of  $\text{CO}_2$  to  $\text{CO}$ .

### 2.1.2 Photochemical $\text{CO}_2$ Activation

The mechanism by which  $\text{CO}_2$  can be activated through photochemical means requires a photosensitizer, a sacrificial reductant, and the transition metal complex. The reaction sequence has been supported to operate through the process below where P is the photosensitizer, D is the sacrificial electron donor, and Cat is the transition metal catalyst.<sup>9</sup>





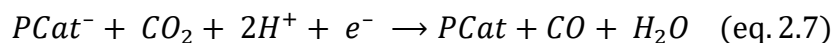
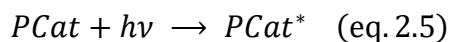
Equations 2.1 to 2.4: Process of photocatalytic CO<sub>2</sub> reduction.

In the first step the molecular photosensitizer absorbs a photon to produce the excited state of the photosensitizer, P\* (Equation 2.1). The excited state is then quenched by a sacrificial electron donor (D), which produces the reduced photosensitizer (P<sup>-</sup>), and a radical cation species of the donor (Equation 2.2). The reduced photosensitizer can then transfer an electron to the transition metal catalyst to produce the reduced catalyst (Cat<sup>-</sup>) and reform the ground state photosensitizer (Equation 2.3). The Cat<sup>-</sup> is the active form of the catalyst and can react with CO<sub>2</sub> and two protons and a second electron to produce CO, H<sub>2</sub>O, and regenerate the catalyst (Equation 2.4). Early examples utilizing this two-part system contained ruthenium(II) trisbipyridine as the photosensitizer and nickel tetraaza macrocyclic complexes as the catalyst.<sup>10</sup> However, there are also examples of transition metal complexes which act as both a photosensitizer and catalyst, as explained below.

### 2.1.3 Rhenium Bipyridine Systems for Photocatalytic CO<sub>2</sub> Activation

Of the many platforms developed for the photochemical activation of carbon dioxide,<sup>11-16</sup> *fac*-Re<sup>I</sup>(CO)<sub>3</sub> derivatives supported by bipyridine ligands have shown excellent efficiencies for the reduction of CO<sub>2</sub> to CO.<sup>17-27</sup> This system, originally reported by Lehn and coworkers,<sup>28,29</sup> was unique in that the rhenium bipyridine complex acted both as a photosensitizer and the catalyst. These single component

systems have been named type II catalysts and follow the sequence of equations below,<sup>9</sup> where Pcat is the complex that acts as both the photosensitizer and catalyst, and D has been previously defined.



Equations 2.5 to 2.6: Photocatalytic CO<sub>2</sub> reduction by type II catalysts.

In this sequence, PCat absorbs a photon to produce the excited state of the complex (Equation 2.5). This metal to ligand charge transfer state (MLCT), is then reductively quenched by a sacrificial electron donor (D) to form the active catalyst, PCat<sup>-</sup> (Equation 2.6). The catalyst can then react with CO<sub>2</sub>, 2H<sup>+</sup> and a second e<sup>-</sup> to produce CO, H<sub>2</sub>O and reform the catalyst (Equation 2.7).

#### 2.1.4 Photocatalytic Cycle of [Re(bpy)(CO)<sub>3</sub>Cl] with CO<sub>2</sub>

Specifically, [Re(bpy)(CO)<sub>3</sub>Cl] has been suggested to operate via the following mechanism.<sup>9,29,30</sup>

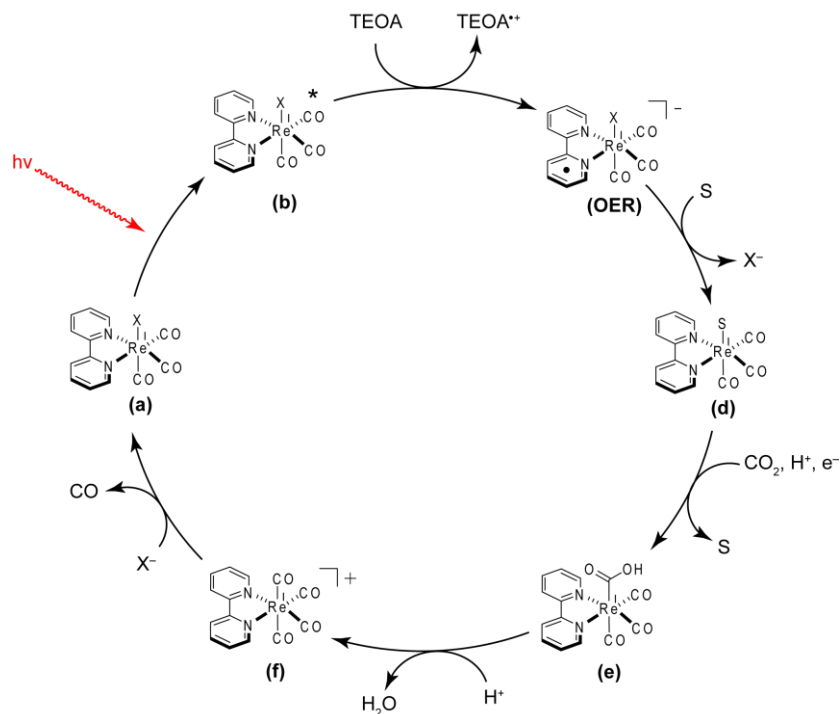


Figure 2.1: Photocatalytic activation of CO<sub>2</sub> by [Re(bpy)(CO)<sub>3</sub>Cl]

Rhenium(I) complex **(a)** absorbs a photon to produce the excited MLCT state **(b)**. The MLCT state is reductively quenched (first electron transfer) by a sacrificial amine donor such as triethanolamine (TEOA) to form the one electron reduced rhenium complex **(OER)** and the radical cation species of TEOA. This OER complex undergoes a ligand exchange of the halide with a solvent molecule to form solvato complex **(d)**, which has been shown to be the likely active catalyst.<sup>9</sup> This nucleophilic Re complex then reacts with CO<sub>2</sub>, a H<sup>+</sup>, and an e<sup>-</sup> (second electron transfer) to form metallocarboxylate **(e)**. Experiments have shown that the second electron comes from rhenium dimers formed during this sequence with the formula  $[(\text{bpy})(\text{CO})_3\text{Re}-\text{CO}_2-\text{Re}(\text{CO})_3(\text{bpy})]$ . This complex was studied and isolated to support its role in the

catalytic cycle.<sup>26,31,32</sup> Metallocoarboxylate (**e**) can then react with a second  $H^+$  to form  $H_2O$  and tetra carbonyl complex (**f**). Dissociation of CO and association of the halide ligand completes the catalytic cycle.

### 2.1.5 Metrics and Drawbacks of $[Re(bpy)(CO)_3Cl]$

This system was shown to be completely selective toward photocatalytic CO production as  $H_2$  or more reduced carbon species were not formed. While this system was selective, it displayed only modest turnover numbers (up to 48) and quantum yields (14%).<sup>28</sup> Furthermore, a major drawback to this rhenium system is the lack of absorption in the visible region. As explained above, photocatalysis of the  $[Re(bpy)(CO)_3Cl]$  complex requires excitation of the MLCT band which is around 385 nm for this complex.<sup>29</sup> The inability of these systems to absorb light at wavelengths longer than ~430 nm is a critical impediment to the use of solar energy to drive  $CO_2$  reduction, since the solar power spectrum is most intense from approximately 425 – 600 nm (Figure 2.3).<sup>33</sup>

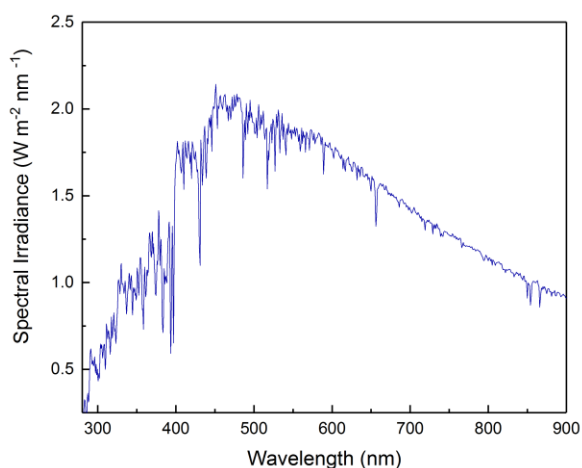


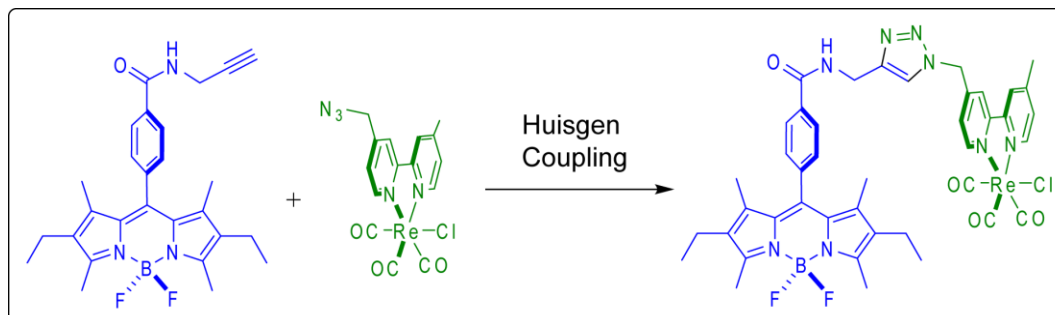
Figure 2.3: Solar power spectrum from 280 to 900 nm.

To address this drawback, systems have been designed to shift or broaden the MLCT band via attachment of covalently bound photosensitizers, such as [Ru(II)(bpy)<sub>3</sub>] and metalloporphyrins to the rhenium complex, and have shown success.<sup>34-39</sup> However, what is not prevalent in the literature is the attachment of organic chromophores to rhenium complexes for photocatalytic CO<sub>2</sub> activation.

### 2.1.6 Design of Ru System with a Tethered BODIPY Organic Chromophore

Due to the success of covalently bound transition metal photosensitizers, we rationalized that tethering an organic chromophore to a [Re(bpy)(CO)<sub>3</sub>Cl] complex might lead to a similar photocatalysis. Furthermore, the use of organic chromophores can be less expensive than their transition metal counterparts and are synthetically less challenging when compared to porphyrin based systems. For the organic chromophore, we chose to study the boron-dipyrromethene (BODIPY) dye, as these compounds have been shown to be stable to prolonged irradiation, display strong molar absorptivities ranging from 40,000 to 110,000 M<sup>-1</sup> cm<sup>-1</sup>, and are capable of photoinduced electron transfer.<sup>40</sup> Furthermore, they display  $\lambda_{\text{max}}$  values around 500 nm<sup>40</sup>, which place them in an ideal range for solar light absorption (Figure 2.3).

To synthesize the BODIPY–Re complex, we chose to target a Huisgen coupling that would allow the facile synthesis of the photocatalyst via formation of a triazole ring (Scheme 2.1).



Scheme 2.1: Synthetic strategy to BODIPY–Re photocatalyst

As shown in Scheme 2.1, our synthetic strategy required the synthesis of two fragments which would be coupled together: An organic fragment with a pendant alkyne and an inorganic rhenium fragment with a pendant azide. The synthesis, characterization, and photocatalytic studies are detailed below. The material presented in this chapter has been published and has been reproduced with permission (see Appendix B for the permission letter).<sup>56</sup>

## 2.2 Experimental

### 2.2.1 General Materials and Methods

Reactions were performed in oven-dried round-bottomed flasks unless otherwise noted. Reactions that required an inert atmosphere were conducted under a positive pressure of N<sub>2</sub> using flasks fitted with Suba-Seal rubber septa or in a nitrogen filled glove box. Air and moisture sensitive reagents were transferred using standard syringe or cannula techniques. Reagents and solvents were purchased from Sigma Aldrich, Acros, Fisher, Strem, or Cambridge Isotopes Laboratories. Solvents for synthesis were of reagent grade or better and were dried by passage through activated

alumina and then stored over 4 Å molecular sieves prior to use.<sup>41</sup> Column chromatography was performed with 40-63 μm silica gel with the eluent reported in parentheses. Analytical thin-layer chromatography (TLC) was performed on precoated glass plates and visualized by UV or by staining with KMnO<sub>4</sub>. 4-Hydroxymethyl-4'-methyl-2,2'-bipyridine,<sup>42</sup> 4-Bromomethyl-4'-methyl-2,2'-bipyridine,<sup>42</sup> and BODIPY-COOH and BODIPY-NHS<sup>43</sup> were prepared as previously described in literature.

### 2.2.2 Compound Characterization

<sup>1</sup>H NMR and <sup>13</sup>C NMR spectra were recorded at 25 °C on a Bruker 400 MHz spectrometer. Proton spectra are referenced to the residual proton resonance of the deuterated solvent (CDCl<sub>3</sub> = δ 7.26; CD<sub>3</sub>CN = δ 1.94; (CD<sub>3</sub>)<sub>2</sub>SO = δ 2.50) and carbon spectra are referenced to the carbon resonances of the solvent (CDCl<sub>3</sub> = δ 77.16; CD<sub>3</sub>CN = δ 1.32, 118.26; (CD<sub>3</sub>)<sub>2</sub>SO = δ 39.52). All chemical shifts are reported using the standard δ notation in parts-per-million. LR-GCMS data were obtained using an Agilent gas chromatograph consisting of a 6850 Series GC System equipped with a 5973 Network Mass Selective Detector. Low resolution MS data was obtained using either a LCQ Advantage from Thermofinnigan or a Shimadzu LC/MS-2020 single quadrupole MS coupled with an HPLC system, with dual ESI/APCI source. High-resolution mass spectrometry analyses were either performed by the Mass Spectrometry Laboratory in the Department of Chemistry and Biochemistry at the University of Delaware or at the University of Illinois at Urbana-Champaign. Infra-red spectra were recorded in KBr using a Nicolet Magna-IR 750 spectrometer.

### 2.2.3 Electrochemical Measurements

All electrochemistry was performed using either a CHI-620D potentiostat/galvanostat or a CHI-760D bipotentiostat. Cyclic voltammetry was performed using a standard three-electrode configuration. CV scans were recorded for quiescent solutions using a glassy carbon working disk electrode (3.0 mm diameter CH Instruments) and a platinum wire auxiliary electrode. All potentials were measured against a silver wire pseudo reference with a ferrocene internal standard and were adjusted to the saturate calomel electrode (SCE) via the relation  $Fc/Fc^+ = 460 \text{ mV} + \text{SCE}$ . CV experiments were performed in DMF using 0.1 M tetrabutylammonium hexafluorophosphate (TBAPF<sub>6</sub>) as the supporting electrolyte. Concentrations of analytes were 1 mM.

### 2.2.4 UV-Vis Absorption Experiments

UV/visible absorbance spectra were acquired on a StellarNet CCD array or Agilent 8453 Diode Array UV-vis spectrometer using screw cap quartz cuvettes (6q or 7q) of 1 cm pathlength from Starna. All absorbance spectra were recorded at room temperature. All samples for spectroscopic analysis were prepared in DMF.

### 2.2.5 Steady-State Fluorescence Measurements

Spectra were recorded on an automated Photon Technology International (PTI) QuantaMaster 40 fluorometer equipped with a 75-W Xenon arc lamp, a LPS-220B lamp power supply and a Hamamatsu R2658 photomultiplier tube. Samples for fluorescence analysis were prepared in an analogous method to that described above for the preparation of samples for UV-vis spectroscopy. Samples were excited at  $\lambda_{\text{ex}} = 500 \text{ nm}$  and emission was monitored from 510–800 nm with a step size of 1 nm and

integration time of 0.5 seconds. Reported spectra are the average of at least three individual acquisitions.

Emission quantum yields were calculated using [Ru(phen)<sub>3</sub>]Cl<sub>2</sub> (phen = 1,10-phenanthroline) in water ( $\Phi_{\text{ref}} = 0.072$ )<sup>44,45</sup> as the reference actinometer using the expression below.<sup>46</sup> where  $\Phi_{\text{em}}$  and  $\Phi_{\text{ref}}$  are the emission quantum yield of the sample and the reference, respectively,  $A_{\text{ref}}$  and  $A_{\text{em}}$  are the measured absorbance of the reference and sample at the excitation wavelength, respectively,  $I_{\text{ref}}$  and  $I_{\text{em}}$  are the integrated emission intensities of the reference and sample, respectively, and  $\eta_{\text{ref}}$  and  $\eta_{\text{em}}$  are the refractive indices of the solvents of the reference and sample, respectively.

$$\Phi_{em} = \Phi_{ref} \left( \frac{A_{ref}}{A_{em}} \right) \left( \frac{I_{em}}{I_{ref}} \right) \left( \frac{\eta_{em}}{\eta_{ref}} \right)^2 \quad (\text{eq. 2.8})$$

Equation 2.8: Equation for calculation of the emission quantum yield ( $\Phi_{\text{em}}$ )

### 2.2.6 Time-Resolved Fluorescence Measurements

Time correlated single photon counting (TCSPC) experiments were performed on an IBH (Jobin Yvon Horiba) model 5000F instrument equipped with single monochromators on both the excitation and emission sides of the instrument. The excitation light source was a NanoLED with a short 1.3 ns pulse width at 458 nm. Emission signals were collected on a picosecond photon detection module (TBX-04) at an angle perpendicular to excitation for samples and blanks. Data was collected at the sample's peak maxima as determined by steady state experiments described above to obtain the decay profile. Decay analysis and curve fitting routines to determine the

sample's lifetimes were performed by the software (DAS6) provided by the manufacturer (IBH).

### **2.2.7 X-Ray Structure Determination**

Crystals were mounted using viscous oil onto a plastic mesh and cooled to the data collection temperature. Data were collected on a Bruker-AXS APEX 2 DUO CCD diffractometer with Mo-K $\alpha$  radiation ( $\lambda=0.71073$  Å) monochromated with graphite. Unit cell parameters were obtained from 60 data frames,  $0.5^\circ$   $\omega$ , from three different sections of the Ewald sphere. The systematic absences in the diffraction data are uniquely consistent with P21/n. The data-set was treated with multi-scan absorption corrections (Apex2 software suite, Madison, WI, 2005). The structure was solved using direct methods and refined with full-matrix, least-squares procedures on F2. All non-hydrogen atoms were refined with anisotropic displacement parameters. The amide H-atom was located from the electron density difference Fourier map and refined with the isotropic parameter constrained to be equal to 1.2 of the equivalent isotropic parameter of the attached N-atom. All other hydrogen atoms were treated as idealized contributions. Atomic scattering factors are contained in the SHELXTL 6.12 program library. The CIF for the transition metal control complex has been deposited under CCDC 936531.

### **2.2.8 Photocatalytic CO<sub>2</sub> Reduction and Headspace Analysis**

Samples (1.5 mM) of **8** and **12** were prepared in 5:1 DMF:triethanol amine to a total volume of 3 mL in a 8 mL cuvette. The samples were charged with a stir bar and the system was sealed with a rubber septum which was tightened with a copper wire. The solution was sparged with CO<sub>2</sub> for 25 minutes to saturate both the solution and

cuvette headspace. The samples were irradiated with light from a 200 W Xe arc lamp (Oriel Instruments Model 66057). The wavelength of light was controlled by passing it through a long pass filter ( $\lambda > 400$  or 495 nm) that was immersed in water. Light was focused onto the stirred sample and irradiated for 4.5 or 17 hrs. After irradiation, aliquots were analyzed by gas chromatography coupled to a methanizer and flame ionization detector (GC-FID) for CO production and a known quantity of CO was injected for normalization purposes.

## 2.2.9 Synthesis and Characterization

### 2.2.9.1 Synthesis of [Re(4-Bromomethyl-4'-methyl-2,2'-bipyridine)(CO)<sub>3</sub>Cl] (2)

This compound was prepared using a slightly modified literature procedure.<sup>47</sup> 4-Bromomethyl-4'-methyl-2,2'-bipyridine (**1**) (0.526 g, 2.0 mmol) and Re(CO)<sub>5</sub>Cl (0.723 g, 2.0 mmol) were dissolved in 100 mL of toluene. The reaction mixture was heated at reflux under air with stirring. After 12 h, the reaction was allowed to cool to room temperature, and the resulting yellow solid that precipitated from solution was collected by filtration and washed with hexanes. The crude yellow material was combined with tetrabutylammonium chloride (0.066g, 0.239 mmol) in 25 mL of MeCN and stirred under air at room temperature. After 12 h, this solution was filtered through a plug of Celite, and the filtrate was concentrated under reduced pressure. The resultant material was purified via flash column chromatography on silica using CH<sub>2</sub>Cl<sub>2</sub> as the eluent to deliver 0.994 g of the title compound in 87% yield. <sup>1</sup>H NMR (400 MHz, DMSO-d<sub>6</sub>, 25 °C)  $\delta$ /ppm: 9.03 (d, J = 5.7 Hz, 1H), 8.87 (d, J = 5.6 Hz, 1H), 8.82 (s, 1H), 8.67 (s, 1H), 7.79 (d, J = 5.7 Hz, 1H), 7.60 (d, J = 5.7 Hz, 1H), 4.99 (s, 2H), 2.57 (s, 3H). <sup>13</sup>C NMR (101 MHz, DMSO-d<sub>6</sub>, 25 °C)  $\delta$ /ppm: 197.41, 197.30,

189.57, 155.77, 154.48, 153.53, 152.55, 152.46, 150.58, 128.71, 127.07, 125.17, 123.66, 43.41, 20.97. HR-LIFDI-MS  $[M]^+$   $m/z$ : calc for  $C_{15}H_{11}BrClN_2O_3Re$ , 567.9177; found, 567.9202.  $\nu_{max}$  (KBr)/ $cm^{-1}$  2026, 1897, 1871 (s, CO).

### 2.2.9.2 Synthesis of [Re(4-Azidomethyl-4'-methyl-2,2'-bipyridine)(CO)<sub>3</sub>Cl] (3)

This compound was prepared using a slightly modified literature procedure.<sup>48</sup> Sodium azide (9.4 mg, 0.15 mmol) was dissolved in 3 ml of DMSO and stirred at room temperature for 12 hrs. This solution was added to 75 mg (0.13 mmol) of [Re(4-Bromomethyl-4'-methyl-2,2'-bipyridine)(CO)<sub>3</sub>Cl] (2) and the resulting mixture was stirred at room temperature for 2 hrs. Water (10 ml) was then added to the reaction and this mixture was allowed to stir for 20 min. The mixture was then extracted three times with  $CH_2Cl_2$  and the organic extract was then washed twice with distilled water (20 ml) and once with brine (20 ml). The organic layer was separated, dried over  $Na_2SO_4$  and the solvent was removed under reduced pressure to yield 65 mg (93%) of the desired product as a dark yellow powder.  $^1H$  NMR (400 MHz, DMSO, 25 °C)  $\delta/ppm$ : 9.00 (d,  $J = 5.7$  Hz, 1H), 8.86 (d,  $J = 5.7$  Hz, 1H), 8.70 (s, 2H), 7.70 (d,  $J = 5.6$  Hz, 1H), 7.60 (d,  $J = 5.5$  Hz, 1H), 4.88 (s, 2H), 2.57 (s, 3H).  $^{13}C$  NMR (101 MHz, DMSO, 25 °C)  $\delta/ppm$ : 197.44, 197.37, 189.63, 155.61, 154.59, 153.25, 152.52, 152.45, 150.03, 128.65, 126.10, 125.19, 122.63, 51.94, 20.96. HR-LIFDI-MS  $[M]^+$   $m/z$ : calc for  $C_{15}H_{11}ClN_5O_3Re$ , 531.0099; found, 531.0076.  $\nu_{max}$  (KBr)/ $cm^{-1}$  2021, 1910, 1886 (s, CO) 2113 (s,  $N_3$ ). Single crystals were obtained by vapor diffusion of diethyl ether into a saturated acetonitrile solution. The thermal ellipsoid plot, experimental data, and bond lengths and tables can be found in Appendix B.

### 2.2.9.3 Synthesis of N-(benzoyloxy)succinimide

DCC (2.68 g, 13.0 mmol) and *N*-hydroxysuccinimide (1.49 g, 13.0 mmol) were added to a solution of benzoic acid (1.24 g, 10.0 mmol) dissolved in 100 mL of THF. The reaction solution was stirred at room temperature for 20 hrs, following which, the mixture was filtered. The filtrate was concentrated under reduced pressure and the resulting residue was purified via flash column chromatography on silica using CH<sub>2</sub>Cl<sub>2</sub> and CH<sub>3</sub>OH (97:3) as the eluent to deliver 2.17 g (92%) of the title compound as a pale yellow solid. <sup>1</sup>H NMR (400 MHz, CDCl<sub>3</sub>, 25 °C) δ/ppm: 8.18 – 8.12 (m, 2H), 7.69 (t, *J* = 7.5 Hz, 1H), 7.52 (t, *J* = 7.8 Hz, 2H), 2.92 (s, 4H). <sup>13</sup>C NMR (101 MHz, CDCl<sub>3</sub>, 25 °C) δ/ppm: 169.46, 162.07, 135.16, 130.81, 129.07, 125.31, 77.23, 25.89. HR-ESI-MS [M+H]<sup>+</sup> *m/z*: calc for C<sub>11</sub>H<sub>10</sub>NO<sub>4</sub>, 220.0610; found, 220.0622.

### 2.2.9.4 Synthesis of N-propargylbenzamide

N-(benzoyloxy)succinimide (100 mg, 0.425 mmol) was dissolved in 10 mL of CH<sub>2</sub>Cl<sub>2</sub> and degassed with N<sub>2</sub> for 5 min. Propargylamine (55 μL, 0.85 mmol) and triethylamine (590 μL, 4.25 mmol) were added and the reaction was stirred at room temperature for 18 hrs under an atmosphere of N<sub>2</sub>. The reaction was then washed twice with water and dried over Na<sub>2</sub>SO<sub>4</sub>. The solvent was removed under reduced pressure and the resulting residue was purified via flash column chromatography on silica using CH<sub>2</sub>Cl<sub>2</sub> and CH<sub>3</sub>OH (95:5) as the eluent to deliver 62 mg (92%) of the title compound as a white solid. <sup>1</sup>H NMR (400 MHz, CDCl<sub>3</sub>, 25 °C) δ/ppm: 7.83 – 7.76 (m, 2H), 7.56 – 7.49 (m, 1H), 7.49 – 7.41 (m, 2H), 6.33 (s, 1H), 4.26 (dd, *J* = 5.2, 2.6 Hz, 2H), 2.29 (t, *J* = 2.6 Hz, 1H). <sup>13</sup>C NMR (101 MHz, CDCl<sub>3</sub>, 25 °C) δ/ppm: 167.29, 133.90, 132.04, 128.86, 127.20, 79.63, 72.16, 30.01. HR-EI-MS [M]<sup>+</sup> *m/z*: calc for C<sub>10</sub>H<sub>9</sub>NO, 159.0684; found, 159.0689.

### 2.2.9.5 Synthesis of [Re(Mebpy)(CO)<sub>3</sub>Cl]-Phenyl

[Re(4-Azidomethyl-4'-methyl-2,2'-bipyridine)(CO)<sub>3</sub>Cl] (**3**) (100 mg, 190 μmol), and N-propargylbenzamide (45 mg, 280 μmol), CuSO<sub>4</sub> (5.0 mg, 19 μmol) and ascorbic acid (5.0 mg, 30 μmol) were combined in an oven dried Schlenk flask that was cooled under vacuum. The reactants were dissolved in 6 mL of anhydrous DMF and the reaction was stirred at room temperature under N<sub>2</sub> for 18 hrs. CH<sub>2</sub>Cl<sub>2</sub> (10 mL) was added to the reaction and the solution was washed three times with brine and dried over Na<sub>2</sub>SO<sub>4</sub>. The solvent was removed under reduced pressure and the resulting residue was purified via flash column chromatography on silica using CH<sub>2</sub>Cl<sub>2</sub> and CH<sub>3</sub>OH (95:5) as the eluent to deliver 97 mg (74%) of the title compound as an orange solid. <sup>1</sup>H NMR (400 MHz, CD<sub>3</sub>CN, 25 °C) δ/ppm: 8.95 (d, J = 5.8 Hz, 1H), 8.84 (d, J = 5.7 Hz, 1H), 8.20 (d, J = 8.9 Hz, 2H), 7.91 (s, 1H), 7.79 (d, J = 5.3, 2H), 7.60 – 7.49 (m, 2H), 7.48 – 7.40 (m, 3H), 7.34 (dd, J = 5.7, 1.7 Hz, 1H), 5.75 (s, 2H), 4.64 (d, J = 5.8 Hz, 2H), 2.53 (s, 3H). <sup>13</sup>C NMR (101 MHz, CD<sub>3</sub>CN, 25 °C) δ/ppm: 198.36, 198.27, 190.15, 167.78, 157.19, 155.65, 154.33, 153.58, 153.40, 149.96, 135.29, 132.34, 129.38, 129.34, 127.93, 126.55, 125.84, 124.59, 123.22, 52.68, 35.97, 21.44. HR-ESI-MS [M-Cl]<sup>+</sup> *m/z*: calc for C<sub>25</sub>H<sub>20</sub>N<sub>6</sub>O<sub>4</sub>Re, 655.1104; found, 655.1117. *v*<sub>max</sub> (KBr)/cm<sup>-1</sup> 2024, 1929, 1885 (s, CO).

### 2.2.9.6 Synthesis of 8-(4-(N-(prop-2-yn-1-yl)benzamide)-2,8-diethyl-1,3,7,9-tetramethyl-BODIPY

BODIPY-NHS<sup>43</sup> (100 mg, 0.19 mmol) was dissolved in 20 mL of CH<sub>2</sub>Cl<sub>2</sub> and the resulting solution was sparged with N<sub>2</sub> for 5 minutes. Propargylamine (26 μL, 0.38 mmol) and triethylamine (264 μL, 1.9 mmol) were added to the solution and the reaction was stirred at room temperature for 18 hrs under an atmosphere of N<sub>2</sub>. The reaction was washed twice with water, dried over Na<sub>2</sub>SO<sub>4</sub> and the solvent was then

removed under reduced pressure. The reaction was purified via flash column chromatography on silica using CH<sub>2</sub>Cl<sub>2</sub> and CH<sub>3</sub>OH (50:1) as the eluent to deliver 74 mg (84%) of the title compound as a red solid. <sup>1</sup>H NMR (400 MHz, CDCl<sub>3</sub>, 25 °C) δ/ppm: 7.93 (d, *J* = 8.2 Hz, 2H), 7.41 (d, *J* = 8.2 Hz, 2H), 6.37 (s, 1H), 4.32 (dd, *J* = 5.1, 2.6 Hz, 2H), 2.53 (s, 6H), 2.33 (t, *J* = 2.67 Hz, 1H), 2.29 (q, *J* = 7.6 Hz, 4H), 1.25 (s, 6H), 0.98 (t, *J* = 7.5 Hz, 6H). <sup>13</sup>C NMR (101 MHz, CDCl<sub>3</sub>, 25 °C) δ/ppm: 166.49, 154.42, 139.68, 138.73, 138.27, 134.15, 133.28, 130.49, 128.97, 128.03, 79.48, 72.17, 30.06, 17.21, 14.78, 12.74, 12.04. HR-EI-MS [M]<sup>+</sup> *m/z*: calc for C<sub>27</sub>H<sub>30</sub>BN<sub>3</sub>OF<sub>2</sub>, 461.2450; found, 461.2459. ν<sub>max</sub> (KBr)/cm<sup>-1</sup> 2021, 1914, 1897 (s, CO).

#### 2.2.9.7 Synthesis of [Re(Mebpy)(CO)<sub>3</sub>Cl]-BODIPY

[Re(4-Azidomethyl-4'-methyl-2,2'-bipyridine)(CO)<sub>3</sub>Cl] (**3**) (40 mg, 75 μmol), 8-(4-(N-(prop-2-yn-1-yl)benzamide)-2,8-diethyl-1,3,7,9-tetramethyl-BODIPY (42 mg, 90 μmol), CuSO<sub>4</sub> (2 mg, 7.5 μmol), and ascorbic acid (2 mg, 11 μmol) were combined in a Schlenk flask that was oven-dried and cooled under vacuum. The flask was evacuated and backfilled with N<sub>2</sub> three times, and the reactants were then dissolved in 4 mL of anhydrous DMF. The reaction mixture was stirred at room temperature for 15 h under an atmosphere of N<sub>2</sub>, after which time, 10 mL of CH<sub>2</sub>Cl<sub>2</sub> was added. The resulting solution was washed twice with brine and dried over Na<sub>2</sub>SO<sub>4</sub>. After removing the solvent under reduced pressure, the resultant material was purified via flash column chromatography on silica using CH<sub>2</sub>Cl<sub>2</sub> and CH<sub>3</sub>OH (9:1) as the eluent to deliver 50 mg (67%) of the title compound as a red solid. <sup>1</sup>H NMR (400 MHz, CD<sub>3</sub>CN, 25 °C) δ/ppm: 8.95 (d, *J* = 5.8 Hz, 1H), 8.83 (d, *J* = 5.7 Hz, 1H), 8.23 (d, *J* = 1.9 Hz, 2H), 7.98–7.91 (m, 3H), 7.77 (t, *J* = 5.8 Hz, 1H), 7.46–7.38 (m, 3H), 7.35 (dd, *J* = 5.9, 1.7 Hz, 1H), 5.76 (s, 2H), 4.67 (d, *J* = 5.7 Hz, 2H), 2.53 (s, 3H), 2.46 (s, 6H),

2.30 (q, J = 7.5 Hz, 4H), 1.24 (s, 6H), 0.94 (t, J = 7.5 Hz, 6H). <sup>13</sup>C NMR (101 MHz, CD<sub>3</sub>CN, 25 °C) δ/ppm: 198.32, 198.23, 190.12, 167.20, 157.19, 155.62, 154.82, 154.32, 153.55, 153.39, 149.89, 146.85, 140.60, 139.53, 139.33, 135.75, 134.10, 131.07, 129.51, 129.34, 128.84, 126.57, 125.85, 124.72, 123.27, 52.70, 36.02, 21.49, 17.42, 14.82, 12.72, 12.09. HR-ESI-MS [M-Cl]<sup>+</sup> m/z: calc for C<sub>42</sub>H<sub>41</sub>BF<sub>2</sub>N<sub>8</sub>O<sub>4</sub>Re, 957.2870; found, 957.2879.

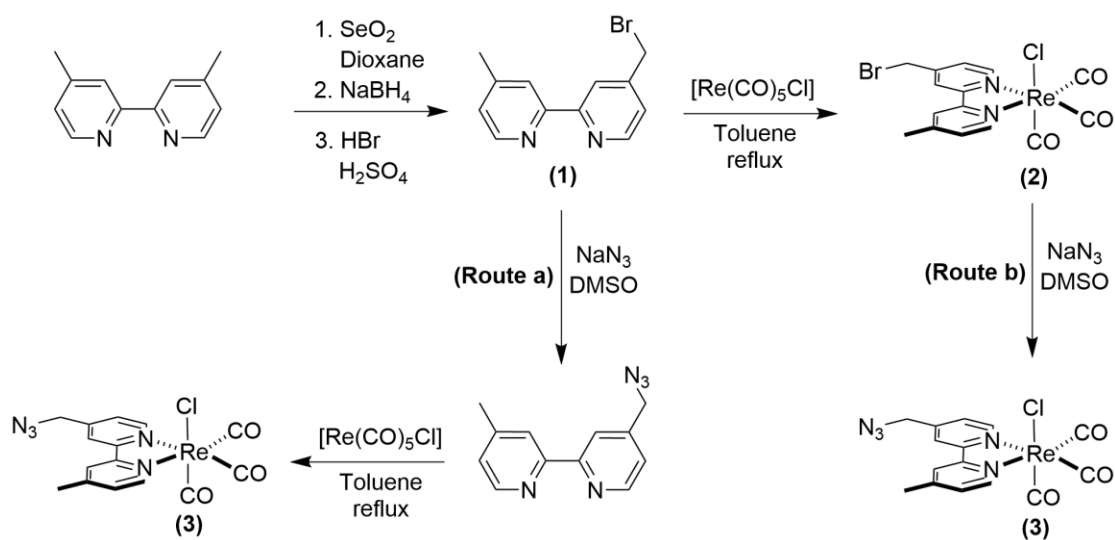
#### **2.2.9.8 Synthesis of 8-(4-(benzamido)methyl-1-benzyl-1H-1,2,3-triazole)-2,8-diethyl-1,3,7,9-tetramethyl-BODIPY**

8-(4-(N-(prop-2-yn-1-yl)benzamide)-2,8-diethyl-1,3,7,9-tetramethyl-BODIPY (33 mg, 72 μmol), benzyl azide (11 mg, 86 μmol), ascorbic acid (2 mg, 11 μmol), and CuSO<sub>4</sub> (2 mg, 7 μmol) were placed in a Schlenk flask under an atmosphere of N<sub>2</sub>. The reactants were dissolved in anhydrous DMF (6 ml) and the resulting mixture was stirred at room temperature under N<sub>2</sub> for 12 hrs. CH<sub>2</sub>Cl<sub>2</sub> (15 mL) was added to the reaction and the resulting solution was washed three times with brine and dried over Na<sub>2</sub>SO<sub>4</sub>. The solvent was removed under reduced pressure and the resulting residue was dissolved in 1 mL of CH<sub>2</sub>Cl<sub>2</sub>. The product was precipitated from the CH<sub>2</sub>Cl<sub>2</sub> solution with diethyl ether (12ml), collected via filtration and washed with an additional 12 ml of diethyl ether to yield 37 mg (86%) of the title compound as a dark red powder. <sup>1</sup>H NMR (400 MHz, DMSO, 25 °C) δ/ppm: 9.22 (t, J = 5.7 Hz, 1H), 8.10 (s, 1H), 8.05 (d, J = 8.3 Hz, 2H), 7.48 (d, J = 8.3 Hz, 2H), 7.41 – 7.30 (m, 5H), 5.58 (s, 2H), 4.53 (d, J = 5.6 Hz, 2H), 2.44 (s, 6H), 2.28 (q, J = 7.4 Hz, 4H), 1.23 (s, 6H), 0.93 (t, J = 7.5 Hz, 6H). <sup>13</sup>C NMR (101 MHz, DMSO, 25 °C) δ/ppm: 165.44, 153.52, 145.14, 139.66, 138.05, 137.71, 136.22, 134.50, 132.79, 129.70, 128.79, 128.31,

128.21, 128.16, 128.07, 123.33, 52.74, 34.96, 16.44, 14.58, 12.32, 11.53. HR-LIFDI-MS  $[M]^+$   $m/z$ : calc for  $C_{34}H_{37}BF_2N_6O$ , 594.3096; found, 594.3076.

## 2.3 Synthetic Pathway to Re-BODIPY Photocatalyst and Control Compounds

### 2.3.1 Synthesis of Rhenium Fragment

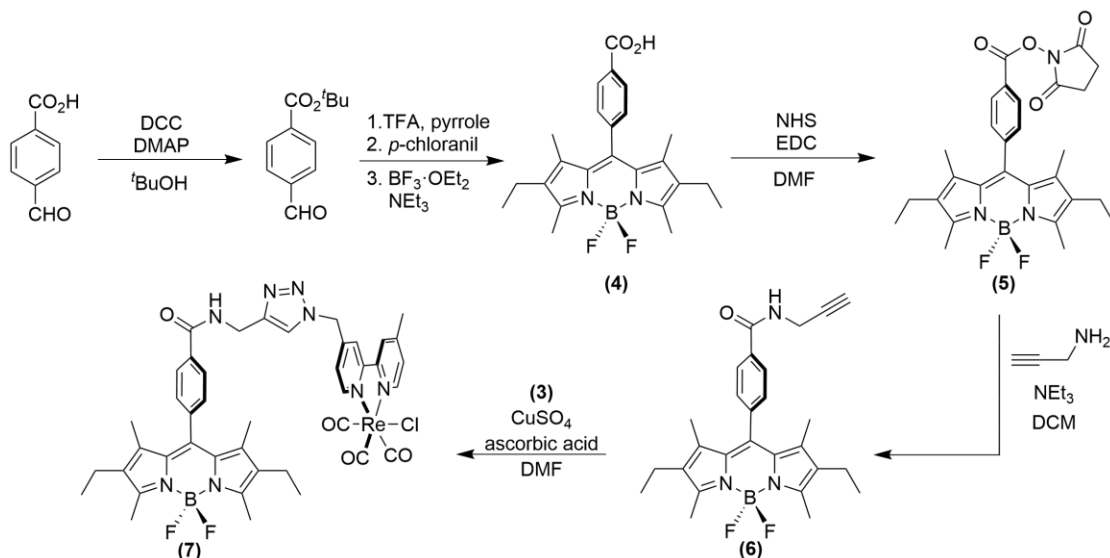


Scheme 2.2: Synthetic pathway to inorganic rhenium fragment (3).

The synthesis of the rhenium fragment is shown above in Scheme 2.2 and began with commercially available 4,4'-dimethyl-2,2'-bipyridine. We found that this synthesis could be accomplished via two routes. Both began with the conversion of the bipyridine to 4-bromomethyl-4'-methyl-2,2'-bipyridine (1), which was accomplished over two steps and was based on a literature procedure.<sup>42</sup> The starting material was first oxidized at the methyl position to the corresponding aldehyde by  $SeO_2$  in dioxane

at reflux under an N<sub>2</sub> environment. The intermediate aldehyde was then reduced to the alcohol with NaBH<sub>4</sub>, which was then collected and purified. The alcohol was then converted to the bromide with a mixture of HBr and H<sub>2</sub>SO<sub>4</sub>. This material was also isolated and purified. From **(1)**, the Re complex could be synthesized via two routes (Scheme 2.2, Route a and b). **Route a** began with conversion of the bipyridine bromide **(1)** to the corresponding azide. As described in the literature,<sup>48</sup> this conversion was accomplished using NaN<sub>3</sub> in DMSO to yield the desired bipyridine azide. The bipyridine azide proligand was then metalated with Re(CO)<sub>5</sub>Cl in refluxing toluene using standard conditions for this type of metalation.<sup>47</sup> Unfortunately, after extraction of the material, due to the reflux temperature leading to product decomposition, we were only able to isolate the Re fragment **(3)** in 10% yield. This led to the discovery of **Route b** which allows the thermally sensitive azide group to be added after the metalation step under mild conditions. The metalation of **(1)** with Re(CO)<sub>5</sub>Cl was also accomplished as described above with refluxing toluene.<sup>47</sup> Initial characterization of the complex showed both Cl and Br bound to the complex. To remedy this, the crude material was treated with tetrabutylammonium chloride in acetonitrile at room temperature over 12 hours to produce **2** in high yield. Using the same strategy as above,<sup>48</sup> the Re-Br complex **(2)** was converted to the azide with NaN<sub>3</sub> dissolved in DMSO at room temperature to give **3** in high yield. As stated above the mild conditions of **Route b** allowed for the high yielding synthesis of the Re fragment **3** without decomposition of the target product. Further, the solid-state structure was obtained and details can be found in Appendix B.

### 2.3.2 Synthesis of Organic BODIPY Fragment and Coupling



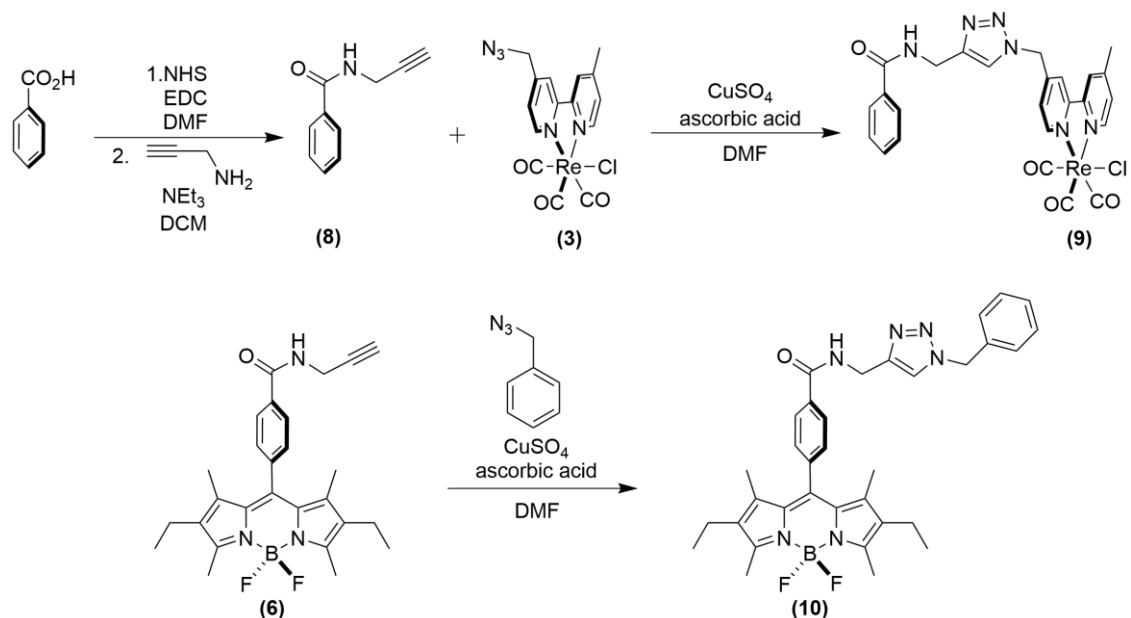
Scheme 2.3: Synthesis of the BODIPY fragment **(6)** and photocatalyst **(7)**

The initial synthesis of the organic compounds BODIPY-COOH **(4)** and BODIPY-NHS **(5)** (Scheme 2.3) have been previously described by our group<sup>43</sup> and began with the protection of the carboxylic acid of 4-formylbenzoic acid for solubility reasons. The carboxylic group was protected via an amide coupling reaction of 4-formylbenzoic acid by activating the carboxylic acid with N’N’-dicyclohexylcarbodiimide (DCC), followed by addition of *tert*-butanol and DMAP. This yielded *tert*-butyl 4 formylbenzoate in good yield.<sup>43</sup> This material was carried on to BODIPY-COOH **(4)** as shown in Scheme 2.3 by activating the aldehyde of *tert*-butyl 4-formylbenzoate with TFA followed by reaction with 2,4-dimethyl-3-ethylpyrrole. Tetrachloro-1,4-benzoquinone (DDQ) was added to oxidize the intermediate followed by addition of triethylamine and BF<sub>3</sub>·OEt<sub>2</sub> to give **(4)** in good yield.<sup>43</sup> BODIPY-COOH **(4)** was then carried on to the NHS ester **(5)** by treatment of

(4) with NHS and N-(3-dimethylaminopropyl)-N'-ethylcarbodiimide (EDC) in an amide coupling reaction to produce BODIPY-NHS (5).<sup>43</sup>

With the BODIPY-NHS (5) in hand, we were able to convert this compound to the final organic BODIPY fragment (6) as shown above in Scheme 2.3. BODIPY-NHS (5) was treated with propargylamine and triethylamine to give the target BODIPY compound (6) in high yield. With both the Re (3) and BODIPY fragments (6) in hand we were then able to couple them using standard conditions for a Huisgen (Click) reaction. Using Schlenk techniques the two fragments were combined with CuSO<sub>4</sub> and ascorbic acid in anhydrous DMF and stirred for 15 hours. After isolation and purification, the photocatalyst (7) was successfully obtained in good yield.

### 2.3.3 Synthesis of Control Compounds



Scheme 2.4: Synthesis of control compounds (9) and (10)

We were also interested in synthesizing additional compounds to serve as controls for the analytical experiments. First a transition metal control, where we have our Re bipyridine complex with an identical linker, however without the organic BODIPY photosensitizer. Second, a photo control compound where the BODIPY is present with an identical linker, however without the Re bipyridine complex. These two complexes are shown above in Scheme 2.4 (**9**) and (**10**). In both cases the absent portion of the molecule is replaced with a phenyl group (Scheme 2.4). As the synthesis of the photocatalyst was split into fragments, this allowed the control compounds to be prepared rapidly as they required the same intermediates. The transition metal control compound (**9**) began with a similar strategy used for the BODIPY synthesis. Benzoic acid was initially converted to NHS ester via an amide coupling reaction with EDC and NHS. The NHS intermediate was then carried on to the alkyne with propargyl amine to give the alkyne-phenyl intermediate (**8**). This intermediate was then coupled to the inorganic Re fragment (**3**) using a Click coupling reaction, as described above, to give the target transition metal compound (**9**). The photo control compound (**10**) was made easily from the click coupling of the BODIPY-alkyne intermediate (**6**) with benzyl azide, again using standard conditions as stated above. With all target compounds in hand we were then able to begin the analytical studies.

## 2.4 Electrochemical Studies

Prior to the photocatalytic studies, we were interested in obtaining the redox properties of our complexes as well as determining if we observed electrocatalytic activity towards CO<sub>2</sub>, as work on the original Re(bpy)(CO)<sub>3</sub>Cl system was shown to be photochemically and electrochemically active toward CO<sub>2</sub> conversion.<sup>28</sup>

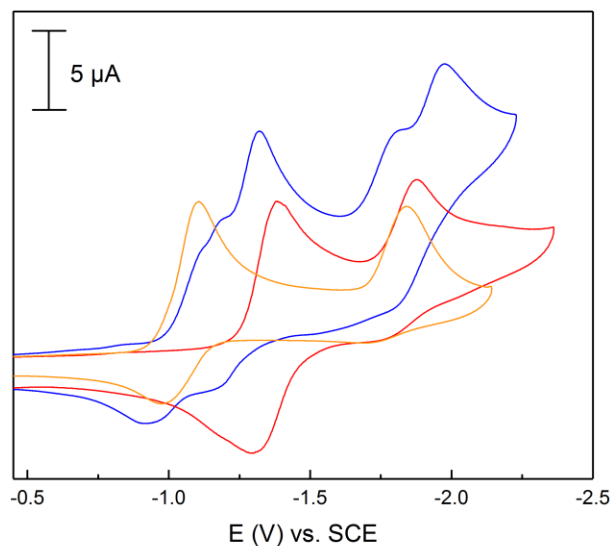


Figure 2.4: Voltammogram of photocatalyst (**7**) (blue trace), transition metal control (**9**) (red trace) and photo control (**10**) (orange trace)

The redox properties of the photocatalyst and control compounds were established using cyclic voltammetry (CV) and are shown in Figure 2.4 above. Voltammograms were obtained with 1.0 mM solutions of the analyte in DMF containing 0.1 M TBAPF<sub>6</sub> under an atmosphere of N<sub>2</sub>. First, looking at the CV trace for our transition metal control compound (**9**) (Figure 2.4, red trace) we observe a reversible reduction at  $-1.39$  V vs. SCE which was attributed to the reduction of the bipyridine ligand followed by an irreversible Re<sup>I/0</sup> couple centered at approximately  $-1.88$  V. These results are similar to other reported Re(bpy)(CO)<sub>3</sub>Cl complexes.<sup>47</sup> The voltammogram of the photocatalyst (**7**) (Figure 2.4, blue trace) is more complex as there are four reductions present. Two of these waves are nearly superimposable with

the bipyridine and metal centered reductions observed for the transition metal control complex (**9**) and are believed to correspond to the analogous processes for the photocatalyst. The additional two waves, which are centered at approximately  $-1.15$  and  $-1.98$  V vs. SCE are consistent with the first and second one electron reduction of the BODIPY moiety.<sup>49–51</sup> This was confirmed when we obtained the voltammogram of our photo control compound (**10**) (Figure 2.4, orange trace) again, the two reductions are nearly superimposable with the reductions observed for the photocatalyst. Thus, we assign the four reductions of our photocatalyst to two reductions of the BODIPY chromophore, a reduction of the bipyridine ligand, and a  $\text{Re}^{I/0}$  couple.

After obtaining the redox properties of the target compounds the voltammograms were then obtained for the photocatalyst and transition metal control compounds in DMF under a  $\text{CO}_2$  environment.

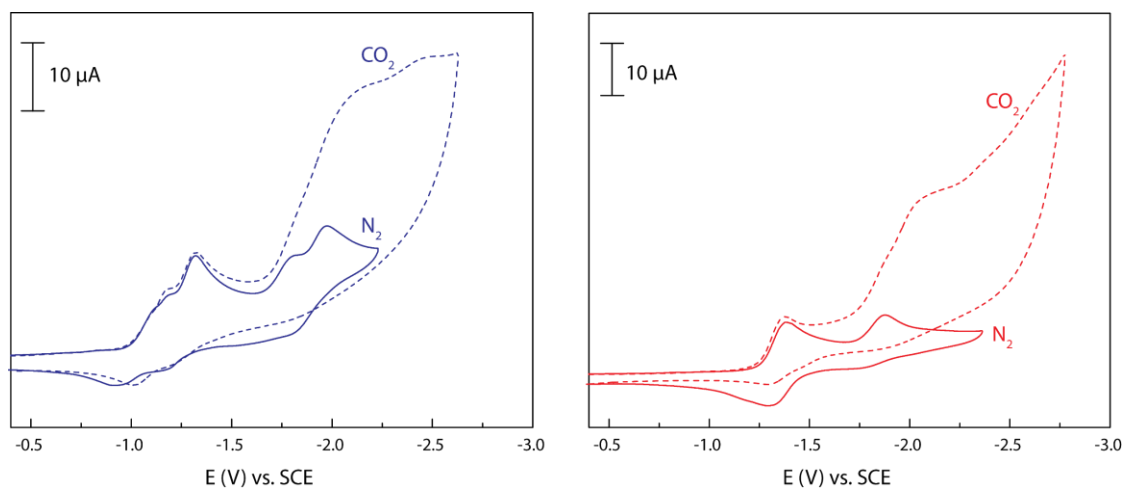


Figure 2.5: Voltammograms of photocatalyst (**7**) (blue data, left box) and transition metal control (**9**) (red data, right box) under a  $\text{N}_2$  environment (solid traces) and under  $\text{CO}_2$  (dashed traces)

As shown in Figure 2.5 the voltammograms are significantly altered compared to the corresponding traces recorded under N<sub>2</sub> (solid data vs. dashed data). The ligand reduction waves are largely unchanged in the presence of CO<sub>2</sub>, however, a large increase in current is observed upon scanning to potentials more negative than approximately -1.75 V (Figure 2.5). This observation is consistent with the electrocatalytic activation of CO<sub>2</sub> upon reduction of the Re<sup>I</sup> centers of the photocatalyst (**7**) and transition metal control (**9**). This mechanistic pathway for CO<sub>2</sub> reduction is consistent with that proposed for other *fac*-Re<sup>I</sup>(CO)<sub>3</sub> complexes supported by bipyridine ligands. The size of the catalytic waves for both (**7**) and (**9**) are comparable, suggesting that both rhenium compounds catalyze the electrochemical reduction of CO<sub>2</sub> to similar extents.

## 2.5 Photophysical Properties

As the photocatalyst and transition metal control compounds were active toward the electrochemical reduction of CO<sub>2</sub>, next and prior to photocatalytic studies, we were interested in obtaining the UV-Vis absorption profiles of the photocatalyst and control compounds.

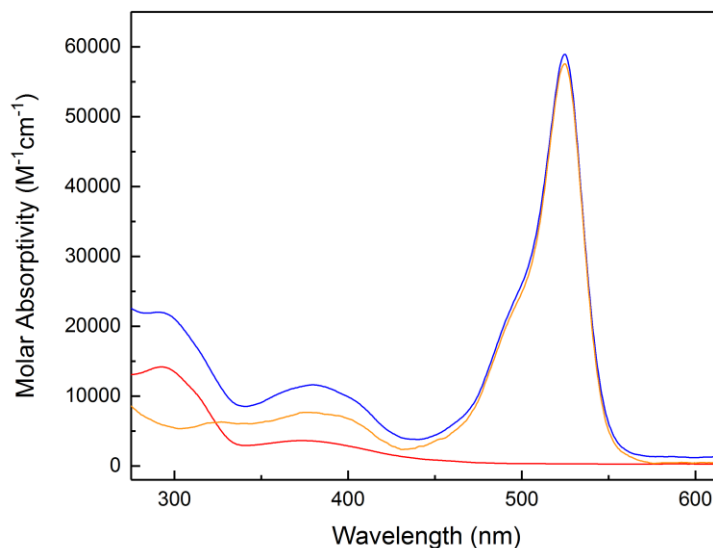


Figure 2.6: Absorbance profile of photocatalyst **(7)** (blue trace), transition metal control **(9)** (red trace), and photo control **(10)** (orange trace)

The absorbance profile of the transition metal control compound **(9)** (Figure 2.6, red trace) shows two major absorptions at 293 nm and the MLCT transition at 375 nm which extends out to 425 nm. The  $\lambda_{\max}$  value has a molar absorptivity just under 15,000  $\text{M}^{-1}\cdot\text{cm}^{-1}$  and shows a typical absorbance profile observed for *fac*- $\text{Re}^{\text{I}}(\text{CO})_3$  complexes containing a bipyridine ligand. The photocatalyst **(7)** (Figure 2.6, blue trace) which contains the BODIPY chromophore also contains these transitions, along with a strong absorption at 525 nm with a molar absorptivity near 60,000  $\text{M}^{-1}\cdot\text{cm}^{-1}$ . This transition was reasoned to be from the BODIPY chromophore and when we compare the absorbance profile of the photocatalyst to the photocontrol compound **(10)** (Figure 2.6, orange trace), we see the overlay of the absorption feature at 525 nm. The addition of the BODIPY

chromophore to the Re complex extends the ability of the designed photocatalyst to absorb light out to nearly 600 nm. As stated in the introduction compounds which absorb light in the 425 – 600 nm range are ideal for solar light harvesting. The absorbance profile of the designed photocatalyst places this compound well in the ideal range, as well as displays strong absorbance in this region.

## 2.6 Photocatalytic Studies

As the photophysical and redox properties were characterized, we next wanted to establish if the photocatalyst, and transition metal control, were able to photochemically activate CO<sub>2</sub>. To do this, photolysis experiments were performed in a collaboration with Dr. Daniel Lutterman at Oak Ridge National Laboratory. Solutions of the compounds, with analyte concentrations of 1.5 mM, in a solution of CO<sub>2</sub> saturated 5:1 DMF: TEOA, where TEOA is the sacrificial electron donor, were exposed to filtered light over the course of 17 hours. Quantification of the gaseous products formed were analyzed by gas chromatography by sampling the headspace of the photolysis cell. The results of the experiments are reported below in Table 2.1.

	$\lambda_{\text{ex}} \geq 400 \text{ nm}$	$\lambda_{\text{ex}} \geq 495 \text{ nm}$	$\Phi_{\text{FI}}$	$\tau_{\text{FI}}$
	TOF/TON	TOF/TON		
<b>Photocatalyst (7)</b>	4 hr <sup>-1</sup> / 17	trace	82 %	4.46 ns
<b>Transition Metal Control (9)</b>	5 hr <sup>-1</sup> / 22	trace	————	————
<b>Photo Control (10)</b>	————	————	86 %	4.87 ns

Table 2.1: Experimental results from photolysis and steady-state and time resolved emission experiments.

We began our investigations with photolysis studies of the transition metal control complex (**9**) (Table 2.1, second entry). Excitation of (**9**) at the MLCT band ( $\lambda_{\text{ex}} \geq 400$  nm) resulted in photochemical activation of CO<sub>2</sub> with a turn over frequency (TOF) of 5 hr<sup>-1</sup> and a turn over number (TON) of 22 over the 17-hour experiment. Excitation of the transition metal control complex using longer wavelength light ( $\lambda_{\text{ex}} \geq 495$  nm) resulted in trace amounts of CO production. This is expected as the control complex has a low absorptivity of light at wavelengths past 425 nm (Figure 2.6, red trace). Both experiments did not produce H<sub>2</sub>, as it typical for *fac*-Re<sup>I</sup>(CO)<sub>3</sub> catalyts. Further, similar results have been obtained using structurally simple rhenium tricarbonyl bipyridine complexes.<sup>29</sup>

The same experiments were carried out for the photocatalyst (**7**) and are reported in Table 2.1 (first entry). Excitation of (**7**) at the MLCT band resulted in similar results from the transition metal control compound with metrics for TOF and TON of 4 hr<sup>-1</sup> and 17 respectively. This result is not surprising as addition of the BODIPY chromophore did not greatly enhance the absorption of the MLCT band (Figure 2.6, blue trace). Disappointingly, excitation of the photocatalyst at longer wavelength light ( $\lambda_{\text{ex}} \geq 495$  nm) resulted in only trace amounts of CO produced, despite the strong absorbance in this region. While H<sub>2</sub> was also not produced in these photolysis experiments, these results suggest that there may be inefficient electronic communication between the BODIPY chromophore and the Re center.

To help rationalize these results the fluorescence quantum yield ( $\Phi_{\text{Fl}}$ ) and fluorescence lifetime ( $\tau_{\text{Fl}}$ ) were acquired via steady-state and time resolved emission experiments and the results are shown in Table 2.1 above. The photocontrol compound (**10**) is highly emissive with a  $\Phi_{\text{Fl}}$  of 86% and a  $\tau_{\text{Fl}}$  of 4.87 ns. Both these

values are typical of BODIPY derivatives derived from substituted pyrrole precursors.<sup>43,50,52</sup> The same experiments were performed for the photocatalyst and the results were nearly identical to the photo control compound with metrics for  $\Phi_{\text{Fl}}$  and  $\tau_{\text{Fl}}$  of 82% and 4.46 ns respectively. These results suggest that upon excitation of the photocatalyst where the BODIPY absorbs ( $\lambda_{\text{ex}} \geq 495$  nm), this complex preferentially takes a radiative pathway, which then in turn does not perform energy transfer to form the MLCT state. As stated in the introduction, generation of the MLCT state is necessary as the MLCT state is quenched by electron donation from the sacrificial electron donor to generate the active species. Thus, when our photocatalyst is excited at longer wavelengths the one electron reduced species is not produced, therefore photo activation of CO<sub>2</sub> cannot take place.

Over the course of the studies we were able to obtain the solid-state structure of the transition metal control compound (**9**), with bromide bound, which further provided evidence for the lack of electronic communication (Experimental data and tables can be found in Appendix B).

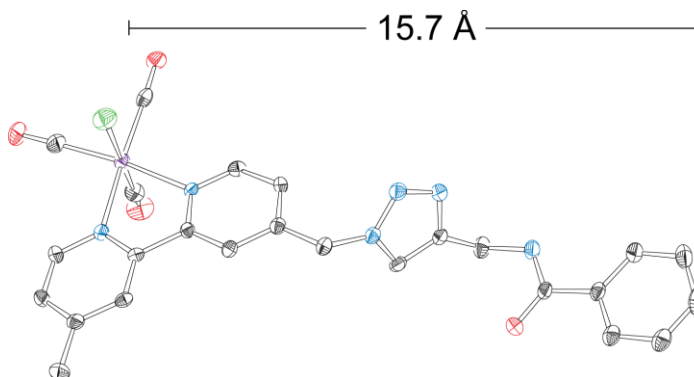


Figure 2.7: Solid state structure of the bromide homologue of the transition metal control compound (**9**). Thermal ellipsoids are shown at the 50% probability level and hydrogen atoms have been removed for clarity

The solid state thermal ellipsoid plot of the complex is shown above in Figure 2.7 and displays a highly-extended structure. The conformation of this complex would place the BODIPY chromophore approximately 15.7 Å from the Re center of the photocatalyst. The long distance between the BODIPY moiety and metal center, coupled with the partially saturated linker would be expected to result in slow electron transfer or energy transfer kinetics.<sup>53,54</sup> Further, longer chain lengths have been supported to hinder catalysis in other tethered systems for photochemical CO<sub>2</sub> activation.<sup>55</sup> Lastly, further evidence can be seen in the absorbance profiles of the photocatalyst (**7**) and the photo control compound (**10**) which are nearly identical (Figure 2.6). If there was efficient electronic communication between the chromophore and Re center, we would expect to see an altered absorbance profile.

## 2.7 Concluding Remarks

A *fac*-Re<sup>I</sup>(CO)<sub>3</sub> complex supported by a bipyridine ligand with a tethered BODIPY photosensitizer was synthesized for the photochemical activation of CO<sub>2</sub>. The synthesis of this complex required the generation of an inorganic Re fragment with a pendant azide, and an organic BODIPY fragment with a pendant alkyne. These two complexes were coupled via click chemistry for the successful synthesis of the target photocatalyst. Control compounds were also synthesized to compare and rationalize the analytical results. Redox properties of the photocatalyst showed multiple redox events which were attributed to two reduction of the BODIPY unit, a single reduction of the bipyridine ligand, and reduction of the Re<sup>I</sup> center. CV experiments in a CO<sub>2</sub> saturated environment showed the Re center of the photocatalyst was still highly active toward CO<sub>2</sub>. The absorbance profile was obtained and showed extension of the absorbance profile, when compared to the transition metal control compound, with a BODIPY absorbance centered at 525 nm and a molar absorptivity of 60,000 M<sup>-1</sup>•cm<sup>-1</sup>. These characteristics place this complex in an ideal range for solar light harvesting. Unfortunately, photolysis experiments at wavelengths greater than 495 nm did not activate CO<sub>2</sub> and the lack of activity was attributed to the lack of electronic communication between the BODIPY unit and the Re center. The lack of communication thus prevents the one electron reduced species from being formed, which is the known active component of photocatalytic CO<sub>2</sub> activation by *fac*-Re<sup>I</sup>(CO)<sub>3</sub> complex supported by a bipyridine ligands.

While the designed photocatalyst was not active toward CO<sub>2</sub> at longer wavelengths, this was the first report of a Re(bpy)(CO)<sub>3</sub>Cl complex with a tethered organic chromophore for CO<sub>2</sub> activation and was reported in the literature.<sup>56</sup> Further it was discovered that triazole linkers, formed from click coupling reactions, do not

interfere with the reductive photochemistry. As such, click coupling may provide a straightforward and versatile method for immobilization of  $\text{Re}(\text{bpy})(\text{CO})_3\text{Cl}$  catalysts onto heterogeneous supports.<sup>57</sup> Lastly, this work supported that the BODIPY unit is tolerated under photocatalytic conditions which could be useful for future catalyst design.

## REFERENCES

- (1) Lewis, N. S.; Nocera, D. G. *PNAS*. 2006, *103*, 15729.
- (2) Olah, G. A.; Goepfert, A.; Prakash, G. K. S. *J. Org. Chem.* **2009**, *74*, 487.
- (3) Olah, G. A.; Prakash, G. K. S.; Goepfert, A. *J. Am. Chem. Soc.* **2011**, *133*, 12881.
- (4) Fisher, Barbara J.; Eisenberg, R. *J. Am. Chem. Soc.* **1980**, *102*, 7361.
- (5) Hawecker, J.; Lehn, J.; Ziessel, R. *J. Chem. Soc. Chem. Comm.*, **1984**, 328.
- (6) DuBois, D. L.; Miedaner, A.; Haltiwanger, C. R. *J. Am. Chem. Soc.* **1991**, *113*, 8753.
- (7) Therrien, Jeffery A.; Wolf, Michael O.; Patrick, Brian O. *Inorg. Chem.* **2014**, *53*, 12962.
- (8) Rosenthal, J. *Prog. Inorg. Chem.* **2014**, *59*, 299.
- (9) Morris, A. J.; Meyer, G. J.; Fujita, E. *Acc. Chem. Res.* **2009**, *42*, 1983.
- (10) Tinnemans, A. H. A.; Koster, T. P. M.; Thewissen, D.; Mackor, A. *Recl. Trav. Chim. Pays-Bas* **1984**, *103*, 288.
- (11) Grodkowski, J.; Dhanasekaran, T.; Neta, P.; Hambright, P.; Brunshwig, B. S.; Shinozaki, K.; Fujita, E. *J. Phys. Chem. A* **2000**, *104*, 11332.
- (12) Grodkowski, J.; Neta, P.; Fujita, E.; Mahammed, A.; Simkhovich, L.; Gross, Z. *J. Phys. Chem. A* **2002**, *106*, 4772.
- (13) Grodkowski, J.; Neta, P. *J. Phys. Chem. A* **2000**, *104*, 1848.
- (14) Grodkowski, J.; Behar, D.; Neta, P.; Hambright, P. *J. Phys. Chem. A* **1997**, *101*, 248.

- 
- (15) Behar, D.; Dhanasekaran, T.; Neta, P.; Hosten, C. M.; Ejeh, D.; Hambright, P.; Fujita, E. *J. Phys. Chem. A* **1998**, *102*, 2870.
- (16) Craig C. A.; Spreer L. O.; Otvos J. W.; Calvin M. *J. Phys. Chem.* **1990**, *94*, 7957.
- (17) Sullivan, B. P.; Meyer, T. J., *Organometallics* **1986**, *5*, 1500.
- (18) O'Toole, T. R.; Sullivan, B. P.; Bruce, M. R. M.; Margerum, L. D.; Murray, R. W.; Meyer, T. J. *J. Electroanal. Chem. Interfacial Electrochem.* **1989**, *259*, 217.
- (19) O'Toole, T. R.; Margerum, L. D.; Westmoreland, T. D.; Vining, W. J.; Murray, R. W.; Meyer, T. J. *Chem. Commun.* **1985**, 1416.
- (20) Agarwal, J.; Sanders, B. C.; Fujita, E.; Schaefer, I. I. H. F.; Harrop, T. C.; Muckerman, J. T. *Chem. Commun.* **2012**, *48*, 6797.
- (21) Agarwal, J.; Johnson, R. P.; Li, G. *J. Phys. Chem. A* **2011**, *115*, 2877.
- (22) Agarwal, J.; Fujita, E.; Schaefer, H. F.; Muckerman, J. T. *J. Am. Chem. Soc.* **2012**, *134*, 5180.
- (23) Sullivan, B. P.; Meyer, T. J. *Organometallics* **1986**, *5*, 1500.
- (24) Sullivan, B. P.; Meyer, T. J., *Chem. Commun* **1984**, 1244.
- (25) Hori, H.; Johnson, F. P. A.; Koike, K.; Ishitani, O.; Ibusuki, T. *J. Photochem. Photobiol. A* **1996**, *96*, 171.
- (26) Takeda, H.; Koike, K.; Inoue, H.; Ishitani, O. *J. Am. Chem. Soc.* **2008**, *130*, 2023.
- (27) Grills, D. C.; Fujita, E. *J. Phys. Chem. Lett.* **2010**, *1*, 2709.
- (28) Hawecker, J.; Lehn, J. M.; Ziessel, R. *J. Chem. Soc. Commun.* **1983**, 536.
- (29) Hawecker, J.; Lehn, J. M.; Ziessel, R. *J. Helv. Chim. Acta.* **1986**, *69*, 1990.
- (30) Reithmeier, R.; Bruckmeier, C.; Rieger, B. *Catalysts* **2012**, *2*, 544.
- (31) Hayashi, Y.; Kita, S.; Brunschwig, B. S.; Fujita, E. *J. Am. Chem. Soc.* **2003**, *125*, 11976.
- (32) Gibson, D. H.; Yin, X. L. *J. Am. Chem. Soc.* **1998**, *120*, 11200.

- 
- (33) Pistner, A. J.; Yap, G. P. A.; Rosenthal, J. J. *J. Phys. Chem. C*, **2012**, *116*, 16918.
- (34) Gholamkhash, B.; Mametsuka, H.; Koike, K.; Tanabe, T.; Furue, M.; Ishitani, O. *Inorg. Chem.* **2005**, *44*, 2326.
- (35) Tamaki, Y.; Watanabe, K.; Koike, K.; Inoue, H.; Morimoto, T.; Ishitani, O. *Faraday Discuss.* **2012**, *155*, 115.
- (36) Gabrielsson, A.; Lindsay Smith, J. R.; Perutz, R. N. *Dalton Trans.* **2008**, 4259.
- (37) Kiyosawa, K.; Shiraishi, N.; Shimada, T.; Masui, D.; Tachibana, H.; Takagi, S.; Ishitani, O.; Tryk, D. A.; Inoue, H. *J. Phys. Chem. C*, **2009**, *113*, 11667.
- (38) Schneider, J.; Vuong, K. Q.; Calladine, J. A.; Sun, X.-Z.; Whitwood, A. C.; George, M. W.; Perutz, R. N. *Inorg. Chem.* **2011**, *50*, 11877.
- (39) Windle, C. D.; Câmpian, M. V.; Duhme-Klair, A.-K.; Gibson, E. A.; Perutz, R. N.; Schneider, J. *Chem. Commun.* **2012**, *48*, 8189.
- (40) Ulrich, G.; Ziesel, R.; Harriman, A. *Angew. Chem. Int. Ed.* **2008**, *47*, 1184.
- (41) Pangborn, A. B.; Giardello, M. A.; Grubbs, R. H.; Rosen, R. K.; Timmers, F. J. *Organometallics* **1996**, *15*, 1518.
- (42) Berg, K. E.; Tran, A.; Raymond, M. K.; Abrahamsson, M.; Wolny, J.; Redon, S.; Andersson, M.; Sun, L.; Styring, S.; Hammarström, L.; Toftlund, H.; Åkermark, B. *Eur. J. Inorg. Chem.* **2001**, 1019.
- (43) Nepomnyashchii, A. B.; Pistner, A. J.; Bard, A. J.; Rosenthal, J. *J. Phys. Chem. C* **2013**, *117*, 5599.
- (44) Juris, A.; Balzani, V.; Barigelletti, F.; Campagna, S.; Belser, P.; Von Zelewsky, A. *Coord. Chem. Rev.* **1988**, *84*, 85.
- (45) Kawanishi, Y.; Kitamura, N.; Kim, Y.; Tazuke, S. *Riken Q.* **1984**, *78*, 212.
- (46) Calvert, J. M.; Caspar, J. V.; Binstead, R. A.; Westmoreland, T. D.; Meyer, T. J. *J. Am. Chem. Soc.* **1982**, *104*, 6620.
- (47) Smeiga, J. M.; Kubiak, C. P. *Inorg. Chem.* **2010**, *49*, 9283.
- (48) Alvarez, S. G.; Alvarez, M. T. *Synthesis.* **1997**, *4*, 413.

- 
- (49) Nepomnyashchii, A. B.; Broring, M.; Ahrens, J.; Bard, A. J. *J. Am. Chem. Soc.* **2011**, *133*, 8633.
- (50) Rosenthal, J.; Nepomnyashchii, A. B.; Kozhukh, J.; Bard, A. J.; Lippard, S. J. *J. Phys. Chem. C*, **2011**, *115*, 17993.
- (51) Nepomnyashchii, A. B.; Bard, A. J. *Acc. Chem. Res.* **2012**, *45*, 11, 1844.
- (52) Rosenthal, J.; Lippard, S. J. *J. Am. Chem. Soc.*, **2010**, *132*, 5536.
- (53) Barbara, P. F.; Meyer, T. J.; Ratner, M. A. *J. Phys. Chem.*, **1996**, *100*, 13148.
- (54) Gietter, A. A. S.; Pupillo, R. C.; Yap, G. P. A.; Beebe, T. P.; Rosenthal, J.; Watson, D. A. *Chem. Sci.*, 2013, *4*, 437.
- (55) Koike, K.; Naito, S.; Sato, S.; Tamaki, Y.; Ishitani, O. *J. Photochem. Photobiol. A* **2009**, *207*, 109.
- (56) Andrade, G. A.; Pistner, A. J.; Yap, G. P. A.; Lutterman, D. A.; Rosenthal, J. *ACS Catal.* **2013**, *3*, 1685.
- (57) Liu, C.; Dubois, K. D.; Louis, M. E.; Vorushilov, A. S.; Li, G. *ACS Catal.* **2013**, *3*, 655.

## Chapter 3

### PALLADIUM CCC PINCER COMPLEXES CONTAINING NHC LIGANDS FOR APPLICATIONS IN EMISSIVE MATERIALS AND SENSING

#### 3.1 Motivation for the Discovery of Palladium Based Materials for Emissive Materials

##### 3.1.1 Applications of Photoactive Transition Metal Complexes

Photoactive transition metal complexes are desired for many applications such as, photosensitizers,<sup>1,2</sup> photocatalysts,<sup>3,4</sup> photodynamic therapy,<sup>5</sup> bio imaging,<sup>6</sup> optical limiting materials,<sup>7,8</sup> OLEDs,<sup>9,10</sup> and sensors,<sup>11</sup> just to name a few. Transition metal complexes continue to be targets for such applications, as ligand frameworks allow for the control of many properties, such as sterics, and more importantly for photochemistry, the electronics.<sup>12,13</sup> The electronics of transition metal complexes can be manipulated by judicious design of the ligand framework, which can add or alter electronic transitions to the metal complex (*vide infra*).<sup>13</sup> This is important for many reasons such as control of radiative processes over nonradiative pathways, as well as control of the absorption/emission wavelengths and lifetimes. Of particular interest to this work is the development of emissive palladium based materials for applications in OLEDs and sensing. Emissive transition metal based sensors are important as they can be used for detection of harmful vapors. For example, a reported cobalt complex, that is blue in color, was shown to have a vapochromic response to pyridine which turned pink when exposed to pyridine vapors.<sup>14</sup> The development of OLEDs has many advantages over LCD technology such as OLEDs consume less power, are brighter

and produce better picture quality, and further, because some OLED materials can be printed, they can be placed on to thin and flexible screens.<sup>15</sup> Of the many design facets of transition metal complexes for OLED applications, the emission color purity is highly important.

### 3.1.2 Color of Materials Based on CIE Coordinates

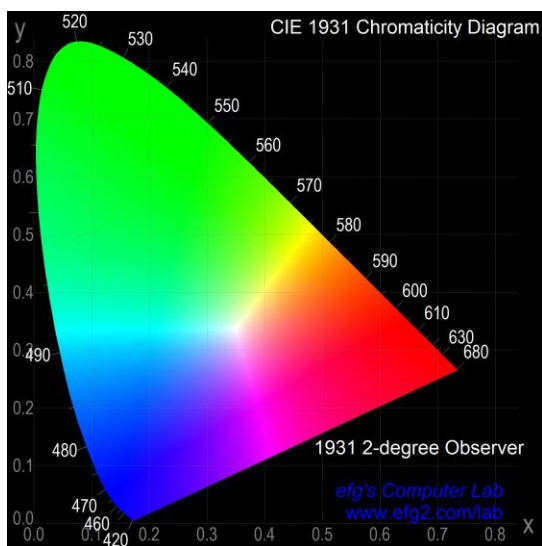


Figure 3.1: 1931 CIE diagram

It is well known that through the combination of red, green, and blue light (RGB), any color in the visible region can be generated, including white light.<sup>16-17</sup> As determined by the Commission Internationale de l'Éclairage (CIE) color matching functions can be used to determine the contributions of RGB light from emission spectra.<sup>17,18</sup> Corrected spectra must be obtained in terms of radiant flux to obtain accurate color determination.<sup>19</sup> From the color matching functions or computer aided

software, one can then obtain (x,y) CIE coordinates which can be plotted on CIE diagrams<sup>17</sup> as shown above in Figure 3.1, which was obtained from free software found online.<sup>20</sup> As stated above the combination of RGB light can produce any color, as such, it would be ideal to have only three emissive materials, a color pure material in each RGB region of the CIE diagram (corners of the diagram). Thus, for OLED applications, the photophysical properties (absorption/emission wavelength and range) of transition metal complexes is important, and can be controlled through ligand design.

### 3.1.3 Successful Metal Based Complexes for OLED Applications and Design Properties

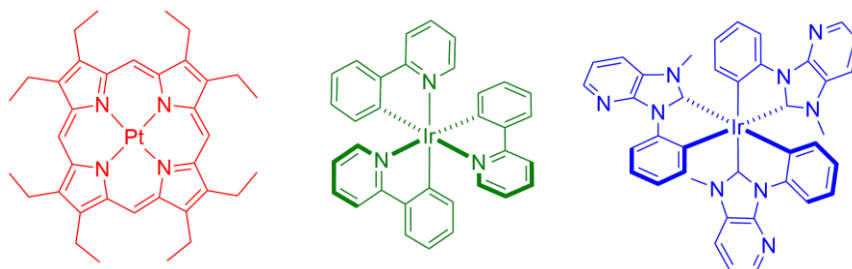


Figure 3.2: RGB emissive transition metal complexes

Transition metal based complexes have shown success as emissive materials in each of the RGB regions. Figure 3.2 displays examples of some of the successful candidates, from left to right, a platinum complex supported by a porphyrin ligand<sup>21</sup> in the red region, an iridium complex supported by three phenyl-pyridine ligands<sup>22</sup> in the green region, and another iridium complex supported by phenyl-N-heterocyclic carbene (NHC) ligands<sup>23</sup> in the blue region. All complexes displayed above include

many design properties which make them successful candidates. As can be seen through this series, numerous emissive transition metal complexes are based on Iridium and Platinum. These metals are targeted largely due to their strong spin-orbit coupling, thus facilitating efficient intersystem crossing to the triplet excited state, followed by phosphorescence.<sup>10,24</sup> Another successful design property for emissive transition metal complexes is incorporation of a rigid ligand. It is known that quenching of excited states can occur through geometric distortions<sup>13,25</sup> thus, as an example, the porphyrin ligand framework can help to prevent non-radiative pathways. Lastly, integration of strong sigma donors from the ligand to the metal center has also been shown to be beneficial for deactivation of non-radiative quenching pathways<sup>26</sup> (vide infra), as can be seen in the Ir complexes (Figure 2.3) with strong phenyl and NHC based donor ligands. This design feature has been suggested to operate through the destabilization of thermally accessible d-d transitions (from the excited state) by strong sigma donation from the ligand.<sup>27</sup> This technique has been successfully demonstrated in many transition metal luminescent complexes including Ir and Pt.

#### **3.1.4 Group 10 Emissive Metals Systems Supported by NHC Ligands**

Metal complexes from groups 7-11 supported by N-heterocyclic carbene (NHC) ligands have shown success in many applications including medicine, catalysis, and emissive materials.<sup>27-32</sup> Ligands incorporating NHCs are of interest due to their ability for strong  $\sigma$ -donation and formation of highly stable bonds with many transition metals. Further, the electronics and sterics of the ligand can be tuned through modification of the NHC core.<sup>33-34</sup> Due to these properties incorporation of NHCs into ligands for emissive materials is attractive in design. As mentioned above, materials which exhibit both efficient intersystem crossing and high triplet state

emission quantum yields are desired for OLED applications. Because NHCs are strong sigma donors, they can destabilize d-d quenching states (as mentioned above), this helps to prevent non-radiative pathways, thus giving rise to more efficient generation of the triplet excited state and greater phosphorescence quantum yields.<sup>35</sup>

Of the group 10 metals, platinum (II) complexes have received most of the attention for emissive materials with relatively few examples incorporating nickel and palladium.<sup>27</sup> Specifically, cyclometallated tris chelating pincer complexes containing an anionic phenyl and NHCs coordinated to the metal center have shown promise as OLED candidates.<sup>36-42</sup>

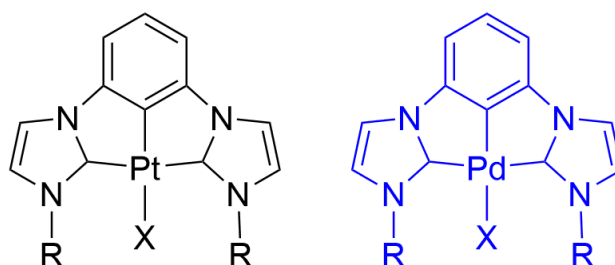


Figure 3.3: Platinum and palladium phenyl spaced bis-NHC pincer complexes

Of these studied complexes the phenyl spaced bis-NHC pincer platinum complex as shown in Figure 3.2 (black), where R = <sup>n</sup>Bu and X = Cl, has shown great potential as a blue light emitter for OLED applications as it is thermally stable, making it ideal for thermodeposition, and is highly resistant to photobleaching.<sup>39</sup> While there are limited examples of palladium based emitters, many of the successful candidates have taken advantage of the strong donor effect discussed above, and contain anionic phenyl and/or NHC donors on the ligand.<sup>43-46</sup> Due to the success of the platinum

phenyl spaced bis-NHC system, it was surprising to find that the palladium analog had not yet been studied as this ligand system inherently contains many of the successful design strategies (discussed above) for emissive complexes. This ligand system should prevent structural distortion of the excited state due to the rigidity of the tris-chelating pincer type ligand, thus favoring radiative pathways. Further, the ligand contains three strong donors, an anionic phenyl and two imidazolium based NHCs which, as noted previously, should destabilize the non-radiative d-d states, yielding higher emission quantum yields. Due to these properties, and our interest in Pd NHC complexes,<sup>47</sup> we wanted to synthesize and investigate the photophysical properties of the palladium analog as shown in Figure 3.2 (blue).

### **3.1.5 Design of a Phenyl Spaced Bis-NHC Palladium Complex**

While it was surprising to see that the palladium analog (Figure 3.3 blue) had not yet been studied as an emissive material, it was further surprising to see that there were no examples in the primary literature for the synthesis of this complex. Activation at the phenyl C2 position of CCC bis-NHC pincer complexes and metalation with palladium has only been accomplished through oxidative addition of a carbon halide bond of xylyl spaced systems<sup>48</sup> as shown in Figure 3.4 (top). However, there is not a known preparation for the analogous phenyl spaced ligand with a halide at the C2 position. Attempts to activate C2 under standard palladium metalation conditions using other terdentate pincer ligands preferentially activate at C4 and C6 to give structures as shown in the bottom right of Figure 3.4 or bridged systems as shown on the bottom left of Figure 3.4.<sup>49</sup>

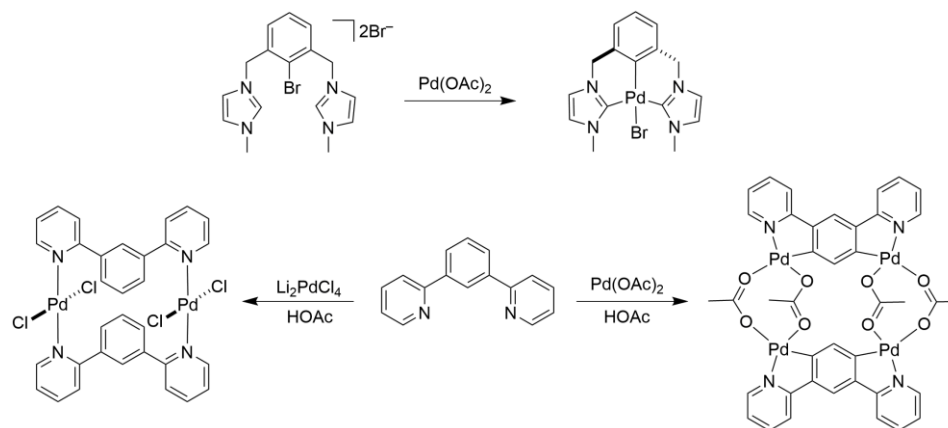


Figure 3.4: Palladium metalation of pincer systems

Work done by Hollis and coworkers for the platinum complex in Figure 3.3 (black) has demonstrated that activation of the C2 position of this ligand can be accomplished through formation of a zirconium intermediate followed by transmetalation to platinum.<sup>39</sup> They have also reported in a patent, a preparation for the palladium analog,<sup>40</sup> however our attempts to recreate their work were unsuccessful. As there were no examples of this complex in the primary literature we were interested in discovering an efficient route to the synthesis of the palladium analog, which we named the phenyl spaced dicarbene complex, or  $[\text{PhDC}^{\text{R}}\text{Pd}(\text{X})](\text{Y})$  where R denotes the substitution on the wingtip, X is the ligand coordinated at the fourth position, and Y is the counterion, if one is present. We were also interested in elucidating the photophysical and redox properties of this complex.

## 3.2 Experimental

### 3.2.1 General Materials and Methods

Reactions were performed in oven-dried round-bottomed flasks unless otherwise noted. Reactions that required an inert atmosphere were conducted under a positive pressure of N<sub>2</sub> using flasks fitted with Suba-Seal rubber septa or in a nitrogen filled glove box. Air and moisture sensitive reagents were transferred using standard syringe or cannula techniques. Reagents and solvents were purchased from Sigma Aldrich, Acros, Fisher, Strem, Pressure Metals or Cambridge Isotopes Laboratories. Solvents for synthesis were of reagent grade or better and were dried by passage through activated alumina and then stored over 4 Å molecular sieves prior to use. Column chromatography was performed with 40-63 μm silica gel with the eluent reported. Analytical thin-layer chromatography (TLC) was performed on precoated glass plates and visualized by UV light. 1,3-Di-N-imidazolyl benzene (2),<sup>50</sup> and [Pd(Br)<sub>2</sub>(MeCN)<sub>2</sub>]<sup>51</sup> were prepared from literature procedures. The synthesis, characterization, and X-ray studies of the [PDC<sup>R</sup>Pd(X)]Y complexes can be found in Chapter 1 of this thesis and in previous work from our lab.<sup>52</sup>

### 3.2.2 Compound Characterization

<sup>1</sup>H NMR and <sup>13</sup>C NMR spectra were recorded at 25 °C on a Bruker 400 MHz spectrometer. Proton spectra are referenced to the residual proton resonance of the deuterated solvent (CDCl<sub>3</sub> = δ 7.26; CD<sub>3</sub>CN = δ 1.94; (CD<sub>3</sub>)<sub>2</sub>SO = δ 2.50) and carbon spectra are referenced to the carbon resonances of the solvent (CDCl<sub>3</sub> = δ 77.16; CD<sub>3</sub>CN = δ 1.32, 118.26; (CD<sub>3</sub>)<sub>2</sub>SO = δ 39.52). All chemical shifts are reported using the standard δ notation in parts-per-million. Low resolution MS data was obtained using either a LCQ Advantage from Thermofinnigan or a Shimadzu LC/MS-2020

single quadrupole MS coupled with an HPLC system, with dual ESI/APCI source. High-resolution mass spectrometry analyses were either performed by the Mass Spectrometry Laboratory in the Department of Chemistry and Biochemistry at the University of Delaware or at the University of Illinois at Urbana-Champaign. Infra-red spectra were recorded in KBr using a Nicolet Magna-IR 750 spectrometer. Elemental analysis was performed at Robertson Microlit Laboratories.

### **3.2.3 Electrochemical Measurements**

All electrochemistry was performed using either a CHI-620D potentiostat/galvanostat or a CHI-760D bipotentiostat. Cyclic voltammetry was performed using a standard three-electrode configuration. CV scans were recorded for quiescent solutions using a glassy carbon working disk electrode (3.0 mm diameter CH Instruments) and a platinum wire auxiliary electrode. All potentials were measured against a silver/ silver chloride reference electrode. CV experiments were performed in DMF using 0.1 M tetrabutylammonium hexafluorophosphate (TBAPF<sub>6</sub>) as the supporting electrolyte. Concentrations of analytes were 1 mM.

### **3.2.4 Photophysical Measurements**

Solution state UV-Vis measurements were acquired on a StellarNet CCD array or Agilent 8453 Diode Array UV-vis spectrometer using screw cap quartz cuvettes (6q or 7q) of 1 cm pathlength from Starna. All absorbance spectra were recorded at room temperature. All samples for spectroscopic analysis were prepared in DMF. Solid state UV-Vis measurements were acquired using a Perkin-Elmer Lambda-750 UV-visible-IR Spectrophotometer fitted with integrating sphere at the Institute of Energy Conversion (IEC) at the University of Delaware. Samples were prepared by dissolving

a small amount of complex in either MeCN, DCM, or MeOH and pipetted onto a quartz plate. The solvent was allowed to evaporate via a stream of N<sub>2</sub> to form a thin film on the quartz plate.

Emission Measurements. Spectra were recorded on an automated Photon Technology International (PTI) QuantaMaster 40 fluorometer equipped with a 75-W Xenon arc lamp, a LPS-220B lamp power supply, a Hamamatsu R2658 photomultiplier tube and a K-Sphere 'Petit' Integrating Sphere. Samples for fluorescence analysis were prepared in an analogous method to that described above for the preparation of samples for UV-vis spectroscopy. Samples were excited at the indicated wavelength in nm and emission was monitored from over the visible range with a step size of 1 nm and integration time of 0.5 seconds. Reported spectra are the average of at least three individual acquisitions. Corrected emission spectra were obtained through calibration of the instrument with known intensities of the dye tetraphenylbutadiene.<sup>19</sup>

### 3.2.5 X-ray Crystallography

X-ray structural analysis for **191** [PhDC<sup>Et</sup>Pd(MeCN)]PF<sub>6</sub>, **204** [PhDC<sup>Et</sup>Pd(Br)], **211** [PhDC<sup>Et</sup>Pd(Py)]PF<sub>6</sub>, **223** [PhDC<sup>Et</sup>Ni(Br)], **224** [PhDC<sup>Et</sup>Ni(MeCN)]PF<sub>6</sub>, **244** [PhDC<sup>Et</sup>Pd(<sup>t</sup>BuNC)]PF<sub>6</sub>, and **249** [PhDC<sup>Et</sup>Pd(PPh<sub>3</sub>)]PF<sub>6</sub>: Crystals were mounted using viscous oil onto a plastic mesh and cooled to the data collection temperature. Data were collected on a Bruker-AXS APEX II DUO CCD diffractometer with Cu-K $\alpha$  radiation ( $\lambda = 1.54178 \text{ \AA}$ ) for **249** focused by Goebbel mirrors. All other data were collected with Mo-K $\alpha$  radiation ( $\lambda = 0.71073 \text{ \AA}$ ) monochromated with graphite. Unit cell parameters were obtained from 36 data frames, 0.5°  $\omega$ , from three different sections of the Ewald sphere. The unit-cell parameters and systematic absences were

uniquely consistent to the reported space groups for 204, 249, and 223. No symmetry higher than triclinic was observed in 191, 211, 224, and 244 and the centrosymmetric space group option yielded chemically reasonable and computationally stable results of refinement. The data were treated with multi-scan absorption corrections (Apex3 software suite; Bruker AXS, Inc., Madison, WI, 2015). The structures were solved using direct methods or intrinsic phasing and refined with full-matrix, least-squares procedures on F<sup>2</sup>. Two ion pairs ( $Z' = 2$ ) were located in the asymmetric unit of 211. Three symmetry unique molecules ( $Z' = 3$ ) were located in 223 with one molecule displaying whole molecule disorder with a refined site occupancy distribution of 60/40. Four symmetry unique molecules ( $Z' = 4$ ) were located in 204 with one molecule displaying whole molecule disorder with a refined site occupancy distribution of 60/40. An acetonitrile molecule was located with the ion pair in 191. The solvent molecules in 204, 244, and 249 precluded satisfactory modeling and were treated as diffused contributions (Squeeze, Platon: Spek, A. L., J. Appl. Cryst., 2003, 36, 7-13). All non-hydrogen atoms were refined with anisotropic displacement parameters. All hydrogen atoms were treated as idealized contributions with geometrically calculated positions and with  $U_{iso}$  equal to 1.2, or 1.5 for methyl,  $U_{eq}$  of the attached atom. Atomic scattering factors are contained in various versions of the SHELXTL program library (Sheldrick, G.M. 2015. Acta Cryst. C71, 3-8).

### 3.2.6 X-ray Photoelectron Spectroscopy

All XPS spectra were acquired using a Thermo Fisher K-alpha+ spectrometer. The X-rays used were monochromatic Al K $\alpha$  X-Rays (1486.7 eV) with a power of 72 W (12 kV, 6 mA). The operating pressure in the main chamber was less than  $1 \times 10^{-8}$  mbarr. The X-Ray spot size was elliptical in shape with a semi-major axis of 400  $\mu\text{m}$

### 3.2.7 Synthesis and Characterization

#### 3.2.7.1 Synthesis of proligand 1H-Imidazolium, 3,3'-(1,3-phenylene)bis[1-ethyl-, bromide (3)

The proligand (3) was prepared based on a literature preps.<sup>53,54</sup> 0.250 g (1.19 mmol) of 1,3-Di-N-imidazolyl benzene, 1.3 g (11.90 mmol) of ethylbromide, and 3 ml of xylenes were added to a pressure tube which was sealed with a cap fitted with a rubber o ring. The reaction vessel was heated to 150 °C for 4 days at which time the mixture was cooled to room temperature. The solid was filtered and then precipitated from a 20 % MeOH in DCM solution with ether. The white solid was then collected via filtration and dried to yield (2) in a 80 % yield. <sup>1</sup>H NMR (400 MHz, DMSO-d<sub>6</sub>) δ 10.20 (s, 2H), 8.56 (s, 2H), 8.51 (s, 1H), 8.17 (s, 2H), 8.08 – 8.03 (m, 2H), 7.97 (dd, J = 9.0, 7.2 Hz, 1H), 4.34 (q, J = 7.3 Hz, 4H), 1.55 (t, J = 7.3 Hz, 6H). <sup>13</sup>C NMR (101 MHz, DMSO) δ 135.78, 135.65, 132.00, 123.34, 122.36, 121.05, 115.48, 45.03, 14.87. HR-LIFDI-MS Calculated for (M-Br) C<sub>16</sub>H<sub>20</sub>N<sub>4</sub>Br: 347.0871, found: 347.0858.

#### 3.2.7.2 Synthesis of [PhDC<sup>Et</sup>Pd(Br)]

This complex was prepared based of a patent preparation.<sup>40</sup> In a glovebox, the proligand (3) (0.130 g, 0.304 mmol) was suspended in dry THF and a solution of [Zr(NMe<sub>2</sub>)<sub>4</sub>] (0.118 g, 0.441 mmol) in THF (10 ml) was added and the reaction was magnetically stirred at room temperature for 2 hours. [Pd(Br)<sub>2</sub>(MeCN)<sub>2</sub>] (0.111 g, 0.319 mmol) was then added and the reaction vessel was sealed with coper wire and taken out of the box. The mixture was then heated to 60 °C for 16 hours after which the solvent was removed under reduced pressure. The crude material was then purified via column chromatography using a 1% MeOH in DCM solution as the eluent and yielded (0.089 g, 65% yield) an analytically pure off white material. X-ray quality crystals were grown via vapor diffusion of pentane into a concentrated DCM solution. <sup>1</sup>H NMR (400 MHz, DMSO-d<sub>6</sub>) δ 8.05 (d, J = 1.9 Hz, 2H), 7.50 (d, J = 2.0 Hz, 2H),

7.32 – 7.10 (m, 3H), 4.69 (q, J = 7.2 Hz, 4H), 1.36 (t, J = 7.1 Hz, 6H).  $^{13}\text{C}$  NMR (101 MHz, DMSO)  $\delta$  174.44, 145.55, 144.00, 125.35, 121.16, 115.79, 108.78, 44.45, 17.10. Elemental Analysis (Calculated: C 42.55; H, 3.79; N, 12.40, Found C, 42.35; H, 3.52, N, 12.19) HR-LIFDI-MS Calculated for ( $\text{M}^+$ ) m/z:  $\text{C}_{16}\text{H}_{17}\text{N}_4\text{BrPd}$ : 451.9666, found: 451.9649.

### 3.2.7.3 Synthesis of $[\text{PhDC}^{\text{Et}}\text{Pd}(\text{MeCN})]\text{PF}_6$

$[\text{PhDC}^{\text{Et}}\text{Pd}(\text{Br})]$  was converted to the solvato complex via a metathesis reaction. A solution of  $\text{AgPF}_6$  (0.042 g 0.166 mmol), in MeCN (3 ml) was added to  $[\text{PhDC}^{\text{Et}}\text{Pd}(\text{Br})]$  (0.075 g 0.166 mmol) dissolved in MeCN (5 ml) in which time a solid began to appear. The reaction vessel was sealed from light and heated to 70 °C for 12 hours after which time the reaction was allowed to cool to room temperature and the mixture was filtered through celite. The solvent was then removed from the filtrate under reduced pressure yielding an analytically pure white solid (0.083 g, 90% yield). X-ray quality crystals were grown via vapor diffusion of ether into a concentrated MeCN solution.  $^1\text{H}$  NMR (400 MHz, Acetonitrile- $d_3$ )  $\delta$  7.56 (d, J = 2.0 Hz, 2H), 7.21 (dd, J = 8.4, 7.4 Hz, 1H), 7.17 (d, J = 2.0 Hz, 2H), 7.04 (d, J = 7.9 Hz, 2H), 4.13 (q, J = 7.3 Hz, 4H), 1.96 (s, 3H), 1.45 (t, J = 7.3 Hz, 6H).  $^{13}\text{C}$  NMR (101 MHz,  $\text{CD}_3\text{CN}$ )  $\delta$  176.11, 147.19, 142.64, 127.73, 121.51, 116.55, 109.99, 46.13, 17.18. Elemental Analysis (Calculated: C 38.76; H, 3.61; N, 12.56, Found C, 38.96; H, 3.42, N, 12.40) HR-ESI-MS Calculated for ( $\text{M}-\text{PF}_6$ )  $\text{C}_{18}\text{H}_{20}\text{N}_5\text{Pd}$ : 412.0748, found: 412.0751

### 3.2.7.4 Synthesis of $[\text{PhDC}^{\text{Et}}\text{Pd}(\text{Py})]\text{PF}_6$

$[\text{PhDC}^{\text{Et}}\text{Pd}(\text{MeCN})]\text{PF}_6$  (0.058 g, 0.104 mmol) was dissolved in 5 ml of pyridine and the solution was magnetically stirred at room temperature for 3 hours.

After completion, the solvent was removed until an oil was left in the reaction vessel. Diethyl ether (15 ml) was added to the reaction vessel and the mixture was sonicated to precipitate the product. The product was collected by filtration and washed with additional diethyl ether (3 x 10 ml) to remove any remaining pyridine. The white solid was vacuum dried yielding analytically pure material (0.048 g, 77% yield).  $^1\text{H}$  NMR (400 MHz, DMSO- $d_6$ )  $\delta$  9.00 (s, 2H), 8.17 – 8.05 (m, 3H), 7.68 (t,  $J = 6.1$  Hz, 2H), 7.52 (d,  $J = 2.0$  Hz, 2H), 7.29 (m, 3H), 3.50 (s, 4H), 1.18 – 1.00 (m, 6H).  $^{13}\text{C}$  NMR (101 MHz, DMSO)  $\delta$  174.30, 145.58, 135.08, 134.99, 133.54, 133.37, 129.99, 129.16, 129.08, 121.23, 117.13, 109.52, 44.36, 16.08. HR-ESI-MS Calculated for (M–PF<sub>6</sub>) C<sub>21</sub>H<sub>22</sub>N<sub>5</sub>Pd: 450.0905, found: 450.0908

### 3.2.7.5 Synthesis of [PhDC<sup>Et</sup>Pd(<sup>t</sup>BuNC)]PF<sub>6</sub>

The synthesis of this complex was carried on in a glovebox. [PhDC<sup>Et</sup>Pd(MeCN)]PF<sub>6</sub> (0.069 g, 0.124 mmol) was dissolved in dry MeCN (15 ml) and tert-Butyl isonitrile (0.098 ml, 0.866 mmol) was added to the solution. The solution was magnetically stirred for 3 hours at room temperature. The solvent was then removed and the solid was recrystallized with MeCN and diethyl ether. The solid was dried on a vacuum yielding the desired product analytically pure (0.055 g, 74% yield).  $^1\text{H}$  NMR (400 MHz, Acetonitrile- $d_3$ )  $\delta$  7.61 (d,  $J = 2.1$  Hz, 2H), 7.32 – 7.19 (m, 3H), 7.09 (d,  $J = 7.9$  Hz, 2H), 4.22 (q,  $J = 7.3$  Hz, 4H), 1.63 (s, 9H), 1.49 (t,  $J = 7.3$  Hz, 6H).  $^{13}\text{C}$  NMR (101 MHz, CD<sub>3</sub>CN)  $\delta$  175.60, 147.73, 128.74, 121.65, 117.13, 110.14, 47.05, 29.98, 17.60. HR-ESI-MS Calculated for (M–PF<sub>6</sub>) C<sub>21</sub>H<sub>26</sub>N<sub>5</sub>Pd: 454.1218, found: 454.1218

### 3.2.7.6 Synthesis of [PhDC<sup>Et</sup>Pd(PPh<sub>3</sub>)]PF<sub>6</sub>

[PhDC<sup>Et</sup>Pd(MeCN)]PF<sub>6</sub> (0.013 g, 0.023 mmol) and triphenylphosphine (PPh<sub>3</sub>) (0.061 g, 0.233 mmol) was dissolved in 3 ml of DMF and magnetically stirred for 3 hours at room temperature. H<sub>2</sub>O was then added to precipitate the product and the excess PPh<sub>3</sub>. The material was collected on a fritted filter and the white solid that was collected was washed with copious amounts of diethyl ether to remove the excess PPh<sub>3</sub>. The solid material was vacuum dried yielding analytically pure material (0.014 g, 80% yield). <sup>1</sup>H NMR (400 MHz, DMSO-*d*<sub>6</sub>) δ 8.18 (s, 2H), 7.56 (d, *J* = 2.0 Hz, 2H), 7.44 (m, 15H), 7.32 (s, 3H), 3.77 (br d, *J* = 7.4 Hz, 4H), 1.12 (t, *J* = 7.2 Hz, 6H). <sup>13</sup>C NMR (101 MHz, DMSO) δ 174.30, 145.58, 135.08, 134.99, 133.54, 133.37, 129.99, 129.16, 129.08, 126.98, 121.23, 117.13, 109.52, 44.36, 16.08. HR-ESI-MS Calculated for (M–PF<sub>6</sub>) C<sub>34</sub>H<sub>32</sub>N<sub>4</sub>PPd: 633.1394, found: 633.13997

### 3.2.7.7 Synthesis of [PhDC<sup>Et</sup>Ni(Br)]

The procedure for the palladium analog was also used for the nickel complex. In a glovebox, the proligand (3) (0.087 g, 0.203 mmol) was suspended in dry THF and a solution of [Zr(NMe<sub>2</sub>)<sub>4</sub>] (0.079 g, 0.295 mmol) in THF (10 ml) was added and the reaction was magnetically stirred at room temperature for 2 hours. [Ni(Br)<sub>2</sub>(DME)] (0.066 g, 0.213 mmol) was then added and the reaction vessel was sealed with copper wire and taken out of the box. The mixture was then heated to 60 °C for 16 hours after which the solvent was removed under reduced pressure. The crude material was then purified via column chromatography using a 1% MeOH in DCM solution as the eluent and yielded (0.038 g, 46% yield) an analytically pure orange material. X-ray quality crystals were grown via vapor diffusion of pentane into a concentrated DCM solution. <sup>1</sup>H NMR (400 MHz, DMSO-*d*<sub>6</sub>) δ 7.95 (br s, 2H), 7.29 (br s, 2H), 7.09 (br s, 3H), 4.62

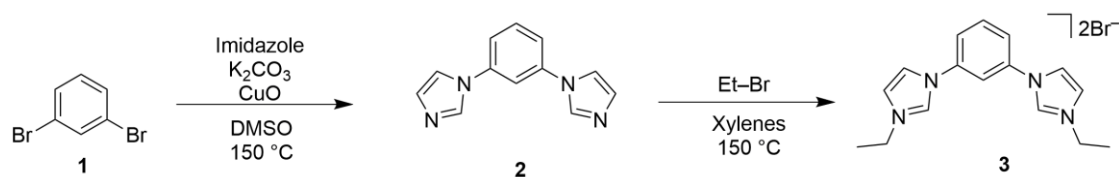
(br s, 4H), 1.37 (br s, 6H). HR-ESI-MS Calculated for (M) C<sub>16</sub>H<sub>17</sub>N<sub>4</sub>BrNi: 401.9985, found: 401.9984

### 3.2.7.8 Synthesis of [PhDC<sup>Et</sup>Ni(MeCN)]PF<sub>6</sub>

[PhDC<sup>Et</sup>Ni(Br)] was converted to the solvato complex via the same procedure as the palladium analog. A solution of AgPF<sub>6</sub> (0.018 g 0.069 mmol), in MeCN (3 ml) was added to [PhDC<sup>Et</sup>Ni(Br)] (0.028 g 0.069 mmol) dissolved in MeCN (5 ml) in which time a solid began to appear. The reaction vessel was sealed from light and heated to 70 °C for 12 hours after which time the reaction was allowed to cool to room temperature and the mixture was filtered through celite. The solvent was then removed from the filtrate under reduced pressure yielding an analytically pure orange material (0.032 g, 90% yield). X-ray quality crystals were grown via vapor diffusion of ether into a concentrated MeCN solution. <sup>1</sup>H NMR (400 MHz, Acetonitrile-*d*<sub>3</sub>) δ 7.50 (d, *J* = 2.2 Hz, 2H), 7.13 (t, *J* = 7.9 Hz, 1H), 7.09 (d, *J* = 2.2 Hz, 2H), 6.90 (d, *J* = 7.8 Hz, 2H), 4.11 (q, *J* = 7.4 Hz, 4H), 1.96 (s, 3H), 1.46 (t, *J* = 7.4 Hz, 6H). HR-ESI-MS Calculated for (M-PF<sub>6</sub>) C<sub>18</sub>H<sub>20</sub>N<sub>5</sub>Ni: 364.1067, found: 364.1066

## 3.3 Synthetic Pathway to PhDC<sup>Et</sup> Palladium Complexes.

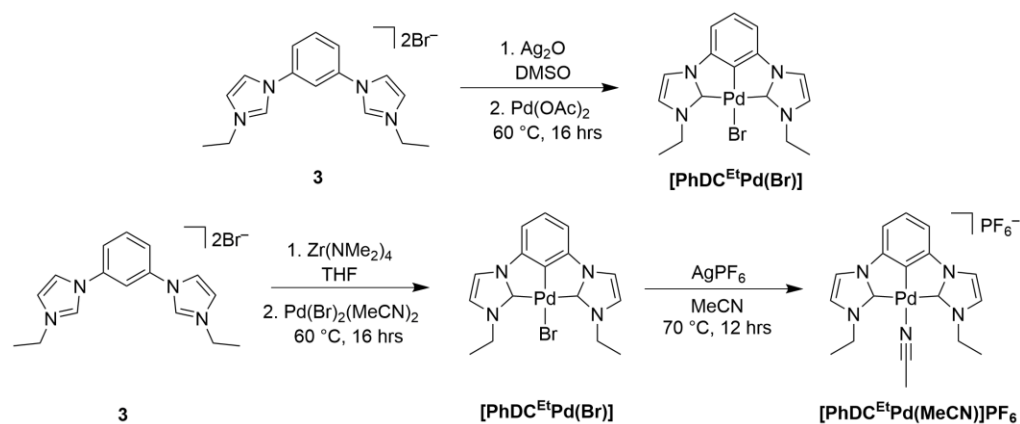
### 3.3.1 Synthesis of the PhDC<sup>Et</sup> Proligand



Scheme 3.1: Synthetic pathway to PhDC<sup>Et</sup> proligand

The preparation of the material began first with the synthesis of the proligand (**3**) as shown in Scheme 3.1. This was accomplished over two steps and began with the Ullmann coupling of imidazole and 1,3-dibromobenzene to give 1,3-di-N-imidazolyl benzene (**2**). This material was then converted to the proligand via a substitution reaction with ethyl bromide at elevated temperatures over the course of 4 days in a sealed pressure tube. With the proligand in hand we were then able to begin our studies to find a method for the palladation of the proligand.

### 3.3.2 Synthesis of [PhDC<sup>Et</sup>Pd] Complexes



Scheme 3.2: Synthetic pathway to PhDC<sup>Et</sup> palladium complexes

As discussed previously our efforts to recreate the synthesis found in the patent were unsuccessful and after isolation we only found unreacted starting material. Since this route showed the most promise for palladation of the ligand, as it was successful for the platinum analog, we decided to target transmetalation strategies. Because we had shown success in palladation for our pyridyl spaced dicarbene (PDC) complexes

using a Ag transmetallation strategy,<sup>54</sup> (See Chapter 1) we were first interested in determining if this could also work for the PhDC ligand. Knowing that the metalation of the PhDC ligand required deprotonation of three hydrogens, we reasoned that Ag<sub>2</sub>O could deprotonate the two imidazole protons to form the Ag carbene intermediate, and that a palladium reagent with a coordinated base, such as acetate (CH<sub>3</sub>COO<sup>-</sup>), might be able to perform the final deprotonation. We attempted this reaction (Scheme 3.2) using similar conditions as found in Chapter 1 by first forming the Ag carbene with one equivalent of Ag<sub>2</sub>O and one equivalent of the proligand in DMSO. Upon confirmation that the Ag intermediate had formed, we added 1.1 equivalents of Pd(OAc)<sub>2</sub> and heated the reaction to 60 °C for 16 hours. After purification on silica and isolation, we found that this route did indeed produce the desired product, albeit in a 7% yield. As this method would not be feasible for the scale and preparation of this material, and also because we discovered unwanted side products during the metalation of the PDC ligands (See Chapter 1) at greater temperatures, we decided to not pursue this method further. However, when comparing the Zr and Ag transmetallation methods for palladation of the PhDC ligand we found that we were successful only when heat was added to the reaction, which was absent in the Zr method. We decided to revisit our synthesis based on the Zr method with the addition of heat and found that we could produce the desired product in a 65% yield after purification via column chromatography (Scheme 3.2). As the majority of our characterization for the PDC complexes (Chapter 1) was performed with the acetonitrile solvato complex, we next wanted to synthesize the acetonitrile bound complex which would allow for direct comparison between the two complexes. Synthesis of [PhDC<sup>Et</sup>Pd(MeCN)]PF<sub>6</sub> was easily accomplished using a metathesis

reaction of the halide complex and  $\text{AgPF}_6$  in acetonitrile which yielded the desired complex without purification in high yield (Scheme 3.2). With the compounds in hand we next began our characterization and comparison to our previously studied  $[\text{PDC}^{\text{Et}}\text{Pd}(\text{X})]\text{Y}$  complexes.

### **3.4 Characterization of $[\text{PhDC}^{\text{Et}}\text{Pd}(\text{Br})]$ and $[\text{PhDC}^{\text{Et}}\text{Pd}(\text{MeCN})]\text{PF}_6$**

#### **3.4.1 Solid State Characterization and Comparison**

Single crystals of both the halide and solvato complexes were obtained by vapor diffusion methods and X-ray diffraction experiments were carried out to obtain the solid-state structures. As we had previously obtained the solid-state structures for the  $\text{PDC}^{\text{Et}}\text{Pd}$  halide and solvato complexes we were able to compare the metrics for bond lengths and angles. The experimental details and full bond lengths and angles can be found in Appendix C.

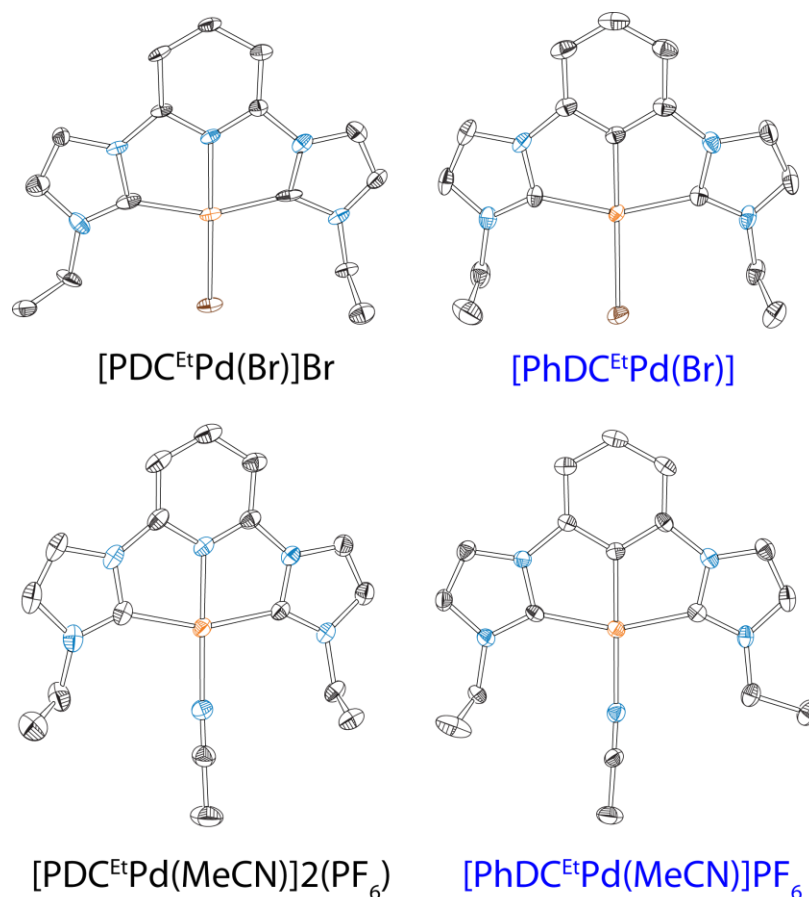


Figure 3.5: Thermal ellipsoids of PDC and PhDC palladium halide and solvato structures shown at the 50% probability level with hydrogens and counterions omitted for clarity.

As shown in Figure 3.5 and in Table 3.1 all PDC and PhDC palladium complexes display a pseudo square planar geometry with  $C_{NHC}-Pd-C_{NHC}$  bond angles around  $156^\circ$ . Similarly, through the entire series the  $C_{NHC}-Pd$  bond lengths are close to  $2 \text{ \AA}$ . Where we begin to see variance in bond length is from the central donor (N from pyridyl and C from phenyl,  $N_{Py}$  and  $C_{Ph}$  respectively) to palladium and the trans bond of palladium to X, where X is Br or MeCN. What we find is that the PhDC complexes have shorter central donor to Pd bonds than the PDC complexes (about

0.03 Å), this is expected as the anionic C<sub>Ph</sub> donor is much stronger than the neutral N<sub>Py</sub>. The bond trans to the central donor has a more pronounced effect where we see a lengthening of the Pd–X bond by nearly 0.1 Å. This is also expected as the strong C<sub>Ph</sub> trans donor weakens this bond as explained by the trans influence. Similar observations have been reported for platinum pincer complexes.<sup>55</sup>

	PDC <sup>Et</sup> Pd(Br)	PhDC <sup>Et</sup> Pd(Br)	PDC <sup>Et</sup> Pd(MeCN)	PhDC <sup>Et</sup> Pd(MeCN)
C <sub>NHC</sub> –Pd	2.047 Å	2.053 Å	2.029 Å	2.046 Å
C <sub>NHC</sub> –Pd	1.994 Å	2.054 Å	2.034 Å	2.049 Å
N <sub>Py</sub> or C <sub>Ph</sub> –Pd	1.980 Å	1.949 Å	1.966 Å	1.940 Å
Pd–X	2.406 Å	2.533 Å	2.004 Å	2.092 Å
C <sub>NHC</sub> –Pd–C <sub>NHC</sub>	156.72 °	156.08 °	158.30 °	156.97 °
N <sub>Py</sub> or C <sub>Ph</sub> –Pd–X	178.14 °	172.47 °	177.50 °	176.85 °

Table 3.1: Selected bond lengths and angles for the PDC<sup>Et</sup> and PhDC<sup>Et</sup> palladium halide and solvato complexes, where the outer sphere counter ions are omitted from the formula and X denotes the ligand at the fourth coordination site which is either Br or MeCN.

### 3.4.2 Redox Properties and Comparison

Upon noticing the differences in bond lengths around the palladium center and because the PhDC ligand is anionic compared to the neutral PDC ligand, we next wanted to investigate the redox properties of the complexes. Cyclic voltammetry experiments were carried out under an inert N<sub>2</sub> environment using a standard three electrode configuration, using a glassy carbon disk working electrode, a platinum wire reference electrode and a Ag/AgCl reference electrode. The complexes were dissolved in a 0.1 M TBAPF<sub>6</sub> in DMF electrolyte solution with an analyte concentration of 1 mM.

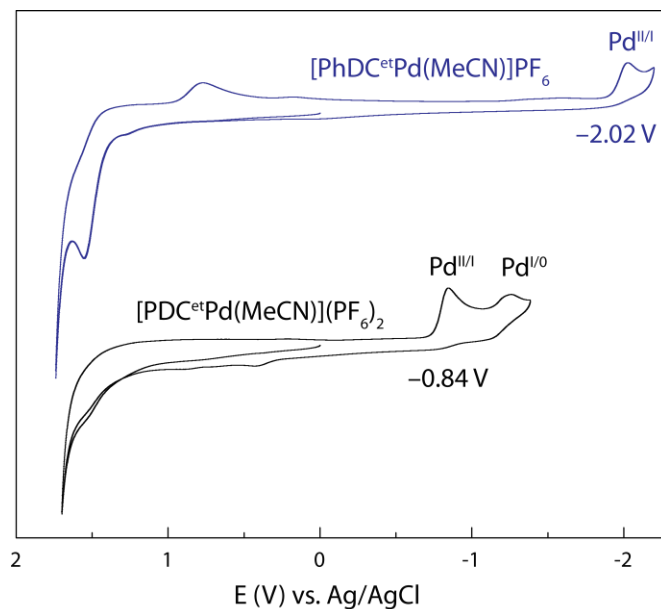


Figure 3.6: Cyclic voltammograms of the PDC<sup>Et</sup> and PhDC<sup>Et</sup> palladium solvato complexes

The PDC<sup>Et</sup>Pd solvato complex had been previously investigated by cyclic voltammetry (Chapter 1) and we found that the redox profile shows two irreversible reductions corresponding to the Pd<sup>II/I</sup> couple followed by the Pd<sup>I/0</sup> couple with the initial reduction having a peak potential of  $-0.84$  V vs Ag/AgCl. These assignments were supported by other investigators studying similar complexes.<sup>56</sup> The PhDC<sup>Et</sup>Pd solvato complex displays significantly altered redox properties. Due to the anionic nature of the PhDC ligand we see the initial Pd<sup>II/I</sup> couple has shifted, by over a volt, to a more negative potential of  $-2.02$  V vs Ag/AgCl. Further, we no longer are able to observe the Pd<sup>I/0</sup> couple within the DMF solvent window, also we begin to see oxidative features on the anodic portion of the voltammogram. As the electronics were

clearly different for the two systems we next wanted to investigate the photo physical properties.

### 3.4.3 Solution State Photophysical Properties

For our photophysical studies we focused on the PhDC palladium complexes as the PDC palladium complexes have been widely explored and their photophysical properties elucidated.<sup>57-59</sup>

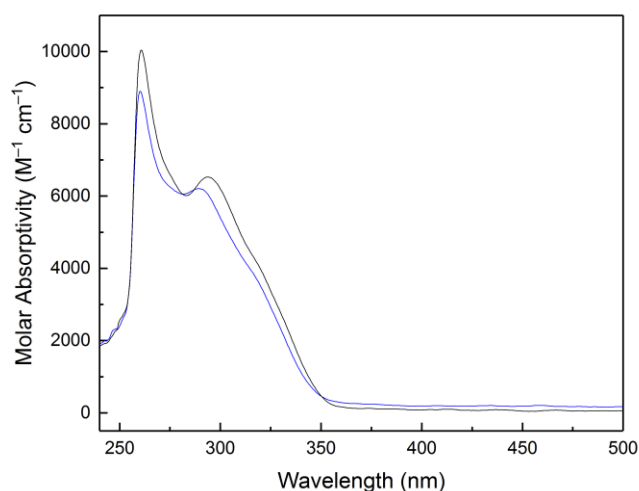


Figure 3.7: Absorbance profile of  $[\text{PhDC}^{\text{Et}}\text{Pd}(\text{Br})]$  (black trace) and  $[\text{PhDC}^{\text{Et}}\text{Pd}(\text{MeCN})]\text{PF}_6$  (blue trace) in DMF.

As shown in Figure 3.7 both complexes display nearly identical absorbance profiles with peak maxima near 260 and 300 nm and extending out to 350 nm. Similar absorbance profiles have been obtained for the  $[\text{PhDC}^n\text{BuPt}(\text{Cl})]^{39}$  and  $[\text{PDC}^n\text{BuPd}(\text{acetylide})](\text{Br}^-)^{57}$  complexes, and correspond to mixed metal to ligand charge transfer and intraligand transitions. While the Pt complex supported by the

same ligand with <sup>t</sup>Bu wingtips and Cl<sup>-</sup> at the X position was reported to be emissive in solution, we found that our palladium analog was not. It has been reported that of the few examples of emissive palladium complexes, many of them were only emissive in a frozen glass matrix or in the solid state.<sup>44,45</sup> This led us to investigate the solid state photophysical properties.

### 3.4.4 Solid State Photophysical Properties

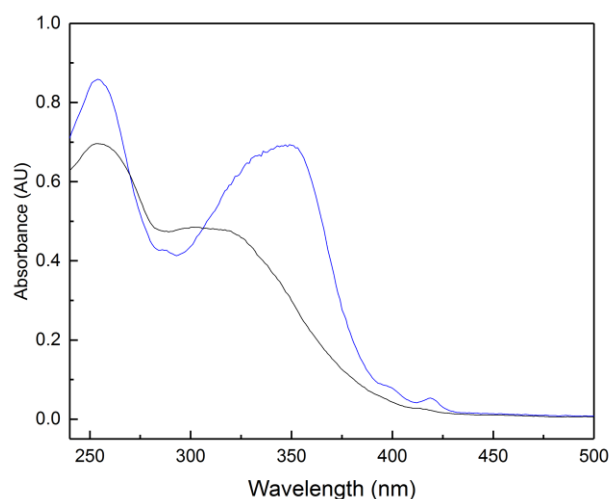


Figure 3.8: Solid state absorbance profile of [PhDC<sup>Et</sup>Pd(Br)] (black trace) and [PhDC<sup>Et</sup>Pd(MeCN)]PF<sub>6</sub> (blue trace).

The solid state photophysical properties were probed with instruments containing integrating spheres. Samples were prepared by dissolving a small amount of material in MeCN or DCM and evaporating the solution on a quartz slide to generate a thin film. As displayed in Figure 3.8 both complexes display broad absorbances in the 250 to 400 nm range with two peak maxima. Also, both complexes show a red shift as

the absorbance profiles extend out to 400 nm. Contrary to the solution state, the solid-state absorbance profiles are not identical. The halide complex displays a small shoulder in the absorbance profile at longer UV wavelengths while the solvato complex shows a strong absorbance with a peak maximum at 357 nm. Excitation with a handheld UV light on the solid materials resulted in the solvato complex displaying bright blue emission while the halide complex was non-emissive. This led us to investigate the emission properties of the solvato complex.

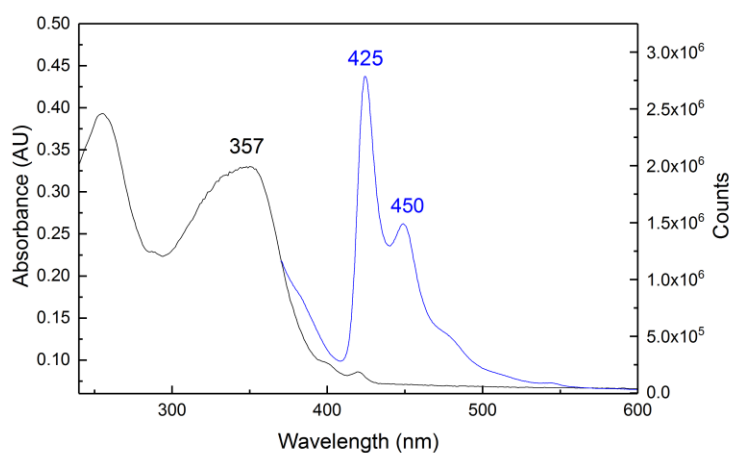


Figure 3.9: Solid state absorbance (black trace) and emission (blue trace) of  $[\text{PhDC}^{\text{Et}}\text{Pd}(\text{MeCN})]\text{PF}_6$

Solid state emission studies of the solvato complex were carried out at room temperature and the solid-state absorbance (black trace) and emission (blue trace) are displayed in Figure 3.9. Excitation of the complex at 357 nm resulted in emission in the blue region with a maximum at 425 nm and a less intense shoulder at 450 nm. The emission was mostly in the visible blue region but extended out to 500 nm. When compared to the  $[\text{PhDC}^{\text{nBu}}\text{Pt}(\text{Cl})]$  complex the palladium analog displays a blue

shifted emission profile as the platinum complex exhibited emission in the 425 to 575 nm range with peak maxima near 475 nm in the solid state.<sup>39</sup> As the [PhDC<sup>Et</sup>Pt(MeCN)]PF<sub>6</sub> complex displayed strong emission in the far blue region we became interested in obtaining the CIE color coordinates to compare to other deep blue emitters.

### 3.4.5 CIE Color Coordinates

As discussed previously the emission of materials can be characterized on a chromaticity diagram through CIE (x,y) coordinates. While successful materials have been designed for red and green emitters, there is still a need for efficient deep blue emissive materials.<sup>23-60</sup> As our complex seemed to be emissive in the deep blue region we undertook experiments to obtain the CIE coordinates. To acquire CIE coordinates, a corrected emission spectrum must be obtained. To do this the fluorimeter was calibrated over the emission range from 390 to 570 nm with a known standard, tetraphenylbutadiene (TPB).<sup>19</sup> Emission data for TPB was acquired and the intensities of emission were adjusted to the known values to calibrate the instrument. After calibration, emission spectra of [PhDC<sup>Et</sup>Pt(MeCN)]PF<sub>6</sub> was obtained and computer software, provided by PTI/Horiba, was used to determine the CIE coordinates.<sup>61</sup> The software uses the emission flux over the visible region to determine emission contribution in the RGB regions and then gives CIE coordinates as the output.

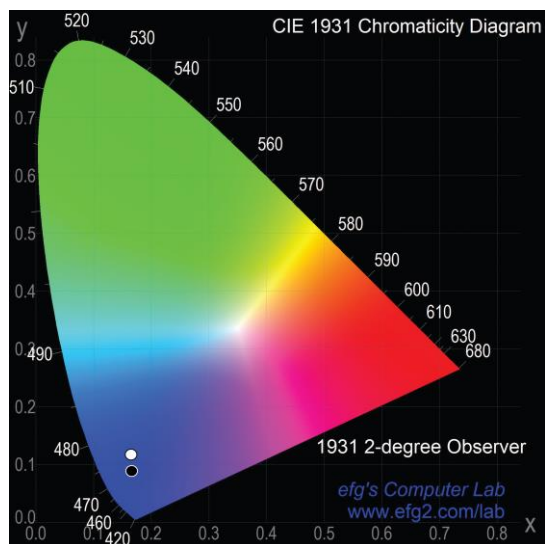


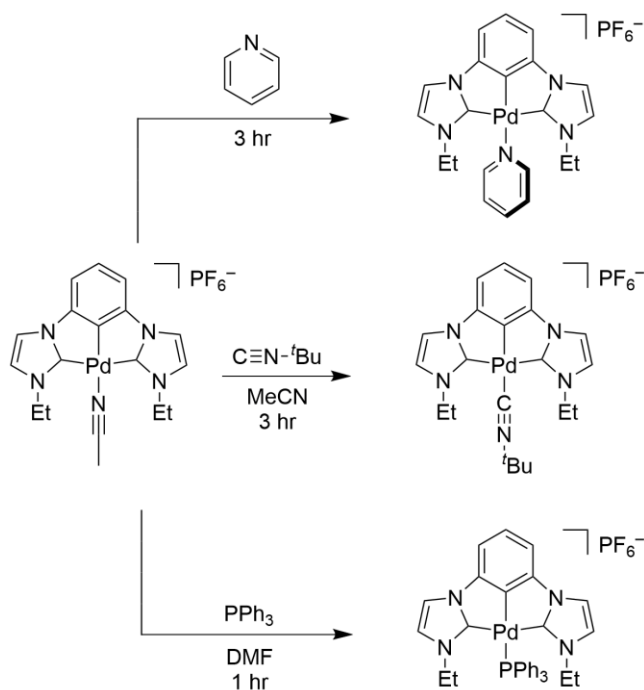
Figure 3.10: CIE coordinates of  $[\text{PhDC}^{\text{Et}}\text{Pt}(\text{MeCN})]\text{PF}_6$  (white dot) and  $\text{fac-Ir}(\text{pmp})_3$  (black dot)

Ideal true deep blue emitters have CIE coordinates of (0.14, 0.08).<sup>62</sup> To our knowledge the deepest blue transition metal based material is the  $\text{fac-Ir}(\text{pmp})_3$  complex shown in Figure 3.2 which has coordinates of (0.16, 0.09) (black dot Figure 3.10).<sup>23</sup> Our  $[\text{PhDC}^{\text{Et}}\text{Pt}(\text{MeCN})]\text{PF}_6$  complex gave CIE coordinates of (0.16, 0.12) (white dot Figure 3.10) just above the Ir complex on the CIE diagram. To our knowledge this is the deepest blue emissive palladium based material to date. Further, palladium based materials are much less expensive than iridium based materials which make them more attractive for integration into devices. From previous work in our lab we discovered that substitution of the ancillary ligand for PDC complexes could be accomplished easily.<sup>52</sup> Thus, next we became interested in substitution of the ancillary ligand and studying the effect on the photophysical properties.

### 3.5 Substitution of the Ancillary Ligand

It has been demonstrated that substitution of the ancillary ligand (X) on  $\text{PhDC}^{\text{R}}\text{Pt}(\text{X})$  complexes alters the photophysical properties.<sup>63</sup> Previous work in our lab showed that substitution of the acetonitrile ligand on  $[\text{PDC}^{\text{R}}\text{Pd}(\text{MeCN})]2\text{PF}_6$  complexes could be quickly accomplished to form complexes with bound pyridine (Py), tert-Butyl isonitrile ( ${}^t\text{BuNC}$ ), and triphenyl phosphine ( $\text{PPh}_3$ ).<sup>52</sup> As such we were interested in synthesizing these derivatives for the PhDC palladium series and studying the effects on the photophysical properties by substitution of the ancillary ligand.

#### 3.5.1 Synthetic Pathway to Pyridine, $\text{PPh}_3$ and ${}^t\text{BuNC}$ Complexes



Scheme 3.3: Synthesis of  $[\text{PhDC}^{\text{Et}}\text{Pd}(\text{X})]\text{PF}_6$  derivatives, where X = pyridine (Py), tert-Butyl isonitrile ( ${}^t\text{BuNC}$ ), and triphenylphosphine ( $\text{PPh}_3$ ).

Substitution of the ancillary ligand was carried out to produce  $\text{PhDC}^{\text{Et}}\text{Pd}$  complexes with bound Py,  $\text{PPh}_3$  and  $^t\text{BuNC}$ . All reactions were done at room temperature and did not require purification aside from precipitation of the material. Contrary to our labs work on the  $\text{PDC}^{\text{R}}\text{Pd}$  systems, the substitution of the ancillary ligand could not all be carried out in acetonitrile, as in some cases we observed reformation of the MeCN bound complex as evident by NMR spectroscopy. To form the pyridine bound complex,  $[\text{PDC}^{\text{R}}\text{Pd}(\text{MeCN})]2\text{PF}_6$  was simply dissolved in pyridine and stirred. Isolation of the material only required removal of the solvent and precipitation. A slight excess of  $^t\text{BuNC}$  was used to generate the isonitrile complex which was accomplished in dry MeCN and similarly only required removal of the solvent and precipitation. Likewise, an excess of  $\text{PPh}_3$  in DMF was used to generate the phosphine bound complex. As  $\text{PPh}_3$  is also a solid, after the precipitation we had a mixture of the product and unreacted phosphine. To separate the two, we were able to simply wash the crude solid with diethyl ether which dissolved the unreacted  $\text{PPh}_3$  and gave our desired product. With the targeted derivatives in hand we were then able to study the photophysical properties.

### **3.6 Photophysical Properties of $[\text{PhDC}^{\text{Et}}\text{Pd}(\text{X})]\text{PF}_6$ complexes**

#### **3.6.1 Solid State Absorbance of $[\text{PhDC}^{\text{Et}}\text{Pd}(\text{X})]\text{PF}_6$ complexes**

As we discovered that all of the  $[\text{PhDC}^{\text{Et}}\text{Pd}(\text{X})]\text{PF}_6$  complexes were non-emissive in solution we focused our efforts on studying the solid state photophysical properties. Films of the samples were prepared on quartz plates as described previously, however as we noted MeCN exchange of some of the new X ligands during the synthesis, solutions were prepared using mixtures of DCM and MeOH.

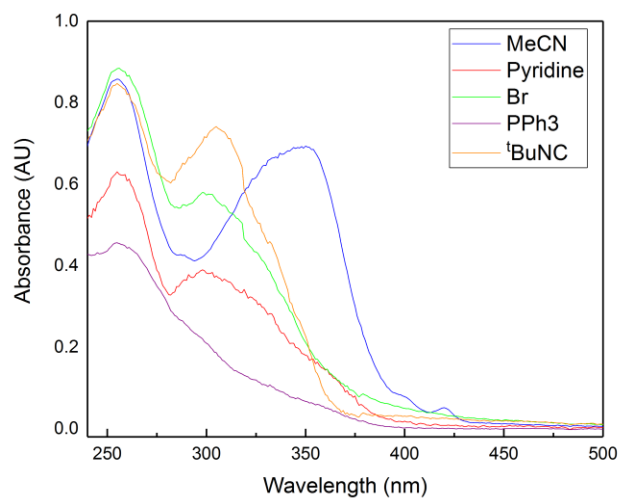


Figure 3.11: Solid state absorbance profiles of  $[\text{PhDC}^{\text{Et}}\text{Pd}(\text{X})]\text{PF}_6$  and  $[\text{PhDC}^{\text{Et}}\text{Pd}(\text{Br})]$  (green trace) complexes where X = MeCN (blue trace), pyridine (red trace), PPh<sub>3</sub> (purple trace), and <sup>t</sup>BuNC (yellow trace).

The solid state absorbance traces are shown in Figure 3.11 and show that all derivatives of the  $[\text{PhDCEtPd}(\text{X})](\text{Y})$  complexes display absorbance spectra with peak maxima near 250 nm. Further all spectra show that the complexes absorb very weakly past 400nm. With the exception of the PPh<sub>3</sub> derivative, the rest of the series show a second absorbance feature, near 300 nm for the Br, Py, and <sup>t</sup>BuNC complexes, and 350 nm for the MeCN complex. Interestingly, the PPh<sub>3</sub> complex only displays a single absorbance and very weak absorption past 375 nm. The MeCN complex shows a red shifted spectrum for the second absorption feature relative to the other X derivatives. As we knew the MeCN complex was blue light emissive, we next wanted to complete emission studies on the new complexes.

### 3.6.2 Solid State Emission of [PhDC<sup>Et</sup>Pd(X)]PF<sub>6</sub> complexes

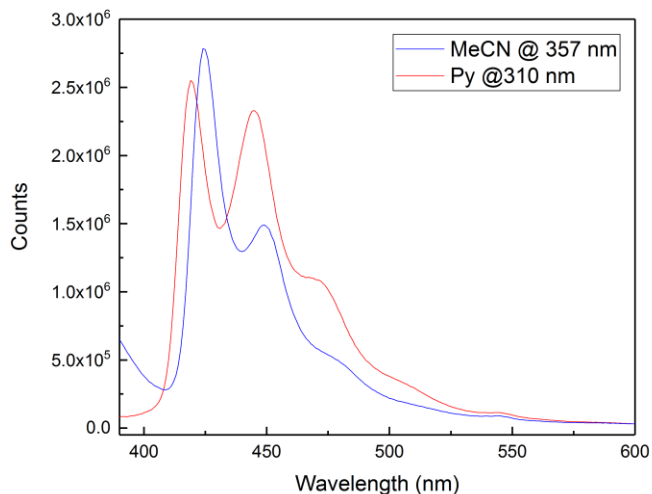


Figure 3.12: Solid state emission of [PhDC<sup>Et</sup>Pd(MeCN)]PF<sub>6</sub> (blue trace) and [PhDC<sup>Et</sup>Pd(Py)]PF<sub>6</sub> (red trace)

The PPh<sub>3</sub> and <sup>t</sup>BuNC complexes were found to be non-emissive in the solid state, however the pyridine complex also displayed blue emission with excitation at 310 nm. As shown in Figure 3.12, the emission spectrum of the pyridine complex (red trace) is quite similar to the MeCN complex (blue trace). The emission spectrum pyridine complex is slightly blue shifted relative to the MeCN complex with peak maxima near 420, and 450 nm with a small shoulder at 475 nm. Also, the emission spectrum for the pyridine derivative is slightly broader, showing greater emission past 470nm, when compared to the MeCN complex. As the pyridine bound complex was also emissive in the blue region, a corrected emission spectrum was obtained and gave CIE coordinates of (0.16, 0.13). This would place this complex nearly in an identical position to the MeCN complex on the chromaticity diagram shown in Figure 3.10,

although it is slightly toward the green region which is expected as the emission is more intense and broad toward the green region (>430 nm Figure 3.12). Intrigued by the fact that despite showing similar absorbance profiles and finding that only the MeCN and Py complexes were emissive, we decided to look at the solid-state structures to see if we observed any correlation.

### 3.7 Solid State Structures and Analysis

Single crystals of the Py, <sup>t</sup>BuNC, and PPh<sub>3</sub> complexes were obtained through vapor diffusion methods and diffraction experiments were carried out to obtain the solid-state structures.

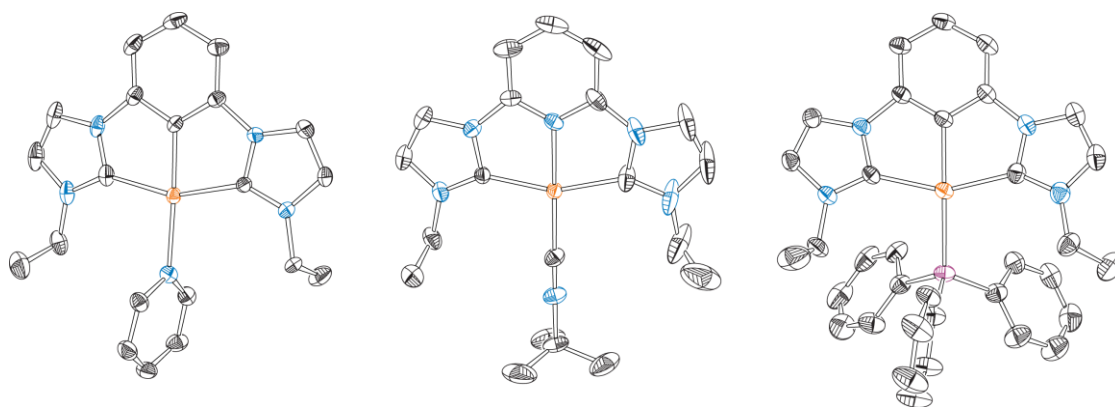


Figure 3.13: Solid state thermal ellipsoid plots for the  $[\text{PhDC}^{\text{Et}}\text{Pd}(\text{X})]\text{PF}_6$  derivatives, from left to right, Py, <sup>t</sup>BuNC, and PPh<sub>3</sub>. All structures are shown at the 50% probability level with hydrogens and a PF<sub>6</sub> counterion omitted for clarity.

The  $\text{PhDC}^{\text{Et}}\text{Pd}$  complexes of Py, <sup>t</sup>BuNC, and PPh<sub>3</sub> display pseudo square planar geometries, similar to the MeCN and Br derivatives, with C<sub>NHC</sub>–Pd–C<sub>NHC</sub> bond

angles ranging from 153 to 156 ° (Table 3.2). Across the entire series, the imidazole carbon to palladium ( $C_{\text{NHC}}\text{-Pd}$ ) distance is similar, near 2Å, with the distance becoming slightly longer with the bulky  $t\text{BuNC}$  and  $\text{PPh}_3$  ligands. It has been reported for a series  $\text{PhDC}^{\text{R}}\text{Pt}$  complexes that their bond lengths and angles varied according to the ligand field strength.<sup>63</sup> Table 3.2 is set up in the order of ligand field strength, from weakest to strongest donor, and unfortunately, we do not see the same correlation. However, what we can see from the crystal data is that the complexes deviate from the ideal square planar bond angle (180 °) according to the bulk of the X ligand. Br, MeCN, and Py (which coordinated orthogonal to the ligand plane, Figure 3.13) all show  $C_{\text{NHC}}\text{-Pd}-C_{\text{NHC}}$  bond angles near 156 °, as the bulk increases to  $t\text{BuNC}$  and  $\text{PPh}_3$  we see bond angles of 155 and 153 ° respectively. To further illustrate the effect of the bulky ligand on the coordination geometry, we can see that the  $C_{\text{Ph}}\text{-Pd-X}$  bond angle for the  $\text{PPh}_3$  complex is greatly altered compared to the rest of the series displaying an angle of 166 ° which is about a 10 ° difference compared to the other complexes.

<b>[PhDC<sup>Et</sup>Pd(X)] X =</b>	<b>Br</b>	<b>MeCN</b>	<b>Py</b>	<b>PPh<sub>3</sub></b>	<b><sup>t</sup>BuNC</b>
C <sub>NHC</sub> -Pd	2.053 Å	2.046 Å	2.054 Å	2.071 Å	2.062 Å
C <sub>NHC</sub> -Pd	2.054 Å	2.049 Å	2.062 Å	2.072 Å	2.064 Å
C <sub>Ph</sub> -Pd	1.949 Å	1.940 Å	1.947 Å	1.981 Å	1.970 Å
Pd-X	2.533 Å	2.092 Å	2.142 Å	2.387 Å	2.027 Å
C <sub>NHC</sub> -Pd-C <sub>NHC</sub>	156.08 °	156.97 °	156.46 °	153.73 °	155.25 °
C <sub>Ph</sub> -Pd-X	172.47 °	176.85 °	178.78 °	166.15 °	177.98 °
Ligand-Ligand	3.289 Å	3.413 Å	3.539 Å	3.459 Å	3.490 Å
Pd-Pd	4.024 Å	3.472 Å	5.169 Å	6.061 Å	5.055 Å

Table 3.2: Top: Selected bond lengths and angles for [PhDC<sup>Et</sup>Pd(X)] complexes, where the outer sphere counter ions (if present) are omitted from the formula and X denotes the ligand at the fourth coordination site which is either bromide (Br), acetonitrile (MeCN), pyridine (Py), tert-butyl isonitrile (<sup>t</sup>BuNC), or triphenylphosphine (PPh<sub>3</sub>). Bottom: Closest ligand-ligand and Pd-Pd distances found in the crystal packing. The blue text denotes the complexes which were found to be emissive.

It has been suggested that the emission of solid state materials can be altered by intermolecular interactions in the crystal lattice. Specifically, Pd and Pt complexes supported by PDC<sup>R</sup> and PhDC<sup>R</sup> ligands have shown emission dependence on the  $\pi$ - $\pi$ , and metal-metal interactions between neighboring complexes in the crystal packing.<sup>37,57,63</sup> These complexes pack on top of one another (in a head to tail fashion) with the X ligands in opposite direction. As our non-emissive X substituted complexes (PPh<sub>3</sub> and <sup>t</sup>BuNC) are considered bulky, we hypothesized that due to this bulk the complexes may not be close enough in the crystal packing to have significant  $\pi$ - $\pi$  and metal-metal interactions. To study this, we looked at the crystal packing from the diffraction experiments and the results are shown in the bottom portion of Table 3.2, where we focused on two distances, the Pd-Pd distance, and the closest distance found

between neighboring ligands. We discovered that the majority of our  $\text{PhDC}^{\text{R}}\text{Pd}$  complexes also crystallize in the same fashion (head to tail) with the exception of the Br complex.

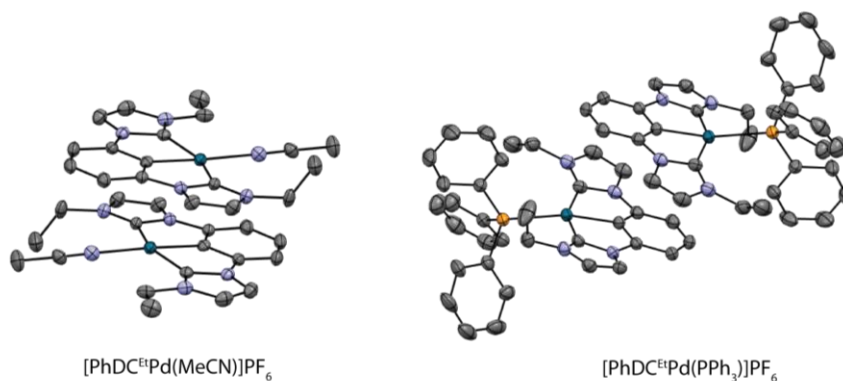


Figure 3.14: Thermal ellipsoid plots of the crystal packing of  $[\text{PhDC}^{\text{Et}}\text{Pd}(\text{MeCN})]\text{PF}_6$  (left) and  $[\text{PhDC}^{\text{Et}}\text{Pd}(\text{PPh}_3)]\text{PF}_6$  (right) complexes shown at the 30% probability level and hydrogens and  $\text{PF}_6$  counterions omitted for clarity.

Figure 3.14 shows the overlapping interactions found for the least bulky and most bulky X substituted complexes (MeCN and  $\text{PPh}_3$ ). First looking at the Pd–Pd distances we see that the MeCN shows the shortest distance of 3.472 Å and not surprisingly the  $\text{PPh}_3$  complex shows the longest, 6.061 Å (Table 3.2). The emissive Py complex shows a Pd–Pd distance of greater than 5 Å and is slightly longer than the non-emissive  $^t\text{BuNC}$  complex. Based on the Pd–Pd distance alone we cannot conclude that this is the reason the MeCN and Py complexes are emissive. Next, we decided to look at the closest ligand to ligand distance as this may be a good indicator of orbital overlap for  $\pi$ – $\pi$  interactions. All complexes, except for the Br derivative, show closest ligand distances near 3.5 Å. However, as shown in Figure 3.14, as the X ligand increases in steric bulk the complexes are pushed farther away from one another,

causing the complexes to translate farther away in opposite x directions. This can be observed in Figure 3.14 where we see N atom of the MeCN ligand is directly under the phenyl ring of the PhDC<sup>R</sup> ligand and the C2 carbon of the phenyl ring is above and between the N<sub>MeCN</sub>-Pd bond. As the X ligand is replaced with PPh<sub>3</sub> we see that the complexes have pushed away from one another where the C2 carbons on the phenyl ring are now nearly on top of one another. Despite this, all complexes show some overlap of the ligands and similar ligand to ligand distances. Unfortunately, we did not see a correlation between the crystal packing and the photophysical properties of the series of PhDC<sup>R</sup>Pd complexes.

While we were not able find a good correlation between photophysical properties and crystal packing, the crystal data did provide insight into the emissive properties of the complexes. As explained above, the non-radiative pathways are destabilized with the addition of strong sigma donors. Without significant overlap of the ligand and metal bonding orbitals, this destabilization effect would be minimized. Phenyl spaced terdentate ligands, such as the PhDC<sup>R</sup> system, crystallize in a pseudo square planar geometry, meaning that the C<sub>NHC</sub>-metal-C<sub>NHC</sub> bond angle deviates from 180 °, decreasing orbital overlap. However, the addition of strong donors to terdentate ligands, such as NHCs, has been shown to still provide significant destabilization of the non-radiative d-d states.<sup>27</sup> To explain the emissive properties of this series of complexes we first know that the PhDC<sup>Et</sup> ligand is capable of producing emissive palladium complexes as evident by the blue light emissive MeCN and Py derivatives. Next, we can consider the ligand field strength of the ancillary ligands, which are in order of weakest to strongest donating, Br<sup>-</sup> < MeCN < Py < PPh<sub>3</sub> < <sup>t</sup>BuNC. While more strongly donating ancillary ligands should also help to destabilize the d-d states,

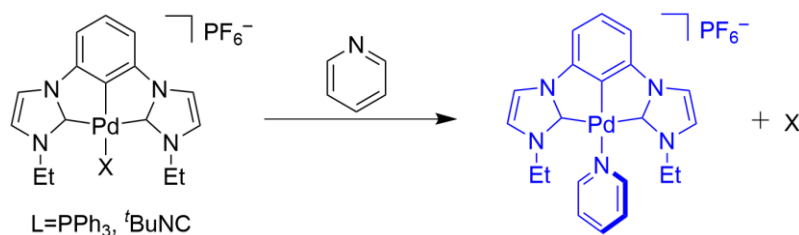
we do not observe emission from the stronger donating phosphine and isonitrile ligands. Where we can find a correlation between emissive properties and crystal data is in the  $C_{\text{NHC}}\text{-Pd-C}_{\text{NHC}}$  and  $C_{\text{Ph}}\text{-Pd-X}$  bond angles. As we see from these angles, as our ancillary ligands become bulkier we deviate further from the ideal  $180^\circ$  geometry of square planar complexes, approaching  $153^\circ$  for the  $\text{PPh}_3$  derivative for the  $C_{\text{NHC}}\text{-Pd-C}_{\text{NHC}}$  and  $166^\circ$  for the  $C_{\text{Ph}}\text{-Pd-X}$  bond angles. As we deviate further from  $180^\circ$  we can expect that orbital overlap will also decrease, which will then no longer destabilize the d-d states and provide non-radiative pathways for the complex. Thus, as a design property for emissive  $[\text{PhDC}^{\text{R}}\text{Pd}(\text{X})](\text{Y})$  complexes, we can conclude that the  $\text{PhDC}^{\text{R}}$  ligand is capable of producing room temperature emissive palladium complexes with strongly donating (X) ligands. However, careful choice of the (X) ligand must be considered, as the coordination of bulky ligands significantly alters the bonding geometry, leading to decreased orbital overlap and thus non-emissive complexes.

### **3.8 Vapochromic Behavior of $\text{PhDC}^{\text{Et}}\text{Pd}$ Complexes**

#### **3.8.1 Vapochromic Response to Pyridine**

It has been demonstrated that emissive transition metal complexes can display a vapochromic response to pyridine vapors and thus be useful in sensing applications.<sup>14,63</sup> Specifically the analogous  $[\text{PhDC}^{\text{R}}\text{Pt}(\text{X})](\text{Y})$  complexes showed vapochromic responses to pyridine vapors.<sup>63</sup> To further explore the capabilities of our palladium system we wanted to determine if these complexes also displayed a vapochromic response to pyridine, as our pyridine complex was blue light emissive. We decided to focus our studies on the non-emissive complexes ( $\text{tBuNC}$  and  $\text{PPh}_3$ ) as

these can be readily exchanged, evident through our synthetic study (*vide supra*). Further we hypothesized that due to the bulkiness of these ancillary ligands (described through single crystal analysis), there may be a driving force for ligand exchange. To probe if our material displayed a vapochromic response to pyridine, solid-state film samples of the <sup>t</sup>BuNC and PPh<sub>3</sub> derivatives were prepared on quartz slides, as previously described, and exposed to pyridine vapors. Scheme 3.4 shows the solid-state ligand exchange we would expect to occur during the exposure to pyridine vapors, where our non-emissive complexes become blue light emissive.



Scheme 3.4: Solid-state ligand exchange of non-emissive complexes to the emissive (Py) bound complex.

We initially probed this transformation with periodic excitation of the samples with a hand-held UV lamp. It was found that the PPh<sub>3</sub> complex was capable of this transformation and the <sup>t</sup>BuNC was not. To probe this transformation further, emission studies were performed with excitation of the starting material, [PhDC<sup>Et</sup>Pd(PPh<sub>3</sub>)]PF<sub>6</sub>, at 310 nm, the excitation wavelength at which the pyridine complex shows the greatest emission intensity. As we can see in Figure 3.15 excitation of the [PhDC<sup>Et</sup>Pd(PPh<sub>3</sub>)]PF<sub>6</sub> complex at 310 nm without exposure to pyridine vapors gave a

flat emission trace (bottom trace, black line). However, as pyridine vapors are introduced we begin to see emission of the complex and over time the emission intensity increases. After twenty minutes of exposure to the pyridine vapors we no longer see an increase in intensity of emission, suggesting that the solid-state exchange is complete.

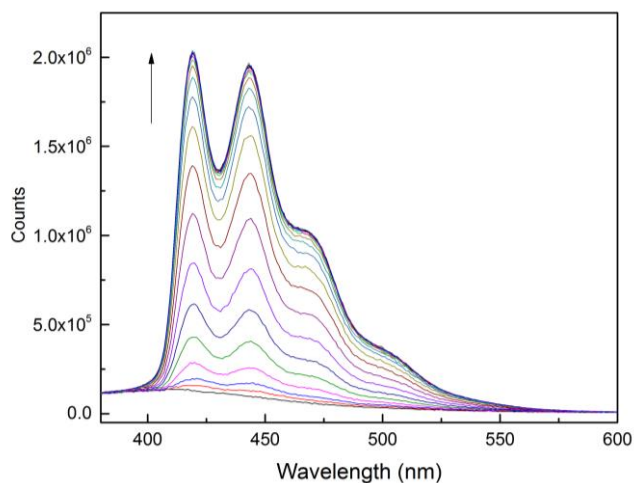


Figure 3.15: Emission studies of  $[\text{PhDC}^{\text{Et}}\text{Pd}(\text{PPh}_3)]\text{PF}_6$  exposed to pyridine vapors with excitation at 310 nm.

It has been suggested for the platinum analogs that instead of an exchange of the ligand trans to the  $\text{C}_{\text{Ph}}$  donor (Scheme 3.4), the vapochromic response may be due to coordination of pyridine to the  $d_z^2$  orbital, orthogonal to the ligand plane.<sup>63</sup> However based on our experiments we feel that we are indeed observing a solid-state exchange of the ancillary ligand. As stated above the emissive character is likely due to the strong ligand donors and destabilization of the d-d states. If both  $\text{PPh}_3$  and Py were bound at the same time the electronics of the system would be perturbed and the

emission profile would likely be different. Further if Py was bound at a large angle to the  $d_{x^2-y^2}$  orbital we may not observe emission as the orbital overlap would be weaker, thus causing decreased destabilization of the d-d states. The emission profile obtained during the experiment is identical to the emission profile of the synthesized Py derivative (Figures 3.15 and 3.12) suggesting the solid-state substitution of the ancillary ligand pathway is more likely. To further support this, we undertook X-ray photoelectron spectroscopy (XPS) experiments to observe any changes in the spectrum or shifts in binding energy between the materials.

### 3.8.2 X-ray Photoelectron Spectroscopy Studies

To study the solid-state exchange further we used XPS to probe the binding energy of three diagnostic regions, the phosphorus, palladium, and nitrogen regions. These regions were chosen as phosphorus regions should provide information about the coordination environment of the  $\text{PPh}_3$  ligand, similarly we chose the nitrogen region for the pyridine ligand. As these two ligands are bound to Pd we also decided to obtain data for the palladium region. High resolution spectra were obtained in the desired regions for the material collected after the solid-state reaction as well as  $\text{PPh}_3$ , and synthesized complexes:  $[\text{PhDC}^{\text{Et}}\text{Pd}(\text{PPh}_3)]\text{PF}_6$ , and  $[\text{PhDC}^{\text{Et}}\text{Pd}(\text{Py})]\text{PF}_6$  to serve as XPS standards.

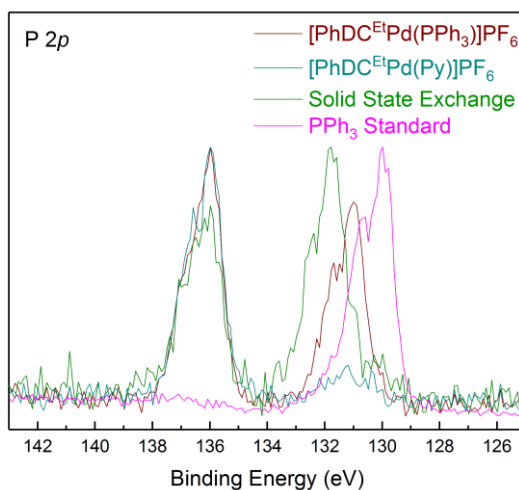


Figure 3.16: High resolution XPS spectra of the phosphorus region for the material obtained after the solid-state exchange reaction (green trace), synthesized  $[\text{PhDC}^{\text{Et}}\text{Pd}(\text{Py})]\text{PF}_6$  (blue trace), synthesized  $[\text{PhDC}^{\text{Et}}\text{Pd}(\text{PPh}_3)]\text{PF}_6$  (maroon trace), and  $\text{PPh}_3$  (pink trace)

As we can see in Figure 3.16 the high-resolution spectra obtained in the P 2p region for the  $[\text{PhDC}^{\text{Et}}\text{Pd}(\text{PPh}_3)]\text{PF}_6$  complex and material obtained from the exchange experiment both display two components near 136 eV and between 129–133 eV. From this data, we can assign the peak near 136 eV to the  $\text{PF}_6$  counterion as there is no deviation between all samples, as would be expected for an outer sphere counterion. Further, the  $[\text{PhDC}^{\text{Et}}\text{Pd}(\text{Py})]\text{PF}_6$  complex does not contain a second phosphorus component, also supporting the assignment of the  $\text{PF}_6$  peak. When looking at the data for the second component we see a clear shift in binding energy between the exchange material (green trace) and the  $[\text{PhDC}^{\text{Et}}\text{Pd}(\text{PPh}_3)]\text{PF}_6$  (maroon trace) suggesting a change in the coordination environment. To see if this data correlated to unbound  $\text{PPh}_3$ , we also obtained the XPS spectrum of reagent grade  $\text{PPh}_3$ . As shown

in Figure 3.16 the unbound  $\text{PPh}_3$  shows a lower binding energy value compared to the complexes. While the data in the phosphorus regions is inconclusive for a solid-state exchange, it does demonstrate that the  $\text{PPh}_3$  is either in a different coordination environment, or not coordinated at all which supports both theories.

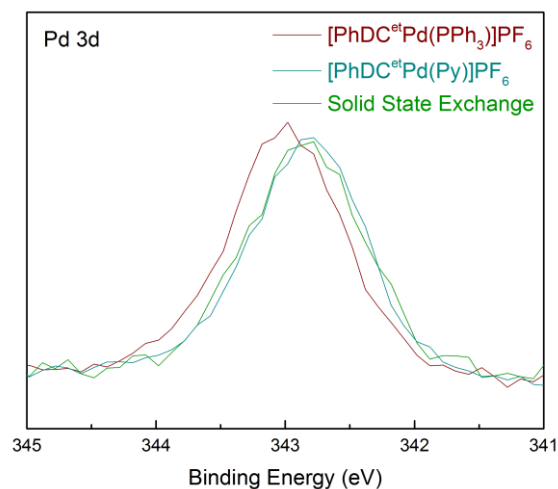


Figure 3.17: High resolution XPS spectra of the palladium region for the material obtained after the solid-state exchange reaction (green trace), synthesized  $[\text{PhDC}^{\text{Et}}\text{Pd}(\text{Py})]\text{PF}_6$  (blue trace), synthesized  $[\text{PhDC}^{\text{Et}}\text{Pd}(\text{PPh}_3)]\text{PF}_6$  (maroon trace).

The high-resolution spectra obtained in the Pd 3d region displayed the expected doublet with binding energies near 343, and 338 eV. Both peaks displayed the same shifts in binding energy for the complexes thus for clarity Figure 3.17 displays the spectra obtained near 343 eV. Comparing the synthesized  $[\text{PhDC}^{\text{Et}}\text{Pd}(\text{Py})]\text{PF}_6$  (blue trace) and synthesized  $[\text{PhDC}^{\text{Et}}\text{Pd}(\text{PPh}_3)]\text{PF}_6$  (maroon trace), we can observe a clear shift in binding energy of palladium attributed to the two

different ligands. Looking at the spectrum obtained for the exchange material (green trace) we can see that it overlays very well with the synthesized  $[\text{PhDC}^{\text{Et}}\text{Pd}(\text{Py})]\text{PF}_6$  complex, suggesting that pyridine is indeed bound to palladium and likely in the same coordination environment.

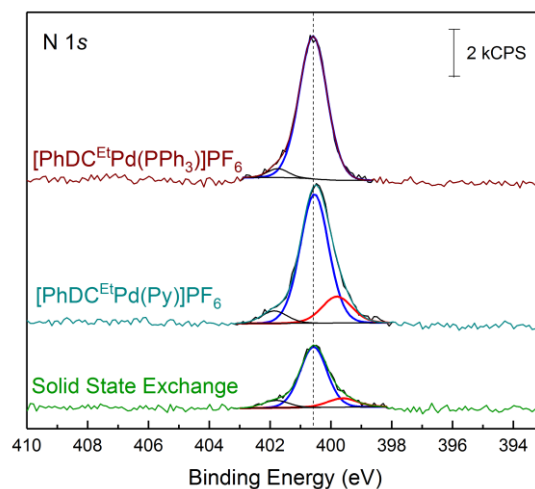


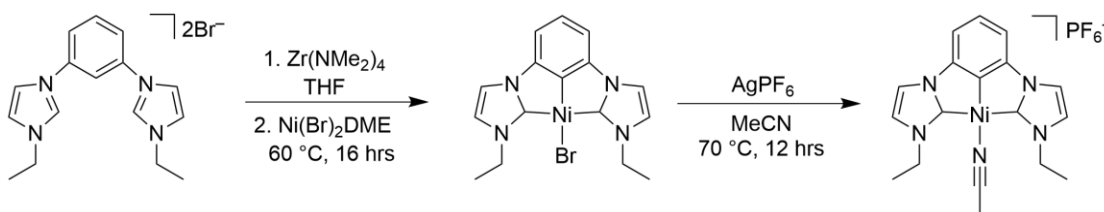
Figure 3.18: High resolution XPS spectra of the nitrogen region for the material obtained after the solid-state exchange reaction (green trace), synthesized  $[\text{PhDC}^{\text{Et}}\text{Pd}(\text{Py})]\text{PF}_6$  (blue trace), synthesized  $[\text{PhDC}^{\text{Et}}\text{Pd}(\text{PPh}_3)]\text{PF}_6$  (maroon trace).

Lastly, we obtained the high-resolution spectra for the materials in the N 1s region. Comparing the two synthesized complexes we can see that the nitrogen region is slightly more complex and required the fitting of multiple nitrogen components. Both complexes showed two components near 400 and 402 eV and the  $[\text{PhDC}^{\text{Et}}\text{Pd}(\text{Py})]\text{PF}_6$  complex displayed a third component near 399 eV. Comparing the two we can assign the peak near 399 eV to the nitrogen from the bound pyridine

ligand as it is absent in the spectrum of the  $\text{PPh}_3$  analog. Comparing these spectra to the spectrum obtained for the material collected after the solid-state exchange reaction, we can clearly see the appearance of the assigned third nitrogen component (near 399 eV). This result also suggests that pyridine is likely in the same coordination environment as the synthesized  $[\text{PhDC}^{\text{Et}}\text{Pd}(\text{Py})]\text{PF}_6$  complex. The XPS results, along with the emission studies, together suggest that this material undergoes a solid-state exchange of the ancillary ligand.

### 3.9 Synthesis of $\text{PhDC}^{\text{Et}}\text{Ni}$ Complexes

Due to the success with the PhDC palladium complexes we became interested in studying the nickel analog. Further, nickel complexes supported by PhDC ligands have also been unexplored, and of the group 10 metals nickel is the least expensive.



Scheme 3.5: Synthesis of  $[\text{PhDC}^{\text{Et}}\text{Ni}(\text{Br})]$  and  $[\text{PhDC}^{\text{Et}}\text{Ni}(\text{MeCN})]\text{PF}_6$

Utilizing the same strategy and methods as described above for the palladium analogs, we found that the nickel halide complex could be synthesized in a one pot, two-step process with initial formation of a  $\text{PhDC}^{\text{Et}}$  zirconium intermediate followed by transmetalation with  $\text{Ni}(\text{Br})_2\text{DME}$  (Scheme 3.5). As the acetonitrile bound palladium complex was found to be highly emissive, we also wanted to synthesize the

analogous nickel complex. This was easily accomplished in high yield using  $\text{AgPF}_6$  in acetonitrile with identical reaction conditions to the palladium synthesis (Scheme 3.5). We were also successful in obtaining single crystals of both complexes and diffraction experiments were carried out to determine the solid-state structures.

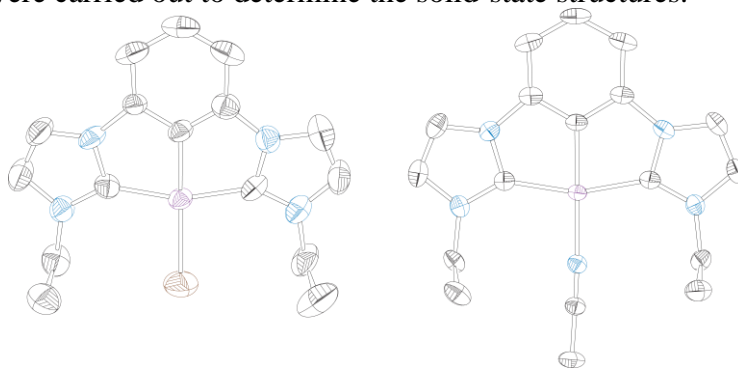


Figure 3.19: Thermal ellipsoid plots of the solid-state structure of  $[\text{PhDC}^{\text{Et}}\text{Ni}(\text{Br})]$  (left) and  $[\text{PhDC}^{\text{Et}}\text{Ni}(\text{MeCN})]\text{PF}_6$  (right) displayed at the 50% probability level with hydrogens and outer sphere counterions omitted (if present) for clarity.

Figure 3.19 displays the solid-state structures obtained from the diffraction experiments and Table 3.3 gives selected bond lengths and angles, full bond lengths and angles along with the experimental parameters can be found in the appendix. Similar to the palladium analogs the nickel complexes display a pseudo square planar geometry with a  $\text{C}_{\text{NHC}}\text{-Ni-C}_{\text{NHC}}$  bond angle near  $160^\circ$  and a  $\text{C}_{\text{Ph}}\text{-Ni-X}$  bond angles of  $172.25^\circ$  and  $177.84^\circ$  where  $\text{X} = \text{Br}$  and  $\text{MeCN}$  respectively. While our lab had not previously made the PDC analogs solid-state structures have been reported for the PDC nickel complexes with methyl groups on the wingtip ( $[\text{PDC}^{\text{Me}}\text{Ni}(\text{Br})]\text{Br}$  and  $[\text{PDC}^{\text{Me}}\text{Ni}(\text{MeCN})]_2(\text{OTf})$ ) which allowed for comparison.<sup>64-65</sup> Similar to the palladium series the  $\text{C}_{\text{NHC}}\text{-Pd}$  bonds are slightly longer for the PhDC complexes when compared to the PDC analogs. Similarly, we can see evidence of the trans influence

through the increased bond length of both the X ligands (Br and MeCN) for the PhDC nickel complexes owing to the strong anionic C<sub>Ph</sub> donor compared to the neutral N<sub>Py</sub> donor.

	<b>PDC<sup>Me</sup>Ni(Br)</b>	<b>PhDC<sup>Et</sup>Ni(Br)</b>	<b>PDC<sup>Me</sup>Ni(MeCN)</b>	<b>PhDC<sup>Et</sup>Ni(MeCN)</b>
C <sub>NHC</sub> -Pd	1.920 Å	1.966 Å	1.912 Å	1.937 Å
C <sub>NHC</sub> -Pd	1.932 Å	1.960 Å	1.921 Å	1.936 Å
N <sub>Py</sub> or C <sub>Ph</sub> -Pd	1.861 Å	1.863 Å	1.851 Å	1.857 Å
Pd-X	2.278 Å	2.327 Å	1.840 Å	1.906 Å
C <sub>NHC</sub> -Pd-C <sub>NHC</sub>	163.04 °	160.35 °	163.15 °	160.05 °
N <sub>Py</sub> or C <sub>Ph</sub> -Pd-X	176.35 °	172.25 °	176.60 °	177.84 °

Table 3.3: Selected bond lengths and angles for the [PDC<sup>Me</sup>Ni(Br)]Br, [PDC<sup>Me</sup>Ni(MeCN)]<sub>2</sub>(OTf), [PhDC<sup>Et</sup>Ni(Br)] and [PhDC<sup>Et</sup>Ni(MeCN)]PF<sub>6</sub> complexes, where X denotes the ligand at the fourth coordination site which is either Br or MeCN and the outer sphere counterions are omitted in the table formula.

Upon completion of the diffraction studies we then wanted to determine if the PhDCEtNi complexes were also emissive. Unfortunately, we found that both complexes were non-emissive in both the solution and solid-state. This can be attributed to the fact that the ligand field d-d splitting decreases as you go up the group on the periodic table, thus for nickel it would be smaller compared to palladium and platinum. Due to this, the non-radiative d-d states would then be accessible causing the nickel complex to be non-emissive. Likewise, the lack of emission of nickel complexes compared to palladium and platinum has also been reported for a series of group 10 complexes supported by bis-NHC tetradentate ligands.<sup>43</sup>

### 3.10 Concluding Remarks

A series of palladium and nickel complexes supported by phenyl spaced dicarbene ligands were synthesized with varying ancillary ligands (Br, MeCN, Py, PPh<sub>3</sub> and <sup>t</sup>BuNC). We discovered that the metalation of these ligands could be accomplished using a one pot, two-step transmetallation strategy with initial formation of a zirconium intermediate, followed by addition of a palladium or nickel source yielding the halide complex. This ancillary ligand was efficiently substituted to the MeCN, Py, PPh<sub>3</sub>, and <sup>t</sup>BuNC complexes under mild conditions and only requiring a precipitation for purification. Analysis of the solid-state structures revealed evidence of the trans influence by the anionic C<sub>Ph</sub> donor when compared to the neutral N<sub>Py</sub> donor of analogous pyridine spaced systems. We discovered that the MeCN and Py bound complexes are emissive at room temperature in the solid-state giving CIE coordinates of (0.16, 0.12) and (0.16, 0.13) respectively, making them the deepest blue emitting palladium complexes to date. Further, we demonstrated that the PPh<sub>3</sub> complex displays a vapochromic response to pyridine vapors making it a candidate for sensor applications. Lastly, while we successfully demonstrated the synthesis of the nickel complexes we found that they were non-emissive, likely due to non-radiative decay from d-d states.

## REFERENCES

- (1) Kalyanasundaram, K.; Grätzel, M. *Coord. Chem. Rev.* **1998**, *177*, 347.
- (2) Polo, A. S.; Itokazu, M. K.; Iha, N. Y. M. *Coord. Chem. Rev.* **2004**, *248*, 1343.
- (3) Prier, C. K.; Rankic, D. A.; MacMillan, D. W. C. *Chem. Rev.* **2013**, *113*, 5322.
- (4) Esswein, A. J.; Nocera, D. G. *Chem. Rev.* **2007**, *107*, 4022.
- (5) Dolmans, D. E. J. G. J.; Fukumura, D.; Jain, R. K. *Nature Reviews Cancer*, **2003**, *3*, 380.
- (6) Shao, Q.; Xing, B. *Chem. Soc. Rev.* **2010**, *39*, 2835.
- (7) Dini, D.; Calvete, M. J. F.; Hanack, M. *Chem. Rev.* **2016**, *116*, 13040.
- (8) Tutt, L. W.; Boggess, T. F. *Prog. Quant. Electr.* **1993**, *17*, 299.
- (9) Choy, W. C. H.; Chan, W. K.; Yuan, Y. *Adv. Mater.* **2014**, *26*, 5368.
- (10) Yersin, H.; Rausch, A. F.; Czerwieniec, R.; Hofbeck, T.; Fischer, T. *Coord. Chem. Rev.* **2011**, *255*, 2622.
- (11) Demas, J. N.; DeGraff, B. A. *Coord. Chem. Rev.* **2001**, *211*, 317.
- (12) Meier, R. M.; Hanusa, T. P. "Symmetry and Steric Effects on Spin States in Transition Metal Complexes." *Encyclopedia of Inorganic Chemistry* **2011**
- (13) Xu, H.; Chen, R.; Sun, Q.; Lai, W.; Su, Q.; Huang, W.; Liu, X. *Chem. Soc. Rev.* **2014**, *43*, 3259.
- (14) Elosa, C.; Bariain, C.; Matias, I. R.; Rodriguez, A.; Colacio, E.; Salinas-Castillo, A.; Segura-Carretero, A.; Fernandez-Gutierrez, A.; *Sensors*. **2008**, *8*, 847.
- (15) Kalyani, N. T.; Dhoble, S. J. *Renewable and Sustainable Energy Reviews* **2012**, *16*, 2696.
- (16) Grassmann, H. G. *Ann. Phys. Chem.* **1853**, *19*, 53.

- 
- (17) Malacara, D. "Color Vision and Colorimetry: Theory and Applications" 2<sup>nd</sup> Ed. 2011 SPIE, Washington
- (18) CIE, *Proc. 1931 Commission Internationale de l'Éclairage* **1932**, Cambridge University Press, Cambridge, U. K.
- (19) Lakowicz, J. R. "Principles of Fluorescence Spectroscopy" 3<sup>rd</sup> Ed. **2006**, Springer
- (20) Glynn II, E. F. efg's Computer Lab, <http://www.efg2.com/> (accessed July 2014)
- (21) Baldo, M. A.; O'Brien, D. F.; You, Y.; Shoustikov, A.; Sibley, S.; Thompson, M. E.; Forrest, S. R. *Nature*. **1998**, *395*, 151.
- (22) Baldo, M. A.; Lamansky, S.; Burrows, P. E.; Thompson, M. E.; Forrest, S. R. *Appl. Phys. Lett.* **1999**, *75*, 4.
- (23) Lee, J.; Chen, H.; Batagoda, T.; Coburn, C.; Djurovich, P. I.; Thompson, M. E.; Forrest, S. R. *Nature Materials*. **2016**, *15*, 92.
- (24) Rausch, A. F.; Homeier, H. H. H.; Yersin, H. *Top. Organomet. Chem.* **2010**, *29*, 193.
- (25) Andrews, L. J.; *J. Phys. Chem.* **1979**, *83*, 3203.
- (26) Chi, Y.; Chou, P-T. *Chem Soc. Rev.* **2010**, *39*, 638.
- (27) Visbal, R.; Gimeno, C. *Chem. Soc. Rev.* **2014**, *43*, 3551.
- (28) E. Peris, J.A. Loch, J. Mata, R.H. Crabtree, *Chem. Commun.* **2001**, 201.
- (29) J. A. Loch, M. Albrecht, E. Peris, J. Mata, J.W. Faller, R.H. Crabtree, *Organometallics* **2002**, *21*, 700
- (30) N. Selander, K.J. Szabó, *Chem.Rev.* **2011**, *11*, 2048.
- (31) Mercs, L.; Albrecht, M. *Chem. Soc. Rev.* **2010**, *39*, 1903.
- (32) Díez-González, S.; Marion, N.; Nolan, S. P. *Chem. Rev.* **2009**, *109*, 3612.

- 
- (33) Farrell, K.; Albrecht, M. in *The Privileged Pincer-Metal Platform: Coordination Chemistry & Applications*, ed. Van Koten, G.; Gossage, A. R. Springer International Publishing, Cham, 2016, 45–91
- (34) Hopkins, M. N.; Richter, C.; Schedler, M.; Glorius, F. *Nature* **2014**, *510*, 485.
- (35) Magee, K. D. M.; Wright, P. J.; Muzzioli, S.; Siedlovska, C. M.; Raiteri, P.; Baker, M. V.; Brown, D. H.; Tagni, S.; Massi, M. *Dalton Trans.* **2013**, *42*, 4233.
- (36) Li, K.; Chen, Y.; Lu, W.; Che, Z.; Che, C.-M. *Chem. Eur. J.* **2011**, *17*, 4109.
- (37) Lee, C.-S.; Sabiah, S.; Wang, J.-C.; Hwang, W.-S.; Lin, I. J. B. *Organometallics* **2010**, *29*, 286.
- (38) Leung, S. Y.-L.; Lam, S.-H.; Lam, W. H.; Wong, K. M.-C.; Wong, W.-T.; Yam, V. W.-W. *Chem. Eur. J.* **2013**, *19*, 10360.
- (39) Zhang, X.; Wright, A. M.; De Yonker, N. J.; Kollis, T. K.; Hammer, N. I.; Webster, C. E.; Valente, E. J. *Organometallics* **2012**, *31*, 1664.
- (40) Hollis, T. K.; Zhang, X. PCT Int. Appl. **2011**, WO 2011050003 A2 20110428
- (41) Zhang, X.; Cao, B.; Valente, E. J.; Hollis, T. K. *Organometallics* **2013**, *32*, 752.
- (42) Huckaba, A. J.; Cao, B.; Hollis, T. K.; Valle, H. U.; Kelly, J. T.; Hammer, N. I.; Oliver, A. G.; Webster, C. E. *Dalton Trans.* **2013**, *42*, 1216.
- (43) Li, K.; Cheng, G.; Ma, C.; Guan, X.; Kwok, W.-M.; Chen, Y.; Lu, W.; Che, C.-M. *Chem. Sci.* **2013**, *4*, 2630.
- (44) Chow, P.-K.; To, W.-P.; Low, K.-H.; Che, C.-M. *Chem. Asian J.* **2014**, *9*, 534.
- (45) Chow, P.-K.; Cheng, G.; Tong, G. S. M.; Ma, C.; Kwok, W.-M.; Ang, W.-H.; Chung, C. Y.-S.; Yang, C.; Wang, F.; Che, C.-M. *Chem. Sci.* **2016**, *7*, 6083.
- (46) Henwood, A. F.; Lesieur, M.; Bansal, A. K.; Lemaur, V.; Beljonne, D.; Thompson, D. G.; Graham, D.; Slawin, A. M. Z.; Samuel, I. D. W.; Cazin, C. S. J.; Colman, E. Z. *Chem. Sci.* **2015**, *6*, 3248.

- 
- (47) Ariyananda, P. W. G.; Yap, G. P. A.; Rosenthal, J. *Dalton Trans.* **2012**, *41*, 7977.
- (48) Gruendemann, S.; Albrecht, M.; Loch, J. A.; Faller, J. W.; Crabtree, R. H. *Organometallics*, **2001**, *20*, 5485.
- (49) Cárdenas, D. J.; Echavarren, A. M.; Ramírez de Arellano, M. C. *Organometallics*. **1999**, *18*, 3337.
- (50) Vargas, V. C.; Rubio, R. J.; Hollis, T. K.; Salcido, M. E. *Org. Lett.* **2003**, *5*, 4847.
- (51) Ebner, D. C.; Trend, R. M.; Genet, C.; McGrath, M. J.; O'Brien, P.; Stoltz, B. M. *Angew. Chem. Int. Ed.* **2008**, *47*, 6367.
- (52) Guardino, E. Effects of Different Ligands on the Binding of a Palladium Center in a Pyridyl Spaced Dicarbene. M. S. Thesis, University of Delaware, 2012
- (53) Clark, Wesley D.; Cho, Joon; Valle, Henry U.; Hollis, T. Keith; Valente, Edward J. *Journal of Organometallic Chemistry.* **2014**, *751*, 534.
- (54) Danopoulos, Andreas, A.; Tulloch, Arran, A. D.; Winston, Scott.; Eastham, Graham.; Hurstnouse, Michael, B. *Dalton Trans.* **2003**, *5*, 1009.
- (55) Jia, Y.-X.; Yang, X.-Y.; Tay, W. S.; Li, Y.; Pullarkat, S. A.; Xu, K.; Hirao, H.; Leung, P.-H. *Dalton Trans.* **2016**, *45*, 2095.
- (56) Therrien, Jeffery A.; Wolf, Michael O.; Patrick, Brian O. *Inorg. Chem.* **2014**, *53*, 12962.
- (57) Hung, F.-F.; Wu, S.-X.; To, W.-P.; Kwong, W.-L.; Guan, X.; Lu, W.; Low, K.-H.; Che, C.-M. *Chem. Asian J.* **2017**, *12*, 145.
- (58) Inés, B.; SanMartin, R.; Moure, M. J.; Domínguez, E. *Adv. Synth. Catal.* **2009**, *351*, 2124.
- (59) Tu, T.; Bao, X.; Assenmacher, W.; Peterlik, H.; Daniels, J.; Dötz, K. H. *Chem. Eur. J.* **2009**, *15*, 1853.
- (60) Giebink, N. C.; D'Andrade, B. W.; Weaver, M. S.; Mackenzie, P. B.; Brown J. J.; Thompson, M. E.; Forrest, S. R. *J. Appl. Phys.* **2008**, *103*, 044509.

- 
- (61) The software, FelixGX, was provided with our fluorimeter from PTI/Horiba
- (62) Fu, H.; Cheng, Y.-M.; Chou, P.-T.; Chi, Y. *Materials Today* **2011**, *14*, 472.
- (63) Lin, W.-J.; Naziruddin, A. R.; Chen, Y.-H.; Sun, B.-J.; Chang, A. H. H.; Wang, W.-J.; Hwang, W.-S. *Chem. Asian. J.* **2015**, *10*, 728.
- (64) Inamoto, K.; Kuroda, J.; Hiroya, K.; Noda, Y.; Watanabe, M.; Sakamoto, T. *Organometallics*. **2006**, *25*, 3095.
- (65) Sheng, M.; Jiang, N.; Gustafson, S.; You, B.; Ess, D. E.; Sun, Y. *Dalton Trans.* **2015**, *44*, 16247.

## Appendix A

### CRYSTALLOGRAPHIC DATA FOR PDC COMPLEXES

#### A.1 General Numbering Scheme for Solid State Structures of PDC Complexes

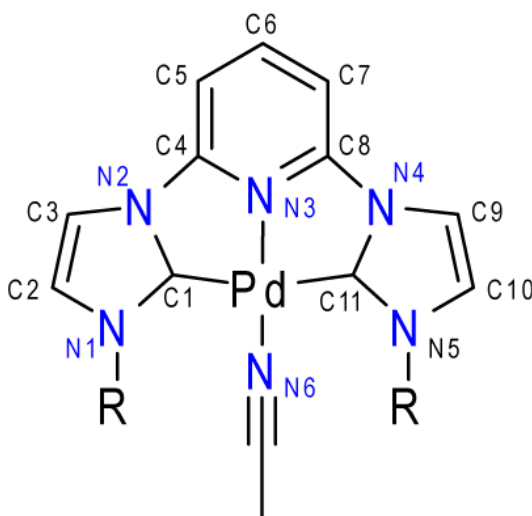


Figure A.1: General numbering scheme used to label the solid-state structures, except for the Mes and Dipp derivative, which contained mirror planes down the center of the complexes in which case C1=C11, N1=N5, C2=C10, C3=C9, N2=N4, etc.

#### A.2 Crystallographic Experimental Data

##### A.2.1 Crystallographic Experimental Data for PDC<sup>Cy</sup>Pd Intermediates

	<b>[PDC<sup>Cy</sup>Pd(Br)<sub>3</sub>]</b>	<b>[PDC<sup>Cy</sup>Ag(Br)]</b>
<b>Formula</b>	C25 H32 Br3 N6 Pd	C46 H58 Ag3 Br3 N10
<b>Fw</b>	762.69	1314.36
<b>Crystal System</b>	Monoclinic	Triclinic
<b>Space Group</b>	P2(1)/n	P-1
<b>a</b>	14.5947(3) Å	15.4629(15) Å
<b>b</b>	14.0590(3) Å	17.3278(16) Å
<b>c</b>	15.2499(3) Å	24.512(2) Å
<b>α</b>	90°	95.109(2) °
<b>β</b>	113.8770(10) °	99.388(2) °
<b>γ</b>	90°	103.836(2) °
<b>V</b>	2861.28(10) Å <sup>3</sup>	6235.2(10) Å <sup>3</sup>
<b>Z</b>	4	4
<b>Temp</b>	200(2) K	200(2) K
<b>D<sub>calcd</sub></b>	1.771 Mg/cm <sup>3</sup>	1.440 Mg/cm <sup>3</sup>
<b>2θ range</b>	7.076 to 147.762 °	3.156 to 52.746 °
<b>μ</b>	10.332 mm <sup>-1</sup> (Cu Kα)	2.889 mm <sup>-1</sup> (Mo Kα)
<b>Relections</b>	57118	75671
<b>Unique</b>	5636	25526
<b>R (int)</b>	0.0685	0.0697
<b>R<sub>1</sub></b>	0.0566	0.0511
<b>wR<sub>2</sub></b>	0.1496	0.1129

Table A.1: Crystallographic experimental data for PDC<sup>Cy</sup>Pd intermediates

### A.2.2 Crystallographic Experimental Data for [PDC<sup>R</sup>Pd(Br)]Br Complexes

<b>R</b>	<b>Et</b>	<b>Cy</b>	<b>Dipp</b>
<b>Formula</b>	C15 H17 Br2 N5 Pd	C25 H31 Br2 Cl6 N5 Pd	C36 H42 Br2 Cl3 N5 Pd
<b>Fw</b>	533.55	880.47	917.31
<b>Crystal System</b>	Triclinic	Triclinic	Triclinic
<b>Space Group</b>	P-1	P-1	P-1
<b>a</b>	7.6190(16) Å	11.5177(7) Å	8.553(2) Å

<b>b</b>	10.166(2) Å	12.8917(7) Å	12.010(3) Å
<b>c</b>	23.992(5) Å	13.6072(8) Å	21.289(5) Å
<b>α</b>	85.431(4) °	108.6040(10) °	74.753(3) °
<b>β</b>	82.199(4) °	93.3470(10) °	83.179(4) °
<b>γ</b>	70.301(4) °	115.7330(10) °	71.365(4) °
<b>V</b>	1732.3 (6) Å <sup>3</sup>	1678.46(17) Å <sup>3</sup>	1997.8(8) Å <sup>3</sup>
<b>Z</b>	4	2	2
<b>Temp</b>	200(2) K	200(2) K	200(2) K
<b>D<sub>calcd</sub></b>	2.046 Mg/cm <sup>3</sup>	1.742 Mg/cm <sup>3</sup>	1.525 Mg/cm <sup>3</sup>
<b>2θ range</b>	1.714 to 55.068 °	3.796 to 55.132 °	3.968 to 55.734 °
<b>μ (Mo Kα)</b>	5.690 mm <sup>-1</sup>	3.436 mm <sup>-1</sup>	2.696 mm <sup>-1</sup>
<b>Relections</b>	46042	22392	24166
<b>Unique</b>	7954	7732	9194
<b>R (int)</b>	0.1411	0.0135	0.0513
<b>R<sub>1</sub></b>	0.0832	0.0336	0.0708
<b>wR<sub>2</sub></b>	0.1829	0.0912	0.2037

Table A.2: Crystallographic experimental data for [PDC<sup>R</sup>Pd(Br)]Br complexes

### A.2.3 Crystallographic Experimental Data for [PDC<sup>R</sup>Pd(MeCN)](PF<sub>6</sub>)<sub>2</sub> Complexes Where R = Me, Et, Ipr

<b>R</b>	<b>Me</b>	<b>Et</b>	<b>Ipr</b>
<b>Formula</b>	C15 H16 F12 N6 P2 Pd	C17 H20 F12 N6 P2 Pd	C21 H27 F12 N7 P2 Pd
<b>Fw</b>	676.68	704.73	773.83
<b>Crystal System</b>	Triclinic	Triclinic	Triclinic
<b>Space Group</b>	P-1	P-1	P-1
<b>a</b>	9.028(4) Å	7.395(2) Å	9.058(2) Å
<b>b</b>	9.907(5) Å	8.526(3) Å	12.639(3) Å
<b>c</b>	13.454(6) Å	20.825(7) Å	14.277(4) Å
<b>α</b>	80.986(7) °	94.377(5) °	109.917(3) °
<b>β</b>	74.254(6) °	99.921(4) °	107.262(4) °
<b>γ</b>	79.486(7) °	106.826(4) °	92.610(4) °
<b>V</b>	1131.4(9) Å <sup>3</sup>	1226.9(7) Å <sup>3</sup>	1447.7(6) Å <sup>3</sup>

<b>Z</b>	2	2	2
<b>Temp</b>	346(2) K	200(2) K	200(2) K
<b>D<sub>calcd</sub></b>	1.986 Mg/cm <sup>3</sup>	1.908 Mg/cm <sup>3</sup>	1.775 Mg/cm <sup>3</sup>
<b>2θ range</b>	4.208 to 56.590 °	4.008 to 56.576 °	3.474 to 56.524 °
<b>μ (Mo Kα)</b>	1.078 mm <sup>-1</sup>	0.998 mm <sup>-1</sup>	0.856 mm <sup>-1</sup>
<b>Relections</b>	15538	12703	19867
<b>Unique</b>	5592	6050	7132
<b>R (int)</b>	0.0316	0.0201	0.0346
<b>R<sub>1</sub></b>	0.0494	0.0396	0.0378
<b>wR<sub>2</sub></b>	0.1343	0.1107	0.0876

Table A.3: Crystallographic experimental data for [PDC<sup>R</sup>Pd(MeCN)](PF<sub>6</sub>)<sub>2</sub> complexes where R = Me, Et, Ipr

#### A.2.4 Crystallographic Experimental Data for [PDC<sup>R</sup>Pd(MeCN)](PF<sub>6</sub>)<sub>2</sub> Complexes Where R = Cy, Mes, Dipp

<b>R</b>	<b>Cy</b>	<b>Mes</b>	<b>Dipp</b>
<b>Formula</b>	C25 H32 F12 N6 P2 Pd	C31 H32 F12 N6 P2 Pd	C37 H44 F12 N6 P2 Pd
<b>Fw</b>	812.90	884.96	969.12
<b>Crystal System</b>	Monoclinic	Orthorhombic	Orthorhombic
<b>Space Group</b>	P2(1)/c	Pnma	Pbcn
<b>a</b>	18.453(10) Å	8.6078(16) Å	19.9269(12) Å
<b>b</b>	13.196(7) Å	22.320(4) Å	13.6058(8) Å
<b>c</b>	12.654(7) Å	23.264(4) Å	15.6797(10) Å
<b>α</b>	90 °	90 °	90 °
<b>β</b>	90.406(7) °	90 °	90 °
<b>γ</b>	90 °	90 °	90 °
<b>V</b>	3081(3) Å <sup>3</sup>	4469.6(14) Å <sup>3</sup>	4251.1(4) Å <sup>3</sup>
<b>Z</b>	4	4	4
<b>Temp</b>	200(2) K	200(2) K	200(2) K

<b>D<sub>calcd</sub></b>	1.752 Mg/cm <sup>3</sup>	1.315 Mg/cm <sup>3</sup>	1.514 Mg/cm <sup>3</sup>
<b>2θ range</b>	2.206 to 56.646 °	3.502 to 56.692 °	3.624 to 55.016 °
<b>μ (Mo Kα)</b>	0.808 mm <sup>-1</sup>	0.563 mm <sup>-1</sup>	0.599 mm <sup>-1</sup>
<b>Relections</b>	35509	53909	53742
<b>Unique</b>	7668	5675	4888
<b>R (int)</b>	0.0232	0.0598	0.0496
<b>R<sub>1</sub></b>	0.0323	0.0913	0.0696
<b>wR<sub>2</sub></b>	0.0940	0.2704	0.2205

Table A.4 Crystallographic experimental data for [PDC<sup>R</sup>Pd(MeCN)](PF<sub>6</sub>)<sub>2</sub> complexes where R = Cy, Mes, Dipp

### A.3 [PDC<sup>Cy</sup>Pd(Br)<sub>3</sub>] Crystal Data

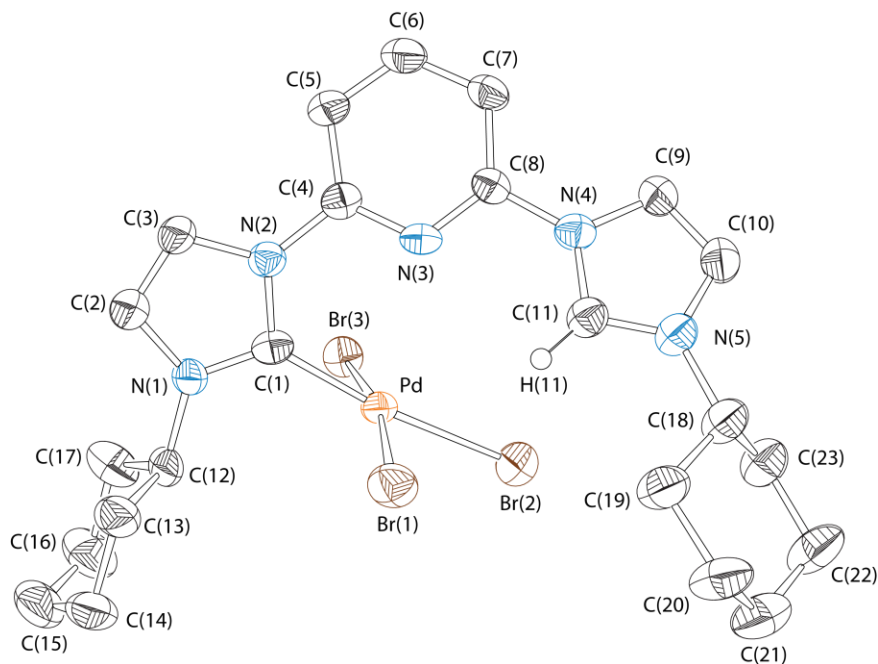


Figure A2: Fully labeled thermal ellipsoid plot of  $[\text{PDC}^{\text{Cy}}\text{Pd}(\text{Br})_3]$  with hydrogens omitted at the 50% probability level

### A.3.1 Bond Lengths and Angles for $[\text{PDC}^{\text{Cy}}\text{Pd}(\text{Br})_3]$

Bond	Length	Bond	Length
Pd-C(1)	1.957(7)	C(12)-H(12)	1
Pd-Br(3)	2.4291(10)	C(13)-C(14)	1.541(12)
Pd-Br(1)	2.4576(10)	C(13)-H(13A)	0.99
Pd-Br(2)	2.4833(11)	C(13)-H(13B)	0.99
N(1)-C(1)	1.329(10)	C(14)-C(15)	1.499(18)
N(1)-C(2)	1.386(10)	C(14)-H(14A)	0.99
N(1)-C(12)	1.467(9)	C(14)-H(14B)	0.99
N(2)-C(1)	1.370(9)	C(15)-C(16)	1.526(17)
N(2)-C(3)	1.399(9)	C(15)-H(15A)	0.99
N(2)-C(4)	1.420(9)	C(15)-H(15B)	0.99
N(3)-C(8)	1.312(9)	C(16)-C(17)	1.530(13)
N(3)-C(4)	1.325(9)	C(16)-H(16A)	0.99
N(4)-C(11)	1.347(9)	C(16)-H(16B)	0.99
N(4)-C(9)	1.388(10)	C(17)-H(17A)	0.99
N(4)-C(8)	1.431(9)	C(17)-H(17B)	0.99
N(5)-C(11)	1.329(10)	C(18)-C(19)	1.484(13)
N(5)-C(10)	1.360(11)	C(18)-C(23)	1.528(12)
N(5)-C(18)	1.491(10)	C(18)-H(18)	1
N(6)-C(24)	1.127(13)	C(19)-C(20)	1.551(12)
C(2)-C(3)	1.338(11)	C(19)-H(19A)	0.99
C(2)-H(2)	0.95	C(19)-H(19B)	0.99
C(3)-H(3)	0.95	C(20)-C(21)	1.530(14)
C(4)-C(5)	1.395(10)	C(20)-H(20A)	0.99
C(5)-C(6)	1.369(11)	C(20)-H(20B)	0.99
C(5)-H(5)	0.95	C(21)-C(22)	1.457(16)
C(6)-C(7)	1.376(11)	C(21)-H(21A)	0.99
C(6)-H(6)	0.95	C(21)-H(21B)	0.99
C(7)-C(8)	1.385(10)	C(22)-C(23)	1.513(12)
C(7)-H(7)	0.95	C(22)-H(22)	0.95
C(9)-C(10)	1.349(11)	C(23)-H(23A)	0.99

C(9)-H(9)	0.95	C(23)-H(23B)	0.99
C(10)-H(10)	0.95	C(24)-C(25)	1.447(15)
C(11)-H(11)	0.95	C(25)-H(25A)	0.98
C(12)-C(13)	1.517(11)	C(25)-H(25B)	0.98
C(12)-C(17)	1.524(13)	C(25)-H(25C)	0.98

Table A5: Bond lengths for [PDC<sup>Cy</sup>Pd(Br)<sub>3</sub>]

Bond	Angle	Bond	Angle
C(1)-Pd-Br(3)	85.6(2)	C(15)-C(14)-C(13)	112.1(9)
C(1)-Pd-Br(1)	90.2(2)	C(15)-C(14)-H(14A)	109.2
Br(3)-Pd-Br(1)	168.31(4)	C(13)-C(14)-H(14A)	109.2
C(1)-Pd-Br(2)	173.2(2)	C(15)-C(14)-H(14B)	109.2
Br(3)-Pd-Br(2)	92.25(4)	C(13)-C(14)-H(14B)	109.2
Br(1)-Pd-Br(2)	93.11(4)	H(14A)-C(14)-H(14B)	107.9
C(1)-N(1)-C(2)	110.9(6)	C(14)-C(15)-C(16)	110.5(9)
C(1)-N(1)-C(12)	123.9(6)	C(14)-C(15)-H(15A)	109.5
C(2)-N(1)-C(12)	125.2(6)	C(16)-C(15)-H(15A)	109.5
C(1)-N(2)-C(3)	109.8(6)	C(14)-C(15)-H(15B)	109.5
C(1)-N(2)-C(4)	124.6(6)	C(16)-C(15)-H(15B)	109.5
C(3)-N(2)-C(4)	125.6(6)	H(15A)-C(15)-H(15B)	108.1
C(8)-N(3)-C(4)	117.4(6)	C(15)-C(16)-C(17)	110.5(9)
C(11)-N(4)-C(9)	108.3(6)	C(15)-C(16)-H(16A)	109.5
C(11)-N(4)-C(8)	125.0(6)	C(17)-C(16)-H(16A)	109.5
C(9)-N(4)-C(8)	126.5(6)	C(15)-C(16)-H(16B)	109.5
C(11)-N(5)-C(10)	109.8(7)	C(17)-C(16)-H(16B)	109.5
C(11)-N(5)-C(18)	127.2(7)	H(16A)-C(16)-H(16B)	108.1
C(10)-N(5)-C(18)	122.9(7)	C(12)-C(17)-C(16)	110.4(9)
N(1)-C(1)-N(2)	105.5(6)	C(12)-C(17)-H(17A)	109.6
N(1)-C(1)-Pd	129.1(5)	C(16)-C(17)-H(17A)	109.6
N(2)-C(1)-Pd	125.3(5)	C(12)-C(17)-H(17B)	109.6
C(3)-C(2)-N(1)	107.6(7)	C(16)-C(17)-H(17B)	109.6
C(3)-C(2)-H(2)	126.2	H(17A)-C(17)-H(17B)	108.1

N(1)-C(2)-H(2)	126.2	C(19)-C(18)-N(5)	111.8(7)
C(2)-C(3)-N(2)	106.2(6)	C(19)-C(18)-C(23)	112.0(8)
C(2)-C(3)-H(3)	126.9	N(5)-C(18)-C(23)	110.6(7)
N(2)-C(3)-H(3)	126.9	C(19)-C(18)-H(18)	107.4
N(3)-C(4)-C(5)	123.4(7)	N(5)-C(18)-H(18)	107.4
N(3)-C(4)-N(2)	116.2(6)	C(23)-C(18)-H(18)	107.4
C(5)-C(4)-N(2)	120.4(7)	C(18)-C(19)-C(20)	109.0(8)
C(6)-C(5)-C(4)	116.7(7)	C(18)-C(19)-H(19A)	109.9
C(6)-C(5)-H(5)	121.6	C(20)-C(19)-H(19A)	109.9
C(4)-C(5)-H(5)	121.6	C(18)-C(19)-H(19B)	109.9
C(5)-C(6)-C(7)	121.6(7)	C(20)-C(19)-H(19B)	109.9
C(5)-C(6)-H(6)	119.2	H(19A)-C(19)-H(19B)	108.3
C(7)-C(6)-H(6)	119.2	C(21)-C(20)-C(19)	109.4(8)
C(6)-C(7)-C(8)	115.7(7)	C(21)-C(20)-H(20A)	109.8
C(6)-C(7)-H(7)	122.2	C(19)-C(20)-H(20A)	109.8
C(8)-C(7)-H(7)	122.2	C(21)-C(20)-H(20B)	109.8
N(3)-C(8)-C(7)	125.2(7)	C(19)-C(20)-H(20B)	109.8
N(3)-C(8)-N(4)	114.3(6)	H(20A)-C(20)-H(20B)	108.2
C(7)-C(8)-N(4)	120.4(6)	C(22)-C(21)-C(20)	112.9(9)
C(10)-C(9)-N(4)	106.8(7)	C(22)-C(21)-H(21A)	109
C(10)-C(9)-H(9)	126.6	C(20)-C(21)-H(21A)	109
N(4)-C(9)-H(9)	126.6	C(22)-C(21)-H(21B)	109
C(9)-C(10)-N(5)	107.5(7)	C(20)-C(21)-H(21B)	109
C(9)-C(10)-H(10)	126.3	H(21A)-C(21)-H(21B)	107.8
N(5)-C(10)-H(10)	126.3	C(21)-C(22)-C(23)	111.9(9)
N(5)-C(11)-N(4)	107.6(7)	C(21)-C(22)-H(22)	124
N(5)-C(11)-H(11)	126.2	C(23)-C(22)-H(22)	124
N(4)-C(11)-H(11)	126.2	C(22)-C(23)-C(18)	111.0(8)
N(1)-C(12)-C(13)	110.5(7)	C(22)-C(23)-H(23A)	109.4
N(1)-C(12)-C(17)	110.4(7)	C(18)-C(23)-H(23A)	109.4
C(13)-C(12)-C(17)	112.2(7)	C(22)-C(23)-H(23B)	109.4
N(1)-C(12)-H(12)	107.9	C(18)-C(23)-H(23B)	109.4
C(13)-C(12)-H(12)	107.9	H(23A)-C(23)-H(23B)	108
C(17)-C(12)-H(12)	107.9	N(6)-C(24)-C(25)	178.8(12)
C(12)-C(13)-C(14)	109.4(8)	C(24)-C(25)-H(25A)	109.5
C(12)-C(13)-H(13A)	109.8	C(24)-C(25)-H(25B)	109.5
C(14)-C(13)-H(13A)	109.8	H(25A)-C(25)-H(25B)	109.5
C(12)-C(13)-H(13B)	109.8	C(24)-C(25)-H(25C)	109.5
C(14)-C(13)-H(13B)	109.8	H(25A)-C(25)-H(25C)	109.5

H(13A)-C(13)-H(13B)	108.2	H(25B)-C(25)-H(25C)	109.5
---------------------	-------	---------------------	-------

Table A.6: Bond angles for [PDC<sup>Cy</sup>Pd(Br)<sub>3</sub>]

#### A.4 Crystal Data for [PDC<sup>Cy</sup>Ag(Br)]

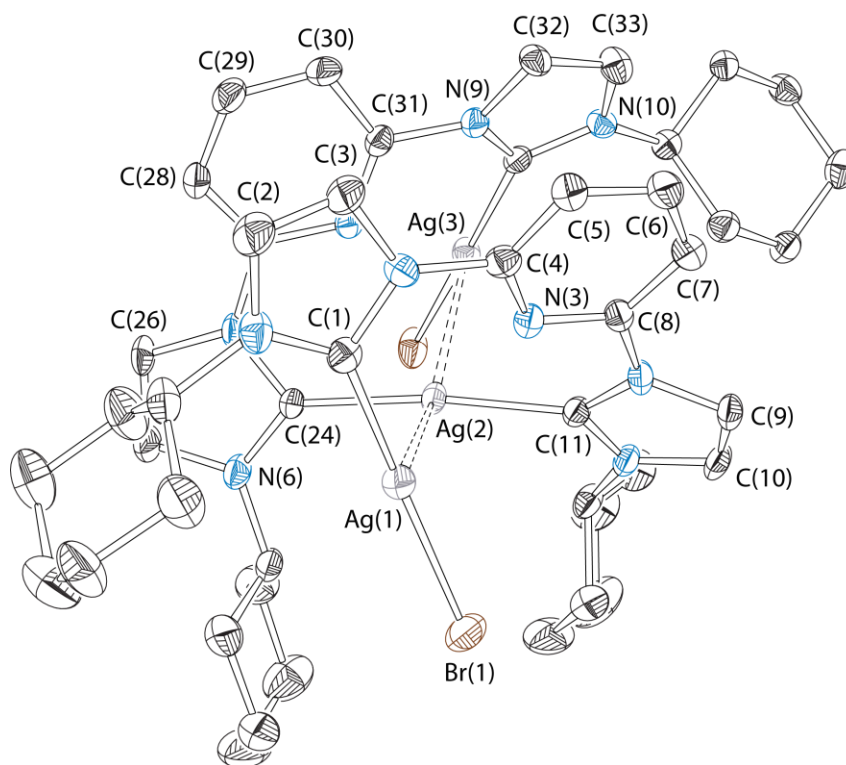


Figure A.3: Labeled thermal ellipsoid plot of [PDC<sup>Cy</sup>Ag(Br)] with hydrogens and an outer sphere Br<sup>-</sup> omitted and shown at the 30% probability level. Numbering follows the general numbering scheme in the appendix.

Bond	Length	Bond	Length
Ag(1)-C(1)	2.107(6)	C(5)-C(6)	1.372(9)
Ag(1)-Br(1)	2.4468(9)	C(6)-C(7)	1.355(9)
Ag(1)-Ag(2)	2.9980(7)	C(7)-C(8)	1.380(8)
Ag(2)-C(24)	2.086(6)	C(9)-C(10)	1.302(9)
Ag(2)-C(11)	2.093(6)	C(12)-C(13)	1.485(10)
Ag(2)-Ag(3)	3.0679(7)	C(12)-C(17)	1.488(10)
Ag(3)-C(34)	2.091(6)	C(13)-C(14)	1.529(10)
Ag(3)-Br(2)	2.4429(8)	C(14)-C(15)	1.473(12)
Ag(4)-C(47)	2.088(6)	C(15)-C(16)	1.556(13)
Ag(4)-Br(3)	2.4389(9)	C(16)-C(17)	1.541(11)
Ag(4)-Ag(5)	2.9931(7)	C(18)-C(23)	1.527(9)
Ag(5)-C(57)	2.098(6)	C(18)-C(19)	1.546(9)
Ag(5)-C(70)	2.107(6)	C(19)-C(20)	1.532(11)
Ag(5)-Ag(6)	2.9758(7)	C(20)-C(21)	1.566(13)
Ag(6)-C(80)	2.101(6)	C(21)-C(22)	1.536(13)
Ag(6)-Br(4)	2.4674(9)	C(22)-C(23)	1.527(11)
Br(5')-Br(5')#1	1.92(2)	C(25)-C(26)	1.347(9)
N(1)-C(1)	1.334(7)	C(27)-C(28)	1.381(8)
N(1)-C(2)	1.357(8)	C(28)-C(29)	1.340(9)
N(1)-C(12)	1.500(8)	C(29)-C(30)	1.392(9)
N(2)-C(1)	1.366(7)	C(30)-C(31)	1.390(8)
N(2)-C(3)	1.388(7)	C(32)-C(33)	1.340(8)
N(2)-C(4)	1.423(8)	C(35)-C(36)	1.501(10)
N(3)-C(4)	1.322(7)	C(35)-C(40)	1.530(10)
N(3)-C(8)	1.325(7)	C(36)-C(37)	1.517(10)
N(4)-C(11)	1.382(7)	C(37)-C(38)	1.514(12)
N(4)-C(9)	1.409(7)	C(38)-C(39)	1.498(13)
N(4)-C(8)	1.418(7)	C(39)-C(40)	1.547(11)
N(5)-C(11)	1.333(7)	C(41)-C(46)	1.515(8)
N(5)-C(10)	1.391(7)	C(41)-C(42)	1.538(8)
N(5)-C(18)	1.467(8)	C(42)-C(43)	1.527(8)
N(6)-C(24)	1.347(7)	C(43)-C(44)	1.519(9)
N(6)-C(25)	1.398(7)	C(44)-C(45)	1.548(9)
N(6)-C(35)	1.482(8)	C(45)-C(46)	1.549(8)
N(7)-C(24)	1.386(7)	C(48)-C(49)	1.328(9)
N(7)-C(26)	1.399(7)	C(50)-C(51)	1.393(9)
N(7)-C(27)	1.417(7)	C(51)-C(52)	1.381(9)
N(8)-C(31)	1.320(7)	C(52)-C(53)	1.389(10)

N(8)-C(27)	1.328(7)	C(53)-C(54)	1.395(9)
N(9)-C(34)	1.363(7)	C(55)-C(56)	1.321(9)
N(9)-C(32)	1.412(7)	C(58)-C(63)	1.474(9)
N(9)-C(31)	1.437(7)	C(58)-C(59)	1.512(9)
N(10)-C(34)	1.353(7)	C(59)-C(60)	1.563(10)
N(10)-C(33)	1.389(7)	C(60)-C(61)	1.521(12)
N(10)-C(41)	1.464(7)	C(61)-C(62)	1.507(11)
N(11)-C(47)	1.335(7)	C(62)-C(63)	1.512(10)
N(11)-C(48)	1.391(8)	C(64)-C(69)	1.507(9)
N(11)-C(58)	1.487(7)	C(64)-C(65)	1.531(9)
N(12)-C(47)	1.349(7)	C(65)-C(66)	1.557(12)
N(12)-C(49)	1.405(8)	C(66)-C(67)	1.519(13)
N(12)-C(50)	1.415(7)	C(67)-C(68)	1.483(12)
N(13)-C(50)	1.320(8)	C(68)-C(69)	1.535(11)
N(13)-C(54)	1.329(7)	C(71)-C(72)	1.304(9)
N(14)-C(57)	1.374(8)	C(73)-C(74)	1.361(8)
N(14)-C(55)	1.392(7)	C(74)-C(75)	1.355(9)
N(14)-C(54)	1.407(8)	C(75)-C(76)	1.386(9)
N(15)-C(57)	1.350(7)	C(76)-C(77)	1.370(8)
N(15)-C(56)	1.396(8)	C(78)-C(79)	1.326(9)
N(15)-C(64)	1.471(8)	C(81)-C(82)	1.498(9)
N(16)-C(70)	1.338(7)	C(81)-C(86)	1.540(9)
N(16)-C(71)	1.391(7)	C(82)-C(83)	1.538(10)
N(16)-C(81)	1.490(8)	C(83)-C(84)	1.493(11)
N(17)-C(70)	1.362(7)	C(84)-C(85)	1.527(12)
N(17)-C(72)	1.416(7)	C(85)-C(86)	1.537(10)
N(17)-C(73)	1.435(7)	C(87)-C(92)	1.5259
N(18)-C(73)	1.316(7)	C(87)-C(88)	1.5391
N(18)-C(77)	1.323(7)	C(88)-C(89)	1.4986
N(19)-C(78)	1.380(7)	C(89)-C(90)	1.5626
N(19)-C(80)	1.383(7)	C(90)-C(91)	1.7306
N(19)-C(77)	1.426(7)	C(91)-C(92)	1.6368
N(20)-C(87')	1.273(7)	C(87')-C(92')	1.5261
N(20)-C(80)	1.356(7)	C(87')-C(88')	1.637
N(20)-C(79)	1.379(8)	C(88')-C(89')	1.7305
N(20)-C(87)	1.489(6)	C(89')-C(90')	1.5625
C(2)-C(3)	1.315(9)	C(90')-C(91')	1.4987
C(4)-C(5)	1.396(9)	C(91')-C(92')	1.5394

Table A.7: Bond lengths for [PDC<sup>Cy</sup>Ag(Br)]

Bond	Angle	Bond	Angle
C(1)-Ag(1)-Br(1)	171.05(16)	N(6)-C(24)-N(7)	104.1(5)
C(1)-Ag(1)-Ag(2)	100.14(17)	N(6)-C(24)-Ag(2)	131.0(4)
Br(1)-Ag(1)-Ag(2)	88.11(3)	N(7)-C(24)-Ag(2)	124.9(4)
C(24)-Ag(2)-C(11)	172.1(2)	C(26)-C(25)-N(6)	107.2(6)
C(24)-Ag(2)-Ag(1)	83.92(17)	C(25)-C(26)-N(7)	106.4(5)
C(11)-Ag(2)-Ag(1)	95.41(16)	N(8)-C(27)-C(28)	123.7(6)
C(24)-Ag(2)-Ag(3)	97.97(17)	N(8)-C(27)-N(7)	114.7(5)
C(11)-Ag(2)-Ag(3)	85.85(16)	C(28)-C(27)-N(7)	121.6(5)
Ag(1)-Ag(2)-Ag(3)	156.04(2)	C(29)-C(28)-C(27)	118.0(6)
C(34)-Ag(3)-Br(2)	175.48(16)	C(28)-C(29)-C(30)	121.0(6)
C(34)-Ag(3)-Ag(2)	92.90(16)	C(31)-C(30)-C(29)	115.9(6)
Br(2)-Ag(3)-Ag(2)	91.62(3)	N(8)-C(31)-C(30)	124.4(6)
C(47)-Ag(4)-Br(3)	175.87(17)	N(8)-C(31)-N(9)	115.3(5)
C(47)-Ag(4)-Ag(5)	98.94(17)	C(30)-C(31)-N(9)	120.3(5)
Br(3)-Ag(4)-Ag(5)	84.34(3)	C(33)-C(32)-N(9)	105.3(5)
C(57)-Ag(5)-C(70)	176.2(2)	C(32)-C(33)-N(10)	108.4(5)
C(57)-Ag(5)-Ag(6)	84.48(17)	N(10)-C(34)-N(9)	104.8(5)
C(70)-Ag(5)-Ag(6)	96.11(15)	N(10)-C(34)-Ag(3)	128.4(4)
C(57)-Ag(5)-Ag(4)	95.67(17)	N(9)-C(34)-Ag(3)	126.7(4)
C(70)-Ag(5)-Ag(4)	85.37(15)	N(6)-C(35)-C(36)	111.4(5)
Ag(6)-Ag(5)-Ag(4)	155.08(2)	N(6)-C(35)-C(40)	110.3(6)
C(80)-Ag(6)-Br(4)	170.65(17)	C(36)-C(35)-C(40)	112.8(6)
C(80)-Ag(6)-Ag(5)	99.40(16)	C(35)-C(36)-C(37)	111.2(7)
Br(4)-Ag(6)-Ag(5)	89.79(2)	C(38)-C(37)-C(36)	110.2(7)
C(1)-N(1)-C(2)	112.3(6)	C(39)-C(38)-C(37)	111.8(8)
C(1)-N(1)-C(12)	125.0(6)	C(38)-C(39)-C(40)	112.2(8)
C(2)-N(1)-C(12)	122.7(6)	C(35)-C(40)-C(39)	109.1(7)
C(1)-N(2)-C(3)	109.6(5)	N(10)-C(41)-C(46)	111.7(5)
C(1)-N(2)-C(4)	125.0(5)	N(10)-C(41)-C(42)	111.1(5)
C(3)-N(2)-C(4)	125.2(5)	C(46)-C(41)-C(42)	111.2(5)
C(4)-N(3)-C(8)	117.4(5)	C(43)-C(42)-C(41)	111.3(5)
C(11)-N(4)-C(9)	109.4(5)	C(44)-C(43)-C(42)	111.1(5)
C(11)-N(4)-C(8)	124.9(5)	C(43)-C(44)-C(45)	111.7(5)
C(9)-N(4)-C(8)	125.6(5)	C(44)-C(45)-C(46)	109.8(5)
C(11)-N(5)-C(10)	110.9(5)	C(41)-C(46)-C(45)	110.7(5)
C(11)-N(5)-C(18)	122.7(5)	N(11)-C(47)-N(12)	105.5(5)

C(10)-N(5)-C(18)	126.4(5)	N(11)-C(47)-Ag(4)	127.5(4)
C(24)-N(6)-C(25)	111.6(5)	N(12)-C(47)-Ag(4)	126.7(4)
C(24)-N(6)-C(35)	123.8(5)	C(49)-C(48)-N(11)	107.8(6)
C(25)-N(6)-C(35)	124.6(5)	C(48)-C(49)-N(12)	105.9(6)
C(24)-N(7)-C(26)	110.7(5)	N(13)-C(50)-C(51)	124.0(6)
C(24)-N(7)-C(27)	123.7(5)	N(13)-C(50)-N(12)	115.1(5)
C(26)-N(7)-C(27)	125.4(5)	C(51)-C(50)-N(12)	120.9(6)
C(31)-N(8)-C(27)	116.9(5)	C(52)-C(51)-C(50)	117.0(7)
C(34)-N(9)-C(32)	111.0(5)	C(51)-C(52)-C(53)	120.5(7)
C(34)-N(9)-C(31)	124.4(5)	C(52)-C(53)-C(54)	116.9(6)
C(32)-N(9)-C(31)	124.6(5)	N(13)-C(54)-C(53)	123.5(6)
C(34)-N(10)-C(33)	110.5(5)	N(13)-C(54)-N(14)	115.8(6)
C(34)-N(10)-C(41)	123.0(5)	C(53)-C(54)-N(14)	120.6(6)
C(33)-N(10)-C(41)	126.5(5)	C(56)-C(55)-N(14)	107.3(6)
C(47)-N(11)-C(48)	110.4(5)	C(55)-C(56)-N(15)	107.5(6)
C(47)-N(11)-C(58)	123.5(5)	N(15)-C(57)-N(14)	104.7(5)
C(48)-N(11)-C(58)	126.0(5)	N(15)-C(57)-Ag(5)	129.0(5)
C(47)-N(12)-C(49)	110.4(5)	N(14)-C(57)-Ag(5)	126.1(4)
C(47)-N(12)-C(50)	124.7(5)	C(63)-C(58)-N(11)	111.8(5)
C(49)-N(12)-C(50)	124.7(5)	C(63)-C(58)-C(59)	111.8(6)
C(50)-N(13)-C(54)	117.9(5)	N(11)-C(58)-C(59)	111.8(5)
C(57)-N(14)-C(55)	110.0(5)	C(58)-C(59)-C(60)	109.3(6)
C(57)-N(14)-C(54)	124.1(5)	C(61)-C(60)-C(59)	110.4(7)
C(55)-N(14)-C(54)	125.8(5)	C(62)-C(61)-C(60)	111.0(6)
C(57)-N(15)-C(56)	110.5(5)	C(61)-C(62)-C(63)	110.3(7)
C(57)-N(15)-C(64)	123.6(5)	C(58)-C(63)-C(62)	112.1(6)
C(56)-N(15)-C(64)	125.8(5)	N(15)-C(64)-C(69)	112.3(5)
C(70)-N(16)-C(71)	111.3(5)	N(15)-C(64)-C(65)	109.3(6)
C(70)-N(16)-C(81)	123.9(5)	C(69)-C(64)-C(65)	111.3(6)
C(71)-N(16)-C(81)	124.8(5)	C(64)-C(65)-C(66)	110.0(7)
C(70)-N(17)-C(72)	109.8(5)	C(67)-C(66)-C(65)	109.3(7)
C(70)-N(17)-C(73)	125.0(5)	C(68)-C(67)-C(66)	113.3(8)
C(72)-N(17)-C(73)	125.2(5)	C(67)-C(68)-C(69)	109.1(8)
C(73)-N(18)-C(77)	116.5(5)	C(64)-C(69)-C(68)	110.5(6)
C(78)-N(19)-C(80)	110.5(5)	N(16)-C(70)-N(17)	104.5(5)
C(78)-N(19)-C(77)	125.2(5)	N(16)-C(70)-Ag(5)	128.6(4)
C(80)-N(19)-C(77)	124.2(5)	N(17)-C(70)-Ag(5)	126.8(4)
C(87')-N(20)-C(80)	142.4(6)	C(72)-C(71)-N(16)	107.7(6)
C(87')-N(20)-C(79)	106.8(6)	C(71)-C(72)-N(17)	106.8(6)

C(80)-N(20)-C(79)	110.6(5)	N(18)-C(73)-C(74)	124.6(6)
C(80)-N(20)-C(87)	125.4(6)	N(18)-C(73)-N(17)	115.2(5)
C(79)-N(20)-C(87)	124.0(5)	C(74)-C(73)-N(17)	120.2(5)
N(1)-C(1)-N(2)	103.8(5)	C(75)-C(74)-C(73)	117.3(6)
N(1)-C(1)-Ag(1)	133.6(5)	C(74)-C(75)-C(76)	120.9(6)
N(2)-C(1)-Ag(1)	122.6(4)	C(77)-C(76)-C(75)	115.8(6)
C(3)-C(2)-N(1)	107.1(6)	N(18)-C(77)-C(76)	124.8(6)
C(2)-C(3)-N(2)	107.1(6)	N(18)-C(77)-N(19)	115.6(5)
N(3)-C(4)-C(5)	123.2(6)	C(76)-C(77)-N(19)	119.6(6)
N(3)-C(4)-N(2)	115.7(5)	C(79)-C(78)-N(19)	106.8(6)
C(5)-C(4)-N(2)	121.2(6)	C(78)-C(79)-N(20)	108.2(6)
C(6)-C(5)-C(4)	117.4(6)	N(20)-C(80)-N(19)	103.8(5)
C(7)-C(6)-C(5)	120.4(6)	N(20)-C(80)-Ag(6)	130.3(5)
C(6)-C(7)-C(8)	117.9(6)	N(19)-C(80)-Ag(6)	125.8(4)
N(3)-C(8)-C(7)	123.8(6)	N(16)-C(81)-C(82)	111.5(6)
N(3)-C(8)-N(4)	116.1(5)	N(16)-C(81)-C(86)	109.6(5)
C(7)-C(8)-N(4)	120.1(5)	C(82)-C(81)-C(86)	111.7(6)
C(10)-C(9)-N(4)	106.7(5)	C(81)-C(82)-C(83)	110.8(6)
C(9)-C(10)-N(5)	108.5(5)	C(84)-C(83)-C(82)	112.2(7)
N(5)-C(11)-N(4)	104.6(5)	C(83)-C(84)-C(85)	112.3(7)
N(5)-C(11)-Ag(2)	127.6(4)	C(84)-C(85)-C(86)	111.2(7)
N(4)-C(11)-Ag(2)	127.5(4)	C(85)-C(86)-C(81)	111.2(6)
C(13)-C(12)-C(17)	113.7(7)	N(20)-C(87)-C(92)	109.1(5)
C(13)-C(12)-N(1)	113.1(6)	N(20)-C(87)-C(88)	112.7(4)
C(17)-C(12)-N(1)	111.0(6)	C(92)-C(87)-C(88)	119.6
C(12)-C(13)-C(14)	111.2(7)	C(89)-C(88)-C(87)	108.5
C(15)-C(14)-C(13)	109.8(7)	C(88)-C(89)-C(90)	111.3
C(14)-C(15)-C(16)	111.1(8)	C(89)-C(90)-C(91)	105
C(17)-C(16)-C(15)	109.7(7)	C(92)-C(91)-C(90)	111
C(12)-C(17)-C(16)	111.3(7)	C(87)-C(92)-C(91)	106.1
N(5)-C(18)-C(23)	110.5(5)	N(20)-C(87')-C(92')	123.9(5)
N(5)-C(18)-C(19)	111.2(5)	N(20)-C(87')-C(88')	102.9(5)
C(23)-C(18)-C(19)	111.0(6)	C(92')-C(87')-C(88')	106.1
C(20)-C(19)-C(18)	108.4(6)	C(87')-C(88')-C(89')	111
C(19)-C(20)-C(21)	111.8(8)	C(90')-C(89')-C(88')	105
C(22)-C(21)-C(20)	108.8(7)	C(91')-C(90')-C(89')	111.3
C(23)-C(22)-C(21)	110.7(8)	C(90')-C(91')-C(92')	108.5
C(22)-C(23)-C(18)	110.8(7)	C(87')-C(92')-C(91')	119.6

Table A.8: Bond angles for [PDC<sup>Cy</sup>Ag(Br)]

### A.5 Crystal Data for [PDC<sup>Et</sup>Pd(Br)](Br)

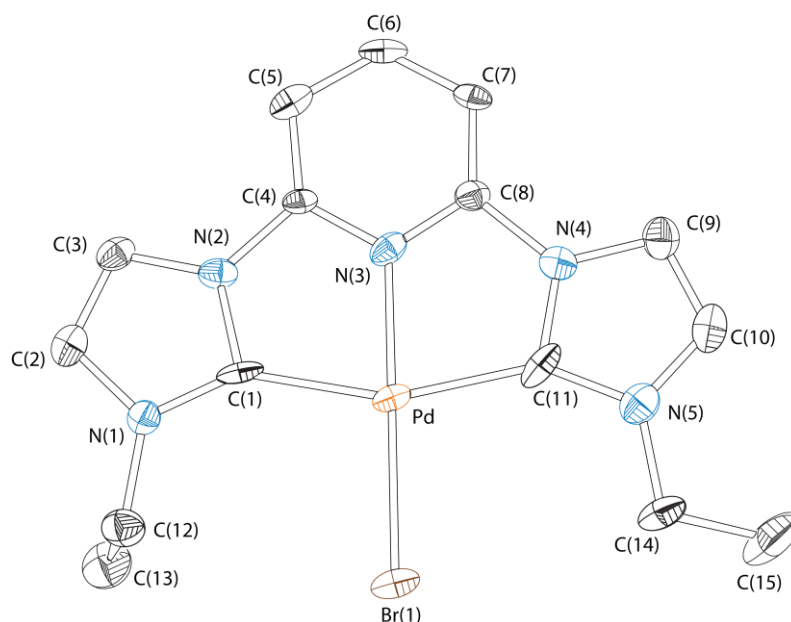


Figure A.4: Fully labeled thermal ellipsoid plot of [PDC<sup>Et</sup>Pd(Br)](Br) with hydrogens and an outer sphere Br<sup>-</sup> omitted and shown at the 50% probability level

Bond	Length	Bond	Length
Pd(1)-N(3)	1.981(10)	N(7)-C(18)	1.369(17)
Pd(1)-C(11)	2.003(15)	N(7)-C(19)	1.425(15)
Pd(1)-C(1)	2.014(14)	N(8)-C(23)	1.345(14)
Pd(1)-Br(1)	2.4077(16)	N(8)-C(19)	1.345(15)
Pd(2)-N(8)	1.979(9)	N(9)-C(24)	1.373(16)
Pd(2)-C(16)	1.990(15)	N(9)-C(26)	1.376(14)
Pd(2)-C(26)	2.047(14)	N(9)-C(23)	1.413(15)
Pd(2)-Br(2)	2.4066(15)	N(10)-C(26)	1.328(17)

N(1)-C(2)	1.372(16)	N(10)-C(25)	1.380(18)
N(1)-C(1)	1.378(17)	N(10)-C(29)	1.478(16)
N(1)-C(12)	1.457(17)	C(2)-C(3)	1.354(19)
N(2)-C(1)	1.350(14)	C(4)-C(5)	1.348(17)
N(2)-C(3)	1.375(16)	C(5)-C(6)	1.41(2)
N(2)-C(4)	1.446(16)	C(6)-C(7)	1.354(19)
N(3)-C(8)	1.323(16)	C(7)-C(8)	1.341(16)
N(3)-C(4)	1.335(15)	C(9)-C(10)	1.35(2)
N(4)-C(11)	1.376(18)	C(12)-C(13)	1.51(2)
N(4)-C(9)	1.393(17)	C(14)-C(15)	1.49(2)
N(4)-C(8)	1.445(16)	C(17)-C(18)	1.325(19)
N(5)-C(10)	1.356(19)	C(19)-C(20)	1.351(16)
N(5)-C(11)	1.377(17)	C(20)-C(21)	1.407(18)
N(5)-C(14)	1.452(17)	C(21)-C(22)	1.368(18)
N(6)-C(17)	1.330(17)	C(22)-C(23)	1.373(15)
N(6)-C(16)	1.396(17)	C(24)-C(25)	1.362(19)
N(6)-C(27)	1.467(15)	C(27)-C(28)	1.507(18)
N(7)-C(16)	1.351(15)	C(29)-C(30)	1.48(2)

Table A.9: Bond lengths for [PDC<sup>Et</sup>Pd(Br)] (Br)

Bond	Angle	Bond	Angle
N(3)-Pd(1)-C(11)	78.9(5)	N(2)-C(1)-N(1)	102.5(11)
N(3)-Pd(1)-C(1)	79.1(5)	N(2)-C(1)-Pd(1)	112.5(10)
C(11)-Pd(1)-C(1)	158.0(5)	N(1)-C(1)-Pd(1)	145.0(8)
N(3)-Pd(1)-Br(1)	178.1(3)	C(3)-C(2)-N(1)	107.9(13)
C(11)-Pd(1)-Br(1)	101.3(4)	C(2)-C(3)-N(2)	104.8(11)
C(1)-Pd(1)-Br(1)	100.6(3)	N(3)-C(4)-C(5)	124.0(12)
N(8)-Pd(2)-C(16)	77.4(4)	N(3)-C(4)-N(2)	109.0(10)
N(8)-Pd(2)-C(26)	79.3(4)	C(5)-C(4)-N(2)	126.9(12)
C(16)-Pd(2)-C(26)	156.7(5)	C(4)-C(5)-C(6)	114.7(12)
N(8)-Pd(2)-Br(2)	179.3(3)	C(7)-C(6)-C(5)	121.9(12)
C(16)-Pd(2)-Br(2)	103.1(3)	C(8)-C(7)-C(6)	117.6(13)
C(26)-Pd(2)-Br(2)	100.1(3)	N(3)-C(8)-C(7)	123.1(12)
C(2)-N(1)-C(1)	111.0(11)	N(3)-C(8)-N(4)	108.3(10)

C(2)-N(1)-C(12)	123.7(12)	C(7)-C(8)-N(4)	128.5(12)
C(1)-N(1)-C(12)	125.2(11)	C(10)-C(9)-N(4)	103.7(13)
C(1)-N(2)-C(3)	113.8(11)	C(9)-C(10)-N(5)	109.6(13)
C(1)-N(2)-C(4)	119.3(11)	N(4)-C(11)-N(5)	101.8(13)
C(3)-N(2)-C(4)	126.9(10)	N(4)-C(11)-Pd(1)	112.2(9)
C(8)-N(3)-C(4)	118.6(10)	N(5)-C(11)-Pd(1)	145.7(12)
C(8)-N(3)-Pd(1)	121.3(8)	N(1)-C(12)-C(13)	109.7(12)
C(4)-N(3)-Pd(1)	120.1(9)	N(5)-C(14)-C(15)	112.7(14)
C(11)-N(4)-C(9)	113.4(11)	N(7)-C(16)-N(6)	102.0(12)
C(11)-N(4)-C(8)	119.1(11)	N(7)-C(16)-Pd(2)	115.7(9)
C(9)-N(4)-C(8)	127.5(11)	N(6)-C(16)-Pd(2)	142.3(9)
C(10)-N(5)-C(11)	111.5(12)	C(18)-C(17)-N(6)	110.9(13)
C(10)-N(5)-C(14)	126.2(13)	C(17)-C(18)-N(7)	104.1(12)
C(11)-N(5)-C(14)	122.3(13)	N(8)-C(19)-C(20)	123.5(11)
C(17)-N(6)-C(16)	109.6(10)	N(8)-C(19)-N(7)	109.5(10)
C(17)-N(6)-C(27)	125.5(12)	C(20)-C(19)-N(7)	127.0(12)
C(16)-N(6)-C(27)	124.9(11)	C(19)-C(20)-C(21)	115.8(12)
C(16)-N(7)-C(18)	113.3(11)	C(22)-C(21)-C(20)	121.7(11)
C(16)-N(7)-C(19)	116.8(11)	C(21)-C(22)-C(23)	118.4(12)
C(18)-N(7)-C(19)	129.7(11)	N(8)-C(23)-C(22)	120.5(11)
C(23)-N(8)-C(19)	120.0(10)	N(8)-C(23)-N(9)	110.8(9)
C(23)-N(8)-Pd(2)	119.3(8)	C(22)-C(23)-N(9)	128.7(11)
C(19)-N(8)-Pd(2)	120.6(8)	C(25)-C(24)-N(9)	104.2(12)
C(24)-N(9)-C(26)	112.6(11)	C(24)-C(25)-N(10)	108.0(13)
C(24)-N(9)-C(23)	127.8(10)	N(10)-C(26)-N(9)	103.6(11)
C(26)-N(9)-C(23)	119.6(11)	N(10)-C(26)-Pd(2)	145.4(9)
C(26)-N(10)-C(25)	111.4(11)	N(9)-C(26)-Pd(2)	110.9(10)
C(26)-N(10)-C(29)	125.6(12)	N(6)-C(27)-C(28)	113.3(11)
C(25)-N(10)-C(29)	122.7(12)	C(30)-C(29)-N(10)	112.1(12)

Table A.10: Bond angles for [PDC<sup>Et</sup>Pd(Br)](Br)

### A.6 Crystal Data for [PDC<sup>Cy</sup>Pd(Br)](Br)

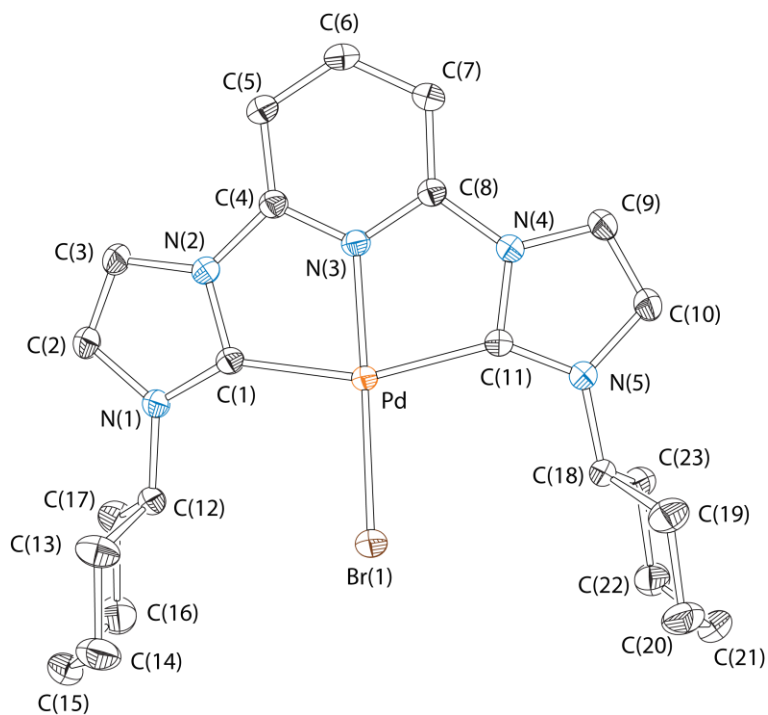


Figure A.5: Fully labeled thermal ellipsoid plot of  $[\text{PDC}^{\text{Cy}}\text{Pd}(\text{Br})](\text{Br})$  with hydrogens and an outer sphere  $\text{Br}^-$  omitted and shown at the 50% probability level

Bond	Length	Bond	Length
Pd-N(3)	1.979(2)	C(12)-C(13)	1.503(5)
Pd-C(1)	2.023(3)	C(12)-C(17)	1.526(5)
Pd-C(11)	2.030(3)	C(12)-H(12)	1
Pd-Br(1)	2.4259(4)	C(13)-C(14)	1.525(5)
Cl(1)-C(24)	1.762(4)	C(13)-H(13A)	0.99
Cl(2)-C(24)	1.736(4)	C(13)-H(13B)	0.99
Cl(3)-C(24)	1.750(5)	C(14)-C(15)	1.512(6)
Cl(4)-C(25)	1.760(5)	C(14)-H(14A)	0.99
Cl(5)-C(25)	1.755(5)	C(14)-H(14B)	0.99
Cl(6)-C(25)	1.756(5)	C(15)-C(16)	1.516(6)
N(1)-C(1)	1.336(4)	C(15)-H(15A)	0.99
N(1)-C(2)	1.394(4)	C(15)-H(15B)	0.99
N(1)-C(12)	1.476(4)	C(16)-C(17)	1.535(5)
N(2)-C(1)	1.374(4)	C(16)-H(16A)	0.99

N(2)-C(3)	1.394(4)	C(16)-H(16B)	0.99
N(2)-C(4)	1.405(4)	C(17)-H(17A)	0.99
N(3)-C(4)	1.338(4)	C(17)-H(17B)	0.99
N(3)-C(8)	1.341(4)	C(18)-C(23)	1.516(5)
N(4)-C(11)	1.383(4)	C(18)-C(19)	1.519(5)
N(4)-C(9)	1.395(4)	C(18)-H(18)	1
N(4)-C(8)	1.403(4)	C(19)-C(20)	1.527(5)
N(5)-C(11)	1.331(4)	C(19)-H(19A)	0.99
N(5)-C(10)	1.399(4)	C(19)-H(19B)	0.99
N(5)-C(18)	1.478(4)	C(20)-C(21)	1.525(6)
C(2)-C(3)	1.340(5)	C(20)-H(20A)	0.99
C(2)-H(2)	0.95	C(20)-H(20B)	0.99
C(3)-H(3)	0.95	C(21)-C(22)	1.513(6)
C(4)-C(5)	1.383(4)	C(21)-H(21A)	0.99
C(5)-C(6)	1.390(5)	C(21)-H(21B)	0.99
C(5)-H(5)	0.95	C(22)-C(23)	1.524(5)
C(6)-C(7)	1.389(5)	C(22)-H(22A)	0.99
C(6)-H(6)	0.95	C(22)-H(22B)	0.99
C(7)-C(8)	1.381(4)	C(23)-H(23A)	0.99
C(7)-H(7)	0.95	C(23)-H(23B)	0.99
C(9)-C(10)	1.344(5)	C(24)-H(24)	1
C(9)-H(9)	0.95	C(25)-H(25)	1
C(10)-H(10)	0.95		

Table A.11: Bond lengths for [PDC<sup>Cy</sup>Pd(Br)](Br)

Bond	Angle	Bond	Angle
N(3)-Pd-C(1)	78.87(10)	C(15)-C(14)-H(14B)	109.4
N(3)-Pd-C(11)	79.02(11)	C(13)-C(14)-H(14B)	109.4
C(1)-Pd-C(11)	157.17(11)	H(14A)-C(14)-H(14B)	108
N(3)-Pd-Br(1)	170.67(7)	C(14)-C(15)-C(16)	111.5(3)
C(1)-Pd-Br(1)	100.95(8)	C(14)-C(15)-H(15A)	109.3
C(11)-Pd-Br(1)	101.79(8)	C(16)-C(15)-H(15A)	109.3
C(1)-N(1)-C(2)	110.7(3)	C(14)-C(15)-H(15B)	109.3
C(1)-N(1)-C(12)	123.8(2)	C(16)-C(15)-H(15B)	109.3

C(2)-N(1)-C(12)	125.5(2)	H(15A)-C(15)-H(15B)	108
C(1)-N(2)-C(3)	111.4(2)	C(15)-C(16)-C(17)	111.4(3)
C(1)-N(2)-C(4)	118.7(2)	C(15)-C(16)-H(16A)	109.4
C(3)-N(2)-C(4)	129.4(2)	C(17)-C(16)-H(16A)	109.4
C(4)-N(3)-C(8)	121.2(2)	C(15)-C(16)-H(16B)	109.4
C(4)-N(3)-Pd	118.97(19)	C(17)-C(16)-H(16B)	109.4
C(8)-N(3)-Pd	119.08(19)	H(16A)-C(16)-H(16B)	108
C(11)-N(4)-C(9)	111.0(2)	C(12)-C(17)-C(16)	109.2(3)
C(11)-N(4)-C(8)	118.7(2)	C(12)-C(17)-H(17A)	109.8
C(9)-N(4)-C(8)	130.1(3)	C(16)-C(17)-H(17A)	109.8
C(11)-N(5)-C(10)	111.3(3)	C(12)-C(17)-H(17B)	109.8
C(11)-N(5)-C(18)	123.2(2)	C(16)-C(17)-H(17B)	109.8
C(10)-N(5)-C(18)	125.2(2)	H(17A)-C(17)-H(17B)	108.3
N(1)-C(1)-N(2)	104.5(2)	N(5)-C(18)-C(23)	110.6(3)
N(1)-C(1)-Pd	143.3(2)	N(5)-C(18)-C(19)	111.4(3)
N(2)-C(1)-Pd	111.86(19)	C(23)-C(18)-C(19)	111.3(3)
C(3)-C(2)-N(1)	108.3(3)	N(5)-C(18)-H(18)	107.8
C(3)-C(2)-H(2)	125.9	C(23)-C(18)-H(18)	107.8
N(1)-C(2)-H(2)	125.9	C(19)-C(18)-H(18)	107.8
C(2)-C(3)-N(2)	105.2(3)	C(18)-C(19)-C(20)	109.8(3)
C(2)-C(3)-H(3)	127.4	C(18)-C(19)-H(19A)	109.7
N(2)-C(3)-H(3)	127.4	C(20)-C(19)-H(19A)	109.7
N(3)-C(4)-C(5)	121.5(3)	C(18)-C(19)-H(19B)	109.7
N(3)-C(4)-N(2)	110.8(2)	C(20)-C(19)-H(19B)	109.7
C(5)-C(4)-N(2)	127.7(3)	H(19A)-C(19)-H(19B)	108.2
C(4)-C(5)-C(6)	116.7(3)	C(21)-C(20)-C(19)	110.7(3)
C(4)-C(5)-H(5)	121.6	C(21)-C(20)-H(20A)	109.5
C(6)-C(5)-H(5)	121.6	C(19)-C(20)-H(20A)	109.5
C(7)-C(6)-C(5)	122.4(3)	C(21)-C(20)-H(20B)	109.5
C(7)-C(6)-H(6)	118.8	C(19)-C(20)-H(20B)	109.5
C(5)-C(6)-H(6)	118.8	H(20A)-C(20)-H(20B)	108.1
C(8)-C(7)-C(6)	116.7(3)	C(22)-C(21)-C(20)	111.7(3)
C(8)-C(7)-H(7)	121.6	C(22)-C(21)-H(21A)	109.3
C(6)-C(7)-H(7)	121.6	C(20)-C(21)-H(21A)	109.3
N(3)-C(8)-C(7)	121.5(3)	C(22)-C(21)-H(21B)	109.3
N(3)-C(8)-N(4)	111.0(2)	C(20)-C(21)-H(21B)	109.3
C(7)-C(8)-N(4)	127.5(3)	H(21A)-C(21)-H(21B)	107.9
C(10)-C(9)-N(4)	105.7(3)	C(21)-C(22)-C(23)	111.4(3)
C(10)-C(9)-H(9)	127.1	C(21)-C(22)-H(22A)	109.3

N(4)-C(9)-H(9)	127.1	C(23)-C(22)-H(22A)	109.3
C(9)-C(10)-N(5)	107.6(3)	C(21)-C(22)-H(22B)	109.3
C(9)-C(10)-H(10)	126.2	C(23)-C(22)-H(22B)	109.3
N(5)-C(10)-H(10)	126.2	H(22A)-C(22)-H(22B)	108
N(5)-C(11)-N(4)	104.3(2)	C(18)-C(23)-C(22)	109.3(3)
N(5)-C(11)-Pd	143.9(2)	C(18)-C(23)-H(23A)	109.8
N(4)-C(11)-Pd	111.55(19)	C(22)-C(23)-H(23A)	109.8
N(1)-C(12)-C(13)	110.7(3)	C(18)-C(23)-H(23B)	109.8
N(1)-C(12)-C(17)	111.8(3)	C(22)-C(23)-H(23B)	109.8
C(13)-C(12)-C(17)	111.8(3)	H(23A)-C(23)-H(23B)	108.3
N(1)-C(12)-H(12)	107.4	Cl(2)-C(24)-Cl(3)	110.3(3)
C(13)-C(12)-H(12)	107.4	Cl(2)-C(24)-Cl(1)	110.0(2)
C(17)-C(12)-H(12)	107.4	Cl(3)-C(24)-Cl(1)	110.6(2)
C(12)-C(13)-C(14)	110.4(3)	Cl(2)-C(24)-H(24)	108.6
C(12)-C(13)-H(13A)	109.6	Cl(3)-C(24)-H(24)	108.6
C(14)-C(13)-H(13A)	109.6	Cl(1)-C(24)-H(24)	108.6
C(12)-C(13)-H(13B)	109.6	Cl(5)-C(25)-Cl(6)	112.4(2)
C(14)-C(13)-H(13B)	109.6	Cl(5)-C(25)-Cl(4)	109.5(3)
H(13A)-C(13)-H(13B)	108.1	Cl(6)-C(25)-Cl(4)	110.1(2)
C(15)-C(14)-C(13)	111.1(3)	Cl(5)-C(25)-H(25)	108.2
C(15)-C(14)-H(14A)	109.4	Cl(6)-C(25)-H(25)	108.2
C(13)-C(14)-H(14A)	109.4	Cl(4)-C(25)-H(25)	108.2

Table A.12: Bond angles for [PDC<sup>Cy</sup>Pd(Br)](Br)

### A.7 Crystal Data for [PDC<sup>Dipp</sup>Pd(Br)](Br)

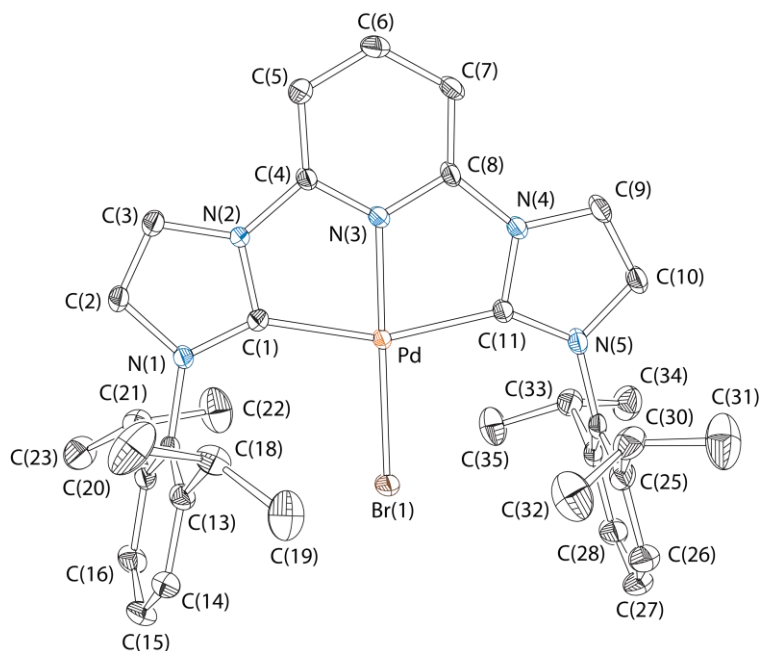


Figure A.6: Labeled thermal ellipsoid plot of  $[\text{PDC}^{\text{Dipp}}\text{Pd}(\text{Br})](\text{Br})$  with hydrogens and an outer sphere  $\text{Br}^-$  omitted and shown at the 50% probability level

Bond	Length	Bond	Length
Pd-N(3)	1.978(5)	C(16)-H(16)	0.95
Pd-C(11)	2.025(6)	C(17)-C(21)	1.527(11)
Pd-C(1)	2.033(6)	C(18)-C(19)	1.495(13)
Pd-Br(1)	2.3996(9)	C(18)-C(20)	1.521(13)
N(1)-C(1)	1.335(8)	C(18)-H(18)	1
N(1)-C(2)	1.399(8)	C(19)-H(19A)	0.98
N(1)-C(12)	1.458(8)	C(19)-H(19B)	0.98
N(2)-C(1)	1.373(8)	C(19)-H(19C)	0.98
N(2)-C(3)	1.396(8)	C(20)-H(20A)	0.98
N(2)-C(4)	1.418(8)	C(20)-H(20B)	0.98
N(3)-C(4)	1.319(8)	C(20)-H(20C)	0.98
N(3)-C(8)	1.343(8)	C(21)-C(23)	1.516(11)
N(4)-C(11)	1.369(8)	C(21)-C(22)	1.537(12)
N(4)-C(9)	1.389(8)	C(21)-H(21)	1
N(4)-C(8)	1.398(8)	C(22)-H(22A)	0.98

N(5)-C(11)	1.340(8)	C(22)-H(22B)	0.98
N(5)-C(10)	1.391(8)	C(22)-H(22C)	0.98
N(5)-C(24)	1.445(9)	C(23)-H(23A)	0.98
C(36)-Cl(2)	1.785(12)	C(23)-H(23B)	0.98
C(36)-Cl(1)	1.790(13)	C(23)-H(23C)	0.98
C(36)-Cl(3)	1.813(13)	C(24)-C(25)	1.396(10)
C(36)-H(36)	1	C(24)-C(29)	1.409(10)
C(36')-Cl(2')	1.818(14)	C(25)-C(26)	1.407(11)
C(36')-Cl(1')	1.822(14)	C(25)-C(30)	1.520(10)
C(36')-Cl(3')	1.856(14)	C(26)-C(27)	1.379(12)
C(36')-H(36')	1	C(26)-H(26)	0.95
Cl(2)-Cl(2)#1	2.213(15)	C(27)-C(28)	1.375(12)
C(2)-C(3)	1.324(10)	C(27)-H(27)	0.95
C(2)-H(2)	0.95	C(28)-C(29)	1.386(10)
C(3)-H(3)	0.95	C(28)-H(28)	0.95
C(4)-C(5)	1.386(9)	C(29)-C(33)	1.515(11)
C(5)-C(6)	1.382(10)	C(30)-C(31)	1.490(13)
C(5)-H(5)	0.95	C(30)-C(32)	1.526(12)
C(6)-C(7)	1.394(10)	C(30)-H(30)	1
C(6)-H(6)	0.95	C(31)-H(31A)	0.98
C(7)-C(8)	1.370(9)	C(31)-H(31B)	0.98
C(7)-H(7)	0.95	C(31)-H(31C)	0.98
C(9)-C(10)	1.321(11)	C(32)-H(32A)	0.98
C(9)-H(9)	0.95	C(32)-H(32B)	0.98
C(10)-H(10)	0.95	C(32)-H(32C)	0.98
C(12)-C(17)	1.373(9)	C(33)-C(34)	1.500(11)
C(12)-C(13)	1.398(10)	C(33)-C(35)	1.531(11)
C(13)-C(14)	1.405(10)	C(33)-H(33)	1
C(13)-C(18)	1.526(10)	C(34)-H(34A)	0.98
C(14)-C(15)	1.382(11)	C(34)-H(34B)	0.98
C(14)-H(14)	0.95	C(34)-H(34C)	0.98
C(15)-C(16)	1.373(12)	C(35)-H(35A)	0.98
C(15)-H(15)	0.95	C(35)-H(35B)	0.98
C(16)-C(17)	1.389(10)	C(35)-H(35C)	0.98

Table A.13: Bond lengths for [PDC<sup>DiPP</sup>Pd(Br)](Br)

Bond	Angle	Bond	Angle
N(3)-Pd-C(11)	79.2(2)	C(19)-C(18)-H(18)	107.6
N(3)-Pd-C(1)	79.0(2)	C(20)-C(18)-H(18)	107.6
C(11)-Pd-C(1)	158.1(3)	C(13)-C(18)-H(18)	107.6
N(3)-Pd-Br(1)	178.94(16)	C(18)-C(19)-H(19A)	109.5
C(11)-Pd-Br(1)	100.32(18)	C(18)-C(19)-H(19B)	109.5
C(1)-Pd-Br(1)	101.56(17)	H(19A)-C(19)-H(19B)	109.5
C(1)-N(1)-C(2)	111.1(5)	C(18)-C(19)-H(19C)	109.5
C(1)-N(1)-C(12)	124.8(5)	H(19A)-C(19)-H(19C)	109.5
C(2)-N(1)-C(12)	123.8(5)	H(19B)-C(19)-H(19C)	109.5
C(1)-N(2)-C(3)	111.9(5)	C(18)-C(20)-H(20A)	109.5
C(1)-N(2)-C(4)	118.7(5)	C(18)-C(20)-H(20B)	109.5
C(3)-N(2)-C(4)	129.4(5)	H(20A)-C(20)-H(20B)	109.5
C(4)-N(3)-C(8)	121.2(5)	C(18)-C(20)-H(20C)	109.5
C(4)-N(3)-Pd	119.8(4)	H(20A)-C(20)-H(20C)	109.5
C(8)-N(3)-Pd	119.0(4)	H(20B)-C(20)-H(20C)	109.5
C(11)-N(4)-C(9)	111.4(6)	C(23)-C(21)-C(17)	114.2(7)
C(11)-N(4)-C(8)	119.5(5)	C(23)-C(21)-C(22)	109.6(8)
C(9)-N(4)-C(8)	129.1(6)	C(17)-C(21)-C(22)	111.2(7)
C(11)-N(5)-C(10)	111.3(6)	C(23)-C(21)-H(21)	107.2
C(11)-N(5)-C(24)	126.4(5)	C(17)-C(21)-H(21)	107.2
C(10)-N(5)-C(24)	122.3(6)	C(22)-C(21)-H(21)	107.2
Cl(2)-C(36)-Cl(1)	108.8(8)	C(21)-C(22)-H(22A)	109.5
Cl(2)-C(36)-Cl(3)	122.5(10)	C(21)-C(22)-H(22B)	109.5
Cl(1)-C(36)-Cl(3)	106.8(8)	H(22A)-C(22)-H(22B)	109.5
Cl(2)-C(36)-H(36)	105.9	C(21)-C(22)-H(22C)	109.5
Cl(1)-C(36)-H(36)	105.9	H(22A)-C(22)-H(22C)	109.5
Cl(3)-C(36)-H(36)	105.9	H(22B)-C(22)-H(22C)	109.5
Cl(2')-C(36')-Cl(1')	109.2(10)	C(21)-C(23)-H(23A)	109.5
Cl(2')-C(36')-Cl(3')	96.3(8)	C(21)-C(23)-H(23B)	109.5
Cl(1')-C(36')-Cl(3')	115.7(11)	H(23A)-C(23)-H(23B)	109.5
Cl(2')-C(36')-H(36')	111.5	C(21)-C(23)-H(23C)	109.5
Cl(1')-C(36')-H(36')	111.5	H(23A)-C(23)-H(23C)	109.5
Cl(3')-C(36')-H(36')	111.5	H(23B)-C(23)-H(23C)	109.5
C(36)-Cl(2)-Cl(2)#1	98.4(7)	C(25)-C(24)-C(29)	123.9(7)
N(1)-C(1)-N(2)	103.6(5)	C(25)-C(24)-N(5)	117.6(6)
N(1)-C(1)-Pd	144.8(5)	C(29)-C(24)-N(5)	118.5(6)
N(2)-C(1)-Pd	111.5(4)	C(24)-C(25)-C(26)	116.8(7)
C(3)-C(2)-N(1)	108.2(6)	C(24)-C(25)-C(30)	123.1(7)

C(3)-C(2)-H(2)	125.9	C(26)-C(25)-C(30)	120.1(7)
N(1)-C(2)-H(2)	125.9	C(27)-C(26)-C(25)	120.3(8)
C(2)-C(3)-N(2)	105.2(6)	C(27)-C(26)-H(26)	119.9
C(2)-C(3)-H(3)	127.4	C(25)-C(26)-H(26)	119.9
N(2)-C(3)-H(3)	127.4	C(28)-C(27)-C(26)	121.2(7)
N(3)-C(4)-C(5)	122.0(6)	C(28)-C(27)-H(27)	119.4
N(3)-C(4)-N(2)	111.1(5)	C(26)-C(27)-H(27)	119.4
C(5)-C(4)-N(2)	126.9(6)	C(27)-C(28)-C(29)	121.6(8)
C(6)-C(5)-C(4)	116.7(6)	C(27)-C(28)-H(28)	119.2
C(6)-C(5)-H(5)	121.7	C(29)-C(28)-H(28)	119.2
C(4)-C(5)-H(5)	121.7	C(28)-C(29)-C(24)	116.2(7)
C(5)-C(6)-C(7)	121.5(6)	C(28)-C(29)-C(33)	120.5(7)
C(5)-C(6)-H(6)	119.3	C(24)-C(29)-C(33)	123.2(6)
C(7)-C(6)-H(6)	119.3	C(31)-C(30)-C(25)	112.5(7)
C(8)-C(7)-C(6)	117.6(6)	C(31)-C(30)-C(32)	109.1(9)
C(8)-C(7)-H(7)	121.2	C(25)-C(30)-C(32)	112.4(7)
C(6)-C(7)-H(7)	121.2	C(31)-C(30)-H(30)	107.5
N(3)-C(8)-C(7)	121.0(6)	C(25)-C(30)-H(30)	107.5
N(3)-C(8)-N(4)	110.8(5)	C(32)-C(30)-H(30)	107.5
C(7)-C(8)-N(4)	128.1(6)	C(30)-C(31)-H(31A)	109.5
C(10)-C(9)-N(4)	106.1(6)	C(30)-C(31)-H(31B)	109.5
C(10)-C(9)-H(9)	127	H(31A)-C(31)-H(31B)	109.5
N(4)-C(9)-H(9)	127	C(30)-C(31)-H(31C)	109.5
C(9)-C(10)-N(5)	107.7(6)	H(31A)-C(31)-H(31C)	109.5
C(9)-C(10)-H(10)	126.2	H(31B)-C(31)-H(31C)	109.5
N(5)-C(10)-H(10)	126.2	C(30)-C(32)-H(32A)	109.5
N(5)-C(11)-N(4)	103.6(5)	C(30)-C(32)-H(32B)	109.5
N(5)-C(11)-Pd	144.9(5)	H(32A)-C(32)-H(32B)	109.5
N(4)-C(11)-Pd	111.5(4)	C(30)-C(32)-H(32C)	109.5
C(17)-C(12)-C(13)	124.0(6)	H(32A)-C(32)-H(32C)	109.5
C(17)-C(12)-N(1)	119.5(6)	H(32B)-C(32)-H(32C)	109.5
C(13)-C(12)-N(1)	116.4(6)	C(34)-C(33)-C(29)	112.9(7)
C(12)-C(13)-C(14)	116.5(6)	C(34)-C(33)-C(35)	109.6(7)
C(12)-C(13)-C(18)	123.0(6)	C(29)-C(33)-C(35)	110.9(7)
C(14)-C(13)-C(18)	120.5(7)	C(34)-C(33)-H(33)	107.8
C(15)-C(14)-C(13)	120.5(7)	C(29)-C(33)-H(33)	107.8
C(15)-C(14)-H(14)	119.8	C(35)-C(33)-H(33)	107.8
C(13)-C(14)-H(14)	119.8	C(33)-C(34)-H(34A)	109.5
C(16)-C(15)-C(14)	120.4(7)	C(33)-C(34)-H(34B)	109.5

C(16)-C(15)-H(15)	119.8	H(34A)-C(34)-H(34B)	109.5
C(14)-C(15)-H(15)	119.8	C(33)-C(34)-H(34C)	109.5
C(15)-C(16)-C(17)	121.4(7)	H(34A)-C(34)-H(34C)	109.5
C(15)-C(16)-H(16)	119.3	H(34B)-C(34)-H(34C)	109.5
C(17)-C(16)-H(16)	119.3	C(33)-C(35)-H(35A)	109.5
C(12)-C(17)-C(16)	117.1(7)	C(33)-C(35)-H(35B)	109.5
C(12)-C(17)-C(21)	121.9(6)	H(35A)-C(35)-H(35B)	109.5
C(16)-C(17)-C(21)	120.9(6)	C(33)-C(35)-H(35C)	109.5
C(19)-C(18)-C(20)	111.5(7)	H(35A)-C(35)-H(35C)	109.5
C(19)-C(18)-C(13)	113.0(7)	H(35B)-C(35)-H(35C)	109.5
C(20)-C(18)-C(13)	109.4(7)		

Table A:14: Bond angles for [PDC<sup>Dipp</sup>Pd(Br)](Br)

#### A.8 Crystal Data for [PDC<sup>Me</sup>Pd(MeCN)](PF<sub>6</sub>)<sub>2</sub>

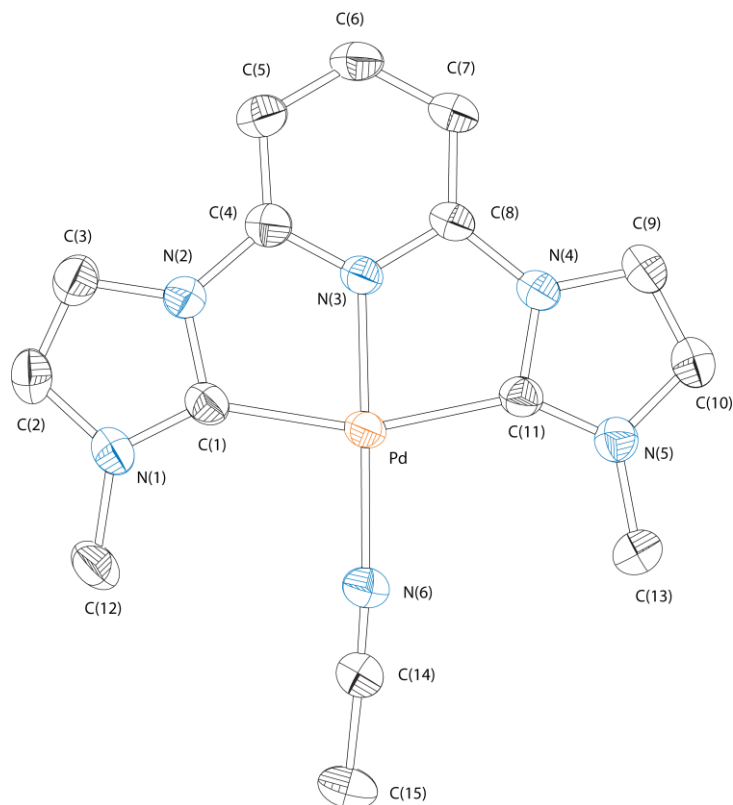


Figure A.7: Fully labeled thermal ellipsoid plot of  $[\text{PDC}^{\text{Me}}\text{Pd}(\text{MeCN})](\text{PF}_6)_2$  with hydrogens and two outer sphere  $\text{PF}_6^-$  ions omitted and shown at the 50% probability level

Bond	Length	Bond	Length
Pd-N(3)	1.961(3)	N(2)-C(1)	1.374(5)
Pd-N(6)	2.003(3)	N(2)-C(3)	1.391(5)
Pd-C(1)	2.030(4)	N(2)-C(4)	1.401(5)
Pd-C(11)	2.031(4)	N(3)-C(4)	1.339(5)
P(1)-F(2)	1.539(5)	N(3)-C(8)	1.341(5)
P(1)-F(4)	1.542(4)	N(4)-C(11)	1.373(5)
P(1)-F(6)	1.549(5)	N(4)-C(9)	1.386(5)
P(1)-F(1)	1.558(4)	N(4)-C(8)	1.408(5)
P(1)-F(3)	1.588(3)	N(5)-C(11)	1.333(5)
P(1)-F(5)	1.593(4)	N(5)-C(10)	1.395(5)
P(2)-F(10)	1.544(5)	N(5)-C(13)	1.461(5)
P(2)-F(8)	1.557(5)	N(6)-C(14)	1.125(6)

P(2)-F(9)	1.561(4)	C(2)-C(3)	1.338(7)
P(2)-F(7)	1.574(4)	C(4)-C(5)	1.383(6)
P(2)-F(12)	1.581(4)	C(5)-C(6)	1.395(6)
P(2)-F(11)	1.598(4)	C(6)-C(7)	1.391(6)
N(1)-C(1)	1.333(5)	C(7)-C(8)	1.384(5)
N(1)-C(2)	1.395(6)	C(9)-C(10)	1.347(6)
N(1)-C(12)	1.465(6)	C(14)-C(15)	1.459(6)

Table A.15: Bond lengths for  $[\text{PDC}^{\text{Me}}\text{Pd}(\text{MeCN})](\text{PF}_6)_2$

Bond	Angle	Bond	Angle
N(3)-Pd-N(6)	178.98(13)	C(1)-N(1)-C(2)	110.5(4)
N(3)-Pd-C(1)	79.42(15)	C(1)-N(1)-C(12)	125.5(4)
N(6)-Pd-C(1)	99.57(15)	C(2)-N(1)-C(12)	124.0(4)
N(3)-Pd-C(11)	79.43(14)	C(1)-N(2)-C(3)	110.8(3)
N(6)-Pd-C(11)	101.57(15)	C(1)-N(2)-C(4)	118.9(3)
C(1)-Pd-C(11)	158.85(15)	C(3)-N(2)-C(4)	130.2(4)
F(2)-P(1)-F(4)	178.6(4)	C(4)-N(3)-C(8)	121.3(3)
F(2)-P(1)-F(6)	91.7(5)	C(4)-N(3)-Pd	119.2(3)
F(4)-P(1)-F(6)	87.0(4)	C(8)-N(3)-Pd	119.5(3)
F(2)-P(1)-F(1)	88.9(4)	C(11)-N(4)-C(9)	110.9(3)
F(4)-P(1)-F(1)	92.4(4)	C(11)-N(4)-C(8)	119.0(3)
F(6)-P(1)-F(1)	179.1(3)	C(9)-N(4)-C(8)	130.1(3)
F(2)-P(1)-F(3)	90.5(3)	C(11)-N(5)-C(10)	110.9(3)
F(4)-P(1)-F(3)	89.0(3)	C(11)-N(5)-C(13)	124.9(4)
F(6)-P(1)-F(3)	87.4(3)	C(10)-N(5)-C(13)	124.1(4)
F(1)-P(1)-F(3)	91.9(2)	C(14)-N(6)-Pd	173.0(4)
F(2)-P(1)-F(5)	89.0(3)	N(1)-C(1)-N(2)	104.9(3)
F(4)-P(1)-F(5)	91.5(3)	N(1)-C(1)-Pd	143.9(3)
F(6)-P(1)-F(5)	92.0(3)	N(2)-C(1)-Pd	111.2(3)
F(1)-P(1)-F(5)	88.7(2)	C(3)-C(2)-N(1)	108.0(4)
F(3)-P(1)-F(5)	179.2(3)	C(2)-C(3)-N(2)	105.7(4)
F(10)-P(2)-F(8)	174.4(4)	N(3)-C(4)-C(5)	121.5(4)
F(10)-P(2)-F(9)	90.1(4)	N(3)-C(4)-N(2)	111.2(3)
F(8)-P(2)-F(9)	95.5(4)	C(5)-C(4)-N(2)	127.3(4)
F(10)-P(2)-F(7)	88.4(4)	C(4)-C(5)-C(6)	116.8(4)

F(8)-P(2)-F(7)	91.4(3)	C(7)-C(6)-C(5)	122.0(4)
F(9)-P(2)-F(7)	92.6(2)	C(8)-C(7)-C(6)	117.0(4)
F(10)-P(2)-F(12)	91.3(4)	N(3)-C(8)-C(7)	121.4(4)
F(8)-P(2)-F(12)	88.7(4)	N(3)-C(8)-N(4)	110.9(3)
F(9)-P(2)-F(12)	89.1(2)	C(7)-C(8)-N(4)	127.7(4)
F(7)-P(2)-F(12)	178.2(2)	C(10)-C(9)-N(4)	106.0(4)
F(10)-P(2)-F(11)	88.7(3)	C(9)-C(10)-N(5)	107.3(4)
F(8)-P(2)-F(11)	85.7(3)	N(5)-C(11)-N(4)	104.8(3)
F(9)-P(2)-F(11)	178.1(3)	N(5)-C(11)-Pd	143.9(3)
F(7)-P(2)-F(11)	88.85(19)	N(4)-C(11)-Pd	111.3(3)
F(12)-P(2)-F(11)	89.4(2)	N(6)-C(14)-C(15)	177.9(5)

Table A.16: Bond angles for  $[\text{PDC}^{\text{Me}}\text{Pd}(\text{MeCN})](\text{PF}_6)_2$

### A.9 Crystal Data for $[\text{PDC}^{\text{Et}}\text{Pd}(\text{MeCN})](\text{PF}_6)_2$

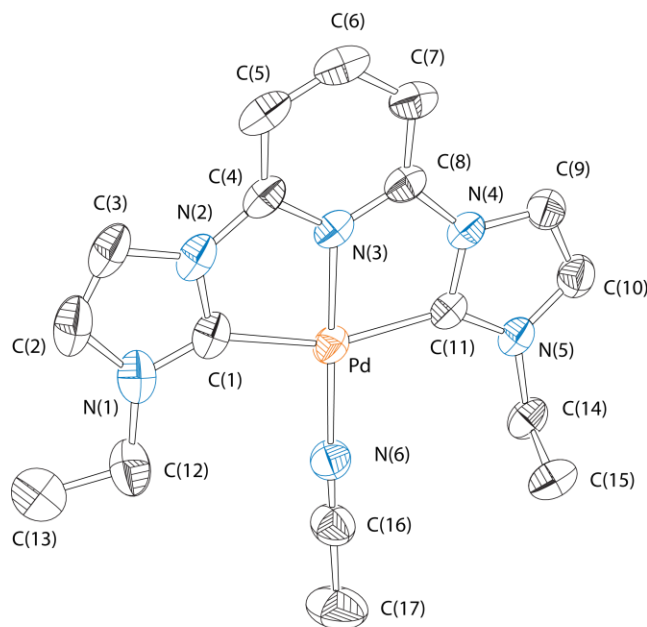


Figure A.8: Fully labeled thermal ellipsoid plot of  $[\text{PDC}^{\text{Et}}\text{Pd}(\text{MeCN})](\text{PF}_6)_2$  with hydrogens and two outer sphere  $\text{PF}_6^-$  ions omitted and shown at the 50% probability level

<b>Bond</b>	<b>Length</b>	<b>Bond</b>	<b>Length</b>
Pd-N(3)	1.966(2)	N(2)-C(3)	1.390(4)
Pd-N(6)	2.004(3)	N(2)-C(4)	1.401(4)
Pd-C(1)	2.029(3)	N(3)-C(8)	1.336(4)
Pd-C(11)	2.034(3)	N(3)-C(4)	1.340(4)
P(1)-F(2)	1.521(5)	N(4)-C(11)	1.368(4)
P(1)-F(4)	1.529(5)	N(4)-C(9)	1.384(4)
P(1)-F(6)	1.551(5)	N(4)-C(8)	1.402(4)
P(1)-F(3)	1.562(4)	N(5)-C(11)	1.332(4)
P(1)-F(1)	1.565(5)	N(5)-C(10)	1.392(4)
P(1)-F(5)	1.615(6)	N(5)-C(14)	1.476(4)
P(2)-F(9)	1.567(3)	N(6)-C(16)	1.125(5)
P(2)-F(12)	1.586(2)	C(2)-C(3)	1.324(6)
P(2)-F(8)	1.590(2)	C(4)-C(5)	1.376(5)
P(2)-F(7)	1.596(2)	C(5)-C(6)	1.384(6)
P(2)-F(10)	1.596(2)	C(6)-C(7)	1.388(5)
P(2)-F(11)	1.608(2)	C(7)-C(8)	1.381(4)
N(1)-C(1)	1.334(5)	C(9)-C(10)	1.335(5)
N(1)-C(2)	1.405(5)	C(12)-C(13)	1.509(15)
N(1)-C(12')	1.47(3)	C(12')-C(13')	1.511(14)
N(1)-C(12)	1.51(4)	C(14)-C(15)	1.512(5)
N(2)-C(1)	1.370(4)	C(16)-C(17)	1.460(5)

Table A.17: Bond lengths for  $[\text{PDC}^{\text{Et}}\text{Pd}(\text{MeCN})](\text{PF}_6)_2$

<b>Bond</b>	<b>Angle</b>	<b>Bond</b>	<b>Angle</b>
N(3)-Pd-N(6)	177.50(10)	C(1)-N(1)-C(12)	121.6(9)
N(3)-Pd-C(1)	79.18(13)	C(2)-N(1)-C(12)	128.2(10)
N(6)-Pd-C(1)	101.12(13)	C(1)-N(2)-C(3)	110.7(3)
N(3)-Pd-C(11)	79.12(11)	C(1)-N(2)-C(4)	118.8(3)

N(6)-Pd-C(11)	100.54(12)	C(3)-N(2)-C(4)	130.5(3)
C(1)-Pd-C(11)	158.30(13)	C(8)-N(3)-C(4)	121.5(3)
F(2)-P(1)-F(4)	95.4(4)	C(8)-N(3)-Pd	119.3(2)
F(2)-P(1)-F(6)	85.6(3)	C(4)-N(3)-Pd	119.2(2)
F(4)-P(1)-F(6)	88.8(4)	C(11)-N(4)-C(9)	111.0(3)
F(2)-P(1)-F(3)	98.6(4)	C(11)-N(4)-C(8)	118.9(3)
F(4)-P(1)-F(3)	92.5(3)	C(9)-N(4)-C(8)	130.0(3)
F(6)-P(1)-F(3)	175.4(4)	C(11)-N(5)-C(10)	110.3(3)
F(2)-P(1)-F(1)	88.0(3)	C(11)-N(5)-C(14)	124.7(3)
F(4)-P(1)-F(1)	176.1(4)	C(10)-N(5)-C(14)	124.8(3)
F(6)-P(1)-F(1)	89.7(3)	C(16)-N(6)-Pd	174.8(3)
F(3)-P(1)-F(1)	88.7(3)	N(1)-C(1)-N(2)	105.3(3)
F(2)-P(1)-F(5)	172.6(4)	N(1)-C(1)-Pd	143.1(3)
F(4)-P(1)-F(5)	89.4(4)	N(2)-C(1)-Pd	111.6(2)
F(6)-P(1)-F(5)	89.0(3)	C(3)-C(2)-N(1)	108.5(3)
F(3)-P(1)-F(5)	86.7(4)	C(2)-C(3)-N(2)	105.9(3)
F(1)-P(1)-F(5)	87.0(4)	N(3)-C(4)-C(5)	120.7(3)
F(9)-P(2)-F(12)	178.55(18)	N(3)-C(4)-N(2)	111.2(3)
F(9)-P(2)-F(8)	91.94(18)	C(5)-C(4)-N(2)	128.0(3)
F(12)-P(2)-F(8)	89.48(16)	C(4)-C(5)-C(6)	117.7(3)
F(9)-P(2)-F(7)	90.46(15)	C(5)-C(6)-C(7)	121.9(3)
F(12)-P(2)-F(7)	89.29(14)	C(8)-C(7)-C(6)	116.7(3)
F(8)-P(2)-F(7)	90.30(13)	N(3)-C(8)-C(7)	121.5(3)
F(9)-P(2)-F(10)	90.62(14)	N(3)-C(8)-N(4)	111.2(2)
F(12)-P(2)-F(10)	89.62(13)	C(7)-C(8)-N(4)	127.2(3)
F(8)-P(2)-F(10)	90.39(13)	C(10)-C(9)-N(4)	105.8(3)
F(7)-P(2)-F(10)	178.70(14)	C(9)-C(10)-N(5)	108.0(3)
F(9)-P(2)-F(11)	89.36(18)	N(5)-C(11)-N(4)	104.9(3)
F(12)-P(2)-F(11)	89.22(16)	N(5)-C(11)-Pd	143.7(2)
F(8)-P(2)-F(11)	178.56(17)	N(4)-C(11)-Pd	111.4(2)
F(7)-P(2)-F(11)	89.07(14)	N(1)-C(12)-C(13)	111(2)
F(10)-P(2)-F(11)	90.21(13)	N(1)-C(12')-C(13')	107.1(17)
C(1)-N(1)-C(2)	109.6(3)	N(5)-C(14)-C(15)	110.4(3)
C(1)-N(1)-C(12')	126.7(9)	N(6)-C(16)-C(17)	179.2(5)
C(2)-N(1)-C(12')	122.9(9)		

Table A.18: Bond angles for  $[\text{PDC}^{\text{Et}}\text{Pd}(\text{MeCN})](\text{PF}_6)_2$

### A.10 Crystal Data for $[\text{PDC}^{\text{Ipr}}\text{Pd}(\text{MeCN})](\text{PF}_6)_2$

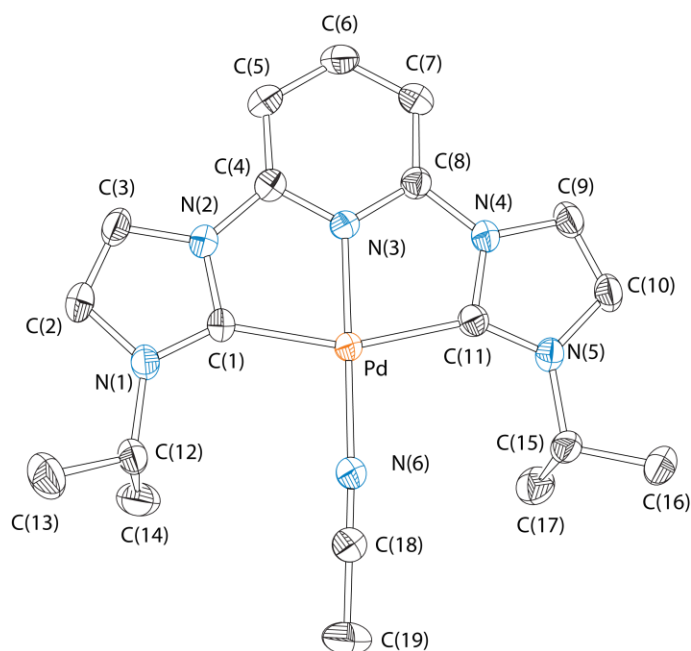


Figure A.9: Fully labeled thermal ellipsoid plot of  $[\text{PDC}^{\text{Ipr}}\text{Pd}(\text{MeCN})](\text{PF}_6)_2$  with hydrogens and two outer sphere  $\text{PF}_6^-$  ions omitted and shown at the 50% probability level

Bond	Length	Bond	Length
Pd-N(3)	1.961(2)	N(3)-C(4)	1.342(3)
Pd-N(6)	2.001(2)	N(3)-C(8)	1.343(3)
Pd-C(1)	2.038(3)	N(4)-C(11)	1.377(3)
Pd-C(11)	2.039(3)	N(4)-C(9)	1.390(3)
P(1)-F(5)	1.584(2)	N(4)-C(8)	1.403(3)
P(1)-F(2)	1.586(2)	N(5)-C(11)	1.336(3)
P(1)-F(3)	1.589(3)	N(5)-C(10)	1.400(3)

P(1)-F(4)	1.596(2)	N(5)-C(15)	1.494(3)
P(1)-F(6)	1.596(3)	N(6)-C(18)	1.126(4)
P(1)-F(1)	1.601(3)	N(7)-C(20)	1.129(4)
P(2)-F(12)	1.562(3)	C(2)-C(3)	1.338(4)
P(2)-F(8)	1.570(2)	C(4)-C(5)	1.382(4)
P(2)-F(7)	1.584(2)	C(5)-C(6)	1.394(4)
P(2)-F(9)	1.585(3)	C(6)-C(7)	1.384(4)
P(2)-F(11)	1.590(3)	C(7)-C(8)	1.380(4)
P(2)-F(10)	1.596(2)	C(9)-C(10)	1.336(4)
N(1)-C(1)	1.332(3)	C(12)-C(14)	1.506(5)
N(1)-C(2)	1.397(4)	C(12)-C(13)	1.519(4)
N(1)-C(12)	1.498(4)	C(15)-C(17)	1.518(4)
N(2)-C(1)	1.375(3)	C(15)-C(16)	1.520(4)
N(2)-C(3)	1.396(3)	C(18)-C(19)	1.462(4)
N(2)-C(4)	1.402(3)	C(20)-C(21)	1.454(5)

Table A.19: Bond lengths for  $[\text{PDC}^{\text{IPr}}\text{Pd}(\text{MeCN})](\text{PF}_6)_2$

Bond	Angle	Bond	Angle
N(3)-Pd-N(6)	178.91(9)	C(1)-N(2)-C(4)	119.4(2)
N(3)-Pd-C(1)	79.20(10)	C(3)-N(2)-C(4)	130.1(2)
N(6)-Pd-C(1)	100.38(10)	C(4)-N(3)-C(8)	120.5(2)
N(3)-Pd-C(11)	79.27(10)	C(4)-N(3)-Pd	119.77(18)
N(6)-Pd-C(11)	101.16(10)	C(8)-N(3)-Pd	119.69(18)
C(1)-Pd-C(11)	158.46(11)	C(11)-N(4)-C(9)	111.0(2)
F(5)-P(1)-F(2)	89.93(14)	C(11)-N(4)-C(8)	119.2(2)
F(5)-P(1)-F(3)	90.75(16)	C(9)-N(4)-C(8)	129.7(2)
F(2)-P(1)-F(3)	89.83(14)	C(11)-N(5)-C(10)	110.5(2)
F(5)-P(1)-F(4)	179.44(16)	C(11)-N(5)-C(15)	123.3(2)
F(2)-P(1)-F(4)	90.10(14)	C(10)-N(5)-C(15)	126.2(2)
F(3)-P(1)-F(4)	88.69(15)	C(18)-N(6)-Pd	175.2(3)
F(5)-P(1)-F(6)	89.45(15)	N(1)-C(1)-N(2)	105.2(2)
F(2)-P(1)-F(6)	179.16(15)	N(1)-C(1)-Pd	143.8(2)
F(3)-P(1)-F(6)	90.74(16)	N(2)-C(1)-Pd	110.97(18)
F(4)-P(1)-F(6)	90.53(15)	C(3)-C(2)-N(1)	108.0(3)
F(5)-P(1)-F(1)	90.28(16)	C(2)-C(3)-N(2)	105.8(3)

F(2)-P(1)-F(1)	89.29(14)	N(3)-C(4)-C(5)	121.7(3)
F(3)-P(1)-F(1)	178.65(16)	N(3)-C(4)-N(2)	110.7(2)
F(4)-P(1)-F(1)	90.28(14)	C(5)-C(4)-N(2)	127.7(3)
F(6)-P(1)-F(1)	90.15(16)	C(4)-C(5)-C(6)	117.0(3)
F(12)-P(2)-F(8)	92.47(18)	C(7)-C(6)-C(5)	121.8(3)
F(12)-P(2)-F(7)	92.0(2)	C(8)-C(7)-C(6)	117.1(3)
F(8)-P(2)-F(7)	91.75(16)	N(3)-C(8)-C(7)	121.8(2)
F(12)-P(2)-F(9)	88.4(2)	N(3)-C(8)-N(4)	110.8(2)
F(8)-P(2)-F(9)	88.79(16)	C(7)-C(8)-N(4)	127.3(3)
F(7)-P(2)-F(9)	179.34(19)	C(10)-C(9)-N(4)	105.8(2)
F(12)-P(2)-F(11)	178.75(19)	C(9)-C(10)-N(5)	108.0(2)
F(8)-P(2)-F(11)	88.72(16)	N(5)-C(11)-N(4)	104.7(2)
F(7)-P(2)-F(11)	88.37(16)	N(5)-C(11)-Pd	144.3(2)
F(9)-P(2)-F(11)	91.26(19)	N(4)-C(11)-Pd	111.01(18)
F(12)-P(2)-F(10)	88.72(17)	N(1)-C(12)-C(14)	110.4(2)
F(8)-P(2)-F(10)	178.54(18)	N(1)-C(12)-C(13)	110.5(3)
F(7)-P(2)-F(10)	89.05(14)	C(14)-C(12)-C(13)	112.8(3)
F(9)-P(2)-F(10)	90.41(15)	N(5)-C(15)-C(17)	109.9(2)
F(11)-P(2)-F(10)	90.09(16)	N(5)-C(15)-C(16)	111.1(2)
C(1)-N(1)-C(2)	110.5(2)	C(17)-C(15)-C(16)	112.1(3)
C(1)-N(1)-C(12)	124.0(2)	N(6)-C(18)-C(19)	179.6(4)
C(2)-N(1)-C(12)	125.5(2)	N(7)-C(20)-C(21)	179.8(4)
C(1)-N(2)-C(3)	110.5(2)		

Table A.20: Bond angles for  $[\text{PDC}^{\text{Ipr}}\text{Pd}(\text{MeCN})](\text{PF}_6)_2$

### A.11 Crystal Data for $[\text{PDC}^{\text{Cy}}\text{Pd}(\text{MeCN})](\text{PF}_6)_2$

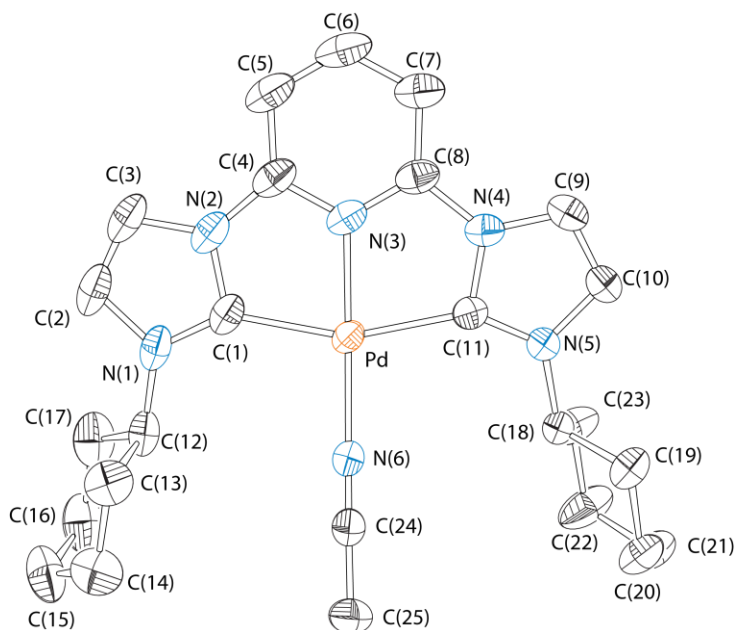


Figure A.10: Fully labeled thermal ellipsoid plot of  $[\text{PDC}^{\text{Cy}}\text{Pd}(\text{MeCN})](\text{PF}_6)_2$  with hydrogens and two outer sphere  $\text{PF}_6^-$  ions omitted and shown at the 50% probability level

Bond	Length	Bond	Length
Pd-N(3)	1.9627(19)	N(4)-C(9)	1.384(3)
Pd-N(6)	2.003(2)	N(4)-C(8)	1.398(3)
Pd-C(1)	2.038(2)	N(5)-C(11)	1.328(3)
Pd-C(11)	2.040(2)	N(5)-C(10)	1.396(3)
P(1)-F(5)	1.571(2)	N(5)-C(18)	1.479(3)
P(1)-F(3)	1.575(2)	N(6)-C(24)	1.129(3)
P(1)-F(2)	1.5756(19)	C(2)-C(3)	1.330(4)
P(1)-F(6)	1.579(2)	C(4)-C(5)	1.379(3)
P(1)-F(4)	1.593(2)	C(5)-C(6)	1.379(4)
P(1)-F(1)	1.6018(19)	C(6)-C(7)	1.392(4)
P(2)-F(12)	1.584(2)	C(7)-C(8)	1.384(3)
P(2)-F(7)	1.591(2)	C(9)-C(10)	1.334(3)
P(2)-F(8)	1.5933(19)	C(12)-C(13)	1.513(3)
P(2)-F(11)	1.5960(19)	C(12)-C(17)	1.521(3)

P(2)-F(10)	1.5967(19)	C(13)-C(14)	1.528(4)
P(2)-F(9)	1.606(2)	C(14)-C(15)	1.508(4)
N(1)-C(1)	1.335(3)	C(15)-C(16)	1.517(5)
N(1)-C(2)	1.399(3)	C(16)-C(17)	1.515(5)
N(1)-C(12)	1.480(3)	C(18)-C(23)	1.515(4)
N(2)-C(1)	1.376(3)	C(18)-C(19)	1.523(3)
N(2)-C(3)	1.393(3)	C(19)-C(20)	1.529(3)
N(2)-C(4)	1.397(3)	C(20)-C(21)	1.516(4)
N(3)-C(8)	1.333(3)	C(21)-C(22)	1.521(4)
N(3)-C(4)	1.343(3)	C(22)-C(23)	1.526(4)
N(4)-C(11)	1.380(3)	C(24)-C(25)	1.448(3)

Table A.21: Bond lengths for [PDC<sup>Cy</sup>Pd(MeCN)](PF<sub>6</sub>)<sub>2</sub>

Bond	Angle	Bond	Angle
N(3)-Pd-N(6)	173.86(7)	C(4)-N(3)-Pd	119.23(17)
N(3)-Pd-C(1)	79.39(9)	C(11)-N(4)-C(9)	110.68(19)
N(6)-Pd-C(1)	100.39(9)	C(11)-N(4)-C(8)	118.88(19)
N(3)-Pd-C(11)	79.22(9)	C(9)-N(4)-C(8)	130.01(19)
N(6)-Pd-C(11)	101.15(8)	C(11)-N(5)-C(10)	111.00(18)
C(1)-Pd-C(11)	158.46(9)	C(11)-N(5)-C(18)	125.06(17)
F(5)-P(1)-F(3)	88.91(15)	C(10)-N(5)-C(18)	123.69(18)
F(5)-P(1)-F(2)	90.99(14)	C(24)-N(6)-Pd	169.7(2)
F(3)-P(1)-F(2)	89.53(12)	N(1)-C(1)-N(2)	105.01(19)
F(5)-P(1)-F(6)	178.01(14)	N(1)-C(1)-Pd	144.14(17)
F(3)-P(1)-F(6)	91.64(15)	N(2)-C(1)-Pd	110.82(17)
F(2)-P(1)-F(6)	90.92(15)	C(3)-C(2)-N(1)	107.6(2)
F(5)-P(1)-F(4)	89.34(13)	C(2)-C(3)-N(2)	106.6(2)
F(3)-P(1)-F(4)	91.36(13)	N(3)-C(4)-C(5)	121.0(2)
F(2)-P(1)-F(4)	179.05(11)	N(3)-C(4)-N(2)	111.1(2)
F(6)-P(1)-F(4)	88.74(15)	C(5)-C(4)-N(2)	127.9(2)
F(5)-P(1)-F(1)	90.92(13)	C(6)-C(5)-C(4)	117.5(2)
F(3)-P(1)-F(1)	179.74(15)	C(5)-C(6)-C(7)	122.1(2)
F(2)-P(1)-F(1)	90.67(10)	C(8)-C(7)-C(6)	116.6(3)
F(6)-P(1)-F(1)	88.52(13)	N(3)-C(8)-C(7)	121.6(2)

F(4)-P(1)-F(1)	88.44(11)	N(3)-C(8)-N(4)	111.46(18)
F(12)-P(2)-F(7)	91.27(12)	C(7)-C(8)-N(4)	126.9(2)
F(12)-P(2)-F(8)	90.98(13)	C(10)-C(9)-N(4)	106.3(2)
F(7)-P(2)-F(8)	90.46(11)	C(9)-C(10)-N(5)	107.5(2)
F(12)-P(2)-F(11)	178.61(12)	N(5)-C(11)-N(4)	104.54(18)
F(7)-P(2)-F(11)	90.09(11)	N(5)-C(11)-Pd	144.14(16)
F(8)-P(2)-F(11)	89.33(12)	N(4)-C(11)-Pd	110.86(15)
F(12)-P(2)-F(10)	89.52(13)	N(1)-C(12)-C(13)	110.8(2)
F(7)-P(2)-F(10)	90.16(10)	N(1)-C(12)-C(17)	111.2(2)
F(8)-P(2)-F(10)	179.20(12)	C(13)-C(12)-C(17)	111.9(2)
F(11)-P(2)-F(10)	90.16(12)	C(12)-C(13)-C(14)	110.0(2)
F(12)-P(2)-F(9)	89.61(11)	C(15)-C(14)-C(13)	111.9(3)
F(7)-P(2)-F(9)	179.12(12)	C(14)-C(15)-C(16)	110.5(2)
F(8)-P(2)-F(9)	89.55(10)	C(17)-C(16)-C(15)	111.2(3)
F(11)-P(2)-F(9)	89.03(10)	C(16)-C(17)-C(12)	111.1(2)
F(10)-P(2)-F(9)	89.82(10)	N(5)-C(18)-C(23)	109.44(18)
C(1)-N(1)-C(2)	110.6(2)	N(5)-C(18)-C(19)	111.37(18)
C(1)-N(1)-C(12)	124.99(18)	C(23)-C(18)-C(19)	111.1(2)
C(2)-N(1)-C(12)	124.4(2)	C(18)-C(19)-C(20)	109.5(2)
C(1)-N(2)-C(3)	110.2(2)	C(21)-C(20)-C(19)	111.5(2)
C(1)-N(2)-C(4)	119.37(19)	C(20)-C(21)-C(22)	110.7(2)
C(3)-N(2)-C(4)	130.4(2)	C(21)-C(22)-C(23)	111.8(2)
C(8)-N(3)-C(4)	121.2(2)	C(18)-C(23)-C(22)	110.1(2)
C(8)-N(3)-Pd	119.52(15)	N(6)-C(24)-C(25)	178.8(3)

Table A.22: Bond angles for [PDC<sup>Cy</sup>Pd(MeCN)](PF<sub>6</sub>)<sub>2</sub>

### A.12 Crystal Data for [PDC<sup>Mes</sup>Pd(MeCN)](PF<sub>6</sub>)<sub>2</sub>

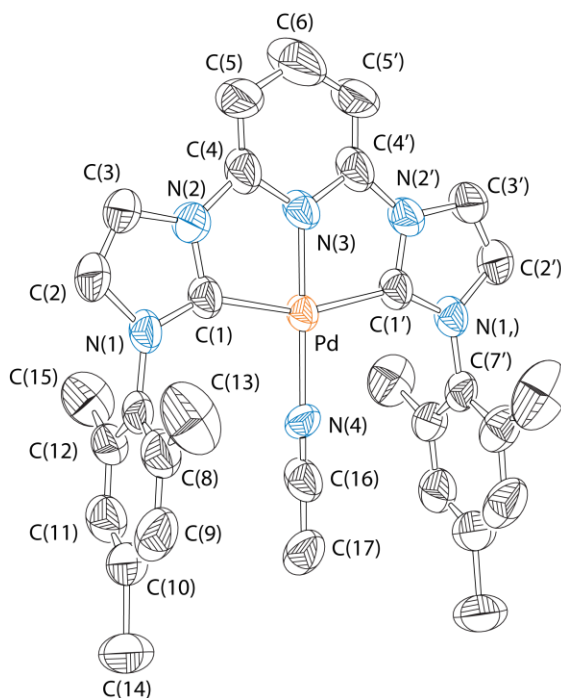


Figure A.11: Fully labeled thermal ellipsoid plot of  $[\text{PDC}^{\text{Mes}}\text{Pd}(\text{MeCN})](\text{PF}_6)_2$  with hydrogens and two outer sphere  $\text{PF}_6^-$  ions omitted and shown at the 50% probability level

Bond	Length	Bond	Length
Pd-N(3)	1.903(7)	C(4)-C(5)	1.315(10)
Pd-N(4)	2.019(7)	C(5)-C(6)	1.374(12)
Pd-C(1)#1	2.024(6)	C(6)-C(5)#1	1.374(11)
Pd-C(1)	2.024(6)	C(7)-C(8)	1.358(9)
N(1)-C(1)	1.329(8)	C(7)-C(12)	1.409(9)
N(1)-C(2)	1.417(9)	C(8)-C(9)	1.418(12)
N(1)-C(7)	1.454(8)	C(8)-C(13)	1.508(12)
N(2)-C(1)	1.377(9)	C(9)-C(10)	1.372(13)
N(2)-C(3)	1.384(8)	C(10)-C(11)	1.344(13)
N(2)-C(4)	1.409(9)	C(10)-C(14)	1.603(11)
N(3)-C(4)#1	1.373(7)	C(11)-C(12)	1.361(10)
N(3)-C(4)	1.373(7)	C(12)-C(15)	1.475(11)
N(4)-C(16)	1.087(13)	C(16)-C(17)	1.368(16)

C(2)-C(3)	1.294(11)
-----------	-----------

Table A.23: Bond lengths for [PDC<sup>Mes</sup>Pd(MeCN)](PF<sub>6</sub>)<sub>2</sub>

Bond	Angle	Bond	Angle
N(3)-Pd-N(4)	179.1(3)	C(5)-C(4)-N(3)	123.6(7)
N(3)-Pd-C(1)#1	79.57(19)	C(5)-C(4)-N(2)	128.7(6)
N(4)-Pd-C(1)#1	100.43(19)	N(3)-C(4)-N(2)	107.7(6)
N(3)-Pd-C(1)	79.57(19)	C(4)-C(5)-C(6)	117.6(9)
N(4)-Pd-C(1)	100.43(19)	C(5)-C(6)-C(5)#1	121.7(14)
C(1)#1-Pd-C(1)	159.1(4)	C(8)-C(7)-C(12)	123.2(7)
C(1)-N(1)-C(2)	109.7(6)	C(8)-C(7)-N(1)	118.7(6)
C(1)-N(1)-C(7)	122.7(5)	C(12)-C(7)-N(1)	118.0(5)
C(2)-N(1)-C(7)	127.5(5)	C(7)-C(8)-C(9)	116.7(8)
C(1)-N(2)-C(3)	110.3(6)	C(7)-C(8)-C(13)	123.6(8)
C(1)-N(2)-C(4)	119.8(5)	C(9)-C(8)-C(13)	119.7(8)
C(3)-N(2)-C(4)	129.9(6)	C(10)-C(9)-C(8)	120.5(8)
C(4)#1-N(3)-C(4)	115.9(8)	C(11)-C(10)-C(9)	119.9(8)
C(4)#1-N(3)-Pd	122.0(4)	C(11)-C(10)-C(14)	122.5(10)
C(4)-N(3)-Pd	122.0(4)	C(9)-C(10)-C(14)	117.4(9)
C(16)-N(4)-Pd	179.0(9)	C(10)-C(11)-C(12)	123.0(8)
N(1)-C(1)-N(2)	104.7(5)	C(11)-C(12)-C(7)	116.6(7)
N(1)-C(1)-Pd	144.4(5)	C(11)-C(12)-C(15)	122.5(7)
N(2)-C(1)-Pd	110.8(4)	C(7)-C(12)-C(15)	120.9(6)
C(3)-C(2)-N(1)	108.0(6)	N(4)-C(16)-C(17)	179.6(13)
C(2)-C(3)-N(2)	107.3(6)		

Table A.24: Bond angles for [PDC<sup>Mes</sup>Pd(MeCN)](PF<sub>6</sub>)<sub>2</sub>

### A.13 Crystal Data for [PDC<sup>Dipp</sup>Pd(MeCN)](PF<sub>6</sub>)<sub>2</sub>

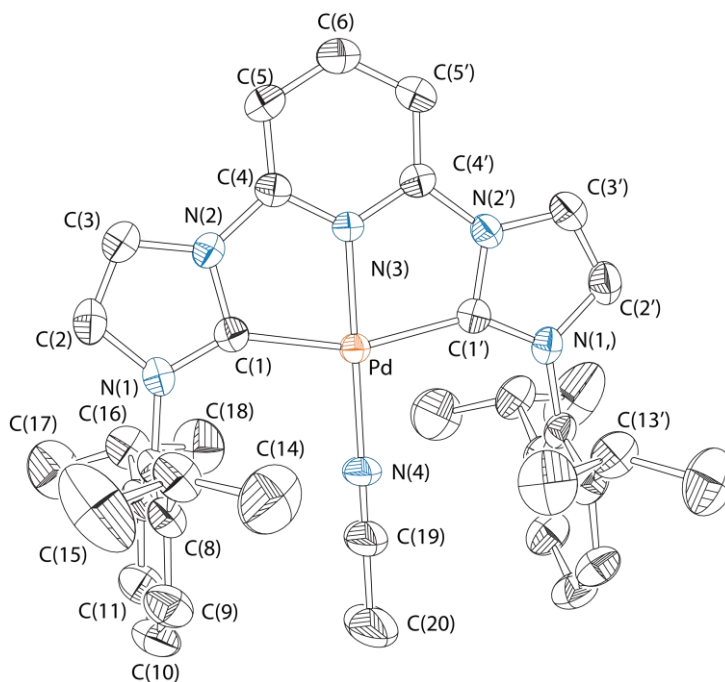


Figure A.12: Fully labeled thermal ellipsoid plot of  $[\text{PDC}^{\text{Dipp}}\text{Pd}(\text{MeCN})](\text{PF}_6)_2$  with hydrogens and two outer sphere  $\text{PF}_6^-$  ions omitted and shown at the 50% probability level

Bond	Length	Bond	Length
Pd-N(3)	1.958(3)	N(4)-C(19)	1.104(6)
Pd-N(4)	2.008(3)	C(2)-C(3)	1.347(4)
Pd-C(1)#1	2.019(3)	C(4)-C(5)	1.372(4)
Pd-C(1)	2.019(3)	C(5)-C(6)	1.384(4)
P(1)-F(4)	1.5742	C(6)-C(5)#1	1.384(4)
P(1)-F(2)	1.5828	C(7)-C(8)	1.385(4)
P(1)-F(6)	1.6006	C(7)-C(12)	1.399(4)
P(1)-F(1)	1.6023	C(8)-C(9)	1.384(4)
P(1)-F(3)	1.6135	C(8)-C(13)	1.530(4)
P(1)-F(5)	1.6445	C(9)-C(10)	1.402(5)
N(1)-C(1)	1.338(3)	C(10)-C(11)	1.380(5)
N(1)-C(2)	1.395(4)	C(11)-C(12)	1.385(4)
N(1)-C(7)	1.451(3)	C(12)-C(16)	1.510(4)
N(2)-C(3)	1.388(4)	C(13)-C(15)	1.518(5)
N(2)-C(1)	1.388(3)	C(13)-C(14)	1.536(5)

N(2)-C(4)	1.407(3)	C(16)-C(18)	1.508(6)
N(3)-C(4)	1.342(3)	C(16)-C(17)	1.532(5)
N(3)-C(4)#1	1.342(3)	C(19)-C(20)	1.456(8)

Table A.25: Bond lengths for [PDC<sup>Dipp</sup>Pd(MeCN)](PF<sub>6</sub>)<sub>2</sub>

Bond	Angle	Bond	Angle
N(3)-Pd-N(4)	180	C(19)-N(4)-Pd	180
N(3)-Pd-C(1)#1	79.27(8)	N(1)-C(1)-N(2)	104.3(2)
N(4)-Pd-C(1)#1	100.73(8)	N(1)-C(1)-Pd	143.6(2)
N(3)-Pd-C(1)	79.27(8)	N(2)-C(1)-Pd	112.15(18)
N(4)-Pd-C(1)	100.73(8)	C(3)-C(2)-N(1)	107.7(3)
C(1)#1-Pd-C(1)	158.55(15)	C(2)-C(3)-N(2)	106.0(3)
F(4)-P(1)-F(2)	93.5	N(3)-C(4)-C(5)	121.5(3)
F(4)-P(1)-F(6)	89.5	N(3)-C(4)-N(2)	111.3(2)
F(2)-P(1)-F(6)	91	C(5)-C(4)-N(2)	127.3(3)
F(4)-P(1)-F(1)	178.3	C(4)-C(5)-C(6)	117.2(3)
F(2)-P(1)-F(1)	87.5	C(5)-C(6)-C(5)#1	122.0(4)
F(6)-P(1)-F(1)	89.1	C(8)-C(7)-C(12)	123.9(3)
F(4)-P(1)-F(3)	90.6	C(8)-C(7)-N(1)	118.5(2)
F(2)-P(1)-F(3)	92.6	C(12)-C(7)-N(1)	117.6(2)
F(6)-P(1)-F(3)	176.3	C(9)-C(8)-C(7)	117.1(3)
F(1)-P(1)-F(3)	90.8	C(9)-C(8)-C(13)	120.9(3)
F(4)-P(1)-F(5)	90.7	C(7)-C(8)-C(13)	122.0(3)
F(2)-P(1)-F(5)	175.5	C(8)-C(9)-C(10)	121.0(3)
F(6)-P(1)-F(5)	87.5	C(11)-C(10)-C(9)	119.8(3)
F(1)-P(1)-F(5)	88.2	C(10)-C(11)-C(12)	121.3(3)
F(3)-P(1)-F(5)	88.9	C(11)-C(12)-C(7)	116.9(3)
C(1)-N(1)-C(2)	111.2(2)	C(11)-C(12)-C(16)	120.6(3)
C(1)-N(1)-C(7)	122.9(2)	C(7)-C(12)-C(16)	122.5(3)
C(2)-N(1)-C(7)	125.9(2)	C(15)-C(13)-C(8)	112.0(3)
C(3)-N(2)-C(1)	110.9(2)	C(15)-C(13)-C(14)	112.1(4)
C(3)-N(2)-C(4)	131.5(2)	C(8)-C(13)-C(14)	109.7(3)
C(1)-N(2)-C(4)	117.6(2)	C(18)-C(16)-C(12)	112.4(3)
C(4)-N(3)-C(4)#1	120.7(3)	C(18)-C(16)-C(17)	111.9(3)

C(4)-N(3)-Pd	119.66(16)	C(12)-C(16)-C(17)	112.2(3)
C(4)#1-N(3)-Pd	119.66(16)	N(4)-C(19)-C(20)	180

Table A.26: Bond angles for  $[\text{PDC}^{\text{Dipp}}\text{Pd}(\text{MeCN})](\text{PF}_6)_2$

## Appendix B

### CRYSTALLOGRAPHIC DATA FOR RE COMPLEXES

#### B.1 Crystallographic Experimental Data

##### B.1.1 Crystallographic Experimental Data for Compounds (3) and (9)

	<b>(3) joer154</b>	<b>(9) joer180</b>
<b>Formula</b>	C15 H11 Cl N5 O3 Re	C25 H20 Br N6 O4 Re
<b>Fw</b>	530.94	734.58
<b>Crystal System</b>	Monoclinic	Monoclinic
<b>Space Group</b>	P2(1)/c	P2(1)/n
<b>a</b>	11.4779(17) Å	11.6786(9) Å
<b>b</b>	13.971(2) Å	19.4125(16) Å
<b>c</b>	12.0980(18) Å	11.7398(9) Å
<b><math>\alpha</math></b>	90°	90°
<b><math>\beta</math></b>	116.719(2)°	104.9320(10)°
<b><math>\gamma</math></b>	90°	90°
<b>V</b>	1732.8(4) Å <sup>3</sup>	2571.7(4) Å <sup>3</sup>
<b>Z</b>	4	4
<b>Temp</b>	200(2) K	200(2) K
<b>D<sub>calcd</sub></b>	2.035 Mg/m <sup>3</sup>	1.897 Mg/m <sup>3</sup>
<b>2<math>\theta</math> range</b>	3.98 to 55.08°	4.16 to 55.18°
<b><math>\mu</math></b>	7.191 mm <sup>-1</sup> (Mo K $\alpha$ )	6.332 mm <sup>-1</sup> (Mo K $\alpha$ )
<b>Relections</b>	22438	33556
<b>Unique</b>	3983	5946
<b>R (int)</b>	0.0545	0.0587
<b>R<sub>1</sub></b>	0.0333	0.0495
<b>wR<sub>2</sub></b>	0.0740	0.1360

Table B.1: Crystallographic experimental data for complexes **(3)** and **(9)**

## B.2 Crystal Data of $\text{ReN}_3$ Intermediate **(3)**

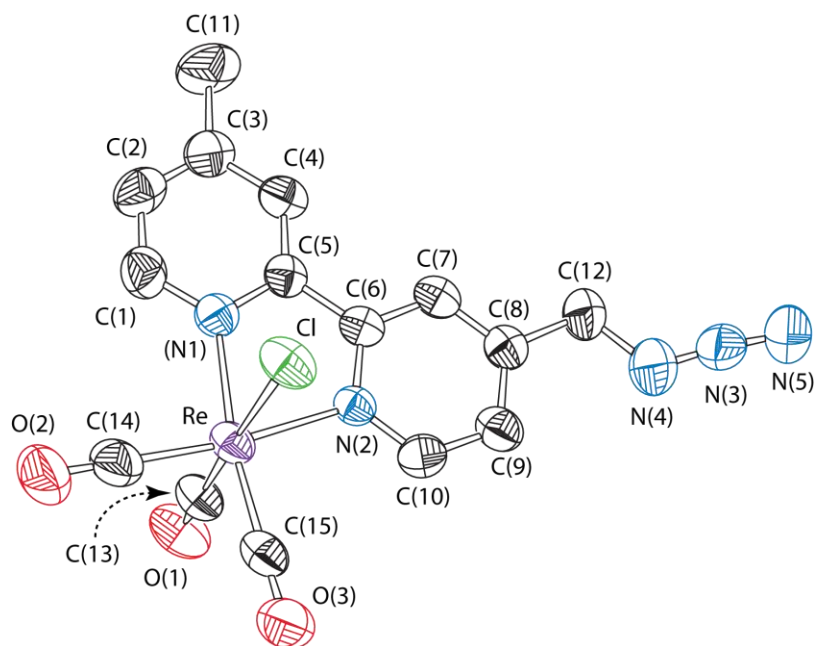


Figure B.1: Fully labeled thermal ellipsoid plot of  $\text{ReN}_3$  Intermediate **(3)** with hydrogens omitted at the 50% probability level

### B.2.1 Bond Lengths and Angles for Intermediate **(3)**

Bond	Length	Bond	Length
Re-C(15)	1.899(8)	C(2)-H(2)	0.95
Re-C(13)	1.909(7)	C(3)-C(4)	1.398(10)
Re-C(14)	1.920(8)	C(3)-C(11)	1.528(10)

Re-N(2)	2.166(4)	C(4)-C(5)	1.369(8)
Re-N(1)	2.190(5)	C(4)-H(4)	0.95
Re-Cl	2.4886(15)	C(5)-C(6)	1.474(8)
N(1)-C(1)	1.344(8)	C(6)-C(7)	1.398(8)
N(1)-C(5)	1.350(7)	C(7)-C(8)	1.385(8)
N(2)-C(10)	1.334(7)	C(7)-H(7)	0.95
N(2)-C(6)	1.353(7)	C(8)-C(9)	1.393(9)
N(3)-N(4)	1.223(11)	C(8)-C(12)	1.495(9)
N(3)-C(12)	1.427(12)	C(9)-C(10)	1.378(9)
N(4)-N(5)	1.185(12)	C(9)-H(9)	0.95
O(1)-C(13)	1.136(7)	C(10)-H(10)	0.95
O(2)-C(14)	1.148(8)	C(11)-H(11A)	0.98
O(3)-C(15)	1.162(7)	C(11)-H(11B)	0.98
C(1)-C(2)	1.401(10)	C(11)-H(11C)	0.98
C(1)-H(1)	0.95	C(12)-H(12A)	0.99
C(2)-C(3)	1.353(10)	C(12)-H(12B)	0.99

**Table B.2:** Bond Lengths for ReN<sub>3</sub> intermediate (**3**)

Bond	Angle	Bond	Angle
C(15)-Re-C(13)	88.8(3)	C(3)-C(4)-H(4)	119.8
C(15)-Re-C(14)	87.6(3)	N(1)-C(5)-C(4)	122.2(6)
C(13)-Re-C(14)	88.4(3)	N(1)-C(5)-C(6)	114.1(5)
C(15)-Re-N(2)	98.1(2)	C(4)-C(5)-C(6)	123.7(6)
C(13)-Re-N(2)	95.0(2)	N(2)-C(6)-C(7)	120.9(5)
C(14)-Re-N(2)	173.4(2)	N(2)-C(6)-C(5)	116.4(5)
C(15)-Re-N(1)	171.5(2)	C(7)-C(6)-C(5)	122.7(5)
C(13)-Re-N(1)	95.4(2)	C(8)-C(7)-C(6)	120.3(6)
C(14)-Re-N(1)	99.9(3)	C(8)-C(7)-H(7)	119.9
N(2)-Re-N(1)	74.16(18)	C(6)-C(7)-H(7)	119.9
C(15)-Re-Cl	91.45(19)	C(7)-C(8)-C(9)	117.8(6)
C(13)-Re-Cl	177.1(2)	C(7)-C(8)-C(12)	120.3(6)
C(14)-Re-Cl	94.5(2)	C(9)-C(8)-C(12)	121.9(6)
N(2)-Re-Cl	82.07(12)	C(10)-C(9)-C(8)	119.1(6)
N(1)-Re-Cl	84.04(13)	C(10)-C(9)-H(9)	120.4
C(1)-N(1)-C(5)	117.7(5)	C(8)-C(9)-H(9)	120.4
C(1)-N(1)-Re	124.5(5)	N(2)-C(10)-C(9)	123.4(6)
C(5)-N(1)-Re	117.6(4)	N(2)-C(10)-H(10)	118.3
C(10)-N(2)-C(6)	118.5(5)	C(9)-C(10)-H(10)	118.3
C(10)-N(2)-Re	124.3(4)	C(3)-C(11)-H(11A)	109.5
C(6)-N(2)-Re	117.0(4)	C(3)-C(11)-H(11B)	109.5
N(4)-N(3)-C(12)	120.0(10)	H(11A)-C(11)-H(11B)	109.5
N(5)-N(4)-N(3)	174.8(11)	C(3)-C(11)-H(11C)	109.5
N(1)-C(1)-C(2)	121.9(7)	H(11A)-C(11)-H(11C)	109.5
N(1)-C(1)-H(1)	119	H(11B)-C(11)-H(11C)	109.5
C(2)-C(1)-H(1)	119	N(3)-C(12)-C(8)	109.7(7)
C(3)-C(2)-C(1)	120.5(7)	N(3)-C(12)-H(12A)	109.7
C(3)-C(2)-H(2)	119.8	C(8)-C(12)-H(12A)	109.7
C(1)-C(2)-H(2)	119.8	N(3)-C(12)-H(12B)	109.7
C(2)-C(3)-C(4)	117.2(7)	C(8)-C(12)-H(12B)	109.7
C(2)-C(3)-C(11)	122.9(7)	H(12A)-C(12)-H(12B)	108.2
C(4)-C(3)-C(11)	119.9(7)	O(1)-C(13)-Re	176.8(6)
C(5)-C(4)-C(3)	120.5(7)	O(2)-C(14)-Re	178.2(8)
C(5)-C(4)-H(4)	119.8	O(3)-C(15)-Re	178.7(5)

Table B.3 Bond Angles for ReN<sub>3</sub> intermediate (3)

### B.3 Crystal Data for Transition Metal Control (9)

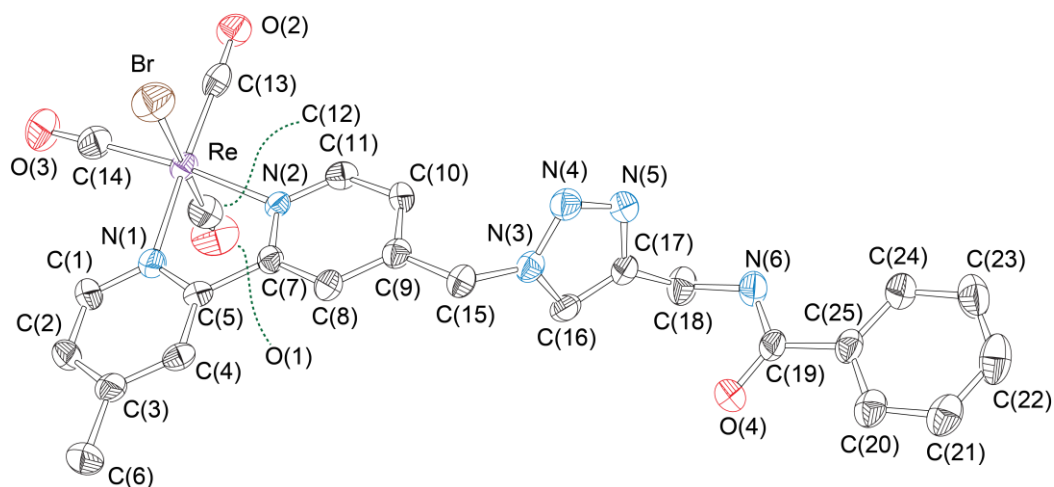


Figure B.2: Fully labeled thermal ellipsoid plot of the transition metal control complex (9) with hydrogens omitted at the 50% probability level

#### B.3.1 Bond Lengths and Angles for Complex (9)

Bond	Length	Bond	Length
Re-C(14)	1.926(10)	C(6)-H(6A)	0.98
Re-C(12)	1.933(10)	C(6)-H(6B)	0.98
Re-C(13)	1.930(10)	C(6)-H(6C)	0.98
Re-N(1)	2.171(7)	C(7)-C(8)	1.382(10)
Re-N(2)	2.178(6)	C(8)-C(9)	1.398(11)
Re-Br	2.5927(12)	C(8)-H(8)	0.95
N(1)-C(1)	1.339(10)	C(9)-C(10)	1.382(11)

N(1)-C(5)	1.348(10)	C(9)-C(15)	1.509(11)
N(2)-C(11)	1.345(10)	C(10)-C(11)	1.388(11)
N(2)-C(7)	1.352(9)	C(10)-H(10)	0.95
N(3)-N(4)	1.322(10)	C(11)-H(11)	0.95
N(3)-C(16)	1.357(10)	C(15)-H(15A)	0.99
N(3)-C(15)	1.447(10)	C(15)-H(15B)	0.99
N(4)-N(5)	1.319(10)	C(16)-C(17)	1.357(12)
N(5)-C(17)	1.341(11)	C(16)-H(16)	0.95
N(6)-C(19)	1.346(12)	C(17)-C(18)	1.498(12)
N(6)-C(18)	1.472(11)	C(18)-H(18A)	0.99
N(6)-H(6)	0.88(11)	C(18)-H(18B)	0.99
O(1)-C(12)	1.103(12)	C(19)-C(25)	1.499(11)
O(2)-C(13)	1.144(11)	C(20)-C(21)	1.395(13)
O(3)-C(14)	1.143(12)	C(20)-C(25)	1.392(13)
O(4)-C(19)	1.228(10)	C(20)-H(20)	0.95
C(1)-C(2)	1.364(12)	C(21)-C(22)	1.340(15)
C(1)-H(1)	0.95	C(21)-H(21)	0.95
C(2)-C(3)	1.379(12)	C(22)-C(23)	1.382(15)
C(2)-H(2)	0.95	C(22)-H(22)	0.95
C(3)-C(4)	1.374(12)	C(23)-C(24)	1.395(14)
C(3)-C(6)	1.525(12)	C(23)-H(23)	0.95
C(4)-C(5)	1.394(10)	C(24)-C(25)	1.389(13)
C(4)-H(4)	0.95	C(24)-H(24)	0.95
C(5)-C(7)	1.486(10)		

**Table B.4:** Bond lengths for complex (9)

<b>Bond</b>	<b>Angle</b>	<b>Bond</b>	<b>Angle</b>
C(14)-Re-C(12)	89.4(4)	C(9)-C(8)-H(8)	120.3
C(14)-Re-C(13)	87.5(4)	C(7)-C(8)-H(8)	120.3
C(12)-Re-C(13)	90.7(4)	C(10)-C(9)-C(8)	118.5(7)
C(14)-Re-N(1)	97.4(3)	C(10)-C(9)-C(15)	123.0(7)
C(12)-Re-N(1)	94.2(3)	C(8)-C(9)-C(15)	118.4(7)
C(13)-Re-N(1)	173.2(3)	C(9)-C(10)-C(11)	119.2(7)
C(14)-Re-N(2)	170.5(3)	C(9)-C(10)-H(10)	120.4

C(12)-Re-N(2)	94.8(3)	C(11)-C(10)-H(10)	120.4
C(13)-Re-N(2)	100.9(3)	N(2)-C(11)-C(10)	122.4(7)
N(1)-Re-N(2)	73.9(2)	N(2)-C(11)-H(11)	118.8
C(14)-Re-Br	91.2(3)	C(10)-C(11)-H(11)	118.8
C(12)-Re-Br	179.2(3)	O(1)-C(12)-Re	177.3(10)
C(13)-Re-Br	89.9(2)	O(2)-C(13)-Re	177.8(8)
N(1)-Re-Br	85.23(19)	O(3)-C(14)-Re	178.4(10)
N(2)-Re-Br	84.54(16)	N(3)-C(15)-C(9)	113.5(7)
C(1)-N(1)-C(5)	118.5(7)	N(3)-C(15)-H(15A)	108.9
C(1)-N(1)-Re	123.5(6)	C(9)-C(15)-H(15A)	108.9
C(5)-N(1)-Re	118.0(5)	N(3)-C(15)-H(15B)	108.9
C(11)-N(2)-C(7)	118.6(6)	C(9)-C(15)-H(15B)	108.9
C(11)-N(2)-Re	123.9(5)	H(15A)-C(15)-H(15B)	107.7
C(7)-N(2)-Re	117.4(5)	N(3)-C(16)-C(17)	105.1(7)
N(4)-N(3)-C(16)	110.0(7)	N(3)-C(16)-H(16)	127.4
N(4)-N(3)-C(15)	120.7(7)	C(17)-C(16)-H(16)	127.4
C(16)-N(3)-C(15)	129.3(7)	N(5)-C(17)-C(16)	108.3(7)
N(5)-N(4)-N(3)	107.7(7)	N(5)-C(17)-C(18)	120.5(8)
N(4)-N(5)-C(17)	108.9(7)	C(16)-C(17)-C(18)	131.2(8)
C(19)-N(6)-C(18)	119.7(8)	N(6)-C(18)-C(17)	112.1(8)
C(19)-N(6)-H(6)	119(7)	N(6)-C(18)-H(18A)	109.2
C(18)-N(6)-H(6)	121(7)	C(17)-C(18)-H(18A)	109.2
N(1)-C(1)-C(2)	122.4(8)	N(6)-C(18)-H(18B)	109.2
N(1)-C(1)-H(1)	118.8	C(17)-C(18)-H(18B)	109.2
C(2)-C(1)-H(1)	118.8	H(18A)-C(18)-H(18B)	107.9
C(1)-C(2)-C(3)	120.0(8)	O(4)-C(19)-N(6)	121.0(8)
C(1)-C(2)-H(2)	120	O(4)-C(19)-C(25)	121.1(8)
C(3)-C(2)-H(2)	120	N(6)-C(19)-C(25)	117.9(8)
C(4)-C(3)-C(2)	118.3(7)	C(21)-C(20)-C(25)	120.8(9)
C(4)-C(3)-C(6)	121.6(8)	C(21)-C(20)-H(20)	119.6
C(2)-C(3)-C(6)	120.1(8)	C(25)-C(20)-H(20)	119.6
C(3)-C(4)-C(5)	119.4(7)	C(22)-C(21)-C(20)	120.0(10)
C(3)-C(4)-H(4)	120.3	C(22)-C(21)-H(21)	120
C(5)-C(4)-H(4)	120.3	C(20)-C(21)-H(21)	120
N(1)-C(5)-C(4)	121.4(7)	C(21)-C(22)-C(23)	120.9(9)
N(1)-C(5)-C(7)	114.6(6)	C(21)-C(22)-H(22)	119.5
C(4)-C(5)-C(7)	124.0(7)	C(23)-C(22)-H(22)	119.5
C(3)-C(6)-H(6A)	109.5	C(22)-C(23)-C(24)	119.9(10)
C(3)-C(6)-H(6B)	109.5	C(22)-C(23)-H(23)	120

H(6A)-C(6)-H(6B)	109.5	C(24)-C(23)-H(23)	120
C(3)-C(6)-H(6C)	109.5	C(25)-C(24)-C(23)	119.9(10)
H(6A)-C(6)-H(6C)	109.5	C(25)-C(24)-H(24)	120
H(6B)-C(6)-H(6C)	109.5	C(23)-C(24)-H(24)	120
N(2)-C(7)-C(8)	121.9(7)	C(24)-C(25)-C(20)	118.5(8)
N(2)-C(7)-C(5)	114.8(6)	C(24)-C(25)-C(19)	124.6(8)
C(8)-C(7)-C(5)	123.3(7)	C(20)-C(25)-C(19)	116.9(8)
C(9)-C(8)-C(7)	119.4(7)		

**Table B.5:** Bond angles for complex (9)

#### B.4 Permission Letter



RightsLink®



**ACS Publications** Title:  
Most Trusted. Most Cited. Most Read.

Photocatalytic Conversion of  
CO<sub>2</sub> to CO Using Rhenium  
Bipyridine Platforms Containing  
Ancillary Phenyl or BODIPY  
Moieties

**Author:** Gabriel A. Andrade, Allen J.  
Pistner, Glenn P. A. Yap, et al

**Publication:** ACS Catalysis

**Publisher:** American Chemical Society

**Date:** Aug 1, 2013

Copyright © 2013, American Chemical Society

#### PERMISSION/LICENSE IS GRANTED FOR YOUR ORDER AT NO CHARGE

This type of permission/license, instead of the standard Terms & Conditions, is sent to you because no fee is being charged for your order. Please note the following:

- Permission is granted for your request in both print and electronic formats, and translations.
- If figures and/or tables were requested, they may be adapted or used in part.

- Please print this page for your records and send a copy of it to your publisher/graduate school.
- Appropriate credit for the requested material should be given as follows: "Reprinted (adapted) with permission from (COMPLETE REFERENCE CITATION). Copyright (YEAR) American Chemical Society." Insert appropriate information in place of the capitalized words.
- One-time permission is granted only for the use specified in your request. No additional uses are granted (such as derivative works or other editions). For any other uses, please submit a new request.

## Appendix C

### CRYSTALLOGRAPHIC DATA FOR PHDC COMPLEXES

#### C.1 Crystallographic Experimental Data

##### C.1.1 Crystallographic Experimental Data for [PhDC<sup>Et</sup>Pd(Br)] and [PhDC<sup>Et</sup>Pd(MeCN)]PF<sub>6</sub>

	[PhDC <sup>Et</sup> Pd(Br)]	[PhDC <sup>Et</sup> Pd(MeCN)]PF <sub>6</sub>
Formula	C16 H17 Br N4 Pd	C20 H23 F6 N6 P Pd
<b>Fw</b>	466.57	598.81
<b>Crystal System</b>	Monoclinic	Triclinic
<b>Space Group</b>	P2(1)/c	P-1
<b>a</b>	20.8065(16) Å	7.1595(15) Å
<b>b</b>	26.1462(19) Å	12.722(3) Å
<b>c</b>	15.5459(10) Å	14.049(3) Å
<b>α</b>	90°	107.123(4) °
<b>β</b>	91.401(2) °	99.155(4) °
<b>γ</b>	90°	95.267(4) °
<b>V</b>	6823.1(9) Å <sup>3</sup>	1194.3(4) Å <sup>3</sup>
<b>Z</b>	16	2
<b>Temp</b>	200(2) K	200(2) K
<b>D<sub>calcd</sub></b>	1.817 Mg/cm <sup>3</sup>	1.665 Mg/cm <sup>3</sup>
<b>2θ range</b>	3.602 to 55.126 °	3.386 to 54.944 °
<b>μ</b>	3.491 mm <sup>-1</sup> (Cu Kα)	0.991 mm <sup>-1</sup> (Mo Kα)
<b>Relections</b>	102983	15898
<b>Unique</b>	15692	5462
<b>R (int)</b>	0.0656	0.0833
<b>R<sub>1</sub></b>	0.0568	0.0538
<b>wR<sub>2</sub></b>	0.1315	0.0984

Table C.1: Crystallographic experimental data for [PhDC<sup>Et</sup>Pd(Br)] and [PhDC<sup>Et</sup>Pd(MeCN)]PF<sub>6</sub>

C.1.2 Crystallographic Experimental Data for [PhDC<sup>Et</sup>Pd(Py)]PF<sub>6</sub>, [PhDC<sup>Et</sup>Pd(<sup>t</sup>BuNC)]PF<sub>6</sub>, and [PhDC<sup>Et</sup>Pd(PPh<sub>3</sub>)]PF<sub>6</sub>

<b>X</b>	<b>Py</b>	<b><sup>t</sup>BuNC</b>	<b>PPh<sub>3</sub></b>
<b>Formula</b>	C21 H22 F6 N5 P Pd	C21 H26 F6 N5 P Pd	C34 H32 F6 N4 P2 Pd
<b>Fw</b>	595.80	599.84	778.97
<b>Crystal System</b>	Triclinic	Triclinic	Monoclinic
<b>Space Group</b>	P-1	P-1	P2(1)/c
<b>a</b>	9.843(3) Å	8.0879(7) Å	10.0170(3) Å
<b>b</b>	15.582(4) Å	11.3826(10) Å	16.3126(5) Å
<b>c</b>	16.391(4) Å	15.5217(14) Å	24.3863(7) Å
<b>α</b>	103.762(5) °	102.047(2) °	90 °
<b>β</b>	106.091(5) °	100.309(2) °	93.417(2) °
<b>γ</b>	93.494(5) °	105.079(2) °	90 °
<b>V</b>	2324.3(10) Å <sup>3</sup>	1307.5(2) Å <sup>3</sup>	3977.7(2) Å <sup>3</sup>
<b>Z</b>	4	2	4
<b>Temp</b>	200(2) K	200(2) K	200(2) K
<b>D<sub>calcd</sub></b>	1.703 Mg/cm <sup>3</sup>	1.524 Mg/cm <sup>3</sup>	1.301 Mg/cm <sup>3</sup>
<b>2θ range</b>	3.272 to 54.462 °	3.848 to 55.378 °	6.522 to 150.856 °
<b>μ</b>	0.935 mm <sup>-1</sup> (Mo Kα)	0.831 mm <sup>-1</sup> (Mo Kα)	5.00 mm <sup>-1</sup> (Cu Kα)
<b>Relections</b>	30838	35637	80811
<b>Unique</b>	10756	6109	8195
<b>R (int)</b>	0.0601	0.0349	0.0791
<b>R<sub>1</sub></b>	0.0507	0.0289	0.0516
<b>wR<sub>2</sub></b>	0.1070	0.0742	0.1381

Table C.2: Crystallographic experimental data for [PhDC<sup>Et</sup>Pd(Py)]PF<sub>6</sub>, [PhDC<sup>Et</sup>Pd(<sup>t</sup>BuNC)]PF<sub>6</sub>, and [PhDC<sup>Et</sup>Pd(PPh<sub>3</sub>)]PF<sub>6</sub> where X is the ancillary ligand.

**C.1.3 Crystallographic Experimental Data for [PhDC<sup>Et</sup>Ni(Br)] and [PhDC<sup>Et</sup>Ni(MeCN)]PF<sub>6</sub>**

	<u>[PhDC<sup>Et</sup>Ni(Br)]</u>	<u>[PhDC<sup>Et</sup>Ni(MeCN)]PF<sub>6</sub></u>
<b>Formula</b>	C16 H17 Br N4 No	C18 H20 F6 N5 Ni P
<b>Fw</b>	403.95	510.07
<b>Crystal System</b>	Orthorhombic	Triclinic
<b>Space Group</b>	Pbca	P-1
<b>a</b>	15.6149(14) Å	7.7213(10) Å
<b>b</b>	17.5980(16) Å	11.7234(15) Å
<b>c</b>	35.167(3) Å	12.1245(15) Å
<b>α</b>	90°	67.229(2) °
<b>β</b>	90 °	86.429(3) °
<b>γ</b>	90°	85.571(3) °
<b>V</b>	9663.7(15) Å <sup>3</sup>	1008.3(2) Å <sup>3</sup>
<b>Z</b>	24	2
<b>Temp</b>	200(2) K	200(2) K
<b>D<sub>calcd</sub></b>	1.666 Mg/cm <sup>3</sup>	1.680 Mg/cm <sup>3</sup>
<b>2θ range</b>	2.316 to 49.996 °	3.646 to 54.980 °
<b>μ</b>	3.686 mm <sup>-1</sup> (Mo Kα)	1.112 mm <sup>-1</sup> (Mo Kα)
<b>Relections</b>	117148	27217
<b>Unique</b>	8503	4615
<b>R (int)</b>	0.1689	0.0553
<b>R<sub>1</sub></b>	0.0912	0.0346
<b>wR<sub>2</sub></b>	0.2348	0.0771

Table C.3: Crystallographic experimental data for  $[\text{PhDC}^{\text{Et}}\text{Ni}(\text{Br})]$  and  $[\text{PhDC}^{\text{Et}}\text{Ni}(\text{MeCN})]\text{PF}_6$

## C.2 $[\text{PhDC}^{\text{Et}}\text{Pd}(\text{Br})]$ Crystal Data

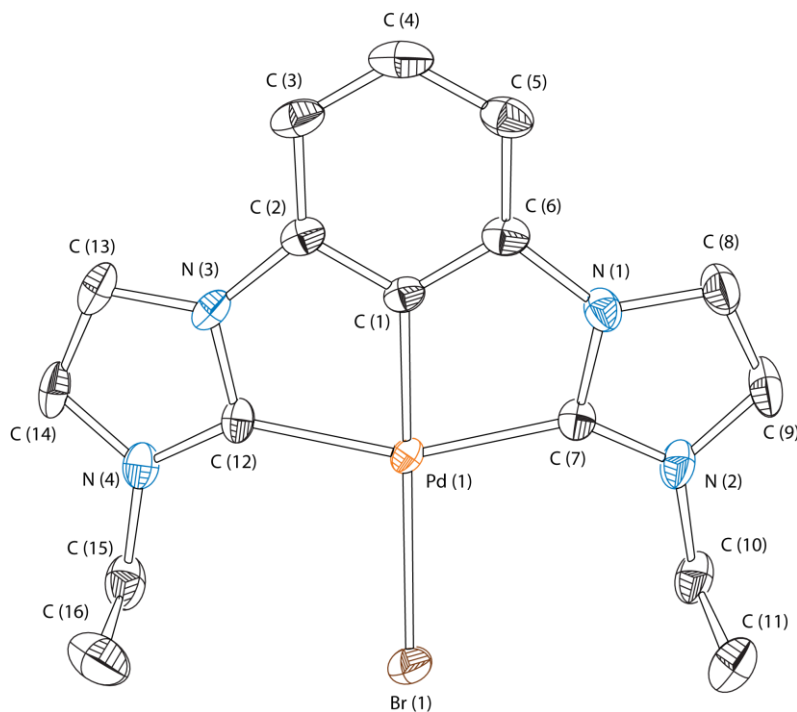


Figure C.1: Fully labeled thermal ellipsoid plot of  $[\text{PhDC}^{\text{Et}}\text{Pd}(\text{Br})]$  with hydrogens omitted at the 50% probability level

### C.2.1 Bond Lengths and Angles for $[\text{PhDC}^{\text{Et}}\text{Pd}(\text{Br})]$

Bond	Length	Bond	Length
Pd(1)-C(1)	1.950(6)	N(12)-C(44)	1.3318

Pd(1)-C(12)	2.054(6)	N(12)-C(46)	1.3701
Pd(1)-C(7)	2.054(6)	N(12)-C(47)	1.4654
Pd(1)-Br(1)	2.5333(8)	C(33)-C(34)	1.3683
N(1)-C(7)	1.375(8)	C(33)-C(38)	1.3773
N(1)-C(8)	1.379(9)	C(34)-C(35)	1.3811
N(1)-C(6)	1.423(9)	C(35)-C(36)	1.3907
N(2)-C(7)	1.331(8)	C(36)-C(37)	1.3769
N(2)-C(9)	1.387(9)	C(37)-C(38)	1.4022
N(2)-C(10)	1.482(10)	C(40)-C(41)	1.3295
N(3)-C(12)	1.368(8)	C(42)-C(43)	1.672(12)
N(3)-C(13)	1.384(8)	C(45)-C(46)	1.3749
N(3)-C(2)	1.421(9)	C(47)-C(48)	1.533(10)
N(4)-C(12)	1.338(8)	Pd(3')-C(33')	1.9462
N(4)-C(14)	1.374(9)	Pd(3')-C(39')	2.0562
N(4)-C(15)	1.464(10)	Pd(3')-C(44')	2.0587
C(1)-C(2)	1.362(9)	Pd(3')-Br(3')	2.5334
C(1)-C(6)	1.382(9)	N(9')-C(39')	1.377
C(2)-C(3)	1.386(9)	N(9')-C(40')	1.3881
C(3)-C(4)	1.389(12)	N(9')-C(38')	1.4113
C(4)-C(5)	1.375(12)	N(10')-C(39')	1.329
C(5)-C(6)	1.387(9)	N(10')-C(41')	1.392
C(8)-C(9)	1.332(11)	N(10')-C(42')	1.482
C(10)-C(11)	1.506(11)	N(11')-C(44')	1.3707
C(13)-C(14)	1.371(11)	N(11')-C(45')	1.3792
C(15)-C(16)	1.522(13)	N(11')-C(34')	1.4217
Pd(2)-C(17)	1.948(6)	N(12')-C(44')	1.3318
Pd(2)-C(23)	2.054(7)	N(12')-C(46')	1.3702
Pd(2)-C(28)	2.069(6)	N(12')-C(47')	1.4651
Pd(2)-Br(2)	2.5306(9)	C(33')-C(34')	1.3683
N(5)-C(23)	1.359(8)	C(33')-C(38')	1.3774
N(5)-C(24)	1.387(9)	C(34')-C(35')	1.3813
N(5)-C(22)	1.420(8)	C(35')-C(36')	1.3906
N(6)-C(23)	1.367(8)	C(36')-C(37')	1.3769
N(6)-C(25)	1.383(10)	C(37')-C(38')	1.4024
N(6)-C(26)	1.460(10)	C(40')-C(41')	1.3295
N(7)-C(28)	1.359(8)	C(42')-C(43')	1.655(14)
N(7)-C(29)	1.375(9)	C(45')-C(46')	1.375
N(7)-C(18)	1.431(9)	C(47')-C(48')	1.575(15)
N(8)-C(28)	1.330(8)	Pd(4)-C(49)	1.953(8)

N(8)-C(30)	1.387(9)	Pd(4)-C(55)	2.062(8)
N(8)-C(31)	1.473(9)	Pd(4)-C(60)	2.064(7)
C(17)-C(18)	1.372(9)	Pd(4)-Br(4)	2.5095(11)
C(17)-C(22)	1.374(9)	N(13)-C(56)	1.354(11)
C(18)-C(19)	1.380(10)	N(13)-C(55)	1.367(11)
C(19)-C(20)	1.383(11)	N(13)-C(54)	1.434(12)
C(20)-C(21)	1.397(11)	N(14)-C(55)	1.351(10)
C(21)-C(22)	1.387(9)	N(14)-C(57)	1.423(12)
C(24)-C(25)	1.324(11)	N(14)-C(58)	1.450(13)
C(26)-C(27)	1.506(11)	N(15)-C(60)	1.357(10)
C(29)-C(30)	1.345(11)	N(15)-C(61)	1.365(10)
C(31)-C(32)	1.515(10)	N(15)-C(50)	1.435(11)
Pd(3)-C(33)	1.9463	N(16)-C(60)	1.335(10)
Pd(3)-C(39)	2.0562	N(16)-C(62)	1.377(11)
Pd(3)-C(44)	2.0586	N(16)-C(63)	1.457(11)
Pd(3)-Br(3)	2.5334	C(49)-C(50)	1.367(11)
N(9)-C(39)	1.3768	C(49)-C(54)	1.383(11)
N(9)-C(40)	1.3882	C(50)-C(51)	1.367(12)
N(9)-C(38)	1.4113	C(51)-C(52)	1.385(15)
N(10)-C(39)	1.329	C(52)-C(53)	1.389(15)
N(10)-C(41)	1.392	C(53)-C(54)	1.391(14)
N(10)-C(42)	1.4822	C(56)-C(57)	1.313(17)
N(11)-C(44)	1.371	C(58)-C(59)	1.494(13)
N(11)-C(45)	1.3792	C(61)-C(62)	1.334(13)
N(11)-C(34)	1.4217	C(63)-C(64)	1.469(14)

Table C.4: Bond lengths for [PhDC<sup>Et</sup>Pd(Br)]

Bond	Angle	Bond	Angle
C(1)-Pd(1)-C(12)	78.2(3)	C(33)-C(34)-C(35)	121.6
C(1)-Pd(1)-C(7)	77.9(3)	C(33)-C(34)-N(11)	111
C(12)-Pd(1)-C(7)	156.0(3)	C(35)-C(34)-N(11)	127.4
C(1)-Pd(1)-Br(1)	172.48(18)	C(34)-C(35)-C(36)	118.5
C(12)-Pd(1)-Br(1)	102.06(19)	C(37)-C(36)-C(35)	121.7
C(7)-Pd(1)-Br(1)	101.91(18)	C(36)-C(37)-C(38)	117.6

C(7)-N(1)-C(8)	111.6(6)	C(33)-C(38)-C(37)	121.6
C(7)-N(1)-C(6)	115.6(5)	C(33)-C(38)-N(9)	111.7
C(8)-N(1)-C(6)	132.6(6)	C(37)-C(38)-N(9)	126.8
C(7)-N(2)-C(9)	111.4(6)	N(10)-C(39)-N(9)	104.2
C(7)-N(2)-C(10)	124.6(6)	N(10)-C(39)-Pd(3)	141.5
C(9)-N(2)-C(10)	124.0(6)	N(9)-C(39)-Pd(3)	114.2
C(12)-N(3)-C(13)	111.8(6)	C(41)-C(40)-N(9)	105.8
C(12)-N(3)-C(2)	116.7(5)	C(40)-C(41)-N(10)	107.9
C(13)-N(3)-C(2)	131.5(6)	N(10)-C(42)-C(43)	103.5(7)
C(12)-N(4)-C(14)	112.0(6)	N(12)-C(44)-N(11)	104.3
C(12)-N(4)-C(15)	124.8(6)	N(12)-C(44)-Pd(3)	142.2
C(14)-N(4)-C(15)	123.0(6)	N(11)-C(44)-Pd(3)	113.4
C(2)-C(1)-C(6)	119.1(6)	C(46)-C(45)-N(11)	105.5
C(2)-C(1)-Pd(1)	120.5(5)	N(12)-C(46)-C(45)	106.6
C(6)-C(1)-Pd(1)	120.3(5)	N(12)-C(47)-C(48)	126.6(5)
C(1)-C(2)-C(3)	121.4(7)	C(33')-Pd(3')-C(39')	77.9
C(1)-C(2)-N(3)	111.1(5)	C(33')-Pd(3')-C(44')	78.3
C(3)-C(2)-N(3)	127.5(6)	C(39')-Pd(3')-C(44')	156
C(2)-C(3)-C(4)	118.2(7)	C(33')-Pd(3')-Br(3')	172.3
C(5)-C(4)-C(3)	122.0(7)	C(39')-Pd(3')-Br(3')	101.9
C(4)-C(5)-C(6)	117.8(7)	C(44')-Pd(3')-Br(3')	102.1
C(1)-C(6)-C(5)	121.6(7)	C(39')-N(9')-C(40')	111
C(1)-C(6)-N(1)	111.4(5)	C(39')-N(9')-C(38')	115.7
C(5)-C(6)-N(1)	127.1(7)	C(40')-N(9')-C(38')	133.1
N(2)-C(7)-N(1)	103.6(6)	C(39')-N(10')-C(41')	111.1
N(2)-C(7)-Pd(1)	141.7(5)	C(39')-N(10')-C(42')	124.8
N(1)-C(7)-Pd(1)	114.6(4)	C(41')-N(10')-C(42')	124.1
C(9)-C(8)-N(1)	105.7(7)	C(44')-N(11')-C(45')	111.3
C(8)-C(9)-N(2)	107.7(6)	C(44')-N(11')-C(34')	116.7
N(2)-C(10)-C(11)	111.3(6)	C(45')-N(11')-C(34')	132
N(4)-C(12)-N(3)	104.1(5)	C(44')-N(12')-C(46')	112.3
N(4)-C(12)-Pd(1)	142.3(5)	C(44')-N(12')-C(47')	124.9
N(3)-C(12)-Pd(1)	113.5(4)	C(46')-N(12')-C(47')	122.6
C(14)-C(13)-N(3)	105.0(6)	C(34')-C(33')-C(38')	119
C(13)-C(14)-N(4)	107.1(6)	C(34')-C(33')-Pd(3')	120.6
N(4)-C(15)-C(16)	111.2(6)	C(38')-C(33')-Pd(3')	120.4
C(17)-Pd(2)-C(23)	78.3(3)	C(33')-C(34')-C(35')	121.5
C(17)-Pd(2)-C(28)	77.8(3)	C(33')-C(34')-N(11')	111
C(23)-Pd(2)-C(28)	155.9(3)	C(35')-C(34')-N(11')	127.4

C(17)-Pd(2)-Br(2)	171.38(17)	C(34')-C(35')-C(36')	118.5
C(23)-Pd(2)-Br(2)	101.28(19)	C(37')-C(36')-C(35')	121.7
C(28)-Pd(2)-Br(2)	102.84(18)	C(36')-C(37')-C(38')	117.6
C(23)-N(5)-C(24)	111.5(6)	C(33')-C(38')-C(37')	121.5
C(23)-N(5)-C(22)	116.3(5)	C(33')-C(38')-N(9')	111.7
C(24)-N(5)-C(22)	132.2(6)	C(37')-C(38')-N(9')	126.8
C(23)-N(6)-C(25)	110.3(6)	N(10')-C(39')-N(9')	104.2
C(23)-N(6)-C(26)	126.8(6)	N(10')-C(39')-Pd(3')	141.5
C(25)-N(6)-C(26)	122.8(6)	N(9')-C(39')-Pd(3')	114.2
C(28)-N(7)-C(29)	111.9(6)	C(41')-C(40')-N(9')	105.8
C(28)-N(7)-C(18)	116.3(5)	C(40')-C(41')-N(10')	107.9
C(29)-N(7)-C(18)	131.7(6)	N(10')-C(42')-C(43')	105.7(10)
C(28)-N(8)-C(30)	111.5(6)	N(12')-C(44')-N(11')	104.3
C(28)-N(8)-C(31)	124.9(6)	N(12')-C(44')-Pd(3')	142.2
C(30)-N(8)-C(31)	123.6(6)	N(11')-C(44')-Pd(3')	113.4
C(18)-C(17)-C(22)	119.3(6)	C(46')-C(45')-N(11')	105.5
C(18)-C(17)-Pd(2)	120.8(5)	N(12')-C(46')-C(45')	106.6
C(22)-C(17)-Pd(2)	119.8(5)	N(12')-C(47')-C(48')	115.0(11)
C(17)-C(18)-C(19)	122.4(7)	C(49)-Pd(4)-C(55)	79.2(4)
C(17)-C(18)-N(7)	110.8(6)	C(49)-Pd(4)-C(60)	77.3(3)
C(19)-C(18)-N(7)	126.8(6)	C(55)-Pd(4)-C(60)	156.4(4)
C(18)-C(19)-C(20)	117.1(7)	C(49)-Pd(4)-Br(4)	172.7(2)
C(19)-C(20)-C(21)	122.4(7)	C(55)-Pd(4)-Br(4)	101.2(3)
C(22)-C(21)-C(20)	117.7(7)	C(60)-Pd(4)-Br(4)	102.4(2)
C(17)-C(22)-C(21)	121.1(6)	C(56)-N(13)-C(55)	111.7(9)
C(17)-C(22)-N(5)	111.5(6)	C(56)-N(13)-C(54)	131.3(9)
C(21)-C(22)-N(5)	127.4(6)	C(55)-N(13)-C(54)	116.8(7)
N(5)-C(23)-N(6)	103.8(6)	C(55)-N(14)-C(57)	109.3(9)
N(5)-C(23)-Pd(2)	114.0(5)	C(55)-N(14)-C(58)	126.4(7)
N(6)-C(23)-Pd(2)	142.3(5)	C(57)-N(14)-C(58)	124.2(8)
C(25)-C(24)-N(5)	106.4(7)	C(60)-N(15)-C(61)	112.1(7)
C(24)-C(25)-N(6)	108.1(7)	C(60)-N(15)-C(50)	115.2(6)
N(6)-C(26)-C(27)	112.1(7)	C(61)-N(15)-C(50)	132.7(8)
N(8)-C(28)-N(7)	104.0(6)	C(60)-N(16)-C(62)	110.9(8)
N(8)-C(28)-Pd(2)	141.8(5)	C(60)-N(16)-C(63)	126.3(7)
N(7)-C(28)-Pd(2)	114.0(5)	C(62)-N(16)-C(63)	122.7(7)
C(30)-C(29)-N(7)	105.7(7)	C(50)-C(49)-C(54)	119.9(8)
C(29)-C(30)-N(8)	106.9(6)	C(50)-C(49)-Pd(4)	120.9(6)
N(8)-C(31)-C(32)	108.1(6)	C(54)-C(49)-Pd(4)	119.1(7)

C(33)-Pd(3)-C(39)	77.9	C(49)-C(50)-C(51)	123.5(9)
C(33)-Pd(3)-C(44)	78.3	C(49)-C(50)-N(15)	111.4(8)
C(39)-Pd(3)-C(44)	156	C(51)-C(50)-N(15)	125.1(9)
C(33)-Pd(3)-Br(3)	172.3	C(50)-C(51)-C(52)	115.6(10)
C(39)-Pd(3)-Br(3)	101.9	C(51)-C(52)-C(53)	123.7(10)
C(44)-Pd(3)-Br(3)	102.1	C(52)-C(53)-C(54)	118.0(10)
C(39)-N(9)-C(40)	111	C(49)-C(54)-C(53)	119.3(10)
C(39)-N(9)-C(38)	115.7	C(49)-C(54)-N(13)	111.6(8)
C(40)-N(9)-C(38)	133.1	C(53)-C(54)-N(13)	129.1(9)
C(39)-N(10)-C(41)	111.1	N(14)-C(55)-N(13)	104.2(7)
C(39)-N(10)-C(42)	124.8	N(14)-C(55)-Pd(4)	142.4(7)
C(41)-N(10)-C(42)	124.1	N(13)-C(55)-Pd(4)	113.2(6)
C(44)-N(11)-C(45)	111.3	C(57)-C(56)-N(13)	107.9(10)
C(44)-N(11)-C(34)	116.7	C(56)-C(57)-N(14)	106.8(9)
C(45)-N(11)-C(34)	132	N(14)-C(58)-C(59)	114.5(8)
C(44)-N(12)-C(46)	112.3	N(16)-C(60)-N(15)	103.8(7)
C(44)-N(12)-C(47)	124.9	N(16)-C(60)-Pd(4)	141.0(7)
C(46)-N(12)-C(47)	122.6	N(15)-C(60)-Pd(4)	115.2(6)
C(34)-C(33)-C(38)	119	C(62)-C(61)-N(15)	105.6(8)
C(34)-C(33)-Pd(3)	120.6	C(61)-C(62)-N(16)	107.6(8)
C(38)-C(33)-Pd(3)	120.4	N(16)-C(63)-C(64)	113.7(8)

Table C.5: Bond angles for [PhDC<sup>Et</sup>Pd(Br)]

### C.3 [PhDC<sup>Et</sup>Pd(MeCN)]PF<sub>6</sub> Crystal Data

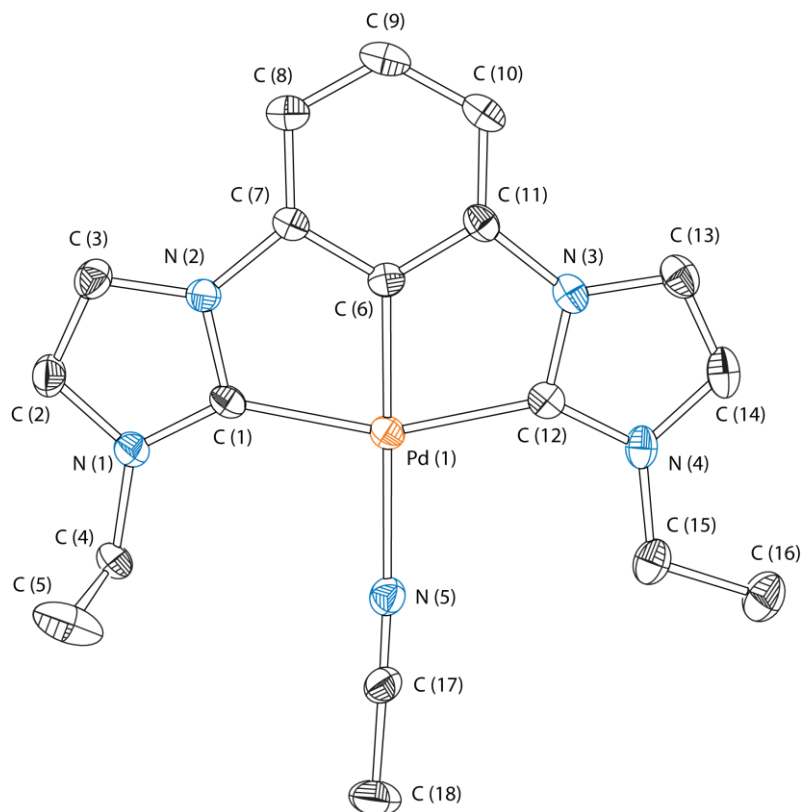


Figure C.2: Fully labeled thermal ellipsoid plot of  $[\text{PhDC}^{\text{Et}}\text{Pd}(\text{MeCN})]\text{PF}_6$  with hydrogens and a  $\text{PF}_6$  counterion omitted, displayed at the 50% probability level

### C.3.1 Bond Lengths and Angles for $[\text{PhDC}^{\text{Et}}\text{Pd}(\text{MeCN})]\text{PF}_6$

Bond	Length	Bond	Length
Pd(1)-C(6)	1.940(5)	C(6)-C(11)	1.387(7)
Pd(1)-C(12)	2.046(5)	C(7)-C(8)	1.382(7)
Pd(1)-C(1)	2.049(5)	C(8)-C(9)	1.383(7)
Pd(1)-N(5)	2.092(5)	C(9)-C(10)	1.395(8)
N(1)-C(1)	1.357(6)	C(10)-C(11)	1.373(7)
N(1)-C(2)	1.396(6)	C(13)-C(14)	1.337(8)

N(1)-C(4)	1.454(6)	C(15)-C(16)	1.503(7)
N(2)-C(1)	1.382(6)	C(17)-C(18)	1.452(7)
N(2)-C(3)	1.388(6)	C(19)-C(20)	1.440(8)
N(2)-C(7)	1.419(6)	P(1)-F(1)	1.587(4)
N(3)-C(12)	1.380(6)	P(1)-F(1)#1	1.587(4)
N(3)-C(13)	1.381(6)	P(1)-F(3)	1.588(4)
N(3)-C(11)	1.428(6)	P(1)-F(3)#1	1.588(4)
N(4)-C(12)	1.341(6)	P(1)-F(2)#1	1.592(4)
N(4)-C(14)	1.394(7)	P(1)-F(2)	1.592(4)
N(4)-C(15)	1.477(7)	P(2)-F(5)	1.552(4)
N(5)-C(17)	1.134(6)	P(2)-F(5)#2	1.552(4)
N(6)-C(19)	1.129(7)	P(2)-F(6)	1.559(4)
C(2)-C(3)	1.345(7)	P(2)-F(6)#2	1.559(4)
C(4)-C(5)	1.495(8)	P(2)-F(4)#2	1.569(4)
C(6)-C(7)	1.383(7)	P(2)-F(4)	1.569(4)

Table C.6: Bond lengths for  $[\text{PhDC}^{\text{Et}}\text{Pd}(\text{MeCN})]\text{PF}_6$

Bond	Angle	Bond	Angle
C(6)-Pd(1)-C(12)	78.5(2)	N(4)-C(12)-Pd(1)	141.8(4)
C(6)-Pd(1)-C(1)	78.5(2)	N(3)-C(12)-Pd(1)	114.0(3)
C(12)-Pd(1)-C(1)	157.0(2)	C(14)-C(13)-N(3)	105.9(5)
C(6)-Pd(1)-N(5)	176.84(18)	C(13)-C(14)-N(4)	108.0(5)
C(12)-Pd(1)-N(5)	101.71(19)	N(4)-C(15)-C(16)	113.8(5)
C(1)-Pd(1)-N(5)	101.18(18)	N(5)-C(17)-C(18)	178.7(6)
C(1)-N(1)-C(2)	110.5(4)	N(6)-C(19)-C(20)	178.6(9)
C(1)-N(1)-C(4)	125.8(4)	F(1)-P(1)-F(1)#1	180
C(2)-N(1)-C(4)	123.7(4)	F(1)-P(1)-F(3)	89.8(2)
C(1)-N(2)-C(3)	111.3(4)	F(1)#1-P(1)-F(3)	90.2(2)
C(1)-N(2)-C(7)	116.8(4)	F(1)-P(1)-F(3)#1	90.2(2)
C(3)-N(2)-C(7)	131.9(4)	F(1)#1-P(1)-F(3)#1	89.8(2)
C(12)-N(3)-C(13)	111.3(4)	F(3)-P(1)-F(3)#1	180
C(12)-N(3)-C(11)	116.2(4)	F(1)-P(1)-F(2)#1	89.4(2)
C(13)-N(3)-C(11)	132.5(5)	F(1)#1-P(1)-F(2)#1	90.6(2)
C(12)-N(4)-C(14)	110.6(5)	F(3)-P(1)-F(2)#1	90.7(2)

C(12)-N(4)-C(15)	122.2(4)	F(3)#1-P(1)-F(2)#1	89.3(2)
C(14)-N(4)-C(15)	127.2(5)	F(1)-P(1)-F(2)	90.6(2)
C(17)-N(5)-Pd(1)	176.1(4)	F(1)#1-P(1)-F(2)	89.4(2)
N(1)-C(1)-N(2)	104.1(4)	F(3)-P(1)-F(2)	89.3(2)
N(1)-C(1)-Pd(1)	142.3(4)	F(3)#1-P(1)-F(2)	90.7(2)
N(2)-C(1)-Pd(1)	113.4(3)	F(2)#1-P(1)-F(2)	180
C(3)-C(2)-N(1)	108.0(5)	F(5)-P(2)-F(5)#2	180
C(2)-C(3)-N(2)	106.1(5)	F(5)-P(2)-F(6)	91.4(3)
N(1)-C(4)-C(5)	112.6(5)	F(5)#2-P(2)-F(6)	88.6(3)
C(7)-C(6)-C(11)	118.4(5)	F(5)-P(2)-F(6)#2	88.6(3)
C(7)-C(6)-Pd(1)	120.9(4)	F(5)#2-P(2)-F(6)#2	91.4(3)
C(11)-C(6)-Pd(1)	120.7(4)	F(6)-P(2)-F(6)#2	180
C(8)-C(7)-C(6)	121.9(5)	F(5)-P(2)-F(4)#2	89.1(3)
C(8)-C(7)-N(2)	127.8(5)	F(5)#2-P(2)-F(4)#2	90.9(3)
C(6)-C(7)-N(2)	110.3(4)	F(6)-P(2)-F(4)#2	91.4(2)
C(7)-C(8)-C(9)	117.6(5)	F(6)#2-P(2)-F(4)#2	88.6(2)
C(8)-C(9)-C(10)	122.5(5)	F(5)-P(2)-F(4)	90.9(3)
C(11)-C(10)-C(9)	117.6(5)	F(5)#2-P(2)-F(4)	89.1(3)
C(10)-C(11)-C(6)	122.0(5)	F(6)-P(2)-F(4)	88.6(2)
C(10)-C(11)-N(3)	127.5(5)	F(6)#2-P(2)-F(4)	91.4(2)
C(6)-C(11)-N(3)	110.5(4)	F(4)#2-P(2)-F(4)	180.0(3)
N(4)-C(12)-N(3)	104.2(4)		

Table C.7: Bond angles for [PhDC<sup>E4</sup>Pd(MeCN)]PF<sub>6</sub>

#### C.4 [PhDC<sup>E4</sup>Pd(Py)]PF<sub>6</sub> Crystal Data

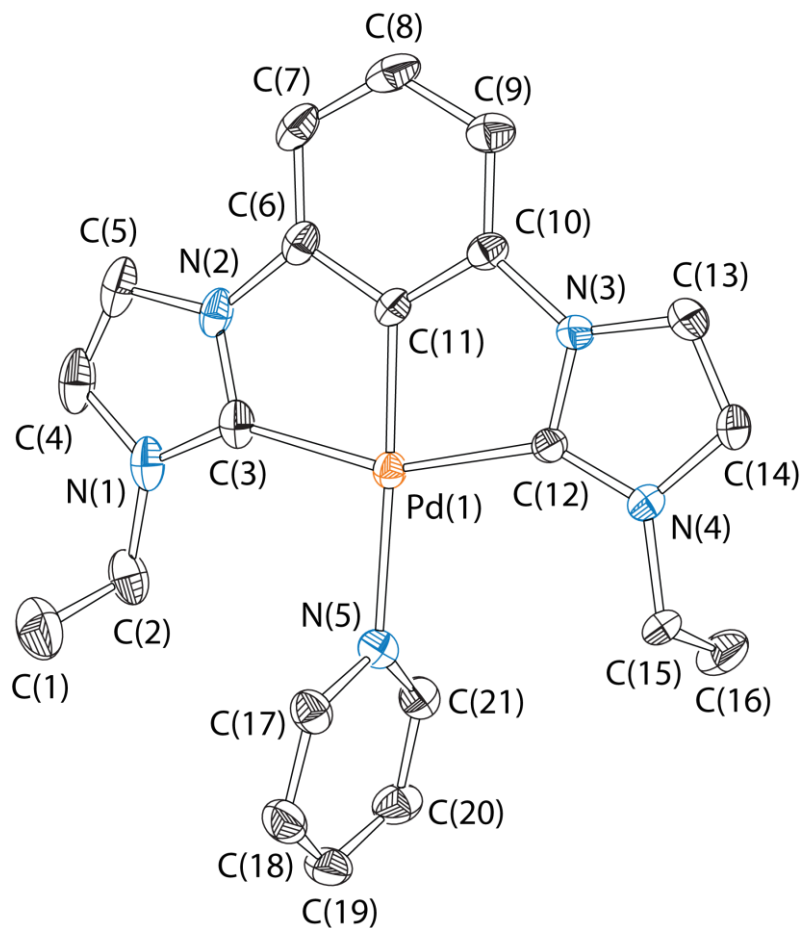


Figure C.3: Fully labeled thermal ellipsoid plot of  $[\text{PhDC}^{\text{Et}}\text{Pd}(\text{Py})]\text{PF}_6$  with hydrogens and a  $\text{PF}_6$  counterion omitted, displayed at the 50% probability level

#### C.4.1 Bond Lengths and Angles for $[\text{PhDC}^{\text{Et}}\text{Pd}(\text{Py})]\text{PF}_6$

Bond	Length	Bond	Length
Pd(1)-C(11)	1.947(4)	C(6)-C(11)	1.372(6)
Pd(1)-C(12)	2.054(4)	C(6)-C(7)	1.387(6)
Pd(1)-C(3)	2.062(4)	C(7)-C(8)	1.394(6)
Pd(1)-N(5)	2.142(4)	C(8)-C(9)	1.387(6)
Pd(2)-C(32)	1.946(5)	C(9)-C(10)	1.386(6)

Pd(2)-C(33)	2.055(4)	C(10)-C(11)	1.392(5)
Pd(2)-C(24)	2.070(5)	C(13)-C(14)	1.341(6)
Pd(2)-N(10)	2.157(4)	C(15)-C(16)	1.445(8)
N(1)-C(3)	1.345(5)	C(17)-C(18)	1.372(7)
N(1)-C(4)	1.386(6)	C(18)-C(19)	1.369(8)
N(1)-C(2)	1.470(6)	C(19)-C(20)	1.368(8)
N(2)-C(3)	1.374(5)	C(20)-C(21)	1.375(7)
N(2)-C(5)	1.382(5)	C(22)-C(23)	1.503(8)
N(2)-C(6)	1.426(5)	C(25)-C(26)	1.333(8)
N(3)-C(12)	1.374(5)	C(27)-C(28)	1.384(7)
N(3)-C(13)	1.387(5)	C(27)-C(32)	1.388(6)
N(3)-C(10)	1.416(5)	C(28)-C(29)	1.375(8)
N(4)-C(12)	1.346(5)	C(29)-C(30)	1.390(7)
N(4)-C(14)	1.390(6)	C(30)-C(31)	1.383(6)
N(4)-C(15)	1.477(6)	C(31)-C(32)	1.386(6)
N(5)-C(21)	1.331(6)	C(34)-C(35)	1.339(7)
N(5)-C(17)	1.349(6)	C(36)-C(37)	1.507(7)
N(6)-C(24)	1.354(6)	C(38)-C(39)	1.383(7)
N(6)-C(25)	1.385(7)	C(39)-C(40)	1.376(8)
N(6)-C(23)	1.461(7)	C(40)-C(41)	1.372(8)
N(7)-C(24)	1.376(6)	C(41)-C(42)	1.364(7)
N(7)-C(26)	1.383(6)	P(1)-F(6)	1.547(4)
N(7)-C(27)	1.426(6)	P(1)-F(2)	1.546(4)
N(8)-C(33)	1.370(5)	P(1)-F(1)	1.551(4)
N(8)-C(34)	1.376(6)	P(1)-F(4)	1.555(4)
N(8)-C(31)	1.421(5)	P(1)-F(3)	1.584(3)
N(9)-C(33)	1.346(5)	P(1)-F(5)	1.612(3)
N(9)-C(35)	1.385(6)	P(2)-F(7)	1.543(4)
N(9)-C(36)	1.465(5)	P(2)-F(8)	1.546(4)
N(10)-C(42)	1.339(6)	P(2)-F(11)	1.558(4)
N(10)-C(38)	1.342(6)	P(2)-F(10)	1.560(4)
C(1)-C(2)	1.514(7)	P(2)-F(12)	1.570(4)
C(4)-C(5)	1.335(6)	P(2)-F(9)	1.580(4)

Table C.8: Bond lengths for [PhDC<sup>Et</sup>Pd(Py)]PF<sub>6</sub>

Bond	Angle	Bond	Angle
C(11)-Pd(1)-C(12)	78.12(17)	C(16)-C(15)-N(4)	110.3(5)
C(11)-Pd(1)-C(3)	78.34(17)	N(5)-C(17)-C(18)	122.6(5)
C(12)-Pd(1)-C(3)	156.47(17)	C(19)-C(18)-C(17)	119.2(5)
C(11)-Pd(1)-N(5)	178.78(15)	C(20)-C(19)-C(18)	118.7(5)
C(12)-Pd(1)-N(5)	102.79(16)	C(19)-C(20)-C(21)	119.3(5)
C(3)-Pd(1)-N(5)	100.75(15)	N(5)-C(21)-C(20)	122.9(5)
C(32)-Pd(2)-C(33)	77.95(18)	N(6)-C(23)-C(22)	111.8(5)
C(32)-Pd(2)-C(24)	78.3(2)	N(6)-C(24)-N(7)	103.5(4)
C(33)-Pd(2)-C(24)	156.22(19)	N(6)-C(24)-Pd(2)	143.2(4)
C(32)-Pd(2)-N(10)	176.74(17)	N(7)-C(24)-Pd(2)	113.3(3)
C(33)-Pd(2)-N(10)	103.55(16)	C(26)-C(25)-N(6)	108.0(5)
C(24)-Pd(2)-N(10)	100.22(18)	C(25)-C(26)-N(7)	106.0(5)
C(3)-N(1)-C(4)	111.0(4)	C(28)-C(27)-C(32)	121.8(5)
C(3)-N(1)-C(2)	125.2(4)	C(28)-C(27)-N(7)	127.8(4)
C(4)-N(1)-C(2)	123.7(4)	C(32)-C(27)-N(7)	110.4(4)
C(3)-N(2)-C(5)	111.5(4)	C(29)-C(28)-C(27)	117.9(5)
C(3)-N(2)-C(6)	116.5(3)	C(28)-C(29)-C(30)	122.6(5)
C(5)-N(2)-C(6)	131.9(4)	C(31)-C(30)-C(29)	117.4(5)
C(12)-N(3)-C(13)	112.0(4)	C(30)-C(31)-C(32)	122.2(4)
C(12)-N(3)-C(10)	116.4(3)	C(30)-C(31)-N(8)	127.7(5)
C(13)-N(3)-C(10)	131.5(4)	C(32)-C(31)-N(8)	110.0(4)
C(12)-N(4)-C(14)	111.3(4)	C(31)-C(32)-C(27)	118.0(4)
C(12)-N(4)-C(15)	124.4(4)	C(31)-C(32)-Pd(2)	121.1(3)
C(14)-N(4)-C(15)	124.2(4)	C(27)-C(32)-Pd(2)	120.9(4)
C(21)-N(5)-C(17)	117.2(4)	N(9)-C(33)-N(8)	104.0(4)
C(21)-N(5)-Pd(1)	121.0(3)	N(9)-C(33)-Pd(2)	142.0(3)
C(17)-N(5)-Pd(1)	121.7(3)	N(8)-C(33)-Pd(2)	114.0(3)
C(24)-N(6)-C(25)	110.9(5)	C(35)-C(34)-N(8)	106.7(4)
C(24)-N(6)-C(23)	125.0(5)	C(34)-C(35)-N(9)	107.0(4)
C(25)-N(6)-C(23)	124.0(5)	N(9)-C(36)-C(37)	111.6(4)
C(24)-N(7)-C(26)	111.6(5)	N(10)-C(38)-C(39)	123.3(5)
C(24)-N(7)-C(27)	117.0(4)	C(40)-C(39)-C(38)	118.1(5)
C(26)-N(7)-C(27)	131.3(5)	C(39)-C(40)-C(41)	119.0(5)
C(33)-N(8)-C(34)	111.1(4)	C(42)-C(41)-C(40)	119.6(5)
C(33)-N(8)-C(31)	117.0(4)	N(10)-C(42)-C(41)	122.9(5)

C(34)-N(8)-C(31)	131.9(4)	F(6)-P(1)-F(2)	90.3(3)
C(33)-N(9)-C(35)	111.2(4)	F(6)-P(1)-F(1)	178.6(3)
C(33)-N(9)-C(36)	124.9(4)	F(2)-P(1)-F(1)	90.7(3)
C(35)-N(9)-C(36)	123.8(4)	F(6)-P(1)-F(4)	89.0(3)
C(42)-N(10)-C(38)	117.1(4)	F(2)-P(1)-F(4)	178.6(2)
C(42)-N(10)-Pd(2)	119.7(3)	F(1)-P(1)-F(4)	90.0(3)
C(38)-N(10)-Pd(2)	122.4(3)	F(6)-P(1)-F(3)	92.5(2)
N(1)-C(2)-C(1)	110.9(4)	F(2)-P(1)-F(3)	90.1(2)
N(1)-C(3)-N(2)	103.7(4)	F(1)-P(1)-F(3)	88.4(2)
N(1)-C(3)-Pd(1)	142.9(3)	F(4)-P(1)-F(3)	91.2(2)
N(2)-C(3)-Pd(1)	113.4(3)	F(6)-P(1)-F(5)	88.94(19)
C(5)-C(4)-N(1)	107.9(4)	F(2)-P(1)-F(5)	90.4(2)
C(4)-C(5)-N(2)	105.9(4)	F(1)-P(1)-F(5)	90.11(19)
C(11)-C(6)-C(7)	122.1(4)	F(4)-P(1)-F(5)	88.32(19)
C(11)-C(6)-N(2)	111.1(4)	F(3)-P(1)-F(5)	178.5(2)
C(7)-C(6)-N(2)	126.8(4)	F(7)-P(2)-F(8)	90.2(3)
C(6)-C(7)-C(8)	117.3(4)	F(7)-P(2)-F(11)	92.5(3)
C(9)-C(8)-C(7)	122.5(4)	F(8)-P(2)-F(11)	90.9(3)
C(8)-C(9)-C(10)	117.9(4)	F(7)-P(2)-F(10)	93.2(3)
C(9)-C(10)-C(11)	121.2(4)	F(8)-P(2)-F(10)	176.4(3)
C(9)-C(10)-N(3)	127.9(4)	F(11)-P(2)-F(10)	90.0(3)
C(11)-C(10)-N(3)	110.8(4)	F(7)-P(2)-F(12)	178.5(3)
C(6)-C(11)-C(10)	119.0(4)	F(8)-P(2)-F(12)	90.9(3)
C(6)-C(11)-Pd(1)	120.6(3)	F(11)-P(2)-F(12)	88.4(3)
C(10)-C(11)-Pd(1)	120.4(3)	F(10)-P(2)-F(12)	85.6(3)
N(4)-C(12)-N(3)	103.5(4)	F(7)-P(2)-F(9)	88.2(3)
N(4)-C(12)-Pd(1)	142.2(3)	F(8)-P(2)-F(9)	90.9(3)
N(3)-C(12)-Pd(1)	114.2(3)	F(11)-P(2)-F(9)	178.0(3)
C(14)-C(13)-N(3)	105.4(4)	F(10)-P(2)-F(9)	88.1(2)
C(13)-C(14)-N(4)	107.8(4)	F(12)-P(2)-F(9)	90.8(2)

Table C.9: Bond angles for [PhDC<sup>Et</sup>Pd(Py)]PF<sub>6</sub>

### C.5 [PhDC<sup>Et</sup>Pd(<sup>i</sup>BuNC)]PF<sub>6</sub> Crystal Data

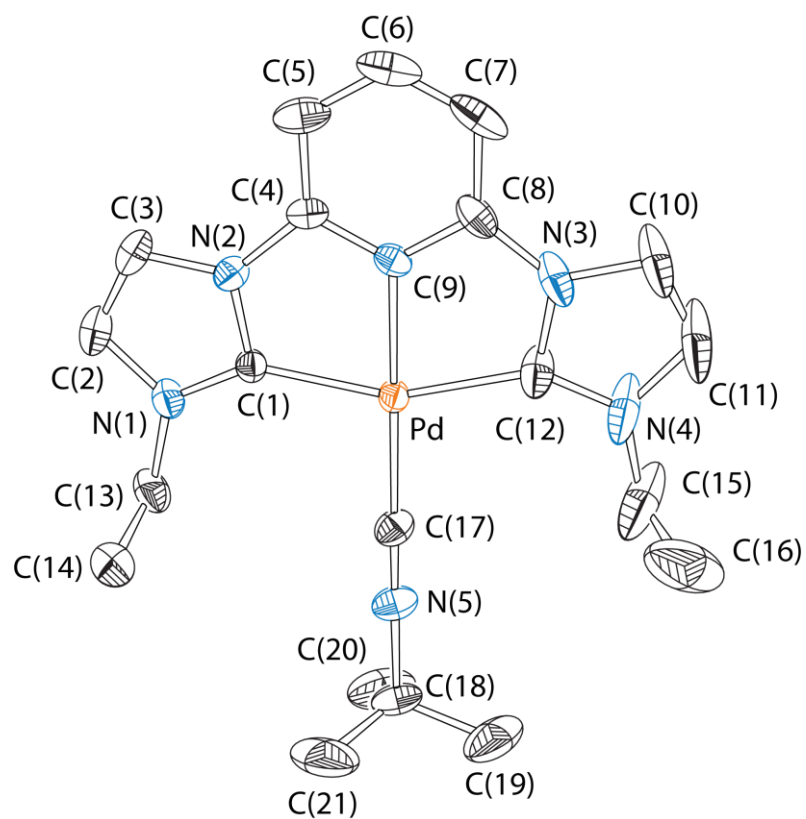


Figure C.4: Fully labeled thermal ellipsoid plot of  $[\text{PhDC}^{\text{Et}}\text{Pd}(\text{tBuNC})]\text{PF}_6$  with hydrogens and a  $\text{PF}_6$  counterion omitted, displayed at the 50% probability level.

### C.5.1 Bond Lengths and Angles for $[\text{PhDC}^{\text{Et}}\text{Pd}(\text{tBuNC})]\text{PF}_6$

Bond	Length	Bond	Length
Pd-C(9)	1.970(2)	C(6)-H(6)	0.93
Pd-C(17)	2.027(2)	C(7)-C(8)	1.381(3)
Pd-C(12)	2.062(2)	C(7)-H(7)	0.93
Pd-C(1)	2.063(2)	C(8)-C(9)	1.386(3)
P(1)-F(6)	1.5830(16)	C(10)-C(11)	1.336(4)

P(1)-F(3)	1.5812(17)	C(10)-H(10)	0.93
P(1)-F(4)	1.5893(17)	C(11)-H(11)	0.93
P(1)-F(2)	1.5908(17)	C(13)-C(14)	1.504(4)
P(1)-F(5)	1.5952(17)	C(13)-H(13A)	0.97
P(1)-F(1)	1.5956(17)	C(13)-H(13B)	0.97
N(1)-C(1)	1.342(3)	C(14)-H(14A)	0.96
N(1)-C(2)	1.392(3)	C(14)-H(14B)	0.96
N(1)-C(13)	1.467(3)	C(14)-H(14C)	0.96
N(2)-C(1)	1.371(3)	C(15)-C(16)	1.504(4)
N(2)-C(3)	1.378(3)	C(15)-H(15A)	0.97
N(2)-C(4)	1.423(3)	C(15)-H(15B)	0.97
N(3)-C(12)	1.366(3)	C(16)-H(16A)	0.96
N(3)-C(10)	1.374(3)	C(16)-H(16B)	0.96
N(3)-C(8)	1.418(3)	C(16)-H(16C)	0.96
N(4)-C(12)	1.341(3)	C(18)-C(21)	1.500(4)
N(4)-C(11)	1.389(3)	C(18)-C(19)	1.498(5)
N(4)-C(15)	1.471(3)	C(18)-C(20)	1.516(4)
N(5)-C(17)	1.148(3)	C(19)-H(19A)	0.96
N(5)-C(18)	1.478(3)	C(19)-H(19B)	0.96
C(2)-C(3)	1.325(4)	C(19)-H(19C)	0.96
C(2)-H(2)	0.93	C(20)-H(20A)	0.96
C(3)-H(3)	0.93	C(20)-H(20B)	0.96
C(4)-C(9)	1.372(3)	C(20)-H(20C)	0.96
C(4)-C(5)	1.393(3)	C(21)-H(21A)	0.96
C(5)-C(6)	1.388(4)	C(21)-H(21B)	0.96
C(5)-H(5)	0.93	C(21)-H(21C)	0.96
C(6)-C(7)	1.390(4)		

Table C.10: Bond lengths for [PhDC<sup>Et</sup>Pd(<sup>t</sup>BuNC)]PF<sub>6</sub>

Bond	Angle	Bond	Angle
C(9)-Pd-C(17)	177.98(8)	C(8)-C(9)-Pd	120.24(16)
C(9)-Pd-C(12)	77.69(9)	C(11)-C(10)-N(3)	106.2(2)
C(17)-Pd-C(12)	101.91(9)	C(11)-C(10)-H(10)	126.9
C(9)-Pd-C(1)	77.56(9)	N(3)-C(10)-H(10)	126.9

C(17)-Pd-C(1)	102.81(9)	C(10)-C(11)-N(4)	107.6(2)
C(12)-Pd-C(1)	155.25(9)	C(10)-C(11)-H(11)	126.2
F(6)-P(1)-F(3)	90.90(11)	N(4)-C(11)-H(11)	126.2
F(6)-P(1)-F(4)	91.01(10)	N(4)-C(12)-N(3)	104.42(19)
F(3)-P(1)-F(4)	90.41(10)	N(4)-C(12)-Pd	141.27(18)
F(6)-P(1)-F(2)	89.90(10)	N(3)-C(12)-Pd	114.29(15)
F(3)-P(1)-F(2)	89.46(11)	N(1)-C(13)-C(14)	111.6(2)
F(4)-P(1)-F(2)	179.08(10)	N(1)-C(13)-H(13A)	109.3
F(6)-P(1)-F(5)	179.15(11)	C(14)-C(13)-H(13A)	109.3
F(3)-P(1)-F(5)	89.85(12)	N(1)-C(13)-H(13B)	109.3
F(4)-P(1)-F(5)	89.39(10)	C(14)-C(13)-H(13B)	109.3
F(2)-P(1)-F(5)	89.70(10)	H(13A)-C(13)-H(13B)	108
F(6)-P(1)-F(1)	90.25(10)	C(13)-C(14)-H(14A)	109.5
F(3)-P(1)-F(1)	178.76(12)	C(13)-C(14)-H(14B)	109.5
F(4)-P(1)-F(1)	90.04(10)	H(14A)-C(14)-H(14B)	109.5
F(2)-P(1)-F(1)	90.08(10)	C(13)-C(14)-H(14C)	109.5
F(5)-P(1)-F(1)	89.00(10)	H(14A)-C(14)-H(14C)	109.5
C(1)-N(1)-C(2)	110.78(19)	H(14B)-C(14)-H(14C)	109.5
C(1)-N(1)-C(13)	125.25(19)	N(4)-C(15)-C(16)	112.6(2)
C(2)-N(1)-C(13)	123.93(19)	N(4)-C(15)-H(15A)	109.1
C(1)-N(2)-C(3)	110.82(19)	C(16)-C(15)-H(15A)	109.1
C(1)-N(2)-C(4)	116.45(17)	N(4)-C(15)-H(15B)	109.1
C(3)-N(2)-C(4)	132.72(18)	C(16)-C(15)-H(15B)	109.1
C(12)-N(3)-C(10)	111.27(19)	H(15A)-C(15)-H(15B)	107.8
C(12)-N(3)-C(8)	116.94(18)	C(15)-C(16)-H(16A)	109.5
C(10)-N(3)-C(8)	131.8(2)	C(15)-C(16)-H(16B)	109.5
C(12)-N(4)-C(11)	110.5(2)	H(16A)-C(16)-H(16B)	109.5
C(12)-N(4)-C(15)	125.0(2)	C(15)-C(16)-H(16C)	109.5
C(11)-N(4)-C(15)	124.5(2)	H(16A)-C(16)-H(16C)	109.5
C(17)-N(5)-C(18)	177.8(3)	H(16B)-C(16)-H(16C)	109.5
N(1)-C(1)-N(2)	104.19(18)	N(5)-C(17)-Pd	177.3(2)
N(1)-C(1)-Pd	141.48(16)	N(5)-C(18)-C(21)	106.8(2)
N(2)-C(1)-Pd	114.32(15)	N(5)-C(18)-C(19)	107.7(2)
C(3)-C(2)-N(1)	107.3(2)	C(21)-C(18)-C(19)	115.5(3)
C(3)-C(2)-H(2)	126.3	N(5)-C(18)-C(20)	107.4(2)
N(1)-C(2)-H(2)	126.3	C(21)-C(18)-C(20)	110.6(3)
C(2)-C(3)-N(2)	106.9(2)	C(19)-C(18)-C(20)	108.6(3)
C(2)-C(3)-H(3)	126.6	C(18)-C(19)-H(19A)	109.5
N(2)-C(3)-H(3)	126.6	C(18)-C(19)-H(19B)	109.5

C(9)-C(4)-C(5)	121.8(2)	H(19A)-C(19)-H(19B)	109.5
C(9)-C(4)-N(2)	111.06(18)	C(18)-C(19)-H(19C)	109.5
C(5)-C(4)-N(2)	127.1(2)	H(19A)-C(19)-H(19C)	109.5
C(6)-C(5)-C(4)	117.0(2)	H(19B)-C(19)-H(19C)	109.5
C(6)-C(5)-H(5)	121.5	C(18)-C(20)-H(20A)	109.5
C(4)-C(5)-H(5)	121.5	C(18)-C(20)-H(20B)	109.5
C(5)-C(6)-C(7)	123.0(2)	H(20A)-C(20)-H(20B)	109.5
C(5)-C(6)-H(6)	118.5	C(18)-C(20)-H(20C)	109.5
C(7)-C(6)-H(6)	118.5	H(20A)-C(20)-H(20C)	109.5
C(8)-C(7)-C(6)	117.4(2)	H(20B)-C(20)-H(20C)	109.5
C(8)-C(7)-H(7)	121.3	C(18)-C(21)-H(21A)	109.5
C(6)-C(7)-H(7)	121.3	C(18)-C(21)-H(21B)	109.5
C(7)-C(8)-C(9)	121.6(2)	H(21A)-C(21)-H(21B)	109.5
C(7)-C(8)-N(3)	127.7(2)	C(18)-C(21)-H(21C)	109.5
C(9)-C(8)-N(3)	110.74(18)	H(21A)-C(21)-H(21C)	109.5
C(4)-C(9)-C(8)	119.16(19)	H(21B)-C(21)-H(21C)	109.5
C(4)-C(9)-Pd	120.58(16)		

Table C.11: Bond angles for [PhDC<sup>Et</sup>Pd(<sup>t</sup>BuNC)]PF<sub>6</sub>

### C.6 [PhDC<sup>Et</sup>Pd(PPh<sub>3</sub>)]PF<sub>6</sub> Crystal Data

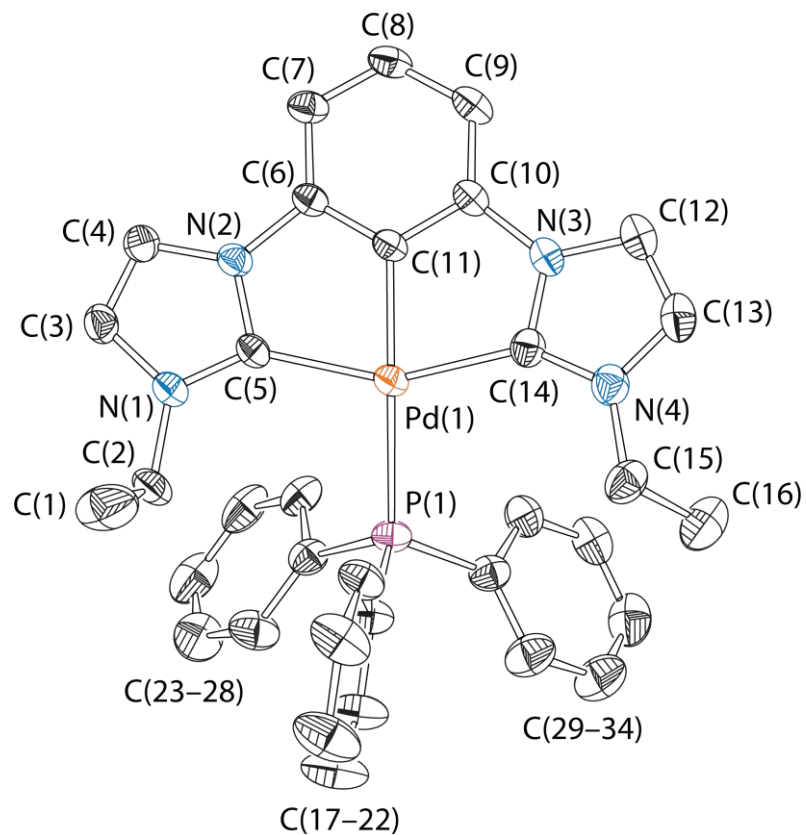


Figure C.5: Labeled thermal ellipsoid plot of  $[\text{PhDC}^{\text{Et}}\text{Pd}(\text{PPh}_3)]\text{PF}_6$  with hydrogens and a  $\text{PF}_6$  counterion omitted, displayed at the 50% probability level.

### C.6.1 Bond Lengths and Angles for $[\text{PhDC}^{\text{Et}}\text{Pd}(\text{PPh}_3)]\text{PF}_6$

Bond	Length	Bond	Length
Pd(1)-C(11)	1.981(4)	C(12)-C(13)	1.341(8)
Pd(1)-C(14)	2.071(4)	C(12)-H(12)	0.95
Pd(1)-C(5)	2.072(4)	C(13)-H(13)	0.95
Pd(1)-P(1)	2.3867(11)	C(15)-C(16)	1.508(8)
P(1)-C(22)	1.812(5)	C(15)-H(15A)	0.99
P(1)-C(34)	1.822(5)	C(15)-H(15B)	0.99

P(1)-C(28)	1.834(5)	C(16)-H(16A)	0.98
P(2)-F(6)	1.546(5)	C(16)-H(16B)	0.98
P(2)-F(3)	1.555(5)	C(16)-H(16C)	0.98
P(2)-F(2)	1.547(5)	C(17)-C(18)	1.380(7)
P(2)-F(1)	1.554(5)	C(17)-C(22)	1.387(7)
P(2)-F(5)	1.564(4)	C(17)-H(17)	0.95
P(2)-F(4)	1.565(5)	C(18)-C(19)	1.359(9)
N(1)-C(5)	1.343(5)	C(18)-H(18)	0.95
N(1)-C(3)	1.396(6)	C(19)-C(20)	1.344(9)
N(1)-C(2)	1.470(6)	C(19)-H(19)	0.95
N(2)-C(5)	1.374(5)	C(20)-C(21)	1.394(8)
N(2)-C(4)	1.388(6)	C(20)-H(20)	0.95
N(2)-C(6)	1.423(5)	C(21)-C(22)	1.396(6)
N(3)-C(14)	1.370(6)	C(21)-H(21)	0.95
N(3)-C(12)	1.379(6)	C(23)-C(28)	1.385(7)
N(3)-C(10)	1.421(6)	C(23)-C(24)	1.408(8)
N(4)-C(14)	1.346(6)	C(23)-H(23)	0.95
N(4)-C(13)	1.378(7)	C(24)-C(25)	1.373(11)
N(4)-C(15)	1.470(7)	C(24)-H(24)	0.95
C(1)-C(2)	1.467(8)	C(25)-C(26)	1.342(11)
C(1)-H(1A)	0.98	C(25)-H(25)	0.95
C(1)-H(1B)	0.98	C(26)-C(27)	1.379(9)
C(1)-H(1C)	0.98	C(26)-H(26)	0.95
C(2)-H(2A)	0.99	C(27)-C(28)	1.394(7)
C(2)-H(2B)	0.99	C(27)-H(27)	0.95
C(3)-C(4)	1.330(6)	C(29)-C(30)	1.380(8)
C(3)-H(3)	0.95	C(29)-C(34)	1.387(7)
C(4)-H(4)	0.95	C(29)-H(29)	0.95
C(6)-C(11)	1.370(6)	C(30)-C(31)	1.376(10)
C(6)-C(7)	1.395(6)	C(30)-H(30)	0.95
C(7)-C(8)	1.385(7)	C(31)-C(32)	1.384(11)
C(7)-H(7)	0.95	C(31)-H(31)	0.95
C(8)-C(9)	1.387(7)	C(32)-C(33)	1.376(9)
C(8)-H(8)	0.95	C(32)-H(32)	0.95
C(9)-C(10)	1.386(6)	C(33)-C(34)	1.388(7)
C(9)-H(9)	0.95	C(33)-H(33)	0.95
C(10)-C(11)	1.381(5)		

Table C.12: Bond lengths for [PhDC<sup>Et</sup>Pd(PPh<sub>3</sub>)]PF<sub>6</sub>

Bond	Angle	Bond	Angle
C(11)-Pd(1)-C(14)	77.22(17)	C(10)-C(11)-Pd(1)	120.0(3)
C(11)-Pd(1)-C(5)	77.44(16)	C(13)-C(12)-N(3)	105.3(5)
C(14)-Pd(1)-C(5)	153.74(16)	C(13)-C(12)-H(12)	127.3
C(11)-Pd(1)-P(1)	166.15(12)	N(3)-C(12)-H(12)	127.3
C(14)-Pd(1)-P(1)	104.45(13)	C(12)-C(13)-N(4)	108.3(4)
C(5)-Pd(1)-P(1)	101.80(11)	C(12)-C(13)-H(13)	125.8
C(22)-P(1)-C(34)	107.4(2)	N(4)-C(13)-H(13)	125.8
C(22)-P(1)-C(28)	107.4(2)	N(4)-C(14)-N(3)	103.9(4)
C(34)-P(1)-C(28)	100.0(2)	N(4)-C(14)-Pd(1)	141.8(4)
C(22)-P(1)-Pd(1)	113.74(15)	N(3)-C(14)-Pd(1)	114.1(3)
C(34)-P(1)-Pd(1)	115.85(16)	N(4)-C(15)-C(16)	111.7(5)
C(28)-P(1)-Pd(1)	111.25(15)	N(4)-C(15)-H(15A)	109.3
F(6)-P(2)-F(3)	179.0(4)	C(16)-C(15)-H(15A)	109.3
F(6)-P(2)-F(2)	90.8(4)	N(4)-C(15)-H(15B)	109.3
F(3)-P(2)-F(2)	88.2(4)	C(16)-C(15)-H(15B)	109.3
F(6)-P(2)-F(1)	91.3(4)	H(15A)-C(15)-H(15B)	107.9
F(3)-P(2)-F(1)	88.4(3)	C(15)-C(16)-H(16A)	109.5
F(2)-P(2)-F(1)	91.5(4)	C(15)-C(16)-H(16B)	109.5
F(6)-P(2)-F(5)	89.2(4)	H(16A)-C(16)-H(16B)	109.5
F(3)-P(2)-F(5)	91.7(4)	C(15)-C(16)-H(16C)	109.5
F(2)-P(2)-F(5)	178.4(4)	H(16A)-C(16)-H(16C)	109.5
F(1)-P(2)-F(5)	90.1(3)	H(16B)-C(16)-H(16C)	109.5
F(6)-P(2)-F(4)	89.3(3)	C(18)-C(17)-C(22)	120.7(5)
F(3)-P(2)-F(4)	91.1(3)	C(18)-C(17)-H(17)	119.6
F(2)-P(2)-F(4)	89.4(4)	C(22)-C(17)-H(17)	119.6
F(1)-P(2)-F(4)	178.9(4)	C(19)-C(18)-C(17)	120.4(6)
F(5)-P(2)-F(4)	89.0(3)	C(19)-C(18)-H(18)	119.8
C(5)-N(1)-C(3)	111.0(4)	C(17)-C(18)-H(18)	119.8
C(5)-N(1)-C(2)	125.7(4)	C(20)-C(19)-C(18)	120.2(6)
C(3)-N(1)-C(2)	123.3(4)	C(20)-C(19)-H(19)	119.9
C(5)-N(2)-C(4)	111.1(3)	C(18)-C(19)-H(19)	119.9
C(5)-N(2)-C(6)	116.9(3)	C(19)-C(20)-C(21)	121.1(5)
C(4)-N(2)-C(6)	131.5(4)	C(19)-C(20)-H(20)	119.5
C(14)-N(3)-C(12)	111.8(4)	C(21)-C(20)-H(20)	119.5
C(14)-N(3)-C(10)	116.8(3)	C(22)-C(21)-C(20)	119.6(5)

C(12)-N(3)-C(10)	130.4(4)	C(22)-C(21)-H(21)	120.2
C(14)-N(4)-C(13)	110.7(4)	C(20)-C(21)-H(21)	120.2
C(14)-N(4)-C(15)	125.5(4)	C(17)-C(22)-C(21)	117.9(4)
C(13)-N(4)-C(15)	123.4(4)	C(17)-C(22)-P(1)	116.4(3)
C(2)-C(1)-H(1A)	109.5	C(21)-C(22)-P(1)	125.5(4)
C(2)-C(1)-H(1B)	109.5	C(28)-C(23)-C(24)	120.4(6)
H(1A)-C(1)-H(1B)	109.5	C(28)-C(23)-H(23)	119.8
C(2)-C(1)-H(1C)	109.5	C(24)-C(23)-H(23)	119.8
H(1A)-C(1)-H(1C)	109.5	C(25)-C(24)-C(23)	120.5(7)
H(1B)-C(1)-H(1C)	109.5	C(25)-C(24)-H(24)	119.7
C(1)-C(2)-N(1)	113.4(5)	C(23)-C(24)-H(24)	119.7
C(1)-C(2)-H(2A)	108.9	C(26)-C(25)-C(24)	118.6(6)
N(1)-C(2)-H(2A)	108.9	C(26)-C(25)-H(25)	120.7
C(1)-C(2)-H(2B)	108.9	C(24)-C(25)-H(25)	120.7
N(1)-C(2)-H(2B)	108.9	C(25)-C(26)-C(27)	122.5(7)
H(2A)-C(2)-H(2B)	107.7	C(25)-C(26)-H(26)	118.7
C(4)-C(3)-N(1)	107.5(4)	C(27)-C(26)-H(26)	118.7
C(4)-C(3)-H(3)	126.2	C(26)-C(27)-C(28)	120.4(7)
N(1)-C(3)-H(3)	126.2	C(26)-C(27)-H(27)	119.8
C(3)-C(4)-N(2)	106.4(4)	C(28)-C(27)-H(27)	119.8
C(3)-C(4)-H(4)	126.8	C(23)-C(28)-C(27)	117.5(5)
N(2)-C(4)-H(4)	126.8	C(23)-C(28)-P(1)	117.1(4)
N(1)-C(5)-N(2)	104.0(4)	C(27)-C(28)-P(1)	125.4(4)
N(1)-C(5)-Pd(1)	142.0(3)	C(30)-C(29)-C(34)	120.6(6)
N(2)-C(5)-Pd(1)	113.7(3)	C(30)-C(29)-H(29)	119.7
C(11)-C(6)-C(7)	122.1(4)	C(34)-C(29)-H(29)	119.7
C(11)-C(6)-N(2)	111.0(3)	C(31)-C(30)-C(29)	120.7(6)
C(7)-C(6)-N(2)	126.9(4)	C(31)-C(30)-H(30)	119.7
C(8)-C(7)-C(6)	117.1(4)	C(29)-C(30)-H(30)	119.7
C(8)-C(7)-H(7)	121.4	C(30)-C(31)-C(32)	119.4(6)
C(6)-C(7)-H(7)	121.4	C(30)-C(31)-H(31)	120.3
C(7)-C(8)-C(9)	122.5(4)	C(32)-C(31)-H(31)	120.3
C(7)-C(8)-H(8)	118.7	C(33)-C(32)-C(31)	119.8(7)
C(9)-C(8)-H(8)	118.7	C(33)-C(32)-H(32)	120.1
C(10)-C(9)-C(8)	117.8(4)	C(31)-C(32)-H(32)	120.1
C(10)-C(9)-H(9)	121.1	C(32)-C(33)-C(34)	121.4(7)
C(8)-C(9)-H(9)	121.1	C(32)-C(33)-H(33)	119.3
C(9)-C(10)-C(11)	121.5(4)	C(34)-C(33)-H(33)	119.3
C(9)-C(10)-N(3)	127.7(4)	C(29)-C(34)-C(33)	118.1(5)

C(11)-C(10)-N(3)	110.8(4)	C(29)-C(34)-P(1)	117.7(4)
C(6)-C(11)-C(10)	118.8(4)	C(33)-C(34)-P(1)	124.3(4)
C(6)-C(11)-Pd(1)	120.2(3)		

Table C.13: Bond angles for  $[\text{PhDC}^{\text{Et}}\text{Pd}(\text{PPh}_3)]\text{PF}_6$

### C.7 $[\text{PhDC}^{\text{Et}}\text{Ni}(\text{Br})]$ Crystal Data

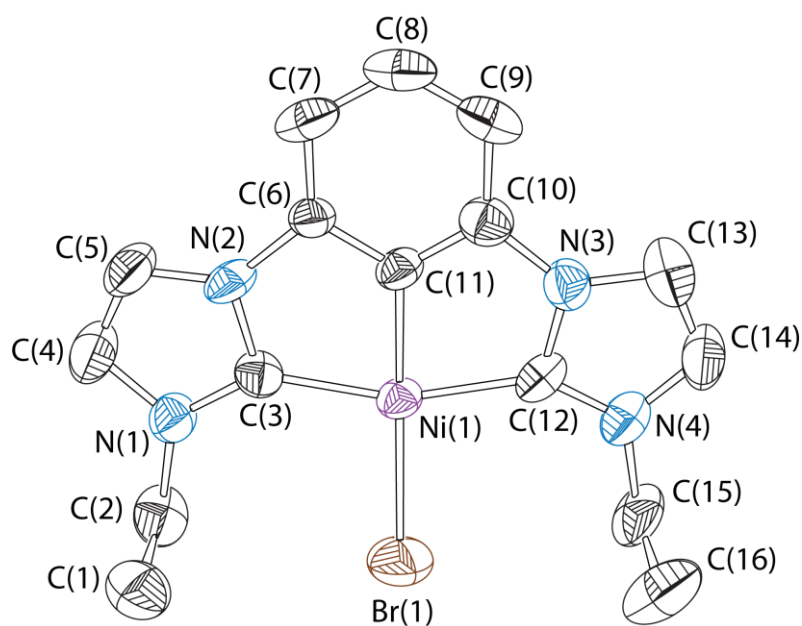


Figure C.6: Fully labeled thermal ellipsoid plot of  $[\text{PhDC}^{\text{Et}}\text{Ni}(\text{Br})]$  with hydrogens omitted, displayed at the 50% probability level.

#### C.7.1 Bond Lengths and Angles for $[\text{PhDC}^{\text{Et}}\text{Ni}(\text{Br})]$

<b>Bond</b>	<b>Length</b>	<b>Bond</b>	<b>Length</b>
Ni(1)-C(11)	1.860(13)	Ni(3)-C(44)	1.823(18)
Ni(1)-C(3)	1.942(13)	Ni(3)-C(45)	1.897(19)
Ni(1)-C(12)	1.961(14)	Ni(3)-C(36)	1.964(19)
Ni(1)-Br(1)	2.316(2)	Ni(3)-Br(3)	2.308(11)
N(1)-C(3)	1.357(14)	N(9)-C(36)	1.37(3)
N(1)-C(4)	1.379(16)	N(9)-C(37)	1.37(3)
N(1)-C(2)	1.468(17)	N(9)-C(35)	1.51(3)
N(2)-C(3)	1.372(15)	N(10)-C(36)	1.37(2)
N(2)-C(5)	1.397(15)	N(10)-C(38)	1.39(3)
N(2)-C(6)	1.411(14)	N(10)-C(39)	1.40(3)
N(3)-C(12)	1.353(18)	N(11)-C(46)	1.35(3)
N(3)-C(13)	1.375(18)	N(11)-C(45)	1.40(3)
N(3)-C(10)	1.424(18)	N(11)-C(43)	1.45(3)
N(4)-C(12)	1.351(17)	N(12)-C(45)	1.39(3)
N(4)-C(14)	1.39(2)	N(12)-C(47)	1.41(3)
N(4)-C(15)	1.45(2)	N(12)-C(48)	1.65(3)
C(1)-C(2)	1.51(2)	C(35)-C(34)	1.48(2)
C(4)-C(5)	1.298(18)	C(37)-C(38)	1.35(5)
C(6)-C(7)	1.359(17)	C(39)-C(44)	1.39(3)
C(6)-C(11)	1.376(17)	C(39)-C(40)	1.40(3)
C(7)-C(8)	1.32(2)	C(40)-C(41)	1.45(4)
C(8)-C(9)	1.38(2)	C(41)-C(42)	1.33(4)
C(9)-C(10)	1.370(19)	C(42)-C(43)	1.43(3)
C(10)-C(11)	1.387(17)	C(43)-C(44)	1.35(3)
C(13)-C(14)	1.30(3)	C(46)-C(47)	1.40(5)
C(15)-C(16)	1.49(2)	C(48)-C(49)	1.48(2)
Ni(2)-C(27)	1.863(10)	Ni(3')-C(44')	1.830(16)
Ni(2)-C(19)	1.960(11)	Ni(3')-C(45')	1.897(17)
Ni(2)-C(28)	1.966(12)	Ni(3')-C(36')	1.956(16)
Ni(2)-Br(2)	2.3272(19)	Ni(3')-Br(3')	2.315(7)
N(5)-C(19)	1.361(14)	N(9')-C(36')	1.37(2)
N(5)-C(20)	1.426(15)	N(9')-C(37')	1.37(3)
N(5)-C(18)	1.452(15)	N(9')-C(35')	1.51(3)
N(6)-C(21)	1.361(15)	N(10')-C(36')	1.38(2)
N(6)-C(19)	1.380(14)	N(10')-C(39')	1.39(3)
N(6)-C(22)	1.438(14)	N(10')-C(38')	1.40(3)
N(7)-C(28)	1.376(14)	N(11')-C(46')	1.34(3)
N(7)-C(29)	1.383(16)	N(11')-C(45')	1.38(2)

N(7)-C(26)	1.412(15)	N(11')-C(43')	1.47(3)
N(8)-C(28)	1.331(14)	N(12')-C(45')	1.41(3)
N(8)-C(30)	1.377(17)	N(12')-C(47')	1.41(3)
N(8)-C(31)	1.461(16)	N(12')-C(48')	1.69(3)
C(17)-C(18)	1.516(19)	C(35')-C(34')	1.48(2)
C(20)-C(21)	1.290(18)	C(37')-C(38')	1.35(4)
C(22)-C(23)	1.355(15)	C(39')-C(44')	1.40(3)
C(22)-C(27)	1.375(14)	C(39')-C(40')	1.40(3)
C(23)-C(24)	1.401(18)	C(40')-C(41')	1.45(4)
C(24)-C(25)	1.352(19)	C(41')-C(42')	1.34(4)
C(25)-C(26)	1.405(16)	C(42')-C(43')	1.41(3)
C(26)-C(27)	1.347(16)	C(43')-C(44')	1.35(3)
C(29)-C(30)	1.32(2)	C(46')-C(47')	1.41(5)
C(31)-C(32)	1.52(2)	C(48')-C(49')	1.48(2)

Table C.14: Bond lengths for [PhDC<sup>Et</sup>Ni(Br)]

Bond	Angle	Bond	Angle
C(11)-Ni(1)-C(3)	79.6(5)	C(44)-Ni(3)-C(45)	79.7(11)
C(11)-Ni(1)-C(12)	79.6(6)	C(44)-Ni(3)-C(36)	80.4(10)
C(3)-Ni(1)-C(12)	159.2(6)	C(45)-Ni(3)-C(36)	160.1(12)
C(11)-Ni(1)-Br(1)	169.4(4)	C(44)-Ni(3)-Br(3)	177.2(18)
C(3)-Ni(1)-Br(1)	99.7(4)	C(45)-Ni(3)-Br(3)	102.4(10)
C(12)-Ni(1)-Br(1)	100.9(4)	C(36)-Ni(3)-Br(3)	97.5(9)
C(3)-N(1)-C(4)	112.5(10)	C(36)-N(9)-C(37)	110(2)
C(3)-N(1)-C(2)	125.0(11)	C(36)-N(9)-C(35)	123(2)
C(4)-N(1)-C(2)	122.3(11)	C(37)-N(9)-C(35)	126(2)
C(3)-N(2)-C(5)	111.1(10)	C(36)-N(10)-C(38)	113(2)
C(3)-N(2)-C(6)	115.4(10)	C(36)-N(10)-C(39)	117(2)
C(5)-N(2)-C(6)	133.5(10)	C(38)-N(10)-C(39)	130(2)
C(12)-N(3)-C(13)	109.2(14)	C(46)-N(11)-C(45)	115(2)
C(12)-N(3)-C(10)	116.5(11)	C(46)-N(11)-C(43)	135(3)
C(13)-N(3)-C(10)	134.3(14)	C(45)-N(11)-C(43)	110(2)
C(12)-N(4)-C(14)	108.5(16)	C(45)-N(12)-C(47)	113(3)
C(12)-N(4)-C(15)	127.6(15)	C(45)-N(12)-C(48)	127(2)
C(14)-N(4)-C(15)	123.9(16)	C(47)-N(12)-C(48)	119(2)

N(1)-C(2)-C(1)	112.1(13)	C(34)-C(35)-N(9)	112(3)
N(1)-C(3)-N(2)	101.9(10)	N(9)-C(36)-N(10)	103.1(18)
N(1)-C(3)-Ni(1)	143.0(9)	N(9)-C(36)-Ni(3)	143.7(18)
N(2)-C(3)-Ni(1)	114.8(8)	N(10)-C(36)-Ni(3)	112.8(17)
C(5)-C(4)-N(1)	107.2(12)	C(38)-C(37)-N(9)	110(3)
C(4)-C(5)-N(2)	107.2(12)	C(37)-C(38)-N(10)	104(3)
C(7)-C(6)-C(11)	122.7(12)	C(44)-C(39)-N(10)	107.7(19)
C(7)-C(6)-N(2)	128.9(11)	C(44)-C(39)-C(40)	126(3)
C(11)-C(6)-N(2)	108.3(10)	N(10)-C(39)-C(40)	126(3)
C(8)-C(7)-C(6)	118.4(15)	C(39)-C(40)-C(41)	113(3)
C(7)-C(8)-C(9)	123.6(14)	C(42)-C(41)-C(40)	124(3)
C(10)-C(9)-C(8)	116.4(13)	C(41)-C(42)-C(43)	117(3)
C(9)-C(10)-C(11)	122.6(14)	C(44)-C(43)-C(42)	125(3)
C(9)-C(10)-N(3)	129.9(13)	C(44)-C(43)-N(11)	110(2)
C(11)-C(10)-N(3)	107.5(12)	C(42)-C(43)-N(11)	125(3)
C(6)-C(11)-C(10)	116.2(12)	C(43)-C(44)-C(39)	115(2)
C(6)-C(11)-Ni(1)	121.7(9)	C(43)-C(44)-Ni(3)	123(2)
C(10)-C(11)-Ni(1)	121.8(11)	C(39)-C(44)-Ni(3)	122.2(19)
N(4)-C(12)-N(3)	106.1(13)	N(11)-C(45)-N(12)	100.4(18)
N(4)-C(12)-Ni(1)	139.5(12)	N(11)-C(45)-Ni(3)	118.0(18)
N(3)-C(12)-Ni(1)	114.4(10)	N(12)-C(45)-Ni(3)	141.0(18)
C(14)-C(13)-N(3)	108.3(17)	N(11)-C(46)-C(47)	106(3)
C(13)-C(14)-N(4)	108.0(16)	C(46)-C(47)-N(12)	105(3)
N(4)-C(15)-C(16)	110.8(15)	C(49)-C(48)-N(12)	106(3)
C(27)-Ni(2)-C(19)	79.8(5)	C(44')-Ni(3')-C(45')	80.2(9)
C(27)-Ni(2)-C(28)	80.5(5)	C(44')-Ni(3')-C(36')	79.9(9)
C(19)-Ni(2)-C(28)	160.3(5)	C(45')-Ni(3')-C(36')	160.1(10)
C(27)-Ni(2)-Br(2)	172.3(3)	C(44')-Ni(3')-Br(3')	173.3(14)
C(19)-Ni(2)-Br(2)	100.4(3)	C(45')-Ni(3')-Br(3')	100.0(7)
C(28)-Ni(2)-Br(2)	99.0(3)	C(36')-Ni(3')-Br(3')	99.8(7)
C(19)-N(5)-C(20)	109.5(10)	C(36')-N(9')-C(37')	111(2)
C(19)-N(5)-C(18)	126.3(10)	C(36')-N(9')-C(35')	123.9(16)
C(20)-N(5)-C(18)	124.1(10)	C(37')-N(9')-C(35')	125(2)
C(21)-N(6)-C(19)	111.9(10)	C(36')-N(10')-C(39')	116.6(17)
C(21)-N(6)-C(22)	134.3(9)	C(36')-N(10')-C(38')	111(2)
C(19)-N(6)-C(22)	113.7(9)	C(39')-N(10')-C(38')	132.2(19)
C(28)-N(7)-C(29)	110.4(11)	C(46')-N(11')-C(45')	115(2)
C(28)-N(7)-C(26)	115.1(9)	C(46')-N(11')-C(43')	135(2)
C(29)-N(7)-C(26)	134.4(11)	C(45')-N(11')-C(43')	110.3(17)

C(28)-N(8)-C(30)	110.8(11)	C(45')-N(12')-C(47')	111(2)
C(28)-N(8)-C(31)	126.7(11)	C(45')-N(12')-C(48')	124.7(18)
C(30)-N(8)-C(31)	122.4(11)	C(47')-N(12')-C(48')	118(2)
N(5)-C(18)-C(17)	112.1(10)	C(34')-C(35')-N(9')	112.5(19)
N(5)-C(19)-N(6)	102.9(9)	N(9')-C(36')-N(10')	103.6(15)
N(5)-C(19)-Ni(2)	141.7(9)	N(9')-C(36')-Ni(3')	142.8(14)
N(6)-C(19)-Ni(2)	115.4(8)	N(10')-C(36')-Ni(3')	113.4(15)
C(21)-C(20)-N(5)	107.6(11)	C(38')-C(37')-N(9')	109(2)
C(20)-C(21)-N(6)	108.0(11)	C(37')-C(38')-N(10')	105(2)
C(23)-C(22)-C(27)	123.3(11)	N(10')-C(39')-C(44')	107.7(16)
C(23)-C(22)-N(6)	127.0(11)	N(10')-C(39')-C(40')	129(2)
C(27)-C(22)-N(6)	109.6(9)	C(44')-C(39')-C(40')	123(2)
C(22)-C(23)-C(24)	117.3(12)	C(39')-C(40')-C(41')	115(2)
C(25)-C(24)-C(23)	121.4(12)	C(42')-C(41')-C(40')	124(2)
C(24)-C(25)-C(26)	118.5(12)	C(41')-C(42')-C(43')	116(3)
C(27)-C(26)-C(25)	121.5(12)	C(44')-C(43')-C(42')	126(3)
C(27)-C(26)-N(7)	110.8(10)	C(44')-C(43')-N(11')	109.7(17)
C(25)-C(26)-N(7)	127.7(11)	C(42')-C(43')-N(11')	124(2)
C(26)-C(27)-C(22)	118.0(10)	C(43')-C(44')-C(39')	115.6(18)
C(26)-C(27)-Ni(2)	120.4(8)	C(43')-C(44')-Ni(3')	121.8(17)
C(22)-C(27)-Ni(2)	121.5(8)	C(39')-C(44')-Ni(3')	122.3(17)
N(8)-C(28)-N(7)	104.3(10)	N(11')-C(45')-N(12')	101.9(15)
N(8)-C(28)-Ni(2)	142.5(9)	N(11')-C(45')-Ni(3')	117.9(15)
N(7)-C(28)-Ni(2)	113.1(8)	N(12')-C(45')-Ni(3')	140.2(16)
C(30)-C(29)-N(7)	106.1(13)	N(11')-C(46')-C(47')	106(2)
C(29)-C(30)-N(8)	108.3(12)	C(46')-C(47')-N(12')	105(3)
N(8)-C(31)-C(32)	111.3(12)	C(49')-C(48')-N(12')	81.2(17)

Table C.15: Bond angles for [PhDC<sup>Et</sup>Ni(Br)]

### C.8 [PhDC<sup>Et</sup>Ni(MeCN)]PF<sub>6</sub> Crystal Data

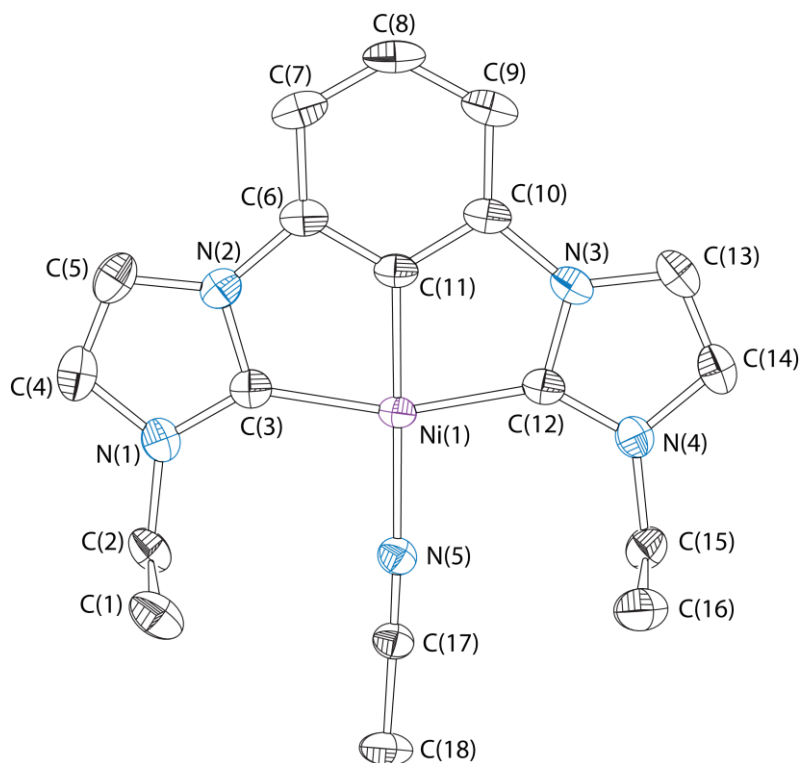


Figure C.7: Fully labeled thermal ellipsoid plot of  $[\text{PhDC}^{\text{Et}}\text{Ni}(\text{MeCN})]\text{PF}_6$  with hydrogens and an outer sphere  $\text{PF}_6$  counterion omitted, displayed at the 50% probability level.

### C.8.1 Bond Lengths and Angles for $[\text{PhDC}^{\text{Et}}\text{Ni}(\text{MeCN})]\text{PF}_6$

Bond	Length	Bond	Length
Ni-C(11)	1.857(2)	N(3)-C(13)	1.372(3)
Ni-N(5)	1.9058(18)	N(3)-C(10)	1.417(3)
Ni-C(12)	1.936(2)	N(4)-C(12)	1.354(3)
Ni-C(3)	1.937(2)	N(4)-C(14)	1.390(3)
P(1)-F(2)	1.5721(17)	N(4)-C(15)	1.466(3)
P(1)-F(1)	1.5742(17)	N(5)-C(17)	1.137(3)
P(1)-F(6)	1.5876(15)	C(1)-C(2)	1.509(3)
P(1)-F(4)	1.5960(16)	C(4)-C(5)	1.338(3)

P(1)-F(5)	1.5992(16)	C(6)-C(11)	1.380(3)
P(1)-F(3)	1.6032(15)	C(6)-C(7)	1.388(3)
N(1)-C(3)	1.353(3)	C(7)-C(8)	1.390(3)
N(1)-C(4)	1.391(3)	C(8)-C(9)	1.389(4)
N(1)-C(2)	1.465(3)	C(9)-C(10)	1.388(3)
N(2)-C(3)	1.371(3)	C(10)-C(11)	1.376(3)
N(2)-C(5)	1.377(3)	C(13)-C(14)	1.343(3)
N(2)-C(6)	1.417(3)	C(15)-C(16)	1.519(3)
N(3)-C(12)	1.372(3)	C(17)-C(18)	1.458(3)

Table C.16: Bond lengths for [PhDC<sup>Et</sup>Ni(MeCN)]PF<sub>6</sub>

Bond	Angle	Bond	Angle
C(11)-Ni-N(5)	177.84(8)	C(12)-N(4)-C(14)	110.74(19)
C(11)-Ni-C(12)	80.09(9)	C(12)-N(4)-C(15)	125.73(19)
N(5)-Ni-C(12)	99.24(8)	C(14)-N(4)-C(15)	123.43(19)
C(11)-Ni-C(3)	80.17(9)	C(17)-N(5)-Ni	177.48(18)
N(5)-Ni-C(3)	100.37(8)	N(1)-C(2)-C(1)	111.69(19)
C(12)-Ni-C(3)	160.04(9)	N(1)-C(3)-N(2)	103.74(18)
F(2)-P(1)-F(1)	92.31(11)	N(1)-C(3)-Ni	140.88(16)
F(2)-P(1)-F(6)	90.66(10)	N(2)-C(3)-Ni	115.33(15)
F(1)-P(1)-F(6)	90.12(10)	C(5)-C(4)-N(1)	107.6(2)
F(2)-P(1)-F(4)	177.96(10)	C(4)-C(5)-N(2)	106.2(2)
F(1)-P(1)-F(4)	89.69(11)	C(11)-C(6)-C(7)	122.0(2)
F(6)-P(1)-F(4)	89.77(9)	C(11)-C(6)-N(2)	109.51(18)
F(2)-P(1)-F(5)	89.92(10)	C(7)-C(6)-N(2)	128.4(2)
F(1)-P(1)-F(5)	90.85(10)	C(6)-C(7)-C(8)	117.4(2)
F(6)-P(1)-F(5)	178.85(10)	C(9)-C(8)-C(7)	122.6(2)
F(4)-P(1)-F(5)	89.61(9)	C(10)-C(9)-C(8)	117.3(2)
F(2)-P(1)-F(3)	89.84(10)	C(11)-C(10)-C(9)	122.2(2)
F(1)-P(1)-F(3)	177.82(11)	C(11)-C(10)-N(3)	109.42(18)
F(6)-P(1)-F(3)	90.23(9)	C(9)-C(10)-N(3)	128.3(2)
F(4)-P(1)-F(3)	88.15(9)	C(10)-C(11)-C(6)	118.53(19)
F(5)-P(1)-F(3)	88.78(9)	C(10)-C(11)-Ni	120.80(16)
C(3)-N(1)-C(4)	110.70(19)	C(6)-C(11)-Ni	120.61(16)
C(3)-N(1)-C(2)	125.42(18)	N(4)-C(12)-N(3)	103.56(18)

C(4)-N(1)-C(2)	123.76(19)	N(4)-C(12)-Ni	141.12(17)
C(3)-N(2)-C(5)	111.71(19)	N(3)-C(12)-Ni	115.29(15)
C(3)-N(2)-C(6)	114.37(17)	C(14)-C(13)-N(3)	106.0(2)
C(5)-N(2)-C(6)	133.86(19)	C(13)-C(14)-N(4)	107.6(2)
C(12)-N(3)-C(13)	112.11(19)	N(4)-C(15)-C(16)	111.57(19)
C(12)-N(3)-C(10)	114.39(18)	N(5)-C(17)-C(18)	178.8(2)
C(13)-N(3)-C(10)	133.46(19)		

Table C.17: Bond angles for  $[\text{PhDC}^{\text{Et}}\text{Ni}(\text{MeCN})]\text{PF}_6$